



**HAL**  
open science

# Modeling of polarization-resolved lidar signals for the characterization of soot fractal aggregates accounting for multiple scattering

Lucas Paulien

► **To cite this version:**

Lucas Paulien. Modeling of polarization-resolved lidar signals for the characterization of soot fractal aggregates accounting for multiple scattering. Instrumentation and Detectors [physics.ins-det]. Université Paris-Saclay, 2022. English. NNT : 2022UPAST054 . tel-03735410

**HAL Id: tel-03735410**

**<https://theses.hal.science/tel-03735410>**

Submitted on 21 Jul 2022

**HAL** is a multi-disciplinary open access archive for the deposit and dissemination of scientific research documents, whether they are published or not. The documents may come from teaching and research institutions in France or abroad, or from public or private research centers.

L'archive ouverte pluridisciplinaire **HAL**, est destinée au dépôt et à la diffusion de documents scientifiques de niveau recherche, publiés ou non, émanant des établissements d'enseignement et de recherche français ou étrangers, des laboratoires publics ou privés.

# Modeling of polarization-resolved lidar signals for the characterization of soot fractal aggregates accounting for multiple scattering

*Modélisation de signaux lidar résolus en polarisation pour la caractérisation d'agrégats fractals de suie avec prise en compte de la diffusion multiple*

## Thèse de doctorat de l'Université Paris-Saclay

École doctorale n° 579, Sciences mécaniques et énergétiques, matériaux et géosciences (SMEMAG)  
Spécialité de doctorat: Energétique  
Graduate School : Sciences de l'ingénierie et des systèmes,  
Réfèrent : CentraleSupélec

Thèse préparée dans le laboratoire EM2C (Université Paris-Saclay, CNRS, CentraleSupélec), sous la direction de **Anouar SOUFIANI**, directeur de recherche, la co-direction de **Romain CEOLATO**, ingénieur de recherche, le co-encadrement de **Franck ENGUEHARD**, professeur et le co-encadrement de **Laurent SOUCASSE**, maître de conférences

Thèse présentée et soutenue à Toulouse, le 2 Mai 2022, par

**Lucas Paulien**

### Composition du jury:

<b>Rodolphe Vaillon</b> Directeur de recherche, Université de Montpellier	Président du jury et examinateur
<b>Alexis Coppalle</b> Professeur émérite, Université de Rouen	Examinateur et rapporteur
<b>Michael Kahnert</b> Associate Professor, Chalmers University of Technology	Examinateur et rapporteur
<b>Pascale Desgroux</b> Directrice de recherche, Université de Lille	Examinatrice
<b>Séverine Barbosa</b> Maîtresse de conférences, Aix-Marseille Université	Examinatrice
<b>Anouar Soufiani</b> Directeur de recherche, Université Paris-Saclay	Directeur
<b>Romain Ceolato</b> Ingénieur de recherche, ONERA, Université de Toulouse	Codirecteur
<b>Franck Enguehard</b> Professeur, Université de Poitiers	Coencadrant



### **Chercheurs invités:**

**Laurent Soucasse**

Maître de conférences, Université Paris-Saclay

Co-encadrant de thèse

**Jérôme Yon**

Directeur d'études, INSA Rouen

Invité



---

# Remerciements

Quatre ans! Une longue période à résumer en quelques lignes, d'autant plus que de nombreuses personnes mériteraient des paragraphes entiers afin que je puisse exprimer mes remerciements à leur égard. J'espère néanmoins que ces quelques mots seront suffisants.

Tout d'abord, je remercie mes directeurs de thèse, Romain Ceolato et Anouar Soufiani. Merci pour vos conseils et votre aide au cours de cette thèse. En particulier, merci à Romain pour ton encadrement et pour avoir su me guider lors des nombreuses difficultés que j'ai pu rencontrer (je pense notamment à la période de rédaction). Merci également à Anouar pour son accueil chaleureux lors de mes visites, ainsi que pour ton aide et ta réactivité. Ma reconnaissance va aussi à Franck Enguehard et à Laurent Soucasse, qui m'ont également encadré pendant cette thèse. Merci à vous deux pour vos conseils lors des réunions que nous avons eues au cours de ces trois ans, ainsi que pour vos retours sur le manuscrit.

Je souhaite également remercier l'équipe du DOTA, sans qui ces trois dernières années auraient sans doute semblé beaucoup plus longues. Merci à Florian, mon premier co-bureau, qui m'a accueilli à Toulouse et avec qui j'ai passé une super première année. Merci à Thomas pour les parties de pétanque, d'AoE2 et surtout pour toutes les discussions que nous avons eues à propos de nos difficultés. Bien sûr, merci également à tous les autres doctorants, CDD et alternants du DOTA pour les pauses-café et autres soirées mouvementées. Sans ordre particulier, merci à Nicolas, Guillaume, Simon R., Simon N., Sandra, Charly, Yohann, Andres, Gabriel, Romain, Matthieu, Rollin, Arnaud, Erwan, Thierry, William, Killian, Benoît, Kevin, Luc et Karl.

Merci également aux permanents du DOTA, tel qu'Ahmed, Aurélie, Marine, Nicolas, Stéphanie, et tous les autres pour leur accueil au sein du département. Un grand merci également à Thomas Rivière, grand gourou informatique du DOTA Toulouse, et Nicolas Rivière, pour leur accueil et leur aide.

Merci également aux copains de Lyon, notamment Anthony, Arthur, Kevin, Guillaume, Raphaël, Émilie, Nelly, Antoine et Nicolas. Un grand merci également à Maxime, Charline, Jérôme, Clément et Alexandre pour les (trop ?) nombreuses heures sur le discord.

Enfin, un grand merci à ma famille, à mes parents Bruno et Marie-Claire, ma grand-mère Mireille, à mon frère Tom et à ma sœur Alix pour leur soutien pendant ces trois années malgré la distance.



# Contents

<b>Contents</b>	<b>i</b>
<b>List of Symbols</b>	<b>v</b>
<b>List of Acronyms</b>	<b>ix</b>
<b>List of Figures</b>	<b>xi</b>
<b>List of Tables</b>	<b>xv</b>
<b>Introduction</b>	<b>1</b>
<b>I Soot particles, electromagnetic light scattering and lidar formalism</b>	<b>9</b>
Introduction . . . . .	9
I.1 Soot particles . . . . .	10
I.1.1 Particle formation . . . . .	10
I.1.2 Aggregates morphology . . . . .	12
I.1.3 Optical index . . . . .	20
I.2 Light scattering and absorption by particles . . . . .	22
I.2.1 Theoretical framework . . . . .	22
I.2.2 The Stokes parameters and the scattering matrix . . . . .	26
I.2.3 Radiative properties . . . . .	31
I.2.4 Modeling methods . . . . .	34
I.3 Light Detection And Ranging . . . . .	41
I.3.1 General description of lidar instruments . . . . .	41
I.3.2 Single scattering approximation and lidar equation . . . . .	45
I.3.3 Polarization lidar framework . . . . .	47
I.3.4 Multiple scattering in lidar . . . . .	50
Conclusion . . . . .	53
<b>II Evaluation of the radiative properties of soot fractal aggregates</b>	<b>55</b>
Introduction . . . . .	55
II.1 Numerical simulations of the radiative properties of soot particles . . . . .	57
II.1.1 General methods . . . . .	57
II.1.2 Soot fractal aggregates with monodisperse monomers . . . . .	58
II.1.3 Soot fractal aggregates with polydisperse monomers . . . . .	69
II.1.4 Superaggregates . . . . .	72
II.2 Evaluation of the Linear Depolarization Ratio of soot fractal aggregates . . . . .	82

II.2.1	Characterization of soot emitted from a kerosene pool-fire and experimental results . . . . .	82
II.2.2	Methods for the numerical evaluation of the LDR . . . . .	85
II.2.3	Numerical results . . . . .	87
	Considerations regarding the characterization of soot using lidars and conclusion . .	92
<b>III</b>	<b>Stochastic method for the simulation of polarization-resolved lidar signals accounting for multiple scattering</b>	<b>97</b>
	Introduction . . . . .	97
III.1	Description of the Monte-Carlo simulation program . . . . .	98
III.1.1	General presentation . . . . .	98
III.1.2	Architecture . . . . .	100
III.1.3	Problem geometry and input parameters . . . . .	101
III.2	Methods and variance reduction techniques . . . . .	104
III.2.1	Initialization . . . . .	104
III.2.2	Photon transport method . . . . .	107
III.2.3	Absorption and the notion of weight . . . . .	112
III.2.4	Peel-off scattering . . . . .	114
III.2.5	Angle sampling method . . . . .	121
III.2.6	Scattering and scattering splitting . . . . .	126
III.2.7	Return signal calculation . . . . .	134
III.3	Program validation . . . . .	138
III.3.1	Validation of the angle sampling method . . . . .	138
III.3.2	Comparison with the single scattering lidar equation . . . . .	154
III.3.3	Inter-comparison with available data from the literature . . . . .	157
	Conclusion . . . . .	161
<b>IV</b>	<b>Impact of multiple scattering on lidar signals for a scattering medium composed of soot particles</b>	<b>165</b>
	Introduction . . . . .	165
IV.1	Radiative properties and plume model . . . . .	166
IV.2	Lidar signals and correction factors . . . . .	171
IV.3	Phenomenological relationships . . . . .	178
IV.4	Analysis of an experimental lidar signal through Monte-Carlo modeling . . . . .	191
	Conclusion . . . . .	195
	<b>General conclusion and prospects</b>	<b>197</b>
<b>A</b>	<b>Standard deviation of the backscattering cross-sections of aggregates composed of monodisperse monomers</b>	<b>205</b>
<b>B</b>	<b>Comparison between the radiative properties aggregates composed of monodisperse and polydisperse monomers and impact of the optical index</b>	<b>215</b>
<b>C</b>	<b>Backscattering experiment set-up and formalism</b>	<b>223</b>
	<b>Synthèse</b>	<b>226</b>

**Bibliography**

**231**



# List of Symbols

$A$	Receiver effective area
$A_S$	Accumulated single-scattering fraction
$a_i, b_j$	Normalized scattering matrix elements
$a_{lm}, b_{lm}, c_{lm}, d_{lm}, p_{lm}, q_{lm}$	VSWF coefficients
$C_{abs}$	Absorption cross-section
$C_{ext}$	Extinction cross-section
$C_{pol}$	Polarized phase function normalization constant
$C_{sca}$	Scattering cross-section
$c_0$	Speed of light in vacuum
$dC_{bac}$	Backscattering cross-section
$dC_{sca}/d\Omega$	Differential scattering cross-section
$D_f$	Fractal dimension
$\mathbf{d}_i$	Photon direction vector
$\mathbf{E}$	Electric field vector
$E_0$	Electric field vector amplitude
$E(m_o)$	Absorption function
$\mathbf{F}$	Scattering matrix
$\tilde{\mathbf{F}}$	Normalized scattering matrix
$F_{ij}$	Scattering matrix elements
$f_{pol}$	Polarized phase function
$f_{\Delta l}, f_{\varphi}, f_{\Theta \varphi}$	Probability density function
$F_{\Delta l}, F_{\varphi}, F_{\Theta \varphi}, F_{\mu \varphi}$	Cumulative distribution function
$F(m_o)$	Scattering function
$g$	Auto-correlation function
$g_0$	Asymmetry parameter
$h$	Cut-off function
$\mathbf{H}$	Magnetic field vector
$H_i$	Slab upper plane distance
$H_0$	Magnetic field vector amplitude
$\mathbf{I}$	Stokes vector
$I, Q, U, V$	Stokes parameters
$j_{max}$	Number of computed scattering order
$k$	Wave number
$\mathbf{k}$	Wave vector
$\mathbf{K}$	Extinction matrix
$k_f$	Fractal prefactor

$k_o$	Absorptive index
$K_0$	Lidar instrumental constant
$L$	Length scale
$LR$	Lidar ratio
$L_{em}$	Pulse spatial with
$MSF$	Mutliple-scattering fraction
$m_o$	Optical index
$N_m$	Number of monomers
$n_o$	Refractive index
$n_p(r)$	Particle number concentration profile
$N_{ph}$	Number of emitted photon
$n_r$	Monomer radius size distribution
$n_s$	Particle size distribution
$O$	Lidar overlap function
$P$	Lidar received power
$\mathcal{P}$	Probability
$\mathbf{p}_{em}$	Emitter position vector
$\mathbf{p}_i$	Photon position vector
$\mathbf{p}_{rec}$	Receiver position vector
$\mathbf{q}$	Scattering wave vector
$q_{PO}, q_{daw}, q_{caw}, q_{ssw}$	Weight
$r$	Range/distance
$\mathbf{R}$	Stokes rotation matrix
$R_{cone}$	Scattering splitting cone radius
$R_{eff}$	Effective radius
$R_{em}$	Emitter radius
$R_g$	Radius of gyration
$r_m$	Monomer radius
$R_m$	Mean geometrical monomer radius
$R_{rec}$	Receiver radius
$r_v, r_s$	Volume-equivalent and surface-equivalent radius
$\mathbf{S}$	Amplitude scattering matrix
$S(q)$	Structure factor
$t_{min}, t_{max}$	Minimum/maximum path length
$U$	Attenuated backscatter function
$\mathbf{Z}$	Stokes phase matrix
$\alpha$	Extinction coefficient
$\alpha_j^p$	Dipole polarizability
$\alpha_l, \beta_l$	Lorenz-Mie coefficients
$\beta$	Backscattering coefficient
$\gamma_r$	Gamma distribution shape parameter
$\delta_p, \delta_v, \delta_{lab}, \delta_{num}$	Linear depolarization ratio
$\delta_{acc}$	Accumulated depolarization ratio
$\Delta t$	Time interval/Length step
$\zeta$	Scattering splitting receiver angle
$\eta$	Multiple-scattering correction factor

---

$\eta_0$	Pseudo-random number
$\theta$	Scattering angle
$\theta_{cone}$	Scattering splitting cone angle
$\theta_{em}$	Laser beam divergence
$\theta_{rec}$	Receiver FOV half-angle
$\theta_{split}$	Scattering splitting angle
$\kappa$	Percent disagreement/error
$\lambda$	Wavelength
$\mu$	Scattering angle cosine
$\rho_i$	Photon reference vector
$\sigma_m$	Monomer radius size distribution standard deviation
$\sigma_r$	Gaussian profile standard deviation
$\tau_0$	Pulse temporal width
$\phi$	Azimuthal angle
$\omega$	Angular frequency
$\omega_0$	Single-scattering albedo



# List of Acronyms

- APD** Avalanche Photodiodes
- AR** Assessment Report
- BA** Ballistic Aggregation
- BCA** Ballistic Cluster Aggregation
- CCA** Cluster-Cluster Aggregation
- CDF** Cumulative distribution function
- CLT** Central Limit Theorem
- DDA** Discrete Dipole Approximation
- DIAL** Differential Absorption Lidar
- DLA** Diffusion-Limited Aggregation
- DLCA** Diffusion-Limited Cluster Aggregation
- FOV** Field-Of-View
- HACA** Hydrogen Abstraction-C<sub>2</sub>H<sub>2</sub> acetylene Addition
- IPCC** Intergovernmental Panel on Climate Change
- lidar** Light Detection and Ranging
- LDR** Linear Depolarization Ratio
- LLN** Law of Large Numbers
- MSF** Multiple Scattering Fraction
- MSTM** Multiple Sphere T-Matrix
- Nd:YAG** Neodymium-doped Yttrium Aluminum Garnet
- PAH** Polycyclic Aromatic Hydrocarbons
- PDF** Probability density function

- PMT** Photomultiplier Tubes
- PLA** Piecewise Linear Approximation
- QSA** Quasi-Small-Angle
- RDG-FA** Rayleigh-Debye-Gans for Fractal Aggregates
- RF** Radiative Forcing
- RLA** Reaction-Limited Aggregation
- RLCA** Reaction-Limited Cluster Aggregation
- RMSE** Root Mean Square Error
- STM** Superposition T-Matrix
- TCCA** Tunable Cluster-Cluster Aggregation
- TEM** Transmission Electron Microscopy
- VSWF** Vector Spherical Wave Function

# List of Figures

1	Global inventory of the radiative forcing induced by different categories of components [1]. . . . .	2
2	TEM image of a soot particle emitted by a JET A-1 pool fire [2]. . . . .	4
I.1	Schematic of the stages leading to the formation of soot particles [3]. . . . .	10
I.2	TEM image of a soot primary particle. Figures taken from [4]. . . . .	12
I.3	Self-similarity of aggregates for (a) deterministic aggregates (b) disordered aggregates as illustrated by Jullien [5]. . . . .	14
I.4	Number of monomers against the radius of gyration normalized by the monomer radius for ensembles of aggregates. . . . .	16
I.5	Examples of (a) overlapping and (b) necking on soot aggregates. Figure taken from [6]. . . . .	20
I.6	Illustrative schematic of the far-field approximation. . . . .	25
I.7	Coordinate system. . . . .	26
I.8	Ellipsometric interpretation of the Stokes parameters. . . . .	28
I.9	Schematic view of an atmospheric lidar instrument. . . . .	43
I.10	Schematic view of the overlap function. . . . .	46
I.11	Frame of reference for the polarization state of the emitted wave and the received wave. . . . .	49
I.12	Example of the mechanism associated with multiple scattering for two particles. . . . .	51
II.1	Extinction (a), scattering (b) and backscattering (c) cross-sections of soot fractal aggregates ensembles. . . . .	61
II.2	Single scattering albedo (left figures; (a), (c) and (e)) and lidar ratio (right figures; (b), (d) and (f)) of ensembles of aggregates. . . . .	64
II.3	Linear depolarization ratios of ensembles of aggregates composed of monodisperse monomers. . . . .	65
II.4	Impact of the number of aggregates per ensemble on the backscattering cross-sections average and standard deviation. . . . .	68
II.5	Scattering matrix elements $a_1$ , $a_2$ and $b_1$ of the aggregates at the different wavelengths. . . . .	71

II.6	Schematic view of the principle of the auto-correlation function calculation algorithm. . . . .	74
II.7	Structure factors $S(q)$ and auto-correlation function $g'(r/r_m)$ of the canonical aggregate and of the superaggregate. . . . .	76
II.8	Scattering and extinction cross-sections of the canonical aggregate and of the superaggregate. . . . .	77
II.9	Backscattering cross-sections and linear depolarization ratio of the canonical aggregate and of the superaggregate. . . . .	78
II.10	Rayleigh-Debye-Gans approximation criterion as a function of wavelength. . . . .	80
II.11	Schematic view of the experimental set-up, TEM image of a soot aggregate and of a monomer generated from the JET A-1 pool fire and corresponding monomer radius size distribution . . . . .	84
II.12	Examples of numerically generated aggregates and corresponding size distribution. . . . .	86
II.13	Simulated scattering matrix elements ratio and LDR for ensembles of aggregates formed by monodisperse monomers. . . . .	88
II.14	Simulated scattering matrix elements ratio and LDR for ensembles of aggregates formed by polydisperse monomers. . . . .	89
II.15	Discrepancy $\kappa$ between the laboratory and numerical experiments. . . . .	91
III.1	Simplified schematic of the program architecture. . . . .	100
III.2	Simplified schematic of the lidar geometry within the program. . . . .	101
III.3	Architecture of the photon initialization process. . . . .	105
III.4	Schematic view of the photon transport process. . . . .	108
III.5	Architecture of the photon transport process. . . . .	109
III.6	Architecture of the peel-off scattering process. . . . .	116
III.7	Schematic view of the architecture of the scattering step. . . . .	127
III.8	Schematic view of the triggering conditions of the scattering splitting technique. . . . .	129
III.9	Complete architecture of the lidar signal simulation program. . . . .	137
III.10	First element of the Stokes vector scattered by Rayleigh scatterers and averaged over the azimuthal angles. . . . .	141
III.11	First element of the tabulated Stokes vector scattered by Rayleigh scatterers. . . . .	142
III.12	Percent disagreements of the sampled first element of the Stokes vector scattered by Rayleigh scatterers. . . . .	143
III.13	Second element of the Stokes vector scattered by Rayleigh scatterers and averaged over the azimuthal angles. . . . .	144

III.14	Second element of the tabulated Stokes vector when scattered by Rayleigh scatterers. . . . .	145
III.15	Percent disagreements of the sampled second element of the Stokes vector scattered by Rayleigh scatterers. . . . .	146
III.16	First element of the Stokes vector scattered by spherical particles and averaged over the azimuthal angles. . . . .	147
III.17	Percent disagreements of the sampled first element of the Stokes vector scattered by spherical particles. . . . .	148
III.18	First element of the tabulated Stokes vector scattered by spherical particles. . .	149
III.19	Second element of the sampled Stokes vector scattered by spherical particles and averaged over the azimuthal angles. . . . .	150
III.20	Second element of the tabulated Stokes vector scattered by spherical particles.	152
III.21	Percent disagreements of the sampled second element of the Stokes vector scattered by spherical particles. . . . .	153
III.22	First case of validation between the output signal of the Monte-Carlo program at first order of scattering and the single scattering lidar equation. . . . .	156
III.23	Second case of validation between the output signal of the Monte-Carlo program at first order of scattering and the single scattering lidar equation. . . . .	156
III.24	Accumulated single scattering fraction as a function of the accumulated depolarization ratio. . . . .	160
IV.1	Example of a multiply-scattered lidar signal, single-scattering signal and associated correction factors. . . . .	171
IV.2	Optical depth and extinction coefficient as a function of the distance to the receiver.	172
IV.3	Examples of simulated signals and multiple scattering correction factors. . . . .	174
IV.4	Polarization-resolved lidar signals, LDR and multiple scattering factors as a function of the distance from the receiver with a receiver FOV of $\theta_{rec} = 0.5$ mrad. . .	177
IV.5	Polarization-resolved lidar signals, LDR and multiple scattering factors as a function of the distance from the receiver with a receiver FOV of $\theta_{rec} = 5$ mrad. . . . .	178
IV.6	Multiple scattering fraction and LDR with varying soot plume optical depth. . . .	180
IV.7	Multiple scattering fraction as a function of the linear depolarization ratio computed with the dispersion law from Chang and Charalampopoulos [7]. . . . .	184
IV.8	Multiple scattering fraction as a function of the linear depolarization ratio computed with the optical index from Bescond et al. [8]. . . . .	185
IV.9	Multiple scattering fraction as a function of the linear depolarization ratio computed with the optical index from Schnaiter et al. [9]. . . . .	186
IV.10	Multiple scattering fraction as a function of the linear depolarization ratio computed with the optical index from Chang and Charalampopoulos [7], with a square profile. . . . .	188

IV.11	Single-scattering and multiple scattering contributions to the total signal. . . . .	190
IV.12	Extinction and backscattering coefficients resulting from the lidar inversion procedure. . . . .	193
IV.13	Multiple scattering fraction and time averaged multiple scattering fraction resulting from the Monte-Carlo simulation. . . . .	195
A.1	Relative standard deviation of the backscattering cross-section, for aggregates with monodisperse monomers and with $r_m = 10$ nm. . . . .	206
A.2	Relative standard deviation of the backscattering cross-section, for aggregates with monodisperse monomers and with $r_m = 20$ nm. . . . .	207
A.3	Relative standard deviation of the backscattering cross-section, for aggregates with monodisperse monomers and with $r_m = 40$ nm. . . . .	208
A.4	Relative standard deviation of the backscattering cross-section, for aggregates with monodisperse monomers and with $r_m = 10$ nm and using the alternative formulation. . . . .	210
A.5	Relative standard deviation of the backscattering cross-section, for aggregates with monodisperse monomers and with $r_m = 20$ nm and using the alternative formulation. . . . .	211
A.6	Relative standard deviation of the backscattering cross-section, for aggregates with monodisperse monomers and with $r_m = 40$ nm and using the alternative formulation. . . . .	212
B.1	Extinction cross-section. . . . .	216
B.2	Scattering cross-section. . . . .	216
B.3	Backscattering cross-section. . . . .	217
B.4	Relative difference between the cross-sections of monodisperse aggregate and polydisperse aggregates . . . . .	218
B.5	Single-scattering albedo. . . . .	219
B.6	Lidar ratio. . . . .	220
B.7	Linear Depolarization Ratio. . . . .	221
C.1	Schematic view of the experimental set-up. . . . .	225

# List of Tables

I.1	Micro-physical parameters of soot aggregates found in the literature. . . . .	18
II.1	Radiative properties of soot aggregates with polydisperse monomers. . . . .	70
II.2	Radiative properties of the canonical aggregate. . . . .	81
II.3	Radiative properties of the superaggregate. . . . .	81
II.4	Evaluation of the ratio $[F_{22}(\pi)/F_{11}(\pi)]_{lab}$ and the LDR $\delta_{lab}$ of soot particles emitted from a JET A-1 pool fire. . . . .	85
III.1	List of the input parameters of the Monte-Carlo program. . . . .	103
III.2	List of the defining parameters of a photon in the Monte-Carlo code. . . . .	104
III.3	List of the parameters used in the transport step. . . . .	107
III.4	List of the parameters used in the peel-off scattering process. . . . .	115
III.5	List of the parameters used in the scattering and scattering splitting process. . . . .	128
III.6	Variable parameters between the different simulated cases. . . . .	158
III.7	Constant parameters for all the simulations. . . . .	158
III.8	Root mean square error of the simulations with geometric thickness $H_c = 1.0$ km. . . . .	159
III.9	Root mean square error of the simulations with geometric thickness $H_c = 0.2$ km. . . . .	159
IV.1	Radiative properties of the modeled soot aggregates with polydisperse monomers, computed with Bescond et al. [8] optical index. . . . .	167
IV.2	Radiative properties of the modeled soot aggregates with polydisperse monomers, computed with Schnaiter et al. [9] optical index. . . . .	168
IV.3	Radiative properties of the modeled soot aggregates with polydisperse monomers, computed with Chang and Charalampopoulos [7] dispersion law. . . . .	168
IV.4	List of the input parameters of the Monte-Carlo program. . . . .	170
IV.5	Coefficients of the regression analyses for the simulations undertaken with soot particles whose optical index is taken from Chang and Charalampopoulos [7]. . . . .	182
IV.6	Coefficients of the regression analyses for the simulation undertaken with soot particles whose optical index is taken from Bescond et al. [8]. . . . .	182

---

IV.7	Coefficients of the regression analyses for the simulation undertaken with soot particles whose optical index is taken from Schnaiter et al. [9]. . . . .	182
IV.8	Parameters of the regression analysis for the simulations undertaken with a square profile, considering a receiver FOV $\theta_{rec} = 5$ mrad. . . . .	189
IV.9	Radiative properties of the modeled soot aggregates using the RDG-FA theory. .	192
IV.10	List of the input parameters of the Monte-Carlo program. . . . .	194

# Introduction

The past forty years have been marked by an increasing awareness of the impacts of the human activities on the environment. These impacts include changes in climate patterns, land transformations, biodiversity collapse, the increased frequency of extreme weather events, sea-level rise and others. The Intergovernmental Panel on Climate Change (IPCC) has been created with the prospect to study these impacts and their causes, and to provide prevision on the evolution of these human-induced changes as well as recommendations based on the scientific consensus. The work of the IPCC is synthesized in Assessment Reports (AR) which are released at regular intervals. The fifth AR [1] indicates the foremost importance of the greenhouse gases and of the aerosols emitted by human activities on the energy budget of the Earth. This budget quantifies the radiative energy reaching the Earth and the outgoing energy. The influence of the different atmospheric components on this budget is quantified using the radiative forcing (RF) expressed in  $\text{W}\cdot\text{m}^{-2}$ . The RF of an atmospheric component can be either positive, which means that this component induces a warming, or negative, which induces cooling. Figure 1 summarizes the current knowledge on the principal atmospheric components RF.

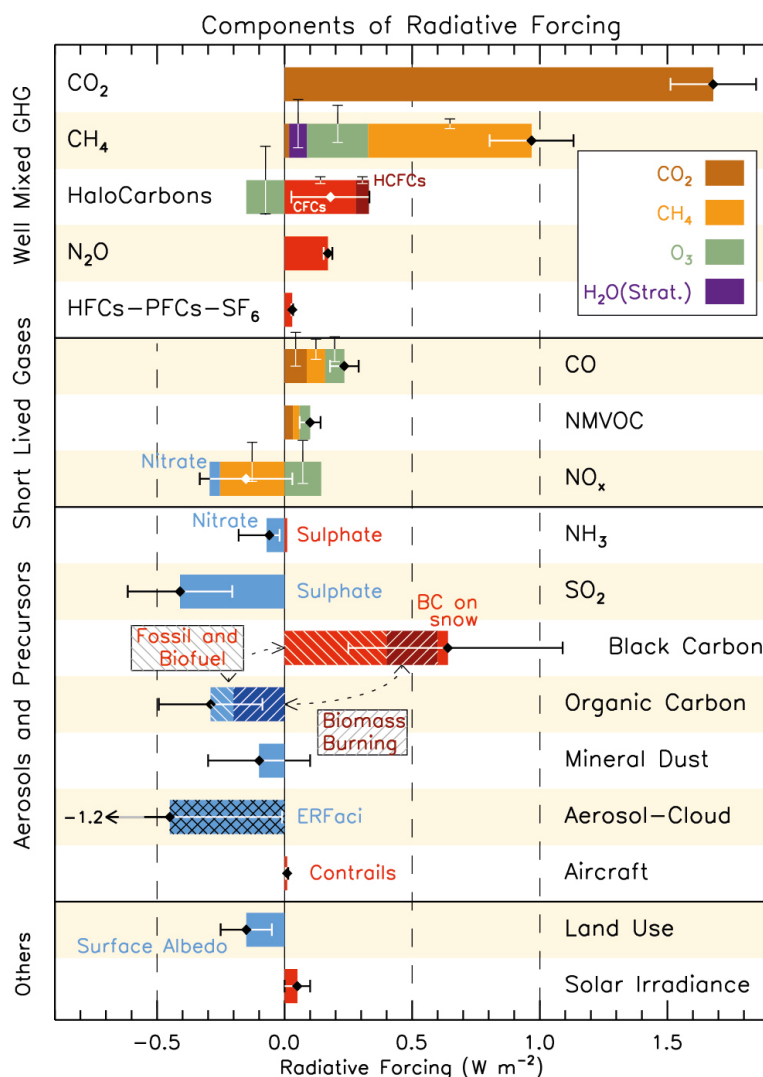


Figure 1: Global inventory of the radiative forcing induced by different categories of components [1].

Several main contributors to the global warming are shown on Figure 1. First, the greenhouse gases CO<sub>2</sub> and CH<sub>4</sub> amount for a majority of the positive RF. Particular matter in suspension in the air, called aerosols, are also accounted for in this figure. Black carbon aerosols are found to also induce a positive RF. Black carbon aerosols are a category of aerosols referring to particles emitted during the incomplete combustion of organic materials, which have a high light-absorbing capacity across the visible to infrared spectrum and are mostly composed of carbon. Black carbon aerosols RF can be caused by two categories of effects; (i) the direct effect, caused by light-absorption by the particles and thermal emission; (ii) the indirect effects, which are caused

through the interaction of black carbon aerosols with other components of the climate system. Among others, indirect effects include the modification of surface albedo caused by black carbon deposited on snow [10] or the nucleation processes leading to the formation of clouds [11, 12]. Black carbon particles also have a negative impact on air quality. Indeed, their sub-micronic size and molecular composition have been found to cause lung and artery diseases, as well as cancers [13, 14].

Figure 1 also shows high uncertainties concerning the exact value of black carbon RF. This uncertainty is partly due to a lack of knowledge on several critical aspects such as the mass of emitted aerosols [15], the atmospheric lifetime of these particles and their radiative properties. This last aspect is also related to several properties of black carbon particles, such as their optical index and their shape.

In the literature, the terms "soot particles" and "black carbon particles" are sometimes used interchangeably [16]. In this thesis, we consider that black carbon aerosols refer to a category of aerosols which regroups several types of particles. Among these particles, soot particles are characterized by their characteristic morphology. Indeed, they are composed of clustered primary particles called monomers, which form aggregates of various shapes and sizes [17, 18, 19]. Figure 2 presents a Transmission Electron Microscopy (TEM) image of a soot particle.

The systematic monitoring of atmospheric components generally requires the use of remote-sensing methods, such as Light Detection And Ranging (lidar) instruments. These instruments emit laser pulses in the atmosphere and measure the radiation elastically-scattered in the backward direction by the atmospheric components [20]. Using inversion methods, the acquired signal can provide information on these components, such as the type of aerosols present during the measurement or their particle number concentration [21, 22]. Nevertheless, these inversion methods require *a priori* knowledge of the particles radiative properties and often makes use of the single scattering approximation [20, 23]. This approximation supposes that the radiation scattered by an aerosol under illumination by a lidar instrument depends solely on the incoming laser radiation. Hence, in the single scattering approximation, the contribution of the interdependence of the scattered radiation is neglected. This neglected contribution is usually called

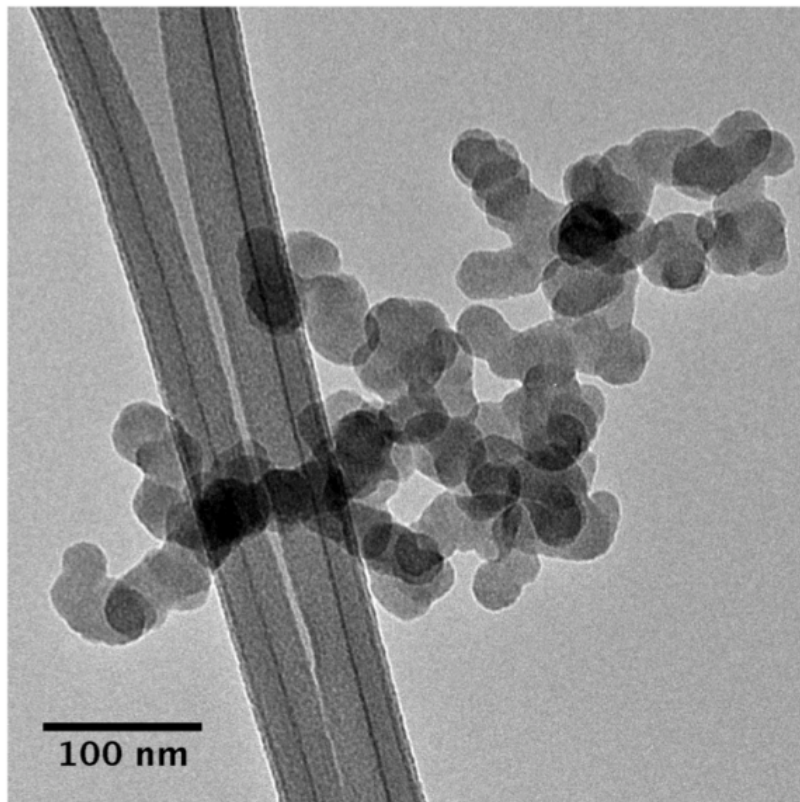


Figure 2: TEM image of a soot particle emitted by a JET A-1 pool fire [2].

multiple scattering, and can induce an increase in the received radiation by the lidar instrument. Hence, the single scattering approximation can induce errors in the retrieved quantities following the use of inversion methods [24].

In the literature, the combustion products under measurement by lidar instruments are most often referred to as smoke [25, 26, 27]. The term soot appears rarely, which can be justified by several reasons. The morphology of the particles under measurements is generally unknown, and the use of more general terms prevents the false identification of a specific type of particles such as soot. Moreover, the volume occupied by the emitted pulse in lidar instrument does not necessarily contain only one type of particle. This is particularly significant in the cases where forest fires are the source of emission. Indeed, in this case, soot particles account for a few percent up to fifteen percent of the emitted particles [28, 29]. The conditions of these fires, and the ageing of the emitted particles during their transport, implies that a large variety of particles can be accounted for in these measurements.

To our knowledge, there exists no lidar measurements yet where the assumption of a scattering medium composed exclusively of freshly emitted soot particles would be justified. Such measurements imply that soot particles must be the predominant type of particles emitted, which depends on the fuel type and on the combustion process [30, 31]. Lidar measurements acquired in close proximity to a source known to release soot particles as its major particulate emissions would allow this assumption to be justified. The proximity to the source would mitigate mixing with other ambient particles and prevent ageing during the atmospheric transport. Nevertheless, such measurements still require *a priori* knowledge on the particles radiative properties, and the evaluation of potential multiple scattering effects. Hence, in order to reduce the uncertainty associated to black carbon particles RF and to better ascertain the effects of these particles on Earth's climate and on air quality, there is a need to expand experimental measurements on soot particles, which requires the determination of their radiative properties.

Two approaches can be used in order to determine the radiative properties of soot particles. Experimental measurements can be performed in order to measure the radiative properties used in lidar inversion processes. The main limitations of these experimental measurements are the need for a controlled laboratory environment which replicates atmospheric conditions, and the cost associated to proceeding to these measurements while exploring the range of variables. On the other hand, the numerical approach can be used to systematically simulate radiative properties for different morphologies, but relies on morphological models which only approximate the shape of soot particles. Similarly, the multiple scattering effects can be modeled using stochastic methods, allowing to correct the lidar signals.

The work presented in this thesis follows the problematic developed in this introduction. In order to better ascertain the effect of black carbon particles on climate change and air quality, the monitoring of the emission of these particles is needed, including soot particles. Lidar instruments can provide such measurements, but require the knowledge of the particles radiative properties and can be subject to error due to multiple scattering effects. Moreover, the radiative properties of such particles depend on their micro-physical characteristics, such as shape and size.

The aim is to simulate polarization-resolved lidar signals acquired on soot particles accounting for multiple scattering. This requires the modeling of the morphology and of the radiative properties of these particles and the development of a lidar signal simulation code. The simulated radiative properties can then be used to provide the *a priori* information in lidar inversion methods, and the simulated signals to evaluate the potential impact of multiple scattering. The outline of this thesis follows this bottoms-up approach and is separated into four chapters:

- Chapter 1 provides more details on the different aspects of this thesis. The mechanisms leading to the formation of soot particles, their morphology, the numerical models used to simulate them are described. A non-exhaustive list of the optical indices of soot particles is also provided. These optical indices are used in light-scattering computation, the formalism of which is described in the second section. Several methods used to compute radiative properties are described. The last section is dedicated to lidar instruments and their framework. Overall, this chapter provides more details on the problematic of this thesis and the multiscale complexity associated with lidar measurements of particles.
- Chapter 2 presents the modeling of soot particles radiative properties. The influence of the soot particles micro-physical parameters on the radiative properties is studied. Moreover, this chapter presents the experimental measurement of airborne soot particles linear depolarization ratio, and the associated numerical study.
- Chapter 3 describes the numerical method developed for the simulation of polarization-resolved lidar signals. The code is presented, and each technique used within it is described. This chapter also presents validation procedures undertaken to assess the code performances.
- Chapter 4 is dedicated to the simulation of lidar signals using the radiative properties computed in chapter 2 and the method developed in chapter 3. Several scattering media aiming to model soot plume are studied. This chapter presents relationships between several quantities of interest quantifying the impact of multiple scattering. Moreover, simulations

are undertaken using a medium reproducing experimental lidar measurements. This allows to assess the validity of the single scattering approximation.



# Chapter I

## Soot particles, electromagnetic light scattering and lidar formalism

### Introduction

The monitoring of soot particles by elastic backscatter lidar instruments is limited by the *a priori* knowledge needed for the inversion of the acquired signal. Among this needed information are the radiative properties of the interacting particles, which in turn depend on the particles size, shape and optical index.

This chapter presents the theoretical basis, the formalism and several examples of methods used to address this problematic. First, emphasis is put on the soot particles themselves. Their morphology and formation process are described. The methods used to numerically simulate these particles are presented, and a summary of different studies on the soot particles optical index is presented. In the second section, the light-scattering formalism, the radiative properties relevant to this thesis and the numerical methods used to compute them are described. The last section of this chapter is dedicated to lidar instruments. A general description of these instruments is provided and the formalism they operate on is described. The distinction is made between the single scattering approximation and the multiple scattering process. The impacts of the latter on the lidar signal are described. Several methods used to evaluate multiple scattering

are described.

## I.1 Soot particles

### I.1.1 Particle formation

The formation of soot particles is due to an incomplete combustion of organic materials. Incomplete combustion occurs when the reaction stoichiometry is not verified, and leads to the production of several byproducts such as carbon monoxide, Polycyclic Aromatic Hydrocarbons (PAH) and soot particles. Several stages lead to the formation of soot particles [3], namely:

- Pyrolysis
- Nucleation
- Surface growth and coalescence
- Agglomeration

Figure I.1 presents a schematic view of these stages.

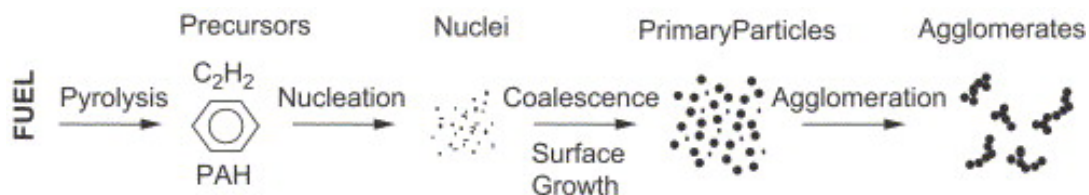


Figure I.1: Schematic of the stages leading to the formation of soot particles [3].

The pyrolysis step occurs when the fuel materials are heated above their decomposition temperature. This results in the breaking of molecular bonds, and the formation of several species involved in the formation of soot particles. Among these products of pyrolysis are PAHs and acetylene (C<sub>2</sub>H<sub>2</sub>) [3].

The nucleation step refers to the transition between gas phase and solid phase in the particle formation process. The Hydrogen abstraction-C<sub>2</sub>H<sub>2</sub> acetylene addition (HACA) process [32, 33] is thought to be the main route leading to soot inception. It consists in a two-step reaction. The

first step converts the PAH to a radical by abstraction of an hydrogen atom. The second step sees the addition of a small hydrocarbon molecule (*e.g.* C<sub>2</sub>H<sub>2</sub>) to the larger PAH radical, resulting in the formation of larger ring structures which eventually transition to the solid phase [34]. The particles formed during this process are called nuclei and have diameters in the range of 1.5-2 nm [3].

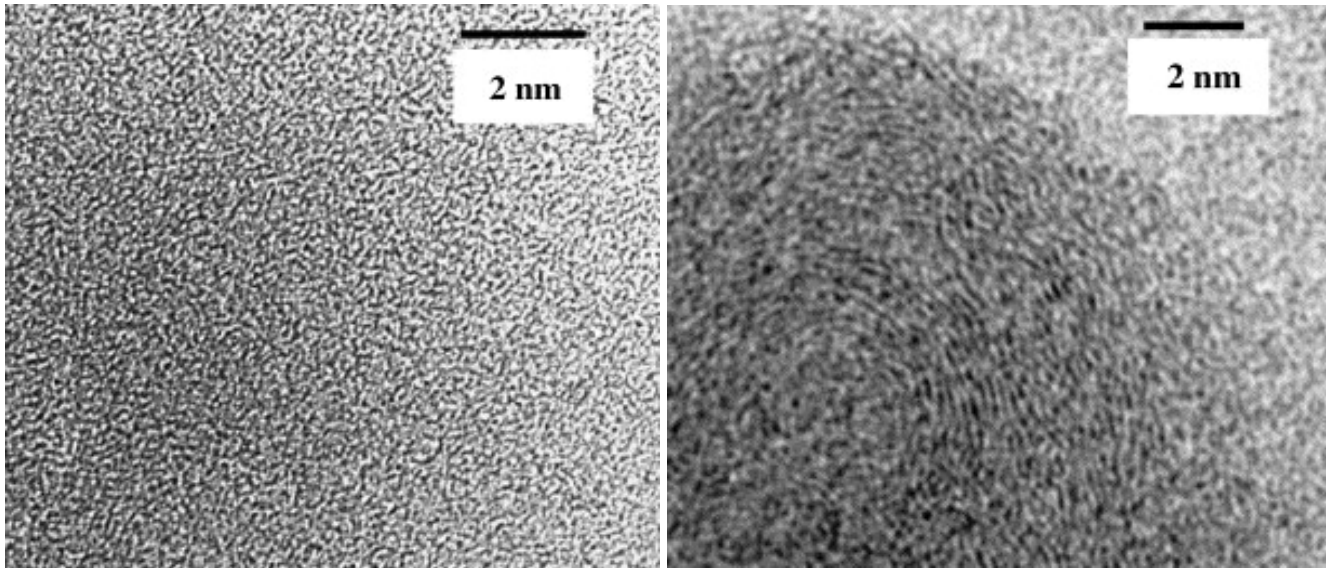
Primary particles are formed by the combination of surface growth and coalescence. Surface growth on the nuclei consists in the addition of C<sub>2</sub>H<sub>2</sub> to the surface of the nuclei on active radical sites [35]. The majority of the soot particles mass is added during this phase [35]. This process is similar to the nucleation stage but is distinct by the involvement of solid-phase matter. On the other hand, coalescence is the process leading to the combination of two nuclei into a single larger particle, decreasing the number of particles and increasing the volume of the remaining particles [36]. These primary particles are also called monomers, and their size range from a few nanometers to several several tens of nanometers.

Finally, the agglomeration stage leads to the formation of aggregates. During this process, two or more particles can enter in contact and stick together. This results in the formation of clusters which can in turn be agglomerated, forming chain-like structures called aggregates. This process occurs rather late in the formation of soot particles, when primary particles are already formed in their final shape [34]. The overall morphology of soot aggregates is described in section I.1.2.

The structure of the primary particles at the mesoscopic scale consists of alternating amorphous carbon and crystalline graphite layers [37]. These layers can be either disordered or in concentric planes [4]. Such layering can be observed by means of the Transmission Electron Microscopy (TEM) method, and are presented in Figure I.2(a) and (b) respectively.

Oxidation is another process which occurs during the whole length of the formation process. During the nucleation stage, PAH oxidation can prevent the further growth of aromatics. In this stage, numerical simulations find that the O<sub>2</sub> molecules and OH radicals can occupy radical sites on the PAH, hence partially suppressing the HACA process effects. Surface growth is also counterbalanced by the oxidation process [3].

All the processes described above are dependent on the combustion conditions, such as tem-



(a) Amorphous, or disordered, monomer structure. (b) Monomer structure with graphitic concentric planes.

Figure I.2: TEM image of a soot primary particle. Figures taken from [4].

perature, flow rate, pressure, fuel composition, fuel/air ratio and the type of flame (*e.g.* laminar or turbulent, premixed). Vander Wal and Tomasek [38] found differences in the curvature of the graphite layer and in the graphite content according to temperature and flow rate. Carbon content in fuel increases soot formation, while oxygen and hydrogen contents decrease it due to the competing oxidation process [3]. Glassman [39] found that higher temperatures decrease soot production in premixed flames, as the oxidation rate increases faster with temperature than the pyrolysis rate forming the PAH. In laminar flames, the production of soot increases with temperature.

### I.1.2 Aggregates morphology

Soot aggregates are formed during the last stage described in section I.1.1. Considering the change of scale between the primary particles inception and the aggregated particles, different models are used in order to describe the aggregates morphology. This section discusses the models used in order to describe such aggregates, as well as several main morphological features.

### Fractal model

The fractal theory, first introduced by Mandelbrot [40, 41], allows to describe repeating geometrical patterns through mathematical models. A fractal is defined as an irregular geometrical pattern which is found to be self-similar when observed from different scales, meaning a closely resembling part of the original pattern can be observed using a change of the observer point-of view (*i.e.* through magnification). Soot aggregates are usually described using a fractal-like model [17], owing to morphological features which are resembling those of fractal objects.

Figure I.3 presents an example of exact self-similarity on subfigure (a), and of a fractal-like object self-similarity on subfigure (b). Figure I.3(a) is known as the Vicsek fractal [42], built by the iterative assembly of four primary particles in a cross shape. The cross-shaped structure is then considered as the primary particle itself, and the process is repeated. If this process is repeated long enough, one can enlarge each picture and find the same pattern for as long as individual particles cannot be discerned, which defines self-similarity. Figure I.3(b) presents a numerically built aggregate using a stochastic Cluster-Cluster Aggregation (CCA) method. During the successive enlargement, the aggregate does not appear identical. Nevertheless, if several aggregates are generated withing the same experiment, the enlarged picture of any formed aggregate would be indistinguishable from any other aggregates. The self-similarity of these aggregates is then valid on average.

Another property of aggregates is the correlation in the mass density distribution as first described by [17]. It can be expressed using the density auto-correlation function  $g(r)$ , which conveys the probability of finding a primary particle at a distance  $r$  of another primary particle. This auto-correlation function varies as a power law such as [43]:

$$g(r) \propto r^{D_f-3}h(r) \quad (I.1.1)$$

where  $h$  is a cut-off function expressing the spatial limit of the particles and  $D_f$  is the fractal dimension. This fractal dimension is also an important feature of fractal aggregates. This parameter expresses the degree of occupation of the primary particles. In a three-dimensional space,

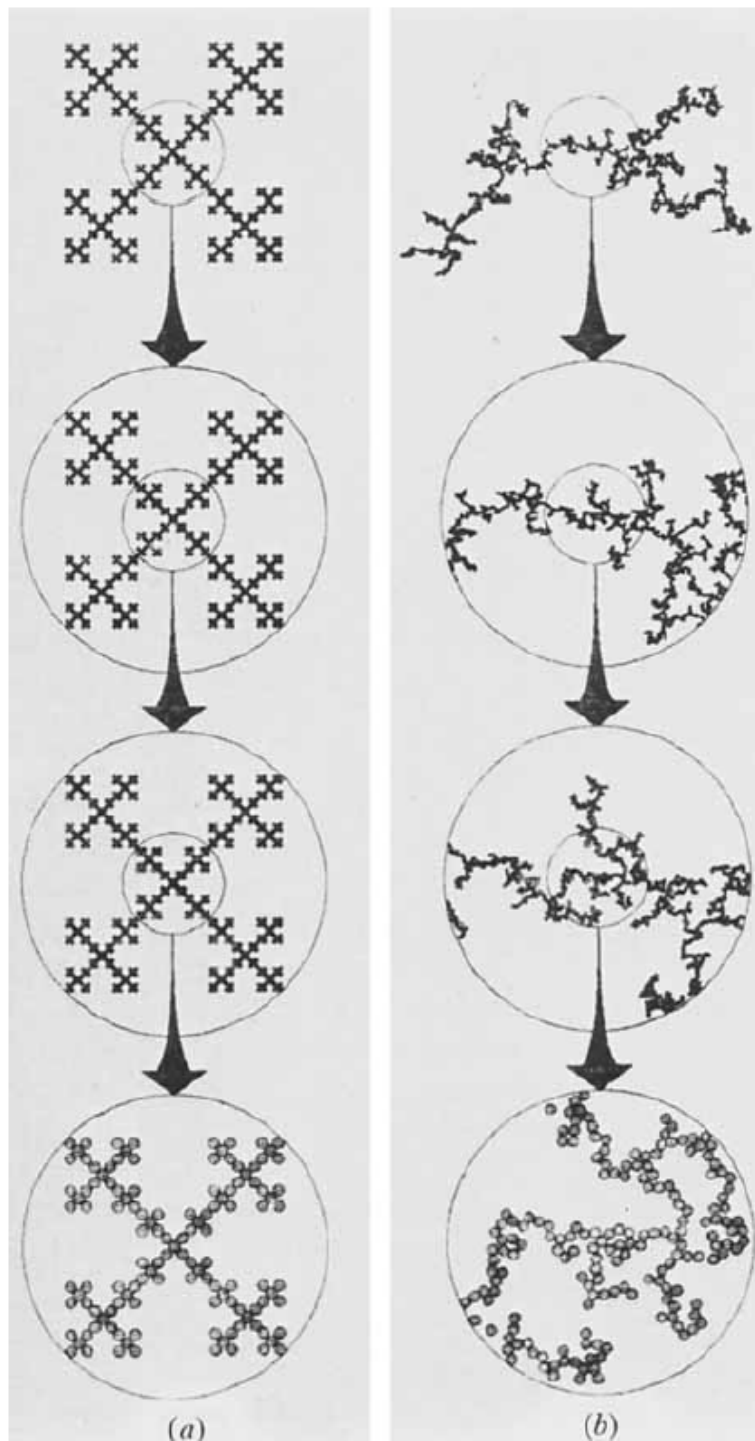


Figure I.3: Self-similarity of aggregates for (a) deterministic aggregates (b) disordered aggregates as illustrated by Jullien [5].

primary particles arranged in a sphere would have a fractal dimension of three, while primary particles arranged in a straight line would have a fractal dimension of one. Figure I.4 presents examples of numerically generated fractal aggregates showing the influence of the fractal di-

mension on the overall shape of the particles. The fractal dimension also intervenes in a scaling relationship characteristic of fractals:

$$N_m \propto L^{D_f} \quad (I.1.2)$$

where  $N_m$  is a number of primary particles (or monomers) and  $L$  is a length scale. This expression gives a qualitative assessment of the number of primary particles that can be expected to be found within a sphere of radius  $r$  centered on the aggregates center of mass [3, 44]. Equation I.1.2 remains valid as long as spherical primary particles are considered, whether monodisperse or polydisperse. Otherwise, the quantity  $N_m$  needs to be replaced by a measure of the mass of the aggregate [45].

In the case of soot fractal aggregates, Equation I.1.2 is written:

$$N_m = k_f \left( \frac{R_g}{r_m} \right)^{D_f} \quad (I.1.3)$$

where  $k_f$  is the fractal prefactor,  $R_g$  is the radius of gyration of the aggregates and  $r_m$  is the monomer radius. This equation introduces the main micro-physical parameters used throughout this study.

The radius of gyration  $R_g$  is a measure of the overall size of the aggregate. It is computed as:

$$R_g = \sqrt{\frac{1}{N_m} \sum_{i=1}^{i=N_m} x_i^2} \quad (I.1.4)$$

where  $x_i$  is the distance from the  $i$ th monomer center to the center of mass of the aggregate. The use of the radius of gyration for the length scale definition stems from its usefulness in the Rayleigh-Debye-Gans theory for Fractal Aggregates, which will be further detailed in Section I.2.4.

The fractal prefactor  $k_f$  is linked to the use of the radius of gyration as the length scale. Indeed, it represents the underlying proportionality constant of Equation I.1.2, and is by consequence dependent on the length scale [45]. The fractal prefactor is also related to the local packing of the monomers [46, 47].

A straightforward application of Equation I.1.3 is the retrieval of the fractal dimension  $D_f$  and of the fractal prefactor  $k_f$ . Knowing the number of monomers, their radius and the radius of gyration, a nonlinear regression method can be used in order to retrieve  $D_f$  and  $k_f$ . This method has been used in a number of studies, including [4, 6, 47, 48]. An example of this method is presented in Figure I.4, using numerically generated aggregates.

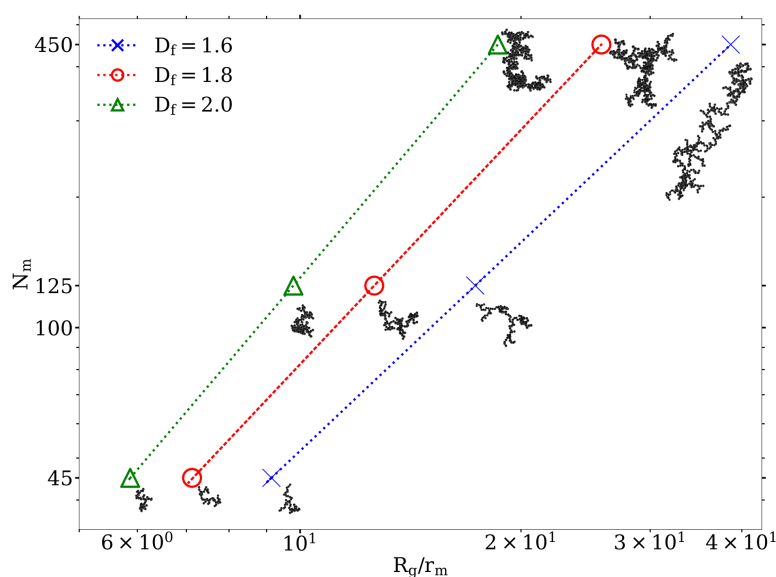


Figure I.4: Number of monomers against the radius of gyration normalized by the monomer radius for ensembles of numerically generated aggregates. The aggregates are originally generated with fractal dimensions of  $D_f = 1.6$ ,  $1.8$  and  $2.0$ . Each marker represents one of the generated aggregate ensembles and the dashed lines are the fitted curves using equation I.1.3. The fitting parameters are  $D_f = 1.5975 \pm 0.0002$  and  $k_f = 1.3127 \pm 0.0009$  (blue curve, cross),  $D_f = 1.7968 \pm 0.0002$  and  $k_f = 1.3141 \pm 0.0010$  (red curve, circles),  $D_f = 1.9965 \pm 0.0002$  and  $k_f = 1.3142 \pm 0.0008$  (green curve, triangles). Examples of the aggregate morphologies are represented nearby the corresponding markers. In these representations, the monomer radius is set to the same value, and the aggregates have been orientated so that the longest vector linking any couple of monomer centers is placed in the plane of the figure. Figure taken from [49].

The primary particles of soot aggregates generated experimentally exhibit a degree of polydispersity. The monomers particle size distribution has been found to be best described by either a normal [50, 51] or a log-normal distribution [48, 52, 53]. These distributions are respectively defined such as:

$$n_r(r_m) = \frac{1}{\sigma_m \sqrt{2\pi}} \exp \left[ -\frac{1}{2} \left( \frac{r_m - R_m}{\sigma_m} \right)^2 \right] \quad (I.1.5a)$$

$$n_r(r_m) = \frac{1}{r_m \log(\sigma_m) \sqrt{2\pi}} \exp \left[ -\frac{1}{2} \left( \frac{\log(r_m) - \log(R_m)}{\log(\sigma_m)} \right)^2 \right] \quad (I.1.5b)$$

where  $n_r$  is the size distribution function (normal in Equation I.1.5a and log-normal in Equation I.1.5b),  $R_m$  is the mean geometrical radius and  $\sigma_m$  is the standard deviation. Equation I.1.3 remains mostly unchanged by the introduction of primary particles polydispersity, with the exception of the monomer radius  $r_m$  being replaced by the monomers mean geometric radius  $R_m$  [54]. The radius of gyration of polydisperse aggregates is computed with:

$$R_g^2 = \frac{\sum_{i=1}^{i=N_m} m_i x_i^2}{\sum m_i} \quad (I.1.6)$$

where  $m_i$  is the mass of the  $i$ th monomer.

Soot aggregates exhibit different morphologies according to the combustion process they are originating from. This is expressed by the different sets of micro-physical parameters (*i.e.*  $N_m$ ,  $r_m$ ,  $k_f$ , and  $D_f$ ) that can be retrieved through measurements. Table I.1 presents an non exhaustive list of experimental evaluations of these micro-physical parameters.

Reference	Fuel	Type of flame	$N_m$	$r_m$ (nm)	$D_f$	$k_f$
Lee et al. [55]	Hydrocarbon	Laminar	-	20	-	-
Prado et al. [56]	Propane	Laminar	-	7.5-13	-	-
Samson et al. [18]	Acetylene	Laminar	-	-	1.66-1.95	-
Zhang et al. [57]	Methane	Laminar	-	10	1.62-1.72	-
Megaridis and Dobbins [58]	Ethylene	Laminar	-	17	-	-
Köylü and Faeth [30]	Toluene	Turbulent	526	25	1.73	-
Köylü and Faeth [30]	Acetylene	Turbulent	417	23	1.79	-
Köylü and Faeth [30]	Benzene	Turbulent	552	24.5	1.71	-
Köylü and Faeth [30]	Propylene	Turbulent	460	20	1.75	-
Köylü and Faeth [30]	Ethylene	Turbulent	467	15.5	1.73	-
Köylü and Faeth [30]	n-heptane	Turbulent	260	17.5	1.73	-
Köylü and Faeth [30]	Propane	Turbulent	364	14.5	1.74	-
Köylü and Faeth [30]	Isopropanol	Turbulent	255	15	1.70	-
Köylü et al. [59]	Acetylene	Laminar	-	-	1.78	1.33
Krishnan et al. [60]	Butadiene	Turbulent	-	21	1.79	-
Krishnan et al. [60]	Cyclohexane	Turbulent	-	18.5	1.8	-
Zhu et al. [61]	Ethene	Laminar	162	23	1.69	6.85
Zhu et al. [61]	Acetylene	Laminar	149	25	1.61	8.76
Hu et al. [62]	Ethylene	Turbulent	-	18-35	1.74	2.2
Williams et al. [63]	Kerosene	Laminar	30	20	-	-
Williams et al. [63]	Ethylene	Laminar	9-62	12.5-22.5	-	-
Williams et al. [63]	Methane	Laminar	11-25	10-12.5	-	-
Jensen et al. [64]	JP-8	Pool-fire	-	28.5-37	1.6-1.7	6.2-6.9
Chu et al. [65]	Ethylene	Laminar	-	10-20	-	-

Table I.1: References of studies investigating the morphologies of soot aggregates. The fuel, type of flame and microphysical parameters values are indicated when available.

## Numerical aggregation methods

As illustrated in Figure I.3(b), aggregates can be numerically generated using iterative processes. In this section, different types of aggregation methods are briefly described.

Aggregate generation methods can be separated into several categories according to the physical process they are modeling. Diffusion-Limited Aggregation (DLA) methods model the primary particles as being in a Brownian motion. The interaction between two particles, and the potential formation of clusters, is then limited by the diffusion process of the particles [66, 67]. Typically, a primary particle is fixed at the center of a modeled 2D or 3D box. Primary particles are then individually created at the boundary of this numerical space. These particles are then transported by means of a random walk process until they either enter in contact with another primary particle, in which case they form a cluster, or are out of predefined boundaries. This

process is repeated until a set number of primary particles has been transported, or alternatively if the cluster reaches a certain size.

Reaction-Limited Aggregation (RLA) methods are a variation of DLA methods in which primary particles do not stick to each other irreversibly at first contact. Instead, a probability that two particles would indeed attach to each other is introduced [68]. Ballistic Aggregation (BA) methods replace the Brownian motion transport model of DLA methods by a purely ballistic motion [69, 70]. Hence, primary particles move in straight lines, and randomness is introduced in either the primary particles position initialization or in the choice of the propagation direction.

In all the aforementioned categories, the moving particles have been considered as being individual primary particles. Subcategories can be formed when also involving the aggregation between clusters, which forms the Cluster-Cluster Aggregation (CCA) methods. Hence, the particle-cluster methods (*i.e.* DLA, RLA and BA) have counterpart CCA methods, namely Diffusion-Limited Cluster-cluster Aggregation (DLCA) [71, 72], Reaction-Limited Cluster-cluster Aggregation (RLCA) [73, 74, 75] and Ballistic Cluster-cluster Aggregation (BCA) [76].

These different methods for the generation of fractal aggregates lead to different values of the micro-physical parameters. DLCA methods typically form aggregates with fractal parameters  $D_f = 1.8$  and  $k_f = 1.3$ , while RLCA aggregates have fractal parameters  $D_f = 2.1$  and  $k_f = 0.94$  [77].

Lastly, Tunable Cluster-Cluster Aggregation (TCCA) methods allow for the generation of fractal aggregates which preserve the user-defined fractal dimension [78] and fractal prefactor [19, 79, 80]. These methods allow for the systematic study of the individual effects of the micro-physical parameters [81].

### **Overlapping, necking and coating**

Overlapping and necking are two morphological features that can be present in soot aggregates. Necking refers to the presence of additional carbonaceous matter in the contact area between monomers, which are no longer in point contact, while overlapping describes the interpenetration of spherical primary particles [6]. Examples of such morphological features are avail-

able on Figure I.5.

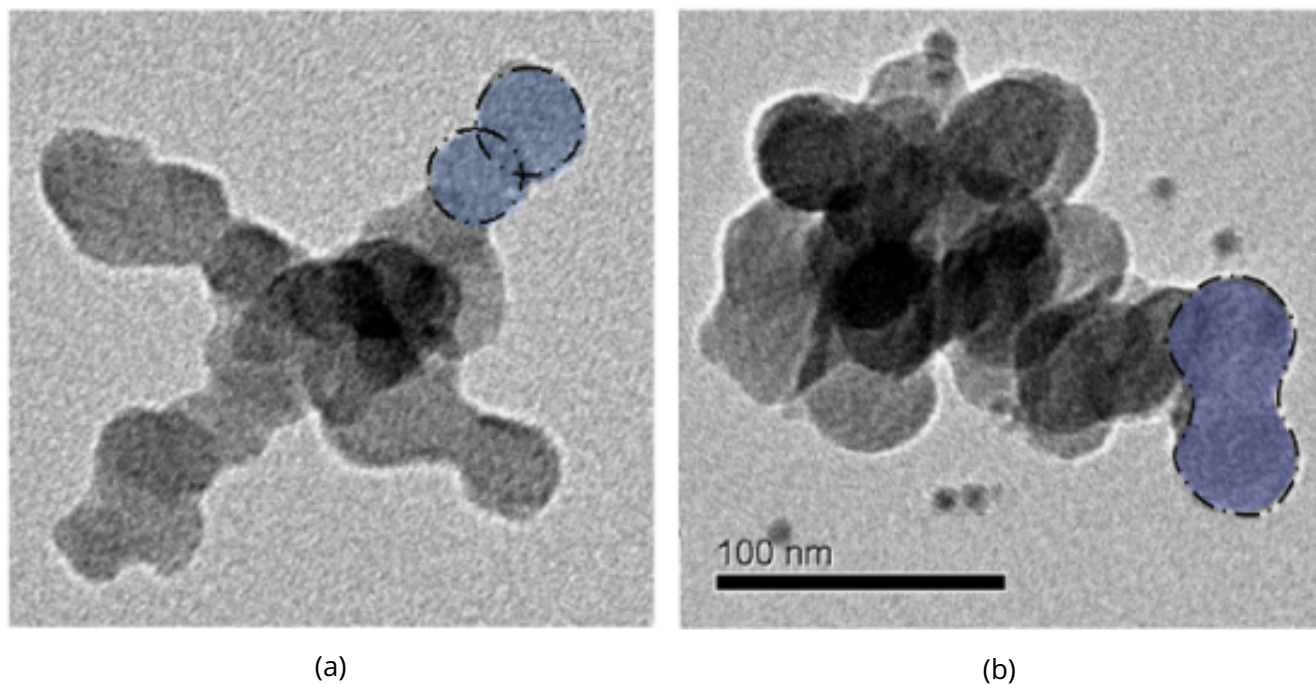


Figure I.5: Examples of (a) overlapping and (b) necking on soot aggregates. Figure taken from [6].

Coating refer to the process of totally or partially embedding an aggregate within another material (*e.g.* sulfate [82, 83]). Soot coating can be observed during the atmospheric ageing of these particles, *i.e.* the chemical and/or morphological changes undergone during atmospheric transport. China et al. [29] have provided evidence that soot aggregates emitted from wildfires can be fully embedded within coating materials, partly coated and that coating inclusion can also be present on soot aggregates. Heinson et al. [84] found that the fractal dimension of DLCA soot aggregates remains unchanged by coating, but that the fractal prefactor increases with coating thickness.

### I.1.3 Optical index

In the following sections of this study, emphasis will be put on the numerical modeling of radiative properties of soot aggregates. In such calculations, the optical index of the material constituting soot aggregates is of foremost importance. The optical index is defined as:

$$m_o(\lambda) = n_o(\lambda) + ik_o(\lambda) \quad (I.1.7)$$

where  $m_o$  is the optical index,  $\lambda$  is the wavelength,  $n_o$  is the real part of the optical index, also called the refractive index, and  $k_o$  is the imaginary part of the optical index, sometimes called the absorptive index and  $i = (-1)^{1/2}$ .

A number of studies have been aiming to retrieve and/or compute the optical index of soot particles. Hereby is provided a non-exhaustive summary of such studies in the ultra-violet, visible and near-infrared spectrum. Ageing processes and coating might significantly alter the retrieved refractive index of soot particles. Therefore, in this section are included only the studies which investigate the optical index of bare, freshly-emitted soot aggregates.

The value of  $m_o = 1.57 + 0.56i$  is one of the most prevalently used values of the optical index of soot and has been attributed to Dalzell and Sarofim [85]. Although this value should be used with care [86], it is still useful in order to compare results with previous studies.

Chang and Charalampopoulos [7] provide analytical expressions for the computation of the real part and imaginary part of the optical index, inferred from extinction measurements and using the Kramers-Krönig relations. These analytical expressions of the optical index are expressed as:

$$n_o(\lambda) = 1.811 + 0.1263 \log(\lambda) + 0.027 \log^2(\lambda) + 0.0417 \log^3(\lambda) \quad (I.1.8a)$$

$$k_o(\lambda) = 0.5821 + 0.1213 \log(\lambda) + 0.2309 \log^2(\lambda) - 0.01 \log^3(\lambda) \quad (I.1.8b)$$

where  $\lambda$  is expressed in  $\mu\text{m}$ . Chang and Charalampopoulos [7] estimate these expressions as being valid in the range  $0.4 \mu\text{m} < \lambda < 30 \mu\text{m}$ .

Schnaiter et al. [9] have inferred the optical index of Palas (spark discharge) soot at 450 nm and 550 nm from specific cross-sections measurements, and found values of  $m_o = 2.18 + 0.94i$  and  $m_o = 2.65 + 1.32i$  respectively. Diesel soot optical indices have also been retrieved at 450 nm, 550 nm and 700 nm with values of  $m_o = 1.41 + 0.64i$ ,  $m_o = 1.49 + 0.67i$  and  $m_o = 1.57 + 0.73i$  respectively.

The optical indices of diesel and diester soot particles have been retrieved at wavelengths of 266 nm, 532 nm, 632 nm and 1064 nm by Yon et al. [51]. The corresponding values of the optical index are  $m_o = 1.16 + 0.71i$  (266 nm),  $m_o = 1.61 + 0.74i$  (532 nm),  $m_o = 1.68 + 0.73i$  (632 nm) and  $m_o = 1.81 + 0.76i$  (1064 nm).

In their review Bond and Bergstrom [87] state that the refractive index of soot particles most likely depends on the state of graphitization of the particles. They provide a review of many of the values of the optical index found in the literature, and recommend the use of optical index which lies on the void fraction line. This void fraction line is computed using the Bruggeman's effective medium approximation, on a continuous range of void fraction values and considering  $m_0 = 1.95 + 0.79i$  as the reference optical index of void-free soot.

Soot aggregates optical index remains a subject of discussion, and a consensus has yet to be reached in order to devise specific sets of rules in order to choose the optical index in light scattering calculations.

## I.2 Light scattering and absorption by particles

In this section, the theoretical basis of light-scattering and absorption by particles is introduced. The radiative properties that will be used throughout this study are also introduced, as well as the numerical methods used to compute them in the case of soot particles.

### I.2.1 Theoretical framework

According to the scale at which light is studied, several formalisms can be used in order to describe the properties of light. At the smallest scale, light-matter interactions are described by the quantum electrodynamics theory. At larger scales, light propagation is best described by classical electromagnetism. In this framework, light is described using electromagnetic waves and the Maxwell equations. The field of radiative transfer is an extension of electromagnetism which focuses on the far-field transport of energy through electromagnetic waves.

In this study, the formalism associated with electromagnetism will be predominantly used. Some elements associated with radiative transfer will also be used in Section I.3.

Light-scattering and absorption by particles refer to two physical phenomena of interaction between light and particulate matter. Mishchenko et al. [88] describe these effects in the following way: Considering an incident parallel monochromatic beam, part of the incident energy is spread out at the same wavelength. This defines the elastic scattering, as opposed to inelastic scattering which involves a change of wavelength. A fraction of the incident energy may also be converted by the particles into another form of energy, such as heat. This phenomenon is called absorption. The process of the overall change in the incident beam energy, by means of both scattering and absorption, is called extinction.

In the electromagnetism framework, the previously mentioned parallel monochromatic beam is represented by a harmonic plane electromagnetic wave such as:

$$\mathbf{E}(\mathbf{r}, t) = \mathbf{E}_0 \exp(i\mathbf{k} \cdot \mathbf{r} - i\omega t) \quad (1.2.1a)$$

$$\mathbf{H}(\mathbf{r}, t) = \mathbf{H}_0 \exp(i\mathbf{k} \cdot \mathbf{r} - i\omega t) \quad (1.2.1b)$$

where  $\mathbf{E}$  is the electric field vector,  $\mathbf{H}$  is the magnetic field vector,  $\mathbf{E}_0$  and  $\mathbf{H}_0$  are their respective amplitudes,  $\mathbf{r}$  is the position vector,  $t$  is time,  $\mathbf{k}$  is the wave vector with  $|\mathbf{k}| = 2\pi/\lambda$  and  $\omega$  is the angular frequency and  $\lambda$  is the wavelength.

When incident on a particle, such an electromagnetic wave induces the excitation of the electric charges present within the particles by means of the Lorentz force. This leads to the oscillation of these charges, which radiate in turn a secondary electromagnetic wave at the same frequency as the incident wave [89]. The secondary wave created by one elementary charge also interacts with all the other charges within the particle, which modifies its respective secondary waves. Hence, the secondary waves become interdependent. Moreover, the secondary waves created by each elementary charge are not necessarily in phase with each other, nor with the incident wave. This effect leads to the dissipation of energy within the particle. The total scattered wave

from this process would then be the superposition of all the interdependent secondary waves.

The Maxwell equations, as well as continuity equations and appropriate boundary conditions, allow to reduce this problem. Only a brief, schematic, summary is provided here, but the reader may refer to Bohren and Huffman [89], Mishchenko et al. [88] or to Berg [90] for a thorough development.

Consider a monochromatic plane electromagnetic wave incident on an arbitrary shaped, non magnetic particle hosted in a non-absorbing medium. The electric field of the incident wave is noted  $\mathbf{E}^{inc}$  and the electric field of the scattered wave is noted  $\mathbf{E}^{sca}$ . By subdividing the particle into elementary volumes small enough that the internal field within them appears uniform, it can be shown [88, 89, 90] that, for an exterior observer, the scattered wave is a superposition of the scattered waves, called wavelets, by all individual elementary volume elements. This discretization allows for a first simplification of the scattering problem. Several methods used to compute the scattered electric field will be presented in Section I.2.4.

The far-field approximation allows to further simplify the expression of the scattered wave. This approximation is valid if the three following conditions are verified:

$$k(r - a) \gg 1 \quad (1.2.2a)$$

$$r \gg a \quad (1.2.2b)$$

$$r \gg \frac{ka^2}{2} \quad (1.2.2c)$$

where  $k$  is the wavenumber such as  $k = 2\pi/\lambda$ ,  $a$  is the radius of the smallest sphere which contains the scattering particle, and  $r$  is the distance from the center of the aforementioned sphere. Equation 1.2.2a indicates that the validity of this approximation is verified for observation points at a distance  $r$  much larger than the wavelength. Similarly, Equation 1.2.2b indicates that the observation distance must be larger than the object size. Equation 1.2.2c is used in order to verify that at the observation point, the differences in phase between two wavelets originating from two different elementary volumes do not depend on the observation distance anymore.

These inequalities lead to the simple formulation of the scattered field as a single transverse spherical wave such as:

$$\begin{aligned} \mathbf{E}^{sca}(\mathbf{r}, t) &= \frac{\exp(i\mathbf{k}\cdot\mathbf{r} - i\omega t)}{r} \mathbf{E}_1^{sca}(\hat{\mathbf{r}}) \\ &= \frac{\exp(i\mathbf{k}\cdot\mathbf{r} - i\omega t)}{r} \overleftrightarrow{\mathbf{A}} \mathbf{E}_0^{inc} \end{aligned} \quad (1.2.3)$$

where  $\mathbf{E}_1^{sca}$  is the scattering amplitude and only depends on the direction vector  $\hat{\mathbf{r}} = \mathbf{r}/|\mathbf{r}|$  and is independent of the distance  $r$  and  $\overleftrightarrow{\mathbf{A}}$  is the scattering dyadic. The scattering dyadic allows for the computation of the scattered wave with any plane incident wave. It depends on the size, morphology, orientation and optical index of the scatterer. Figure I.6 presents an illustration of wavelets and of the implications of the far-field approximation.

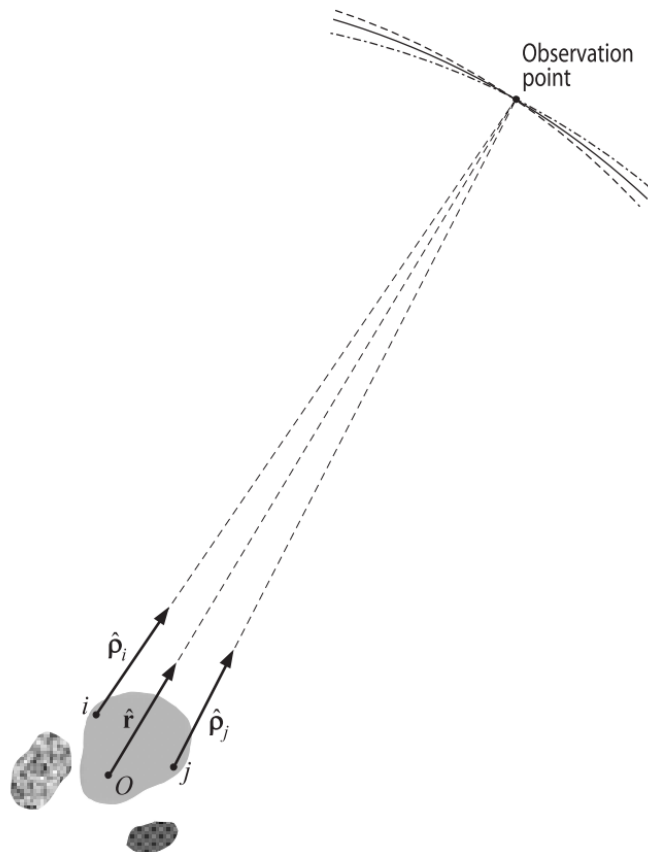


Figure I.6: Illustrative schematic of the far-field approximation. The volume elements  $i$  and  $j$  each scatter a wavelet.  $\rho_{i,j}$  are the direction vectors between the observation point and the corresponding volume elements. If the far-field approximation conditions are verified, each wavelet becomes eventually indistinguishable. This figure is taken from [88].

In most applications in the optical domain, the measured quantities are not the electromagnetic fields, but rather intensities and time-averaged quantities.

## I.2.2 The Stokes parameters and the scattering matrix

Considering a spherical coordinate system, as in Figure I.7, any transverse electric field can be expressed as:

$$\mathbf{E} = \mathbf{E}_\theta + \mathbf{E}_\phi = E_\theta \hat{\mathbf{e}}_\theta + E_\phi \hat{\mathbf{e}}_\phi = \begin{bmatrix} E_\theta \\ E_\phi \end{bmatrix} \quad (1.2.4)$$

where  $\mathbf{E}_\theta$  and  $\mathbf{E}_\phi$  are the components of the electric field along the vectors  $\hat{\mathbf{e}}_\theta$  and  $\hat{\mathbf{e}}_\phi$  respectively, with magnitudes  $E_\theta$  and  $E_\phi$ . The time dependence and dependence on the direction vector is implied. Being a transverse wave, the component along the  $\hat{\mathbf{n}}$  vector is null.

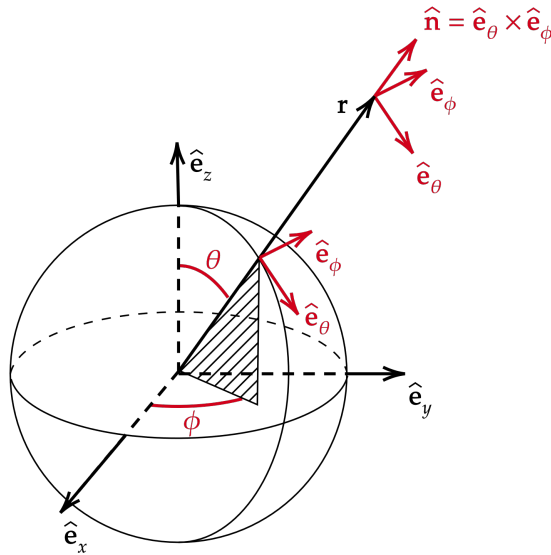


Figure I.7: Coordinate system.

Considering a transverse electromagnetic wave as described by Equations I.2.1, and using the conversion in spherical coordinates as in Equation I.2.4, sets of combination of the electric fields

components can be build such as:

$$\langle E_\theta(\mathbf{r}, t)[E_\theta(\mathbf{r}, t)]^* \rangle_t = E_{0\theta}E_{0\theta}^* \quad (1.2.5a)$$

$$\langle E_\theta(\mathbf{r}, t)[E_\phi(\mathbf{r}, t)]^* \rangle_t = E_{0\theta}E_{0\phi}^* \quad (1.2.5b)$$

$$\langle E_\phi(\mathbf{r}, t)[E_\theta(\mathbf{r}, t)]^* \rangle_t = E_{0\phi}E_{0\theta}^* \quad (1.2.5c)$$

$$\langle E_\phi(\mathbf{r}, t)[E_\phi(\mathbf{r}, t)]^* \rangle_t = E_{0\phi}E_{0\phi}^* \quad (1.2.5d)$$

where the notation  $\langle \rangle_t$  indicates the time average.

These four combinations have the dimension of an intensity. The Stokes vector is then defined as:

$$\mathbf{I} = \begin{bmatrix} I \\ Q \\ U \\ V \end{bmatrix} = \frac{1}{2} \sqrt{\frac{\epsilon}{\mu}} \begin{bmatrix} E_{0\theta}E_{0\theta}^* + E_{0\phi}E_{0\phi}^* \\ E_{0\theta}E_{0\theta}^* - E_{0\phi}E_{0\phi}^* \\ -E_{0\theta}E_{0\phi}^* - E_{0\phi}E_{0\theta}^* \\ i(E_{0\phi}E_{0\theta}^* - E_{0\theta}E_{0\phi}^*) \end{bmatrix} \quad (1.2.6)$$

where  $I$ ,  $Q$ ,  $U$  and  $V$  are the Stokes vector elements, and  $\epsilon$  and  $\mu$  are the electric permittivity and magnetic permeability respectively. The parameter  $I$  expresses the wave intensity, and the parameters  $Q$ ,  $U$  and  $V$  describe the polarization state of the wave. This polarization state description is called the ellipsometric interpretation and can be summarized by means of Figure I.8.

Using the spherical coordinate system, Equation I.2.3 can be modified by introducing the amplitude scattering matrix  $\mathbf{S}$  such as:

$$\mathbf{E}^{sca}(r\hat{\mathbf{n}}^{sca}) = \frac{\exp(ikr)}{r} \mathbf{S}(\hat{\mathbf{n}}^{sca}, \hat{\mathbf{n}}^{inc}) \mathbf{E}_0^{inc} \quad (1.2.7)$$

where  $\hat{\mathbf{n}}^{sca}$  and  $\hat{\mathbf{n}}^{inc}$  are the propagation direction vectors of the scattered and incident wave respectively. The amplitude scattering matrix is computed using the scattering dyadic introduced in Equation I.2.3 such as:

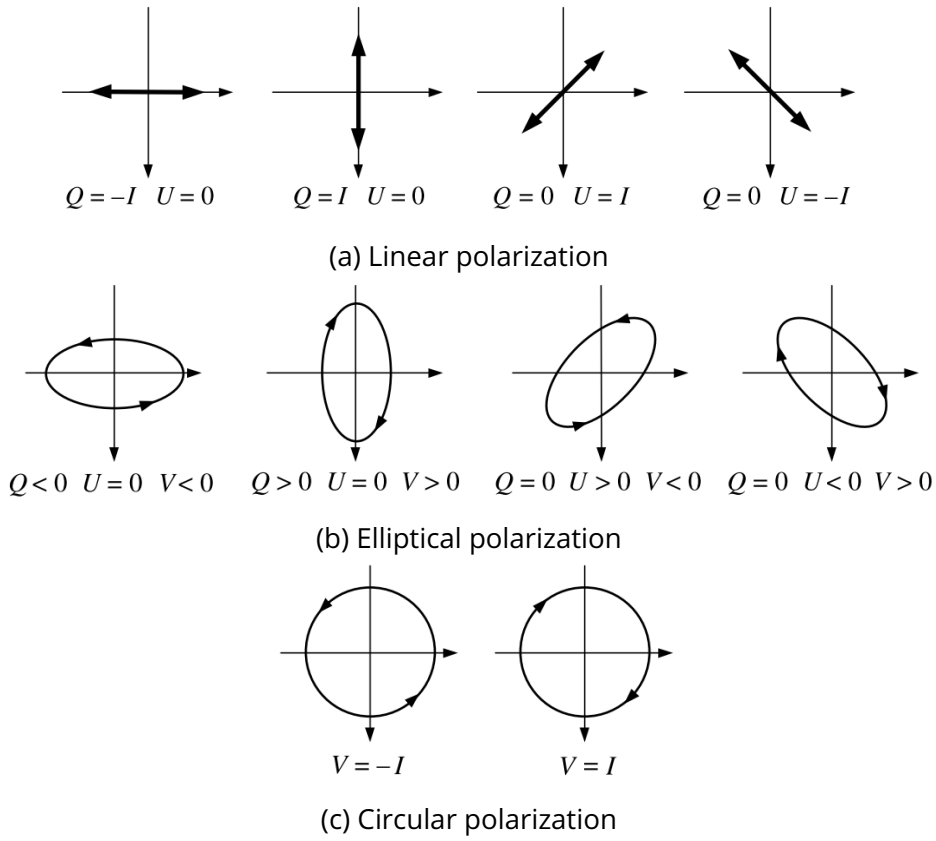


Figure I.8: Ellipsometric interpretation of the Stokes parameters. The wave propagates toward the reader. In subfigure (a), the bold arrow describes the oscillation of the real electric vector, while this oscillation is described by the rotating arrow in subfigures (b) and (c). Figure from [88].

$$\mathbf{S} = \begin{bmatrix} S_{11} & S_{12} \\ S_{21} & S_{22} \end{bmatrix} \quad (1.2.8)$$

and:

$$S_{11} = \hat{\mathbf{e}}_{\theta}^{sca} \cdot \overleftrightarrow{\mathbf{A}} \cdot \hat{\mathbf{e}}_{\theta}^{inc} \quad (1.2.9a)$$

$$S_{12} = \hat{\mathbf{e}}_{\theta}^{sca} \cdot \overleftrightarrow{\mathbf{A}} \cdot \hat{\mathbf{e}}_{\phi}^{inc} \quad (1.2.9b)$$

$$S_{21} = \hat{\mathbf{e}}_{\phi}^{sca} \cdot \overleftrightarrow{\mathbf{A}} \cdot \hat{\mathbf{e}}_{\theta}^{inc} \quad (1.2.9c)$$

$$S_{22} = \hat{\mathbf{e}}_{\phi}^{sca} \cdot \overleftrightarrow{\mathbf{A}} \cdot \hat{\mathbf{e}}_{\phi}^{inc} \quad (1.2.9d)$$

The amplitude scattering matrix differs from the scattering dyadic as it only account for the in-

dependent terms of the latter. Indeed, in a spherical coordinate system  $(\hat{\mathbf{n}}, \hat{\mathbf{e}}_\theta, \hat{\mathbf{e}}_\phi)$  and considering transverse waves, the following identities are verified:

$$\overleftrightarrow{\mathbf{A}} \cdot \hat{\mathbf{n}}^{inc} = 0 \quad (I.2.10a)$$

$$\hat{\mathbf{n}}^{sca} \cdot \overleftrightarrow{\mathbf{A}} = 0 \quad (I.2.10b)$$

The Stokes phase matrix  $\mathbf{Z}$  can then be introduced. This matrix allows the computation of the scattered Stokes vector such as:

$$\mathbf{I}^{sca}(r\hat{\mathbf{n}}^{sca}) = \frac{1}{r^2} \mathbf{Z}(\hat{\mathbf{n}}^{sca}, \hat{\mathbf{n}}^{inc}) \mathbf{I}^{inc} \quad (I.2.11)$$

The  $4 \times 4$  Stokes phase matrix elements are computed as:

$$\begin{aligned} Z_{11} &= (1/2)(|S_{11}|^2 + |S_{12}|^2 + |S_{21}|^2 + |S_{22}|^2) & Z_{31} &= -\Re(S_{11}S_{21}^* + S_{22}S_{12}^*) \\ Z_{12} &= (1/2)(|S_{11}|^2 - |S_{12}|^2 + |S_{21}|^2 - |S_{22}|^2) & Z_{32} &= -\Re(S_{11}S_{21}^* - S_{22}S_{12}^*) \\ Z_{13} &= -\Re(S_{11}S_{12}^* + S_{22}S_{21}^*) & Z_{33} &= \Re(S_{11}S_{22}^* + S_{12}S_{21}^*) \\ Z_{14} &= -\Im(S_{11}S_{12}^* - S_{22}S_{21}^*) & Z_{34} &= \Im(S_{11}S_{22}^* + S_{21}S_{12}^*) \\ Z_{21} &= (1/2)(|S_{11}|^2 + |S_{12}|^2 - |S_{21}|^2 - |S_{22}|^2) & Z_{41} &= -\Im(S_{21}S_{11}^* + S_{22}S_{12}^*) \\ Z_{22} &= (1/2)(|S_{11}|^2 - |S_{12}|^2 - |S_{21}|^2 + |S_{22}|^2) & Z_{42} &= -\Im(S_{21}S_{11}^* - S_{22}S_{12}^*) \\ Z_{23} &= -\Re(S_{11}S_{12}^* - S_{22}S_{21}^*) & Z_{43} &= \Im(S_{22}S_{11}^* - S_{12}S_{21}^*) \\ Z_{24} &= -\Im(S_{11}S_{12}^* + S_{22}S_{21}^*) & Z_{44} &= \Re(S_{22}S_{11}^* + S_{12}S_{21}^*) \end{aligned} \quad (I.2.12)$$

This matrix contains the main parameters that will be used in order to compute the radiative properties in Section I.2.3. The elements of this matrix have the dimension of an area per unit solid angle, and depend on the shape, orientation, refractive index and size of the scatterer, as well as the direction of incidence of the incoming electromagnetic wave and the direction of propagation of the observed scattered wave. Considering a group of randomly moving particles, each in a random orientation and far enough away from each other so that the far-field approxima-

tion is verified, the scattering medium can be considered isotropic and mirror-symmetric. These considerations allow to reduce the number of independent elements in the Stokes phase matrix and to introduce the scattering matrix  $\mathbf{F}$  such as:

$$\begin{aligned} \langle \mathbf{F}(\theta^{sca}) \rangle_{\xi} &= \begin{cases} \langle \mathbf{Z}(\theta^{sca}, \phi^{sca} = 0; \theta^{inc} = 0, \phi^{inc} = 0) \rangle_{\xi} & \text{for } \theta^{sca} \in [0, \pi) \\ \langle \mathbf{Z}(\theta^{sca} = \pi, \phi^{sca} = \pi; \theta^{inc} = 0, \phi^{inc} = 0) \rangle_{\xi} & \text{for } \theta^{sca} = \pi \end{cases} \\ &= \begin{bmatrix} \langle F_{11}(\theta^{sca}) \rangle_{\xi} & \langle F_{12}(\theta^{sca}) \rangle_{\xi} & 0 & 0 \\ \langle F_{12}(\theta^{sca}) \rangle_{\xi} & \langle F_{22}(\theta^{sca}) \rangle_{\xi} & 0 & 0 \\ 0 & 0 & \langle F_{33}(\theta^{sca}) \rangle_{\xi} & \langle F_{34}(\theta^{sca}) \rangle_{\xi} \\ 0 & 0 & -\langle F_{34}(\theta^{sca}) \rangle_{\xi} & \langle F_{44}(\theta^{sca}) \rangle_{\xi} \end{bmatrix} \end{aligned} \quad (1.2.13)$$

where the notation  $\langle \rangle_{\xi}$  denotes the ensemble averaging. As a result from these considerations, the scattering matrix only depends on the scattering angle  $\theta$ , which is the angle between the incidence and scattering directions. In the rest of this study, the ensemble averaging notation  $\langle \rangle_{\xi}$  will be implied, and the scattering matrix and its elements simply noted  $\mathbf{F}(\theta)$  and  $F_{ij}(\theta)$  respectively. The scattering matrix can be normalized such as:

$$\tilde{\mathbf{F}}(\theta) = \frac{4\pi}{C_{sca}} \mathbf{F}(\theta) = \begin{bmatrix} a_1(\theta) & b_1(\theta) & 0 & 0 \\ b_1(\theta) & a_2(\theta) & 0 & 0 \\ 0 & 0 & a_3(\theta) & b_2(\theta) \\ 0 & 0 & -b_2(\theta) & a_4(\theta) \end{bmatrix} \quad (1.2.14)$$

where  $\tilde{\mathbf{F}}$  is the dimensionless scattering matrix,  $a_i$  and  $b_j$  are its dimensionless elements and  $C_{sca}$  is the scattering cross-section, which will be further detailed in Section I.2.3. This matrix also depends on the shape, size and refractive index of the scatterers. When considering a scattering medium composed exclusively of spherical particles, the following identities are verified.

$$a_2(\theta) = a_1(\theta) \quad (1.2.15a)$$

$$a_4(\theta) = a_3(\theta) \quad (1.2.15b)$$

Moreover, in the backward direction, the following identities are verified:

$$b_1(\pi) = 0 \quad (I.2.16a)$$

$$b_2(\pi) = 0 \quad (I.2.16b)$$

$$a_3(\pi) = -a_2(\pi) \quad (I.2.16c)$$

$$a_4(\pi) = a_1(\pi) - 2a_2(\pi) \quad (I.2.16d)$$

### I.2.3 Radiative properties

In this section, the definitions of the radiative properties used throughout this study are given. These definitions stem from the references [91, 92].

The extinction, scattering and absorption cross-sections are three quantities which quantitatively describe the losses of energy by an electromagnetic wave incident on a particle or propagating through a scattering medium. These cross-sections have the dimension of an area, and are related by:

$$C_{ext} = C_{sca} + C_{abs} \quad (I.2.17)$$

where  $C_{ext}$  is the extinction cross-section and  $C_{abs}$  is the absorption cross-section. This expression is specific to the case of elastic scattering.

The extinction cross-section  $C_{ext}$  characterizes the attenuation of an electromagnetic wave through the scattering and absorption processes. In the general case, the extinction cross-section depends on the particles orientation and on the polarization of the incident wave. Hence, an extinction matrix  $\mathbf{K}$  is generally needed in order to compute the extinction cross-section. Nevertheless, considering an isometric and mirror-symmetric medium, this extinction matrix becomes diagonal with only one independent parameter. The extinction cross-section can then be defined

as:

$$C_{ext} = K_{11} = \frac{4\pi}{k|\mathbf{E}_0^{inc}|^2} \text{Im} (\mathbf{E}_1^{sca}(\hat{\mathbf{n}}^{inc}) \cdot [\mathbf{E}_0^{inc}]^*) \quad (1.2.18)$$

where  $K_{11}$  is the first element of the extinction matrix  $\mathbf{K}$ . Note that the extinction cross-section depends on the imaginary part of the scattered electric field in the forward direction. Considering Equations 1.2.1(a) and 1.2.3, the extinction cross-section has the dimension of an area. This dependence is linked to the optical theorem, and is further detailed in the papers from Berg et al. [93, 94].

The scattering cross-section  $C_{sca}$ , already introduced in Equation 1.2.14, expresses the scattering part of the extinction process. Considering an unpolarized incident light, it is defined as:

$$C_{sca} = 2\pi \int_0^\pi F_{11}(\theta) \sin(\theta) d\theta \quad (1.2.19)$$

The absorption cross-section can then be computed by isolating it in Equation 1.2.17.

The integrand of Equation 1.2.19 is often referred to as the differential scattering cross-section and is defined as:

$$\frac{dC_{sca}}{d\Omega} = F_{11}(\theta) = \frac{C_{sca}}{4\pi} a_1(\theta) \quad (1.2.20)$$

The backscattering cross-section is a special case of the differential scattering cross-section for the angle  $\theta = \pi$ , or in other words if the incident and scattered direction of propagation vectors are related such as  $\hat{\mathbf{n}}^{sca} = -\hat{\mathbf{n}}^{inc}$ . It is noted:

$$dC_{bac} = F_{11}(\theta = \pi) = \frac{C_{sca}}{4\pi} a_1(\pi) \quad (1.2.21)$$

Both the differential cross-sections and the backscattering cross-section have the dimension of an area per unit solid angle. These quantities quantify the angular distribution of the scattered energy through a solid angle. This distribution is often represented by the phase function, which actually is the first element  $a_1$  of the normalized scattering matrix. The normalization relationship of the phase function is:

$$\frac{1}{2} \int_0^\pi a_1(\theta) \sin(\theta) d\theta = 1 \quad (1.2.22)$$

Several dimensionless quantities can also be constructed using the previously defined cross-sections and the scattering matrix. The single scattering albedo  $\omega_0$  expresses the ratio between the scattering and the extinction processes and is defined as:

$$\omega_0 = \frac{C_{sca}}{C_{ext}} \quad (1.2.23)$$

Similar to the single scattering albedo, the lidar ratio  $LR$  expresses the ratio between the extinction process and the scattering process in the backward direction. It is defined as:

$$LR = \frac{C_{ext}}{dC_{bac}} \quad (1.2.24)$$

The asymmetry parameter is the average cosine of the scattering angle weighted by the first element of the  $\tilde{\mathbf{F}}$  matrix. It expresses the overall shape of the scattering pattern, *i.e.* whether it is more peaked in the forward or backward direction, and it is computed as:

$$g_0 = \frac{1}{2} \int_0^\pi a_1(\theta) \sin(\theta) \cos(\theta) d(\theta) \quad (1.2.25)$$

The particle backscattering linear depolarization ratio (LDR)  $\delta_p$  expresses the change of linear polarization of the scattered wave during the scattering process. It is expressed as:

$$\delta_p = \frac{F_{11}(\pi) - F_{22}(\pi)}{F_{11}(\pi) + F_{22}(\pi)} = \frac{a_1(\pi) - a_2(\pi)}{a_1(\pi) + a_2(\pi)} \quad (1.2.26)$$

Considering Equation I.2.15(a), it becomes obvious that the LDR of ensembles of spherical particles should be null. This result is at the basis of the differentiation between spherical and non-spherical particles in polarized lidar measurements but is also associated with the understanding of the multiple scattering process in lidar. These two considerations will be further detailed in the Sections I.3.3 and I.3.4 respectively.

## I.2.4 Modeling methods for the computation of the radiative properties of soot particles

Several methods can be used in order to numerically compute the radiative properties of soot particles. These methods make use of different approximations and hypotheses, and have different execution times and accuracies. In this section, the main methods mentioned or used in this study are introduced and described.

### Lorenz-Mie theory

The Lorenz-Mie theory is a numerical method used to solve the Maxwell equations when applied to the scattering problem by spherical particles. It is based on the early work by Lorenz and Mie [95]. Several works of reference detail the conception and the demonstration of this theory [89, 96]. Hereby is only provided a short description of the basis of this theory, and the references for the detailed calculation are given. It consists in expanding the equations describing the incident, internal and electric fields into Vector Spherical Wave Functions (VSWF) such as:

$$\mathbf{E}^{inc} = \sum_{l=0}^{\infty} \sum_{m=-l}^l \left[ p_{lm} \mathbf{N}_{lm}^{(1)}(k\mathbf{r}) + q_{lm} \mathbf{M}_{lm}^{(1)}(k\mathbf{r}) \right] \quad (1.2.27)$$

$$\mathbf{E}^{sca} = \sum_{l=0}^{\infty} \sum_{m=-l}^l \left[ a_{lm} \mathbf{N}_{lm}^{(3)}(k\mathbf{r}) + b_{lm} \mathbf{M}_{lm}^{(3)}(k\mathbf{r}) \right] \quad (1.2.28)$$

$$\mathbf{E}^{int} = \sum_{l=0}^{\infty} \sum_{m=-l}^l \left[ c_{lm} \mathbf{N}_{lm}^{(3)}(k^{int}\mathbf{r}) + d_{lm} \mathbf{M}_{lm}^{(3)}(k^{int}\mathbf{r}) \right] \quad (1.2.29)$$

where  $k^{int} = m_o k$ ,  $\mathbf{E}^{int}$  is the internal field and the subscripts  $l$  and  $m$  indicate the order and degree of the vector spherical harmonics  $\mathbf{N}$  and  $\mathbf{M}$  [97]. In practice, the infinite sum  $\sum_{l=0}^{\infty}$  is truncated when the difference between two successive partial summation is below a threshold. The superscripts <sup>(1)</sup> and <sup>(3)</sup> denote whether the vector spherical harmonics are based on Bessel or Hankel functions respectively [89].  $p_{lm}$  and  $q_{lm}$  are the incident field coefficients,  $a_{lm}$  and  $b_{lm}$  are the scattered field coefficients and  $c_{lm}$  and  $d_{lm}$  are the internal field coefficients. The incident field coefficients can be expressed knowing the incident wave direction of propagation and

polarization [89].

The scattered field coefficients are related to the incident field coefficients by the Lorenz-Mie coefficients such as:

$$a_{lm} = \alpha_l p_{lm} \quad (I.2.30a)$$

$$b_{lm} = \beta_l q_{lm} \quad (I.2.30b)$$

where  $\alpha_l$  and  $\beta_l$  are the Lorenz-Mie coefficients. These coefficients depend on the sphere radius and permittivity, on wavelength, and on the surrounding medium permittivity [96].

The procedure of this method is to compute the incident field coefficients and the Lorenz-Mie coefficients at the order  $l = 0$ , where the incident field coefficients depend only on the incoming wave. The scattered field coefficients can then be calculated. This is repeated at order  $l = 1$  and greater until a predefined convergence criterion is met. The radiative properties can then be computed using the scattered field coefficients for each order.

As the Lorenz-Mie theory is only valid for spheres, the morphology of soot particles can be approximated by spheres with various equivalent radii. Such radii are the volume-equivalent radius, the surface-equivalent radius or the radius of gyration [98]. The volume-equivalent radius  $r_v$  and the surface-equivalent radius  $r_s$  are defined as:

$$r_v = (N_m)^{1/3} r_m \quad (I.2.31)$$

$$r_s = (N_m)^{1/2} r_m \quad (I.2.32)$$

### Rayleigh-Debye-Gans theory for Fractal Aggregates

The Rayleigh-Debye-Gans for Fractal Aggregates (RDG-FA) theory is a method which provides direct analytical equations for the computation of an aggregate radiative properties, knowing its morphology and optical index [99]. It is based on the Rayleigh-Debye-Gans approximation, which assumes that each primary particle is small enough to be considered as a spherical Rayleigh scatterer. This assumption can be written in the form  $2x_m |m_o - 1| \ll 1$ , where  $x_m = 2\pi r_m / \lambda$  is the

size parameter. Moreover, another assumption is made that there is no interdependence of the scattered field by each primary particle, or in other words that the internal-field within the particle is uniform and only depends on the external, incident field. The scattering and absorption cross-sections can then be computed as [100]:

$$C_{sca} = (N_m)^2 \frac{8}{3} \pi k^4 (r_m)^6 \left( 1 + \frac{4}{3D_f} k^2 (R_g)^2 \right)^{-D_f/2} F(m_o) \quad (1.2.33)$$

$$C_{abs} = -N_m 4\pi k (r_m)^3 E(m_o) \quad (1.2.34)$$

where  $F(m_o)$  and  $E(m_o)$  are the scattering function and absorption function respectively, such as:

$$F(m_o) = \left| \frac{m_o^2 - 1}{m_o^2 + 2} \right|^2 \quad (1.2.35a)$$

$$E(m_o) = \Im \left[ \frac{m_o^2 - 1}{m_o^2 + 2} \right] \quad (1.2.35b)$$

The differential scattering cross-sections are computed using the structure factor. The structure factor can be computed by means of the Fourier transform of the auto-correlation function, which has already been mentioned in section I.1.2. The density auto-correlation function can be expressed as [101]:

$$g(\mathbf{u}) = \int n(\mathbf{r}) n(\mathbf{r} - \mathbf{u}) d\mathbf{r} \quad (1.2.36)$$

where  $n$  is the density function and  $\mathbf{u}$  is a position vector.  $n(\mathbf{r} - \mathbf{u})$  is equal to one if there is matter at the position described by the vector  $\mathbf{u}$  from another monomer at position  $\mathbf{r}$  and null otherwise. The structure factor is then computed as [100]:

$$S(\mathbf{q}) = \int g(\mathbf{u}) \exp(i\mathbf{q} \cdot \mathbf{u}) d\mathbf{u} \quad (1.2.37)$$

which, provided that  $S(\mathbf{q}) = S(q)$  and  $g(\mathbf{u}) = g(u)$ , gives:

$$S(q) = 4\pi \int g(u) \frac{\sin(qu)}{qu} u^2 du \quad (1.2.38)$$

where  $S$  is the structure factor and  $q$  is the scattering wave vector amplitude such as  $q = |\mathbf{q}| = 2k \sin(\theta/2)$ . By multiplying the scattering wave vector by the gyration radius, two regimes of the structure factor can be identified as [100]:

$$S(qR_g < 1) \simeq 1 - \frac{1}{3} q^2 R_g^2 \quad (1.2.39a)$$

$$S(qR_g > 1) = C(qR_g)^{-D_f} \quad (1.2.39b)$$

where  $C$  is a constant. Other analytical expressions of the structure factor and of the constant  $C$  can be found in the review from Sorensen [100] and references therein.

The structure factor can then be used in order to compute the differential scattering cross-sections as:

$$\frac{dC_{sca}}{d\Omega} = (N_m)^2 k^4 (r_m)^6 F(m_o) S(q) \quad (1.2.40)$$

which leads to the expression of the backscattering cross-section such as:

$$dC_{bac} = (N_m)^2 k^4 (r_m)^6 F(m_o) S(2k) \quad (1.2.41)$$

This theory provides good angle-integrated results, *e.g.* the extinction cross-sections. However, the angle dependent results obtained using RDG-FA such as the scattering matrix elements can be inaccurate, especially for high primary particle size parameters [102]. Several correction factors have been developed in order to address this limitation, to account for the interdependent scattering and to include other complex morphological properties such as overlapping [6, 101, 103].

### Superposition T-Matrix Method

The Superposition T-Matrix Method (STMM) uses the same basic principle as the Lorenz-Mie theory, but applied to assemblies of spheres [96, 97]. This method makes use of the superposition property of the scattered fields, as already mentioned in Section I.2.1, such as:

$$\mathbf{E}^{sca} = \sum_{i=1}^{N_s} \mathbf{E}^{sca,i} \quad (1.2.42)$$

where  $\mathbf{E}^{sca,i}$  is the scattered electric field by sphere  $i$  and  $N_s$  is the number of spheres. The scattered electric field of each sphere is still expressed in terms of VSWFs and is computed using Equation I.2.28. However, the relationship between the incident field coefficients and the scattered field coefficients differs sensibly in order to account for the contribution of one sphere scattered field on another sphere incident field. Equations I.2.30(a) and (b) are therefore written as [97]:

$$a_{lm}^i = \alpha_l^i \left( p_{mn}^i - \sum_{\substack{j=1 \\ j \neq i}}^{N_s} \sum_{l'=1}^{\infty} \sum_{m'=-l'}^{l'} \left[ a_{l'm'}^j A_{lm'l'm'}^{(3)}(kR^{ij}, \theta^{ij}, \phi^{ij}) + b_{l'm'}^j B_{lm'l'm'}^{(3)}(kR^{ij}, \theta^{ij}, \phi^{ij}) \right] \right) \quad (1.2.43a)$$

$$b_{lm}^i = \beta_l^i \left( q_{mn}^i - \sum_{\substack{j=1 \\ j \neq i}}^{N_s} \sum_{l'=1}^{\infty} \sum_{m'=-l'}^{l'} \left[ b_{l'm'}^j A_{lm'l'm'}^{(3)}(kR^{ij}, \theta^{ij}, \phi^{ij}) + a_{l'm'}^j B_{lm'l'm'}^{(3)}(kR^{ij}, \theta^{ij}, \phi^{ij}) \right] \right) \quad (1.2.43b)$$

where  $j$  is another index indicative of the spheres,  $R^{ij}$  is the distance between the centers of the spheres  $i$  and  $j$ ,  $\theta^{ij}$  and  $\phi^{ij}$  are the angles between the position vectors of these two centers in the reference frame and in a spherical coordinate system, and  $A$  and  $B$  are the vector harmonic addition coefficients [97].

By comparing Equations I.2.30 and I.2.43, one can clearly see the added terms which represent the contribution of the interdependence of the scattered field of each sphere. The term T-Matrix of the STM method comes from the simplification of the Equations I.2.43(a) and (b) into a more compact form which introduces a transition matrix  $\mathbf{T}$ . This involves the translation of each field

(incident and scattered) about the cluster origin [97]. The following equation is then obtained:

$$\mathbf{a}_{lmp}^0 = \mathbf{T}_{lmp'l'm'q}^0 \mathbf{p}_{l'm'q}^0 \quad (1.2.44)$$

where the superscript <sup>0</sup> indicates that the coefficients are referring to the fields expanded about the cluster origin, and not about the sphere centers as they previously were. The subscripts <sub>p</sub> and <sub>q</sub>, both equal to either 1 or 2, indicate which field coefficient is referred to such as:

$$\begin{aligned} \mathbf{a}_{lm1}^0 &= a_{lm}^0 & \mathbf{p}_{l'm'1}^0 &= p_{l'm'}^0 \\ \mathbf{a}_{lm2}^0 &= b_{lm}^0 & \mathbf{p}_{l'm'2}^0 &= q_{l'm'}^0 \end{aligned} \quad (1.2.45)$$

As in the Lorenz-Mie theory, the computation of the scattered field coefficients, and then the scattering matrix, requires the input of a convergence criterion. The STMM is able to compute the radiative properties of soot particles provided that the assumption is made that their morphology consists of spherical monomers in point contact. Hence, more complex morphological properties such as overlapping or necking can not be accounted for using the STMM.

### Discrete Dipole Approximation

The Discrete Dipole Approximation (DDA) is a method first introduced by Purcell and Pennypacker [104] and used to compute the radiative properties of arbitrary particles. The main principle of this method is to discretize the volume occupied by a scatterer into a set of elementary volumes, each occupied by a dipole. These dipoles interact with the incident field and with the other dipoles scattered fields. Each dipole  $j$  presents a dipole moment  $\mathbf{\Pi}_j$  such as:

$$\mathbf{\Pi}_j = \alpha_j^p \mathbf{E}_j \quad (1.2.46)$$

where  $\mathbf{E}_j$  is the electric field at the position of dipole  $j$  and  $\alpha_j^p$  is the dipole polarizability for an isotropic material. The electric field  $\mathbf{E}_j$  is computed as:

$$\mathbf{E}_j = \mathbf{E}_j^{inc} - \sum_{\substack{k=1 \\ k \neq j}}^{N_d} \mathbf{A}_{jk} \mathbf{\Pi}_k \quad (1.2.47)$$

where  $\mathbf{E}_j^{inc}$  is the electric field of the wave incident on dipole  $j$ ,  $N_d$  is the number of dipoles and  $\mathbf{A}_{jk}$  is a  $3N_d \times 3N_d$  matrix. The expressions of this matrix can be found in [105]. For an isotropic material, the diagonal elements are  $A_{jj} = 1/\alpha_j^p$  and the expression of Equation 1.2.47 can be reduced to:

$$\mathbf{E}_j^{inc}(\mathbf{r}) = \sum_{k=1}^{N_d} \mathbf{A}_{jk} \mathbf{\Pi}_k \quad (1.2.48)$$

Solving the system of equations described by Equation 1.2.48 yields the dipole moment of each volume, which in turn yields the internal electric field as of Equation 1.2.47. The scattered field in the far-field can also be computed as:

$$\mathbf{E}^{sca} = \frac{k^2 \exp(ikr)}{r} \sum_{j=1}^{N_d} \exp(-ik\hat{\mathbf{r}} \cdot \mathbf{r}_j) (\hat{\mathbf{r}}\hat{\mathbf{r}} - \mathbb{I}_3) \mathbf{\Pi}_j \quad (1.2.49)$$

Hence, the DDA method allows to compute the scattered field of particles of any morphology, and by consequence their radiative properties. The limitations of this technique stem from the number of dipoles required. This number is expressed through the criterion:

$$N_d > \frac{4\pi}{3} |m_o|^3 x_p^3 \quad (1.2.50)$$

This equation indicates that the elementary volumes dimension are small when compared to wavelength. Moreover, it implies that a larger number of dipoles is needed for large size parameters and optical index, which increases the size of the matrix  $\mathbf{A}_{jk}$  and the computation time needed to solve the system of Equations 1.2.48.

## I.3 Light Detection And Ranging

Lidar instruments are a type of active remote-sensing instruments which operate in the optical spectrum. In contrast with passive techniques, lidar instruments use an artificial and controlled light source in order to study a medium. In this section, a general description of the different types of lidar instruments is provided. The single scattering approximation and the signal inversion methods used in lidar signal analysis are briefly presented. The polarization framework in lidar is then introduced and the multiple scattering effects are described.

### I.3.1 General description of lidar instruments

The overall principle of lidar<sup>1</sup> instruments is closely related to sonar<sup>1</sup> (Sound Navigation And Ranging) and radar<sup>1</sup> (Radio Detection And Ranging) instruments. These three types of instruments emit a wave, electromagnetic for lidars and radars and acoustic for sonars. These waves are scattered or reflected by objects or particles during their propagation. A receiver, placed in the close vicinity of the wave generator, is used in order to acquire a signal which provides information on the scattering medium or on the objects with which the wave has interacted. By measuring the time of emission of the wave and the time of reception of its scattered or reflected part, the distance between the instrument and the interacting medium can be computed knowing only the speed of propagation of the wave. Hence, this procedure allows the detection and ranging of objects. Considering an electromagnetic wave, this is expressed as [106]:

$$r = \frac{c_0 \Delta t}{2} \quad (1.3.1)$$

where  $r$  is the distance between the receiver and the location of the interaction that resulted in the reflection/scattering of the wave,  $c_0$  is the speed of light in vacuum and  $\Delta t$  is the time interval between the emission and the reception of the wave. The denominator indicates that the wave

<sup>1</sup>Although sonar and radar are acronyms, their use has become common enough that the lower case writing has become predominant. While the word lidar is not as widely used as sonar and radar yet, lidar instruments are so closely related to them, in both pronunciation and overall concept, that the use of the lower case writing is justified. Please note that the spellings LiDAR and LIDAR are also commonly used in the literature.

has undergone a round trip. This equation expresses the ranging capacity of lidar instruments, as it allows for a measure of the distance between the instrument and the interacting medium.

Lidar instruments can be classified into different categories and subcategories. The two main categories of lidar can be differentiated by the type of target that is studied. The so-called 3D-lidar systems typically use either a laser source coupled with a scanning apparatus or a flash source (*i.e.* a wide-diverging laser) [107]. These lidars produce a three-dimensional set of data points representing the surface of the surrounding area or of remote targets. They have many applications, *e.g.* to supplement computer vision for the development of autonomous vehicles [108, 109] or in topographical surveys [110, 111].

The second category of lidars concerns instruments whose main purpose is to study the scattering medium in which the electromagnetic wave propagates, in contrast with the solid surfaces that are of interest in 3D-lidars. Hence, these lidars are called atmospheric lidars or diffuse-target lidars. These instruments typically use laser sources coupled with optics that produce well-collimated laser beams or pulses. Several subcategories of atmospheric lidars can be defined [112]:

- Elastic lidars instruments rely on the light scattered by the atmospheric components at the same wavelength as the emitted light. They can provide insights on the presence of particular and molecular content of the atmosphere [106] or on the temperature profile across the different atmospheric layers [113].
- Differential Absorption Lidars (DIAL) are instruments based on the simultaneous measurement of the absorption properties of a single medium at several different wavelengths. The emitted radiation is backscattered by the molecular and particular content of the atmosphere, or by surfaces. By comparing the absorption properties at a wavelength corresponding to a molecule absorption line and those near this absorption line, the concentration of this molecule can be calculated [114].
- Raman lidars are also used to monitor the molecular and particular content and the temperature profile of the atmosphere [115, 116]. These lidars analyze the light scattered by

molecules through the Raman scattering effect. This effect induces a shift in the scattered light wavelength, which is referred to as a type of inelastic scattering. The wavelength shift is specific to each molecule, and by measuring the amplitude of the acquired signal, the molecule concentration can be retrieved [117].

- Fluorescence lidars also use inelastic scattering in order to acquire information on the target. Fluorescence is a phenomenon which can occur when a photon is absorbed by a molecule. The excited molecule then relaxes to a lower energy level and emits a photon in the process. This emitted light can be at the same wavelength as the incident light or at longer wavelength. This type of lidar can be used to detect specific substances in the atmosphere or on surfaces [112, 118].
- Doppler lidars measure the shift in wavelength caused by the Doppler effect induced by wind. The determination of this shift allows to evaluate the wind flow speed [119].

In this thesis, we exclusively consider atmospheric elastic lidar instruments as our object of study. For ease of reading, they are referred to as lidars or lidar instruments in the following. The components of lidar instruments can be schematically organized into three modules as presented in Figure I.9.

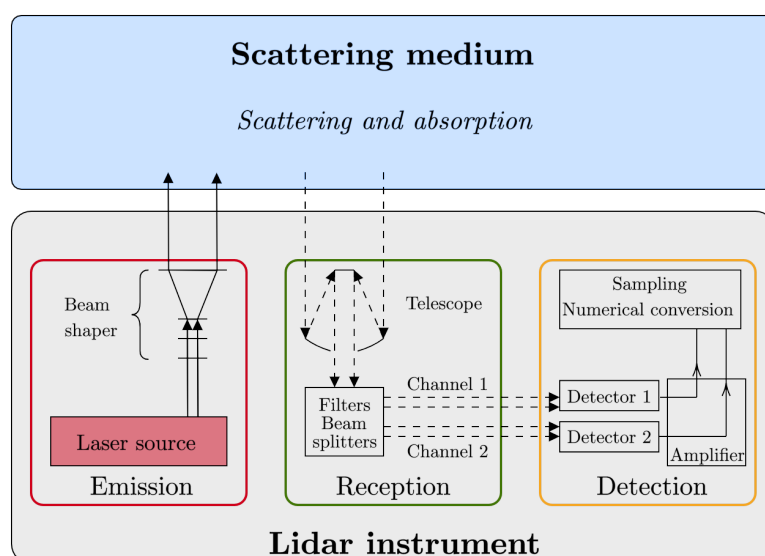


Figure I.9: Schematic view of an atmospheric lidar instrument.

The design of each lidar instrument is application specific. Numerous variations of the three modules have been presented in the literature [120, 121, 122, 123, 124]. In this thesis, we primarily focus on pulsed, polarization-resolved, multiple-wavelengths lidars with dedicated reception channels for each wavelength and polarization state. Hence, a number of lidar designs and optomechanical devices that are less relevant to this focus will not be described in the following.

The emission module contains the laser source and the optomechanical system used to shape the emitted light. The laser source emits a laser pulse whose energy, profile, repetition rate and wavelength depend on the type of laser used. Multiple wavelength lidars use a nonlinear crystal material in order to double or triple the frequency of the light emitted by the laser source. For example, Nd:YAG (Neodymium-doped Yttrium Aluminum Garnet) lasers have an original wavelength of 1064 nm, but wavelengths of 532 nm and 355 nm can be obtained through frequency doubling and tripling. The optomechanical emission system can also control the emitted pulse polarization, divergence and width.

The reception module contains the optics which collect and filter the backscattered light. The collection is achieved by means of the primary mirror of a telescope. The light is then guided to wavelength filters, which are used to filter out the background radiation. Wavelength beam-splitters are used in order to separate the received light into different channels. Polarization beam-splitters can also be used in polarization-resolved lidars in order to split the fraction of the backscattered light whose polarization is different from the emitted pulse polarization. Two channels are then created for each wavelength channel.

The detection module converts the received light into an electric signal which is then amplified and converted again into a numerical signal. The conversion is achieved by sensors such as photomultiplier tubes (PMT) [121, 125] or avalanche photodiodes (APD) [124, 126]. The amplified signal is then sampled and converted into a numerical signal. The sampling frequency, along with the laser pulse width and the sensor response time, will determine the spatial resolution of the numerical signal.

### I.3.2 Single scattering approximation and lidar equation

Describing mathematically the received signal from a lidar instrument requires to account for three factors: (i) the instrument characteristics, (ii) the problem geometry, and (iii) the light-matter interaction processes occurring in the scattering medium. Under the single scattering approximation, the latter can be approached in a simplified manner. In Section I.2.4, we approached the phenomenon of light-scattering by particles by first considering the light scattered by single elementary volumes, and then considering the interdependence between all the elementary volumes within the particle. A similar approach can be undertaken in describing light scattering by ensembles of particles. We first account for the light scattered by a single particle, scaled by the number of particles present in the scattering volume, which corresponds to the single scattering approximation. The interdependence between the scatterers, called multiple scattering, is then introduced later, as it will be in Section I.3.4.

Under the single scattering approximation, the lidar received power can be interpreted using the following equation [20, 92]:

$$P(r) = \frac{1}{r^2} K_0 O(r) U_{SS}(r) \quad (1.3.2)$$

where  $P$  is the received power,  $r$  is the range between the instrument and the scattering volume,  $K_0$  is the instrumental constant,  $O$  is the overlap function and  $U_{SS}$  is the attenuated backscatter function under the single scattering approximation. The  $r^{-2}$  dependence can be physically interpreted by the classical decay of the intensity of a spherical electromagnetic wave. The three other components correspond to the factors described at the beginning of this section.

Considering an instrument whose optics have perfect efficiencies (*i.e.* there is no loss of radiation power within the transmissive optics), the instrumental constant can be expressed as:

$$K_o = P_0 \frac{c_0 \tau_0}{2} A \quad (1.3.3)$$

where  $P_0$  is the emitted pulse integrated power,  $\tau_0$  is the pulse temporal width, and  $A$  is the receiver effective area. The overlap function expresses the fraction of emitted power within the receiver field-of-view as a function of range. Figure I.10 presents a schematic representation

of a lidar instrument emitted beam and receiver field-of-view and of the corresponding overlap function.

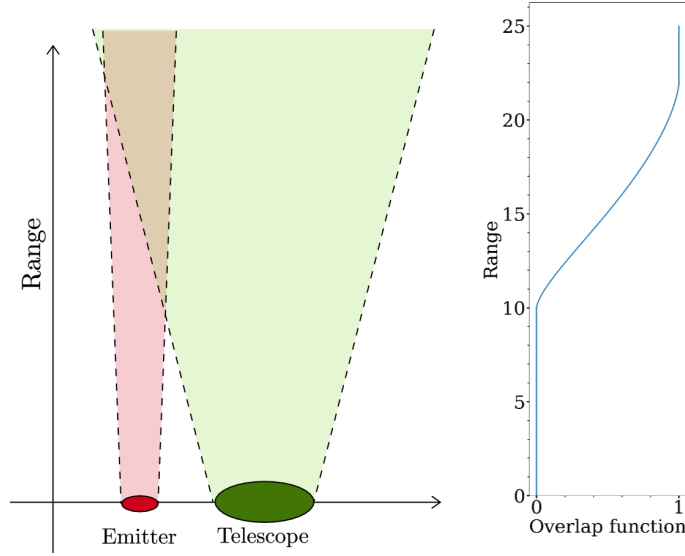


Figure I.10: Schematic view of the emitter beam (red) and receiver field-of-view (green). The corresponding overlap function is computed using the method described in the annexes of Halldorsson and Langerholc [127].

The attenuated backscatter function  $U_{SS}(r)$  expresses the radiation backscattered by the atmospheric component at range  $r$ , and attenuated by the extinction occurring along the optical path between the instrument and the scattering volume. Under the single scattering approximation, it is expressed as:

$$U_{SS}(r) = \beta(r) \exp\left(-2 \int_0^r \alpha(r') dr'\right) \quad (1.3.4)$$

where  $\beta(r)$  and  $\alpha(r)$  are the backscattering and extinction coefficients at range  $r$  respectively. Considering a scattering medium composed only of one type of polydisperse particles, these coefficients, called the lidar coefficients, are expressed as:

$$\beta(r) = \int_0^\infty n_s(r, R) dC_{bac}(r, R) dR \quad (1.3.5a)$$

$$\alpha(r) = \int_0^\infty n_s(r, R) C_{ext}(r, R) dR \quad (1.3.5b)$$

where  $n_s(r, R)$  is the particle size distribution, with  $R$  being a characteristic length of the con-

sidered particle type. Equations I.3.5(a) and (b) are at the source of the underdetermination of the lidar problem, and by consequence of the need of *a priori* information on the particles radiative properties. Indeed, the only measurable quantity is the received power  $P(r)$  in Equation I.3.2, and the lidar coefficients  $\beta$  and  $\alpha$  are unknown. In order to retrieve any information on the scattering medium, say the particle number concentration, *a priori* information are then needed.

Inversion methods are used in order to retrieve information on the scattering medium, the most well-known being the solution developed by Klett [23]. Assuming a relationship between the backscattering and extinction coefficients such as  $\beta(r) = C(\alpha(r))^u$ , where  $C$  and  $u$  are constants, and by rearranging the terms in Equation I.3.4 and differentiating it with respect to range, we have:

$$\frac{u}{\alpha(r)} \frac{d\alpha(r)}{dr} - 2\alpha(r) = \frac{1}{U_{SS}(r)} \frac{dU_{SS}(r)}{dr} \quad (1.3.6)$$

This differential equation is known as a Bernoulli equation, whose solution is:

$$\alpha(r) = \frac{U_{SS}(r)^{1/u}}{\frac{U_{SS}(r_f)^{1/u}}{\alpha(r_f)} + \frac{2}{u} \int_r^{r_f} U_{SS}(r')^{1/u} dr'} \quad (1.3.7)$$

where  $r_f$  is a boundary value.

Hence the retrieval of the extinction coefficients  $\alpha(r)$  requires *a priori* information on the value of the constant  $u$  and on the extinction coefficient at the defined boundary range  $\alpha(r_f)$ . In practice the constant  $u$  is often approximated as  $u \approx 1$ , so that the constant  $C$  is equivalent to the lidar ratio  $LR$ .

### I.3.3 Polarization lidar framework

In the last section, only the unpolarized case has been considered. In order to account for the polarization of the emitted and received radiations, a frame of reference describing the emitted light polarization frame is introduced. Considering linear polarization such as  $\mathbf{I}^{inc} = [1 \ 1 \ 0 \ 0]^T$ , the emitted wave is described as being  $\parallel$ -polarized. According to Equations I.2.14 and I.2.16 and

in the single scattering approximation, the backscattered Stokes vector  $\mathbf{I}^{bac}$  is expressed as:

$$r^2 \mathbf{I}^{bac} = F_{11}(\pi) \begin{bmatrix} 1 \\ F_{22}(\pi)/F_{11}(\pi) \\ 0 \\ 0 \end{bmatrix} = \begin{bmatrix} F_{11}(\pi) & 0 & 0 & 0 \\ 0 & F_{22}(\pi) & 0 & 0 \\ 0 & 0 & F_{33}(\pi) & 0 \\ 0 & 0 & 0 & F_{44}(\pi) \end{bmatrix} \begin{bmatrix} 1 \\ 1 \\ 0 \\ 0 \end{bmatrix} = \mathbf{F}(\pi) \mathbf{I}^{sca} \quad (1.3.8)$$

Considering a non-spherical particle with  $F_{22}(\pi) < F_{11}(\pi)$ , the Stokes elements verify the properties  $Q^{bac} < I^{bac}$  and  $U^{bac} = V^{bac} = 0$ , as there can be no change of polarization plane in the backward direction due to the lack of dependence on the angle  $\phi$ . Following this, the identity  $I > \sqrt{Q^2 + U^2 + V^2}$  indicates that the backscattered radiation is composed of a  $\parallel$ -polarized component and an unpolarized component [128].

Consider a polarization-resolved lidar experiment in which the received radiation is split into two different channels. An analyzer on the first channel filters out the radiation whose polarization is not parallel to the emitted pulse. This channel acquires a signal which is proportional to the  $\parallel$ -polarized component of the received radiation and to half the unpolarized component. The second channel contains an analyzer which filters out the  $\parallel$ -component, so that only half of the unpolarized component remains [128]. In the lidar formalism, it is referred to as the  $\perp$ -component, in contrast with the  $\parallel$ -component.

Using this framework, the emitted pulses are exclusively  $\parallel$ -polarized, while the received radiation can be composed of both a  $\parallel$ -component and a  $\perp$ -component. Equation 1.3.2 can then be rewritten taking into account the polarization such as:

$$P_T(r) = \sum_{i=\parallel, \perp} P_i(r) \quad (1.3.9)$$

with:

$$P_i(r) = \frac{1}{r^2} K_0 O(r) U_i(r) \quad (1.3.10)$$

where the  $i$  defines which component is considered ( $\parallel$  or  $\perp$ ) and the subscript  $T$  is used to re-

fer to the total received power. In this equation, the instrumental constant is considered independent of polarization. Defining the polarized backscattering cross-sections such as:  $C_{bac,\parallel} = (1/2)(F_{11}(\pi) + F_{22}(\pi))$  and  $C_{bac,\perp} = (1/2)(F_{11}(\pi) - F_{22}(\pi))$ , the attenuated backscatter function  $U_i(r)$  now depends on the polarization as a result of the polarization dependence of the backscattering coefficients  $\beta_i = \int_0^\infty n_s(r, R)C_{bac,i}(r, R)dR$ . Defining  $F_{22}(\pi) = F_{11}(\pi) - d F_{11}(\pi)$ , where  $d$  is an adimensional parameter, the same set of equations as in [128] are found. The volume LDR can then be computed such as:

$$\delta_v = \frac{P_\perp}{P_\parallel} = \frac{C_{bac,\perp}}{C_{bac,\parallel}} = \frac{F_{11}(\pi) - F_{22}(\pi)}{F_{11}(\pi) + F_{22}(\pi)} \quad (I.3.11)$$

In practice, an angle of collection is always present in lidar applications, so that the exact backscattering condition is not verified and the identities I.2.16 do not hold. Moreover, changes of polarization plane of the scattered wave occur in those non-exact backscattering angles because of the added dependence on the  $\phi$ -angle. This implies that the backscattered radiation is composed of polarized components on both the  $\parallel$ -axis and the  $\perp$ -axis and of potentially an unpolarized component on these two axes as well. The polarized components of the emitted and received electric fields are illustrated on Figure I.11.

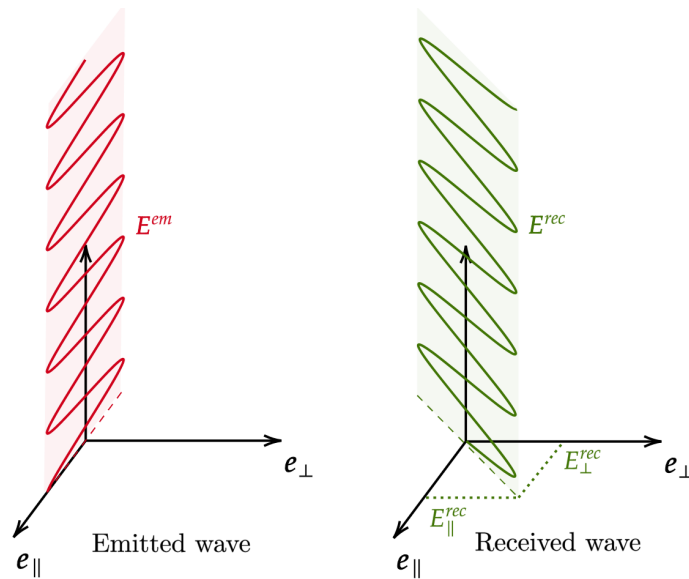


Figure I.11: Frame of reference for the polarization state of the emitted wave and the received wave.

### I.3.4 Multiple scattering in lidar

In the single scattering approximation, it is assumed that the incoming radiation on any particle in the scattering volume is the laser emitted beam. The contributions of the fields scattered by the other scatterers on the other particles are neglected. Multiple scattering refers to the part of the scattered radiation which is not accounted for in the single scattering approximation [24].

In order to describe multiple scattering, consider a system of two identical particles interacting with the same incident field  $\mathbf{E}^{inc}$  as illustrated on Figure I.12. The scattered field by particle 1 is emitted at time  $t_1$ , and the scattered field by particle 2 at time  $t_2 > t_1$ . The time of flight between particles 1 and 2 is  $t_{1-2} > t_2 - t_1$ . We consider that the field scattered by particle 2 in the direction of particle 1 is negligible. Three "echoes" will then be sensed by the lidar instrument. The first corresponds to the backscattered field by particle 1 and the second to the backscattered field by particle 2. The third echo corresponds to the field scattered by particle 2, which only depends on the field scattered by particle 1 in the direction of particle 2. Hence, in this configuration and without *a priori* knowledge on the scattering medium except that it is composed of single particles, the straightforward interpretation of the lidar signal would be that there are three particles within the scattering medium. Moreover, it could be deduced that the returned lidar signal should follow the relationship  $r_1^2 P_1 = r_2^2 P_2 \neq r_3^2 P_3$ , where the numeric subscript indicates which particle is concerned, and the third "virtual" particle is designed by the number 3. The ranges  $r_i$  are still computed using Equation I.3.1.

Several other cases can be considered. If  $t_2 - t_1 = t_{1-2}$ , then only two "echoes" are observed and the relationship between the signals powers is expressed as  $r_2^2 P_2 > r_1^2 P_1$ . In this case,  $P_2$  is related to the superposition of the field scattered by particle 2 with the incident fields  $\mathbf{E}^{inc}$  and  $\mathbf{E}_{1-2}^{sca}$  and of the field scattered by particle 1 with incident field  $\mathbf{E}_{2-1}^{sca}$ .

Following this simple example, two different effects can be attributed to multiple scattering in the lidar framework: (i) a stretch of the lidar signal, (ii) an increase in backscattered power [24].

Another effect associated with multiple scattering is the increase in depolarization of the lidar signals. This effect is particularly striking in water clouds. These clouds are composed of spherical water droplets, which retain the polarization state of the incident light (see Equation I.2.15(a)). In

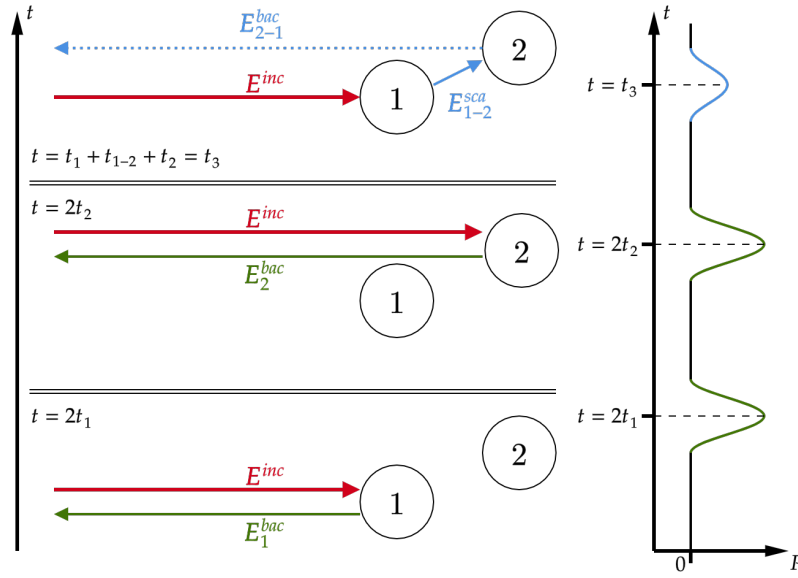


Figure I.12: Example of the mechanism associated with multiple scattering for two particles. The electric fields are represented with arrows. The time-dependent backscattered power is schematically represented on the right-hand side.

the single scattering approximation, this implies an observed LDR that should be null. However, lidar measurements over water clouds have provided non-zero values of the LDR in numerous occasion [129, 130, 131, 132]. This behavior is attributed to multiple scattering.

In order to account for multiple scattering, Platt [133] introduced a multiple scattering correction factor into Equation I.3.4 such as:

$$U_{corr}(r) = \beta(r) \exp\left(-2\eta(r) \int_0^r \alpha(r') dr'\right) \quad (I.3.12)$$

where  $\eta$  is the multiple scattering correction factor, which can be computed as:

$$\eta = 1 - \frac{1}{2\tau} \log\left(\frac{U(r)}{U_{SS}(r)}\right) \quad (I.3.13)$$

where  $U_{SS}(r)$  is the contribution of the attenuated backscatter function attributed to single scattering and  $\tau$  is the optical depth with  $\tau = \int_0^r \alpha(r') dr'$ . The multiple scattering correction factor allows to account for the pulse stretching effect, but does not reproduce the increase in backscattered power. The increase in LDR can be reproduced by introducing polarization dependent correction factors.

Stochastic and phenomenological approaches have produced several formal equations allowing to account for multiple scattering in lidar [24]. Stochastic approaches formulate a multiple scattering lidar equation as the sum of the contributions of all scattering orders. Each scattering order contribution itself is the joint probability density of the trajectories, which depends on the radiative properties of the scattering medium [134, 135]. Phenomenological approaches describe multiple scattering as a chain of elementary scattering processes. The radiation outgoing from an elementary volume at scattering order  $n$  depends on the incident radiation, which itself depends on the outgoing radiation from all elementary volumes at order  $n - 1$ . The integration over  $n$  sets of volume integrals then yields an analytical formulation of the backscattered power [136]. While the equations derived from these methods provide exact formulations of the multiple scattering problem in lidar, they also present a large degree of mathematical complexity and a non-negligible time-cost for their numerical computation [24].

In the Quasi-Small-Angle (QSA) approximation, the measured backscattered radiation is considered to be exclusively due to the successive scatterings occurring at scattering angles near forward scattering ( $\theta_{sca} \approx 0$ ) or near backscattering ( $\theta_{sca} \approx \pi$ ). This allows the simplification of the radiative transfer equation applied to lidar geometry [24].

Monte-Carlo methods are a set of numerical methods allowing to model a number of physical phenomena. As this method is at the foundation of Chapter III, only a brief description is given here. For lidar applications, a specific subset of Monte-Carlo methods is used; the Monte-Carlo transport methods. They consist in modeling the transport of elementary objects through a medium. These objects are subject to absorption and scattering events, and follow trajectories that are determined by means of the random sampling of probability density functions based on the radiative properties of the scattering and absorbing medium. By computing a large number of trajectories, the multiply scattered lidar signal can be computed. Moreover, polarization can be introduced and each scattering order contribution to the signal can be retrieved separately. The elementary objects whose trajectories are computed are hereby referred to as photons. The term "photons" is used as a proxy for these purely numerical objects considering that they are the elementary bricks of the Monte-Carlo methods and that they are subject to probability distri-

butions based on the interacting medium radiative properties properties. Monte-Carlo methods have the advantage of relying on few approximations and being applicable to a large number of cases, but can be computationally demanding.

If not considered, multiple scattering effects induce errors in the retrieved values of the extinction and backscattering coefficients [24]. Moreover, differentiation between particle types is often achieved by means of the LDR [137], which can also be affected by multiple scattering effects.

## Conclusion

In this chapter, a bottom-up approach has been undertaken in order to describe the multiscale complexity of light scattering by soot particles in the lidar framework. At the fundamental level lie the soot particles themselves, whose morphology is described by a fractal model. This fractal model introduces micro-physical parameters, namely the number of monomers, their radius, the fractal prefactor and the fractal dimension. Soot aggregates can be numerically generated using different types of aggregation codes. In the next chapters of this thesis, these aggregation codes are used in order to generate the aggregates of which the radiative properties will be computed in Chapter II, using the optical indices presented in Subsection I.1.3.

The radiative properties computation relies on the theoretical basis described in the second section of this chapter. Elements of electromagnetic scattering by particles are presented, as well as the Stokes formalism and the definition of the radiative properties that will be used. Different modeling methods used to compute the radiative properties have also been described. Emphasis is put on the underlying assumptions of these methods, such as the interdependence of the scattered fields or the shape of the scatterers. Considering these hypotheses and the computational cost of these methods, most of the radiative properties computation of this studies have been achieved using the STM method, although the RDG-FA theory has also been used in some cases. These results are presented in Chapter II.

An overall description of lidar instruments and their characteristics is provided in the final

section of this chapter. The mathematical formulation of the lidar signal is presented in the single scattering approximation, and polarization is later introduced. The multiple scattering phenomenon is described in simple terms, and its effects on lidar signals are underlined. Different methods used to account for multiple scattering in the lidar framework are presented. Chapter III presents the Monte-Carlo method developed in this thesis in order to simulate polarization-resolved lidar signals, accounting for multiple scattering.

Hence, the next chapter presents several studies which pertain to the radiative properties of soot particles, as these radiative properties are needed in order to simulate lidar signals.

## Chapter II

# Evaluation of the radiative properties of soot fractal aggregates

### Introduction

The first step leading to the simulation of lidar signals measured on soot particles is the determination of the radiative properties of these particles. The results obtained from the numerical computation and of the experimental evaluation of the radiative properties are presented in this chapter.

As described in the previous chapter, the radiative properties of particles depend on their size, morphology and optical index. Numerical Cluster-Cluster Aggregation (CCA) methods allow to generate aggregates presenting a fractal-like morphology. However, each set of fractal parameters still corresponds to multiple different arrangements of the primary particles themselves. Moreover, the fractal description of soot aggregates is only valid on average. This implies that the computation of the radiative properties of soot fractal aggregates with a specific set of micro-physical parameters must be averaged over several realizations of aggregates. Hence, in the following, the presented radiative properties are associated with ensembles of aggregates in most cases. The number of aggregates per ensemble will also be stated. Among the presented radiative properties, the single scattering albedo and the asymmetry parameter can provide a

first qualitative evaluation of the multiple scattering. Indeed, the single scattering albedo can be envisioned as the probability of scattering during a single extinction event, while the asymmetry parameter expresses the overall shape of the scattering pattern. These radiative properties will be used and commented upon in the following chapters, and are mostly presented here as a byproduct of the radiative properties computation.

The evaluation of the radiative properties of soot fractal aggregates can be achieved by several methods. In the first section of this chapter, these properties are evaluated by means of numerical methods. Different types of aggregates are under study: (i) aggregates with monodisperse monomers, (ii) aggregates with polydisperse monomers and (iii) superaggregates, also called hybrid aggregates, with monodisperse monomers. The radiative properties are computed at wavelengths that are of primary interest in lidar applications, *i.e.* from the ultraviolet to near-infrared spectrum.

The numerical generation of fractal aggregates with known morphological parameters allows to study the individual impacts of these parameters on the radiative properties. To that end, a comparative study of the radiative properties of ensembles of aggregates with different sets of morphological parameters is presented in the first section. The radiative properties of aggregates with polydisperse monomers are also presented, as they will be used in Chapter IV. The computations are mainly performed using the STM method, using the Multiple-Sphere T-Matrix (MSTM) code [138]. Finally, the radiative properties of superaggregates are presented. This type of aggregates presents specific morphological features, which are highlighted by differences in the structure factor when compared to standard aggregates. This allows for the comparison between superaggregates and standard aggregates radiative properties, but also for the comparison between radiative properties computed with the STM method and using the RDG-FA theory.

The second section of this chapter is dedicated to the experimental evaluation of the LDR of soot particles. To our knowledge, this study is the first experimental evaluation of the LDR of soot particles in the backward direction and in ambient air conditions. A numerical study is also presented in order to identify which sets of morphological properties and optical indices provide the smallest discrepancy with the measurements, and to investigate the limits of the numerical

models.

## **II.1 Numerical simulations of the radiative properties of soot particles**

### **II.1.1 General methods**

In sections II.1.2 and II.1.3, the radiative properties of ensembles of numerically-generated aggregates will be presented. These aggregates are generated using a Tunable Cluster-Cluster Aggregation (TCCA) code, which allows to control their fractal parameters. Although the aggregates of one same ensemble are characterized by the same morphological parameters, each aggregate still presents its own disposition of the monomers in space. These different morphologies within the same ensemble can result in variations of the radiative properties. Indeed, previous studies have highlighted the importance of using ensemble averaging, as well as orientation averaging [139]. In this thesis, random-orientation radiative properties are computed. Then, they are averaged according to the size of each ensemble. In Sections II.1.2 and II.1.3, ensembles of one hundred aggregates are generated. This number is chosen as a compromise between the representativity of the aggregate morphologies, with their associated radiative property standard deviations and the computation time and resources. The impact of the number of aggregates on the standard deviation will be briefly presented in section II.1.2, and is more thoroughly investigated in Appendix A.

The main numerical method used for the computation of the radiative properties is the STM method. Specifically, the MSTM code [138] is used. The MSTM code uses a convergence criterion in order to define the stopping condition of the calculation. In the calculations presented in this study, the choice of this convergence criterion has been found to induce discontinuities in the radiative properties according to wavelength in some cases. In the MSTM code, this convergence criterion is applied to individual monomers. Depending on wavelength, the value of the maximum order of the computed VSWFs may vary for the same convergence criterion. A procedure

implemented in the MSTM code allows to avoid this issue. Instead of defining a convergence criterion, the maximum order of the VSWF for each and every monomer can be defined prior to the computations. Hence, the radiative properties are first computed at the lowest wavelength, and the maximum order of the VSWFs is then used in later computations. While this technique is efficient in the case of monodisperse particles, it can induce a non-negligible increase in computation time. Indeed because the convergence criterion is applied to individual primary particles, the maximum order of the VSWFs for each monomer may be different. This is particularly observable in the case of the superaggregates and aggregates composed of polydisperse monomers. Indeed, superaggregates, which will be further described in section II.1.4, are composed of a very large number of primary particles which can also be found in a more compact arrangement. The interdependence of the scattered field is then increased, which potentially increases the maximum order of VSWFs on some primary particles. Similarly, individual primary particles of aggregates composed of polydisperse monomers may present different maximum orders of the VSWFs according to their size. In the procedure described above, the computation time would then be increased because of the use of the maximum order of the VSWFs of the first computation for all the primary particles.

In order to reduce this computational cost, the MSTM code has been slightly modified. Instead of retrieving the maximum order of the VSWFs in the first computation, the maximum order of the VSWF are retrieved for every individual monomer. This set of maximum orders of the VSWFs is retrieved in the first calculation and then passed on to the next. We found that this alternative procedure allows to suppress the discontinuities and that the results obtained do not present significant differences to those obtained with the previous implementation. Hence, this modified convergence criterion is used during the computation of all the radiative properties when using the MSTM code.

### II.1.2 Soot fractal aggregates with monodisperse monomers

This section presents the methods for the computation of the radiative properties of soot aggregates ensembles with monodisperse monomers. Most of the results presented in this section

have been published during this thesis [49], but some additions have been made in the present report.

## Methods

The fractal aggregates used in this study have been generated using the TCCA algorithm developed by Mackowski [79, 140]. This algorithm has allowed the generation of the monomer positions for an aggregate while fixing the values of the fractal parameters  $k_f$  and  $D_f$  and of the number of monomers  $N_m$ . Twenty-seven ensembles of one hundred soot fractal aggregates have been generated using this algorithm, with the fractal prefactor always set to  $k_f = 1.3$  and the number of monomers to  $N_m = 45, 90$  or  $450$ . The fractal dimension has been set to either  $D_f = 1.6, 1.8$  or  $2.0$  and the monomer radius to  $r_m = 10$  nm,  $20$  nm or  $40$  nm. These values of the morphological parameters have been chosen in order to account for the range values presented in Table I.1. They represent approximately their minimal, maximal and medium values. Examples of generated aggregates are shown in Figure I.4. Using Equation I.1.4, we calculated the radius of gyration of each aggregate. When averaging these radii over ensembles of same morphological parameters, we found less than 0.3% deviation from the mean value of the radius of gyration. The average results are represented by the markers on Figure I.4.

The fractal parameters  $D_f$  and  $k_f$  of each ensemble have been retrieved by fitting the number of monomers against the radius of gyration normalized by the monomer radius using Equation I.1.3. The relative discrepancies between the initial and the retrieved values of the fractal parameters are less than 1.5%, hence being in very good agreement as shown in Figure I.4. Hereafter, the initial values are used in order to lighten the notations.

The radiative properties are computed on a large spectrum, from  $\lambda = 300$  nm to  $\lambda = 1100$  nm, with a wavelength step of  $\Delta\lambda = 20$  nm. These wavelengths are chosen in order to address the wide range of lidar instruments operating in this spectrum, but also to address emerging lidar technologies such as those using a supercontinuum laser [141]. Because the radiative properties are computed on such a wide spectrum, the choice of the optical index is mainly limited to explicit wavelength-dependent formulations of the optical index. Hence, we used the wavelength-

dependent dispersion law as in Equation I.1.8 [7].

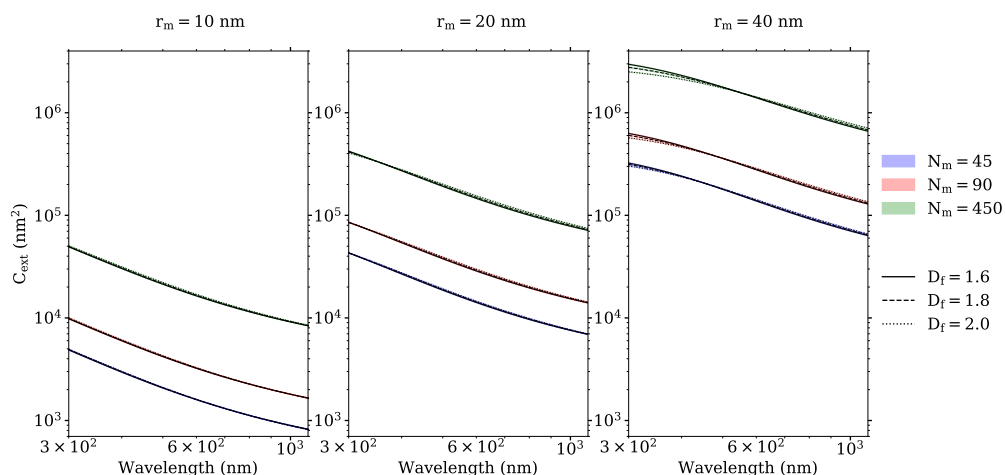
### Cross-sections

According to Figure II.1a, the extinction cross-sections present a consistent spectral and morphological dependence across all ensembles. The extinction cross-sections are decreasing with wavelength, and increasing with monomer radius. A higher number of monomers also results in higher extinction cross-sections. Fractal dimension variations produce a negligible effect on the extinction cross-section, with the exception of the largest aggregate ensembles (*i.e.*  $r_m = 40$  nm,  $N_m = 450$ ). In these cases, higher fractal dimensions result in lower extinction cross-sections in the UV part of the spectrum. The standard deviations of the extinction cross-sections across all wavelength and ensembles are below 0.1%.

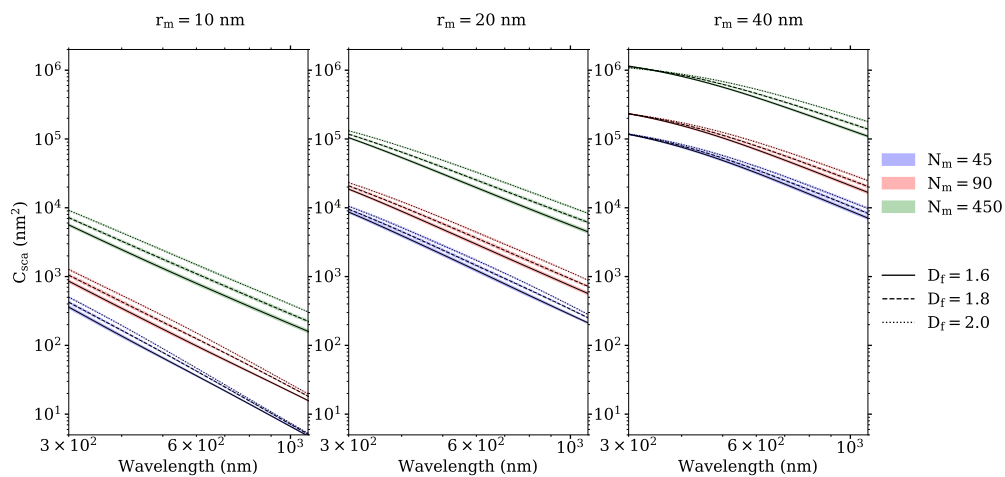
The scattering cross-sections presented in Figure II.1b follow trends similar to those observed in the extinction cross-sections. The same impacts of the monomer radius and number are observed. However, higher fractal dimension produces larger scattering cross-sections across all ensembles and wavelengths, except in the UV range for aggregates of monomer radius  $r_m = 40$  nm.

As shown in Figure II.1c, the backscattering cross-sections are also decreasing with wavelength, with a standard deviation of about 10% over the whole spectrum for each ensemble of aggregates. A difference of up to more than one order of magnitude between the backscattering cross-sections in the UV and in the NIR can be observed. This decrease with wavelength is more important for smaller aggregates, *i.e.* as the monomers are few and small. Comparing Figures II.1a and II.1c, it is apparent that the values of the backscattering cross-sections are decreasing more rapidly with wavelength than the extinction cross-sections.

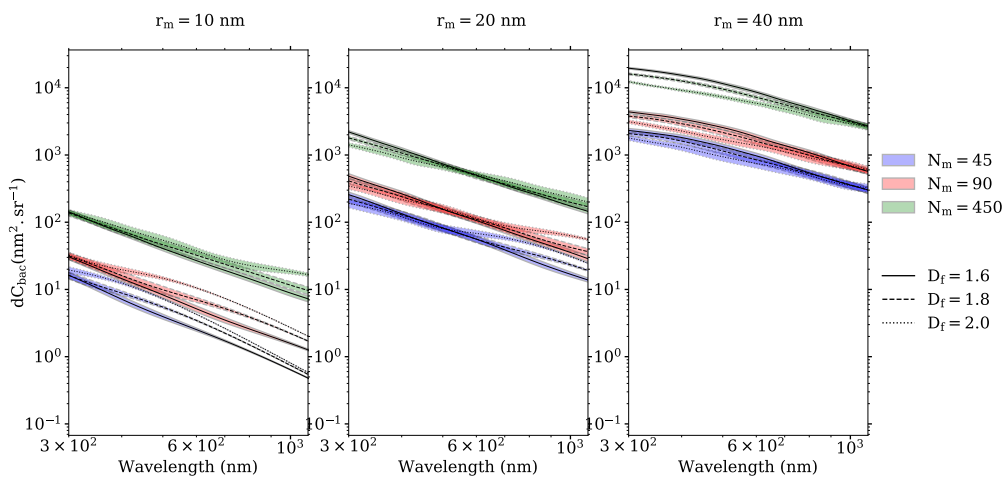
For the same fractal dimension and monomer radius, doubling the monomer radius leads to a backscattering cross-section increase by a factor ranging from 10 in the UV part of the spectrum up to 50 in the NIR part. The backscattering cross-section decrease with wavelength is greater for smaller monomer radius. Hence, the monomer radius of the aggregates also influences the wavelength dependence of the radiative properties.



(a) Extinction cross-sections.



(b) Scattering cross-sections.



(c) Backscattering cross-sections.

Figure II.1: Extinction (a), scattering (b) and backscattering (c) cross-sections of soot fractal aggregates ensembles.

Increasing tenfold the number of monomers induces a 6 to 12 times increase of the backscattering cross-section when the monomer radius is equal to either  $r_m = 20$  nm or  $r_m = 40$  nm. For monomer radius  $r_m = 10$  nm, this factor ranges from 7 to 29. This difference for smaller monomers is most certainly due to the different spectral dependence of the backscattering cross-sections. Indeed, the wavelength dependence of the backscattering cross-sections is also influenced by the number of monomers, with lower number of monomers inducing a steeper decrease. In particular, the 10 nm radius ensembles present the strongest variations.

The impact of the fractal dimension on the backscattering cross-section varies with different monomer radii and numbers. Indeed, for small monomer radius as represented on the left panel of Figure II.1c, the compact aggregates with higher fractal dimension present higher backscattering cross-sections. In this panel, soot aggregates with few monomers, *i.e.*  $N_m = 45$ , present a noticeable separation of the curves for different fractal dimensions (blue curves) from the UV part to the NIR, while curves associated with higher numbers of monomers are separated at higher wavelengths. For  $r_m = 20$  nm, low fractal dimension aggregates present higher backscattering cross-sections in the UV part of the spectrum, and conversely in the NIR part. Soot aggregates ensembles of  $r_m = 40$  nm monomer radius present increasingly ordered backscattering cross-sections with decreasing fractal dimension.

Some features of the different curves seem to be shifted to larger wavelengths when increasing the overall size of the aggregates. For example, on the left panel of Figure II.1c, the separation of the curves of different fractal dimensions occurs at larger wavelengths with higher monomer radius and/or number. The considered complex optical index varying only slightly in this spectrum, this indicates that a parameter similar to the usual size parameter  $x = 2\pi a/\lambda$  could be driving the wavelength dependence of these radiative properties.

### **Albedo, lidar ratio and linear depolarization ratio**

The single scattering albedo being the ratio between the scattering and extinction cross-sections, it allows to further investigate the relative wavelength dependence between these two parameters. Figures II.2(a), (c) and (e) show that in all cases, the single scattering albedo decreases with

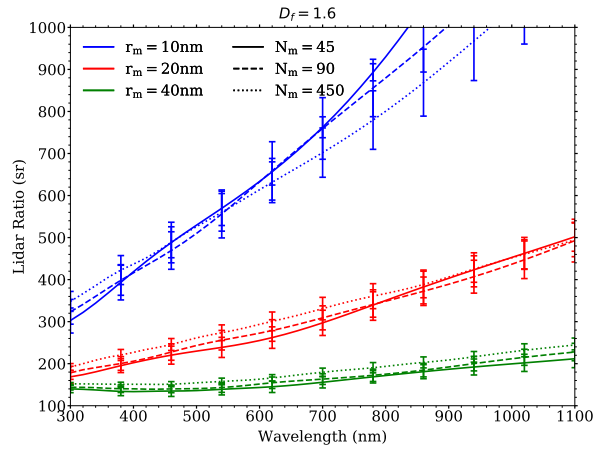
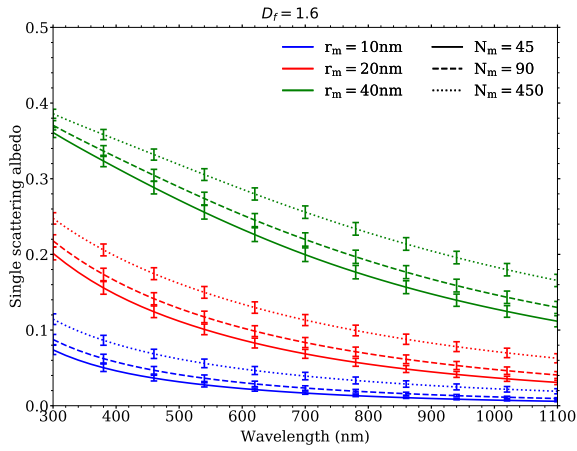
larger wavelength. This indicates that the scattering cross-section decreases with wavelength at a higher rate than the extinction cross-section. The impacts of the monomer radius, of the number of monomers and of the fractal dimension can also be evaluated using these figures.

The dependencies of the single scattering albedo with the monomer radius and number are similar to those of the cross-sections. Indeed, larger single scattering albedos are found for aggregates with a larger overall volume, which can be owed to either a larger number of monomers or a larger monomer radius. Larger fractal dimensions also induce larger single scattering albedos. This effect also depends on the number of monomers, as the increase with fractal dimension is more pronounced in ensembles with a higher number of monomers.

As the lidar ratio is the ratio between the extinction cross-section and the backscattering cross-section, both morphological and spectral dependencies of the lidar ratio are closely related to those of the cross-sections. Indeed, Figures II.2(b), (d) and (f) show an increasing lidar ratio with larger wavelengths, which is consistent with the wavelength dependence of the backscattering and extinction cross-sections. Moreover, the lidar ratio and the single scattering albedo  $\omega_0$  seems anti-correlated, with higher single scattering albedos being associated with lower lidar ratios. This is also explained by the respective formulations of these two quantities. Indeed, the extinction cross-section intervenes in the numerator of the expression of the lidar ratio (see Equation I.2.24 and in the denominator of the expression of the single scattering albedo I.2.23).

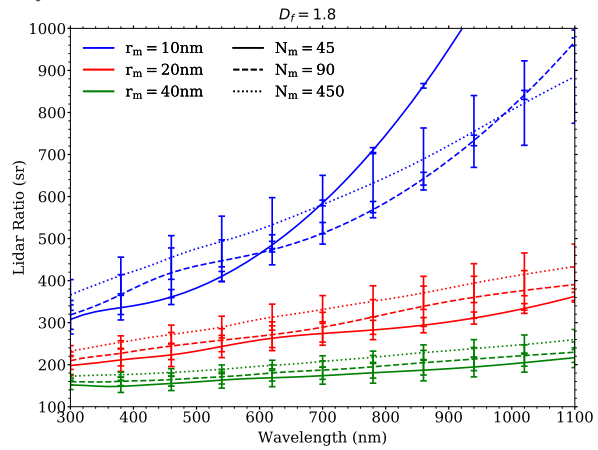
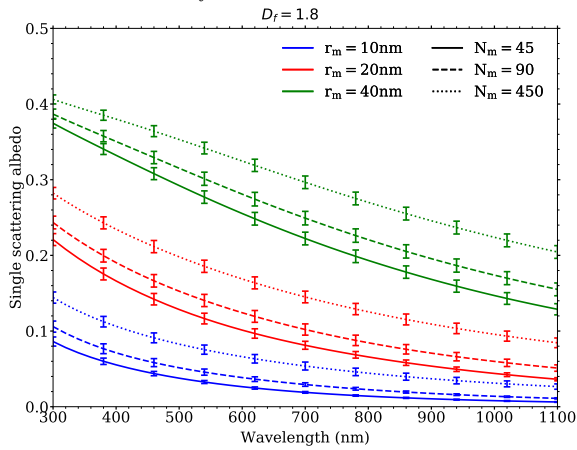
A larger monomer radius reduces the lidar ratio, which is consistent with the increasing backscattering cross-section presented in Figure II.1c. Lidar ratio values with different monomer radii show close values in the UV part of the spectrum, and diverge in the near infrared. Aggregates with smaller monomer radii present a more important increase of the lidar ratio. This behavior is also in accordance with the spectral dependence of the backscattering cross-section in Figure II.1c. A higher number of monomers also induces a higher lidar ratio, with the noticeable exception of the ensemble of smallest aggregates (*i.e.*  $r_m = 10$  nm,  $N_m = 45$ ). This ensemble wavelength dependence is most probably due to the steeper decrease of the backscattering cross-section of this ensemble as shown in Figure II.1c (left panel; blue dashed line). The variation of the lidar ratio with the number of monomers is still small, the associated standard deviations overlapping

on many parts of the spectrum.



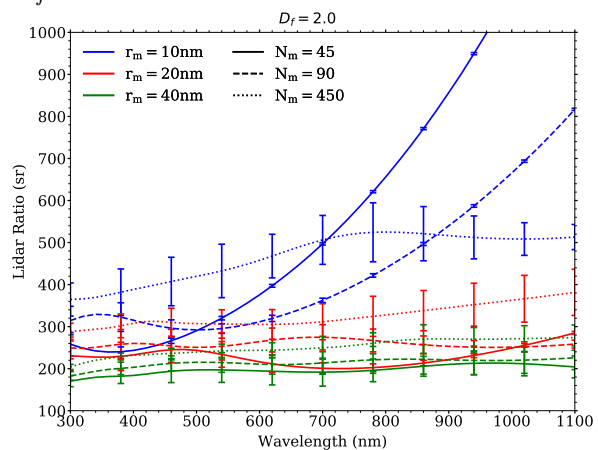
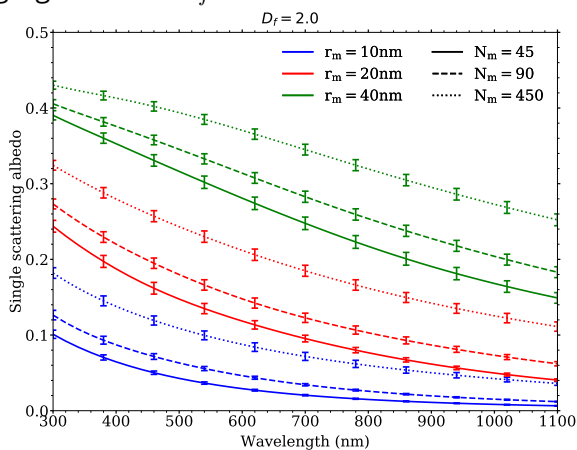
(a) Single scattering albedo of ensembles of aggregates with  $D_f = 1.6$ .

(b) Lidar ratio of ensembles of aggregates with  $D_f = 1.6$



(c) Single scattering albedo of ensembles of aggregates with  $D_f = 1.8$ .

(d) Lidar ratio of ensembles of aggregates with  $D_f = 1.8$

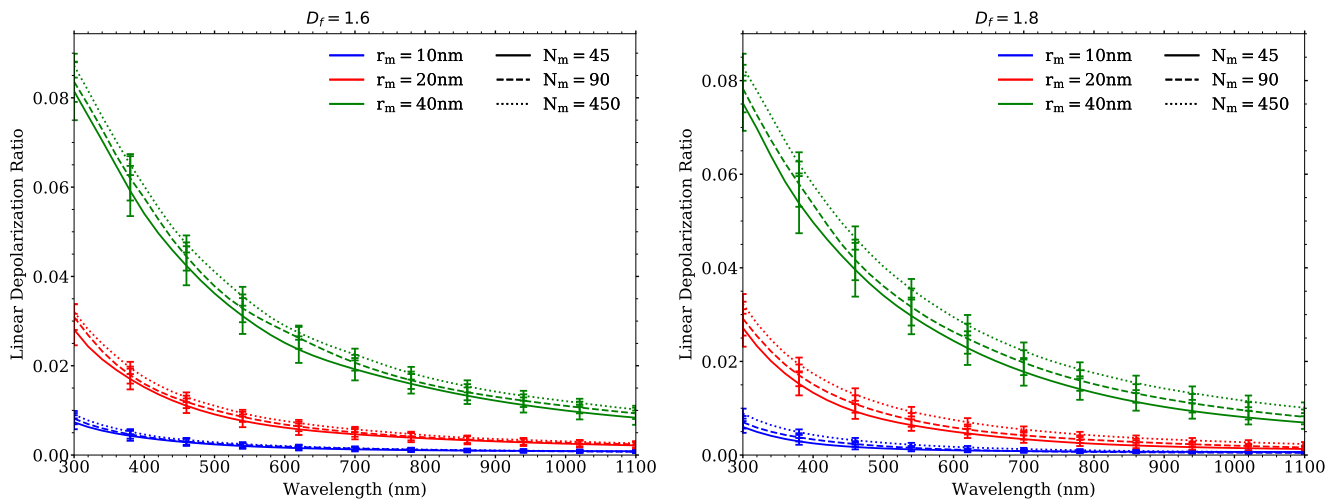


(e) Single scattering albedo of ensembles of aggregates with  $D_f = 2.0$ .

(f) Lidar ratio of ensembles of aggregates with  $D_f = 2.0$

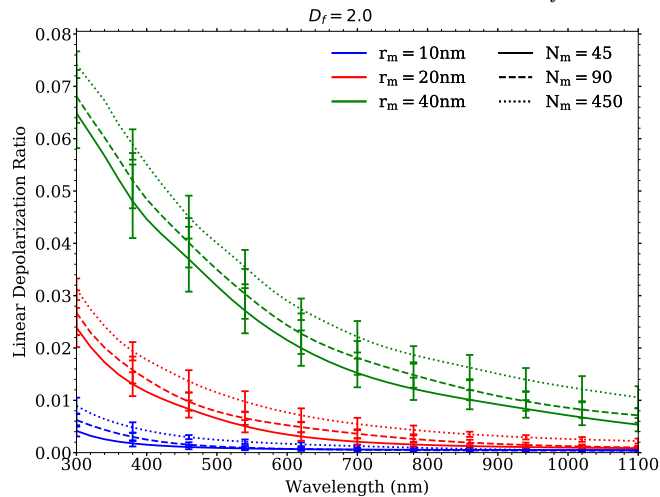
Figure II.2: Single scattering albedo (left figures; (a), (c) and (e)) and lidar ratio (right figures; (b), (d) and (f)) of ensembles of aggregates.

Impacts of the fractal dimension on the lidar ratio are harder to evaluate, as several distinctive trends occur as a function of both wavelength and monomer radius. Indeed, the comparison between Figures II.2b and II.2f shows that for small aggregates (blue curves), a more compact aggregate induces a lower lidar ratio, while large aggregates (green curves) present the inverse feature. Intermediate size (red curves) presents both trends, the former in the NIR part and the latter in the UV part of the spectrum. Similarly, the standard deviations of the lidar ratios are predominantly affected by the backscattering cross-section standard deviations.



(a) Linear depolarization ratio of ensembles of aggregates with  $D_f = 1.6$

(b) Linear depolarization ratio of ensembles of aggregates with  $D_f = 1.8$



(c) Linear depolarization ratio of ensembles of aggregates with  $D_f = 2.0$

Figure II.3: Linear depolarization ratios of ensembles of aggregates composed of monodisperse monomers.

Figure II.3 shows a decrease of the LDR and its associated standard deviation with increasing wavelength. LDR variation with monomer radius is similar to the backscattering cross-section dependence on  $r_m$ , with the LDR increasing for larger monomer radius. For example, the LDR increases about tenfold when the monomer radius is increased from  $r_m = 10$  nm to  $r_m = 40$  nm at 300 nm wavelength. The 10 nm monomer radius LDRs are progressively reaching a near-zero threshold as the wavelength increases. Ensembles with  $r_m = 20$  nm and  $r_m = 40$  nm are also approaching this value at large wavelengths.

The LDR also increases with increasing number of monomers, although this effect is far less noticeable than the one induced by the monomer radius. A modification of the fractal dimension also induces small variations of the LDR. Indeed, lower fractal dimensions induce slightly higher LDR values. Similar to its impact on the single scattering albedo, the fractal dimension seems to amplify the modification of the LDR due to a variation in the number of monomers.

### **Discussion on the impacts of the morphological parameters on the computed radiative properties**

Overall, the monomer radius  $r_m$  appears to be the morphological parameter that influences the most the considered radiative properties of soot aggregates, as they all show large variations according to  $r_m$ . The number of monomers has a strong impact on the cross-sections ( $C_{ext}$ ,  $C_{sca}$  and  $dC_{bac}$ ) and on the single scattering albedo, and a weak impact on the lidar ratio and the LDR. The relatively strong dependencies of the cross-sections on the monomer radius and number seem to be related to the overall size of the aggregate, with larger geometrical cross-sections and volumes of matter resulting in higher radiative cross-sections. The fractal dimension, although being an essential parameter of the fractal model, only induces low variations on the lidar-relevant radiative properties.

The spectral dependence of the LDR is consistent with the consideration that as the wavelength increases, the illuminating wave is less sensitive to the non-sphericity of the soot aggregates. Indeed, as previously mentioned, spherical particles do not depolarize the scattered light in the backward direction. As the wavelength increases, the relative size of the aggregates com-

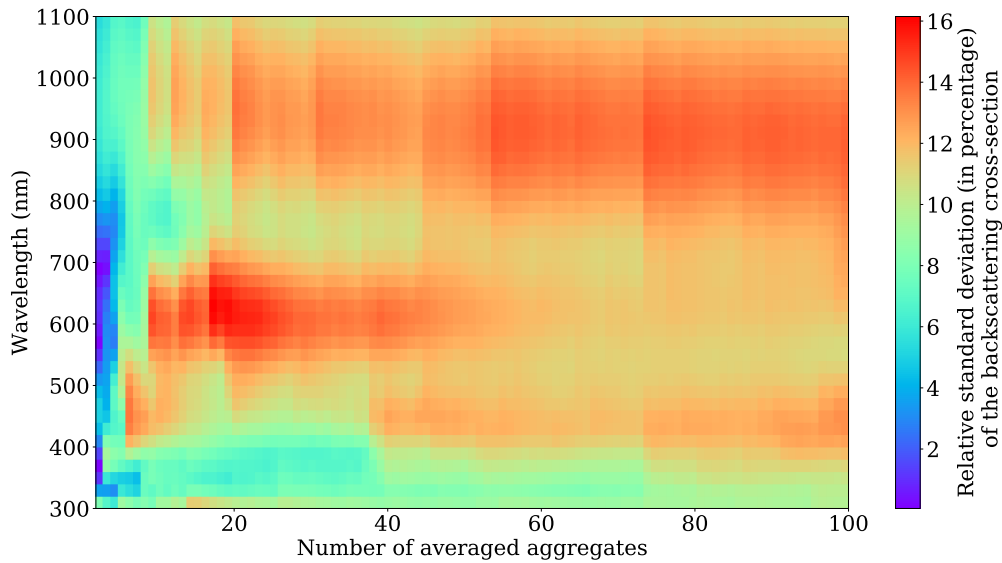
pared to the wavelength is smaller, and light is less sensitive to the shape irregularities. This is further supported by the low LDR values of the  $r_m = 10$  nm soot aggregates ensembles. The increasing LDR for lower fractal dimension, *i.e.* more linear soot aggregates, is again consistent with argument of the non-sphericity of an aggregate inducing more depolarization in the backward direction. The depolarization by a soot fractal aggregate is a byproduct of the multiple scattering or coupling among primary particles [142], and is sensitive to the internal fine structure of the aggregate. By increasing the monomer radius, or equivalently reducing the wavelength, the LDR is increasingly sensitive to the fractal dimension.

### Standard deviation

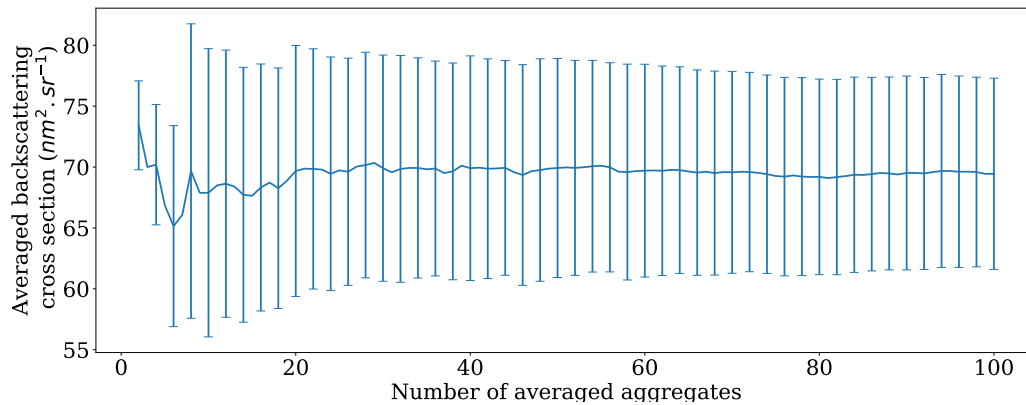
Even averaged over one hundred aggregates, the standard deviations of the backscattering cross-section, of the lidar ratio and of the LDR are important. As both the LDR and the lidar ratio are dependent on the backscattering cross-section, these statistical deviations indicate that the backscattering cross-section is sensitive to the fine structure of the aggregates. The fractal parameters being nearly constant in each ensemble, it can be assumed that this morphological description is not sufficient in order to precisely describe an aggregate morphology. The impact of the sizes of the ensembles, *i.e.* the numbers of aggregates that they contain, can be evaluated by calculating the standard deviations of the radiative properties according to the number of aggregates they are averaged on.

Figure II.4a presents the evolution of the standard deviation of the backscattering cross-section of aggregates with monomer radius  $r_m = 20$  nm, number of monomers  $N_m = 90$  and fractal dimension  $D_f = 1.8$ . These morphological parameters correspond to the intermediate values of their respective range. The standard deviation is computed as a function of the number of aggregates in the ensemble and as a function of wavelength.

The results presented in Figure II.4a show that when increasing the number of aggregates per ensemble from one to around fifty, there can be strong variations of the standard deviation depending on the considered wavelengths. Variations of the standard deviation are less significant at larger numbers of aggregates, and the standard deviations are seemingly reaching a threshold.



(a) Relative standard deviation of the backscattering cross-section.



(b) Average and absolute standard deviation of the backscattering cross-section at  $\lambda = 600$  nm.

Figure II.4: Impact of the number of aggregate per ensemble on the backscattering cross-sections average and standard deviation. Results are presented for the ensemble with morphological parameters  $r_m = 20$  nm,  $N_m = 90$  and  $D_f = 1.8$ .

Figure II.4b presents the average backscattering cross-section at 600 nm for the same ensemble and as a function of the number of aggregates within the ensemble. The absolute standard deviations are represented every two increment in order to lighten the figure. This wavelength is chosen as it presents a distinguishable change in the standard deviation when increasing the number of aggregates. Figure II.4b shows that the average backscattering cross-section is also subject to perceivable variation at low number of aggregates, but it stabilizes for a number of

aggregate per ensemble above 20 – 30. Fairly similar behaviours have been observed for all the other ensembles and radiative properties.

The results obtained for the other ensembles, presented in Appendix A, show that the change of monomer radius induces a shift similar to the one observed in Figure II.1c, with smaller radii generally inducing lower standard deviations. Larger numbers of monomers and smaller fractal dimensions also seem to induce lower standard deviations.

In the study presented after, the number of aggregates per ensemble is either kept to one hundred or reduced to fifty. This reduced number is considered as it reduces the computational cost of the calculations. Moreover, according to our observations, this number is sufficient in order to account for the standard deviations and to provide correct evaluations of the radiative properties.

### II.1.3 Soot fractal aggregates with polydisperse monomers

In this section, the radiative properties of aggregates composed of polydisperse monomers are presented. The number of variables has been largely reduced in this section compared to the one relative to monodisperse aggregates. Indeed, the results presented here will be later used in Chapter IV, in which multiply-scattered polarization-resolved lidar signals are presented. Due to the added analysis complexity, the decision has been made to reduce the problem dimension by fixing some of the variables to intermediate values.

#### Methods

As in the previous section, the radiative properties presented here are averaged over several aggregate realizations with the same micro-physical parameters. Because the polydispersity of the monomers is now considered, the TCCA code used for the generation of the aggregates needs to account for this morphological property. The FracVAL code by Morán et al. [80] allows to generate polydisperse fractal aggregates with an user-defined set of micro-physical parameters. The monomer size distribution is described by the log-normal size distribution as expressed in Equation I.1.5(b), with a monomer mean geometrical radius  $R_m = 20$  nm and a monomer radius

standard deviation  $\sigma_m = 1.1$ . The fractal dimension is set to  $D_f = 1.8$ , while the fractal prefactor and the number of monomers are set to  $k_f = 1.3$  and  $N_m = 100$  respectively. An ensemble of one hundred aggregates is generated using these micro-physical parameters.

The radiative properties of the aggregates are once again computed using the MSTM code [138] with the random-orientation option and at three wavelengths, namely  $\lambda = 355$  nm (UV),  $\lambda = 532$  nm (VIS) and  $\lambda = 1064$  nm (IR). These wavelengths are considered in order to represent the main emission wavelength, the frequency doubled wavelength and frequency tripled wavelength of Nd:YAG lasers. As in the previous section, the optical index is also computed using the wavelength-dependent dispersion law from [7]. The optical properties of each aggregate realization are computed individually, and the arithmetic averages are then computed.

### Radiative properties

$\lambda$ (nm)	355	532	1064
$m_o$	$1.663 + i0.715$	$1.732 + i0.600$	$1.819 + i0.591$
$C_{ext}(\text{nm}^2)$	$74978 \pm 763$	$40071 \pm 501$	$16574 \pm 184$
$C_{sca}(\text{nm}^2)$	$17434 \pm 551$	$6419 \pm 274$	$997 \pm 41$
$C_{abs}(\text{nm}^2)$	$57544 \pm 473$	$33652 \pm 291$	$15578 \pm 151$
$\omega_0$	$0.232 \pm 0.006$	$0.160 \pm 0.005$	$0.060 \pm 0.002$
$dC_{bac}(\text{nm}^2.\text{sr}^{-1})$	$349 \pm 34$	$191 \pm 19$	$53 \pm 6$
$LR$	$217 \pm 21$	$212 \pm 21$	$319 \pm 33$
$\delta_p$	$0.022 \pm 0.003$	$0.009 \pm 0.001$	$0.002 \pm 0.001$
$g_0$	$0.663 \pm 0.020$	$0.534 \pm 0.021$	$0.320 \pm 0.021$

Table II.1: Radiative properties of soot aggregates with polydisperse monomers.

Table II.1 summarizes the numerical results obtained on these polydisperse aggregates. The radiative properties presented in this table present strong similarities with those of monodisperse aggregates. The differences in number of monomers and wavelength do not allow for a direct comparison between these results, but such a comparison is made in Appendix B, based on the calculations presented in Section II.2.2. Still, the same wavelength dependence can be observed, and the different radiative properties and their associated standard deviations are found in the same range as those of aggregates composed of monodisperse monomers. The asymmetry parameter is also presented in Table II.1. It assesses the unbalance between the forward

scattering and the backward scattering, which is explicitly characterized by the phase function. This phase function, as well as the normalized scattering matrix elements  $a_2$  and  $b_1$  are presented in Figure II.5.

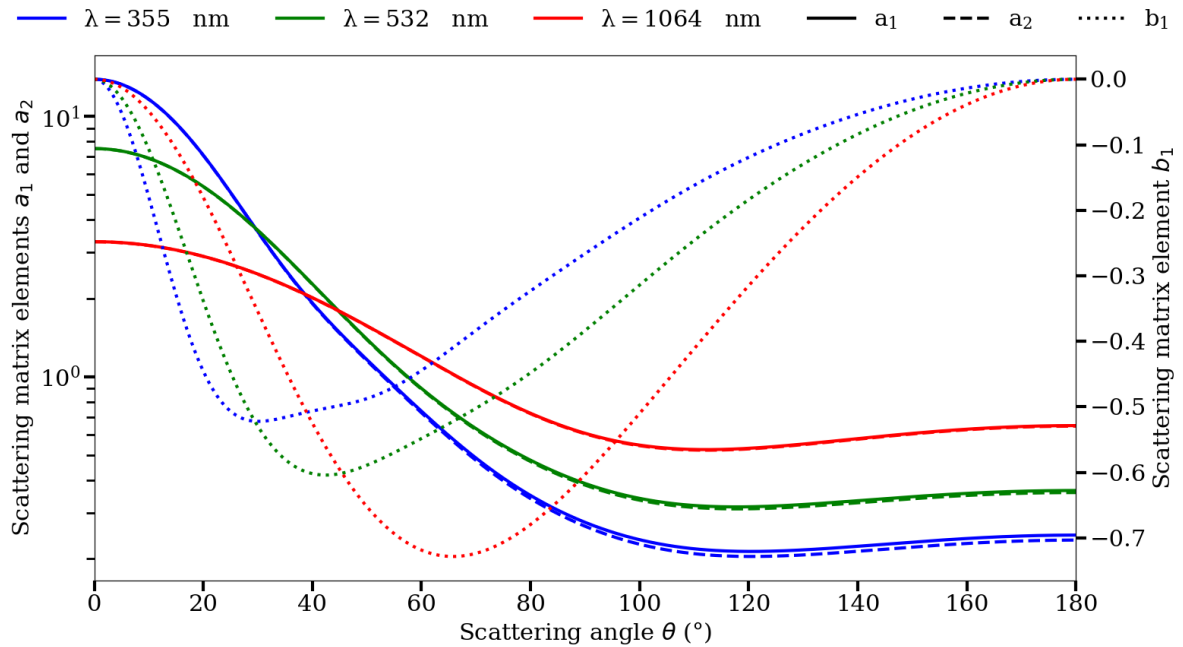


Figure II.5: Scattering matrix elements  $a_1$ ,  $a_2$  and  $b_1$  of the aggregates at the different wavelengths.

The scattering phase function is represented on Figure II.5 by the normalized scattering matrix element  $a_1$ . Comparing this phase function with the values of the asymmetry parameter  $g_0$  on Table II.1, the higher asymmetry parameters can be identified with the scattering phase functions that are more peaked in the forward direction. This occurs at shorter wavelengths, where the size parameter is further away from the Rayleigh limit. Indeed, for Rayleigh scatterers, the scattering phase function is symmetrical, and the asymmetry parameter is null.

Figure II.5 also presents the normalized scattering matrix elements  $a_2$  and  $b_1$ . These elements are used in the description of the change of polarization during the scattering process. The element  $b_1$  verifies the identity described in Equation I.2.16(a) in the backward direction. As expected, the element  $a_2$  does not verify the identity I.2.15(a), which is a marker of non-sphericity. However, as the wavelength increases, the value of the scattering element  $a_2$  approaches the value of  $a_1$ . This further supports the interpretation that the process of light-scattering by the aggregates more closely resembles the scattering by Rayleigh scatterers as the wavelength increases.

### II.1.4 Superaggregates

Superaggregates, or superaggregates, are a singular type of soot aggregates that have been observed in large-scale wild fires [143], inverted flame laboratory experiments [144] and pool fires [145]. In this section, the morphological features of a numerically generated superaggregate are described and evidenced by the auto-correlation function and the structure factor. The radiative properties of this aggregate are also computed using both the STM method and the RDG-FA theory. The differences between the results obtained using these two methods are also discussed. The radiative properties of superaggregates are also compared to those of "canonical" soot aggregates, as those presented in Section II.1.2. The majority of the results presented here have been published in an article of ours [146], which stems from a collaboration with the Kansas State University. Several clarifications and additional results are presented here which are not in the published version of this study.

#### Morphological features and methods

Superaggregates form in heavily sooting flames and intense fires. In these conditions, turbulent airflow can locally increase the volume concentration of aggregates, allowing different aggregates, with potentially different fractal dimensions, to come into contact and "stick" together. The structures formed in this process can then be described as aggregates of aggregates. Because they can originate from aggregates with different fractal dimensions, the term hybrid aggregates is also used. Hence, this type of aggregate can exhibit a fractal dimension which is different according to the considered length scale. Being aggregates of aggregates, they also exhibit a larger overall size and a larger number of monomers than canonical soot aggregates.

In this section, only one superaggregate is put under study. This is due to the increased computational time of the MSTM code associated with the larger number of monomers. This aggregate has been generated using the DLCA code described by Pierce [147]. A canonical aggregate is also generated using the same code in order to compare the radiative properties of these two types of particle. The monomer radius size distribution of both of these aggregates is considered monodisperse with  $r_m = 20$  nm. Their radii of gyration are  $R_{g,c} = 220$  nm for the canonical ag-

aggregate (subscript  $c$ ) and  $R_{g,s} = 593$  nm for the superaggregate (subscript  $s$ ), and their numbers of monomers are  $N_{m,c} = 90$  and  $N_{m,s} = 4275$  respectively.

As in Section II.1.2, the radiative properties of these two types of aggregate are computed on the wavelength range  $\lambda = 300 - 1100$  nm. The same optical index relationship from Chang and Charalampopoulos [7] is also used, as it provides a wavelength-dependent relationship. Moreover, this index is commonly used for the computation of soot particles emitted from pool-fires [148, 149, 150], which is a confirmed source of emission of superaggregates [145]. The radiative properties are computed using the STM method, using the MSTM code, and with the RDG-FA theory. As presented in Section I.2.4, in the RDG-FA framework, analytical expressions can be used in order to compute the radiative properties of soot aggregates if their micro-physical parameters are known. Indeed, if the number of monomers, their radius and the radius of gyration are known, the scattering, extinction and absorption cross-sections can be computed. Moreover, if the fractal dimension is known, an approximate formulation of the structure factor can be used, which allows the computation of the angle-dependent radiative properties such as the differential scattering cross-section. In the case considered here, the fractal dimensions of both aggregates are unknown. This implies that the computation of the aggregates auto-correlation functions and the derivation of their respective structure factors are necessary in order to compute the angle-dependent radiative properties.

### Computation of the auto-correlation function and of the structure factor

An algorithm has been developed in order to compute the auto-correlation function of these two aggregates. This algorithm is based on the computation of the fraction of volume occupied by monomers in a shell of inner radius  $r$  and outer radius  $r + dr$  and centered on a monomer center. Considering that  $dr \ll r_m$ , the principle of this algorithm can be schematized as in Figure II.6.

Figure II.6 presents a step of the autocorrelation function calculation scheme. It consists in computing the fraction of volume of a shell that is occupied by monomers, the shell being centered on a monomer center. The volume of the intersections is then the sum of the volumes of intersection of the shell with the 5<sup>th</sup>, 6<sup>th</sup> and 7<sup>th</sup> monomers. These intersections correspond to

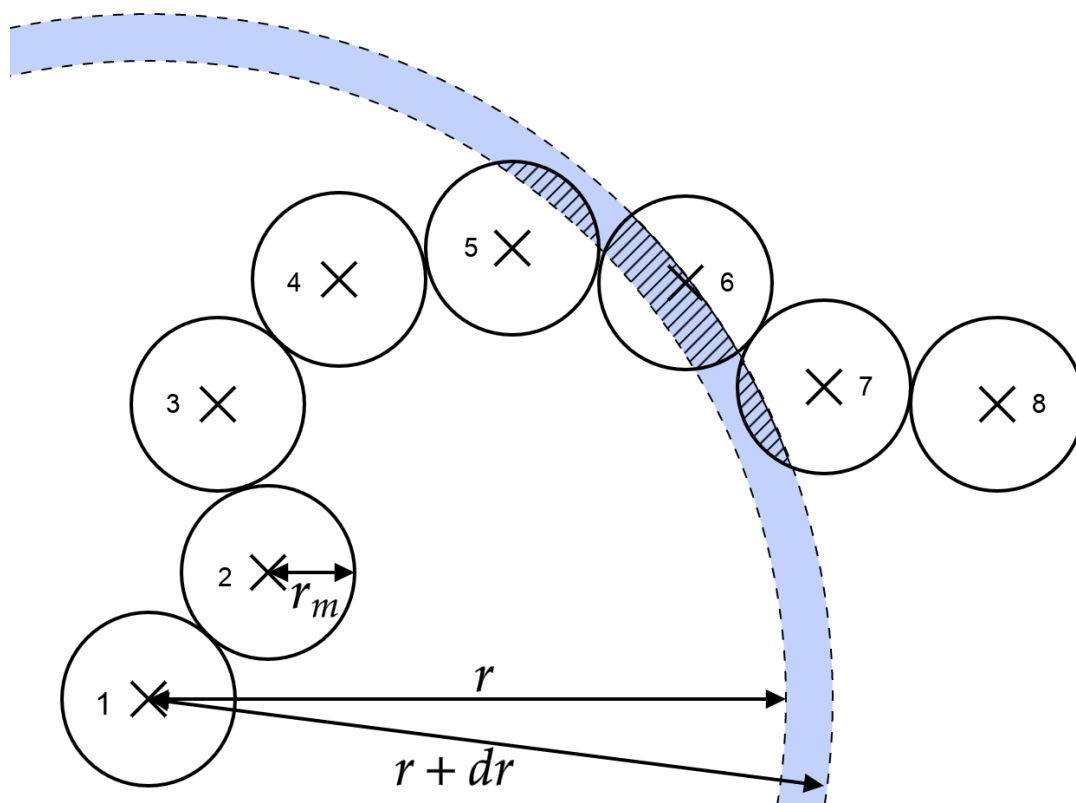


Figure II.6: Schematic view of the principle of the auto-correlation function calculation algorithm. The aggregate is composed of eight monomers which are numbered, with monomer radius  $r_m$ . The shell in which the fraction of volume occupied by monomers is computed is represented in light blue, with its boundaries represented by dashed lines. The inner radius of the shell is represented by the distance  $r$  and its outer radius by the distance  $r + dr$ . The striped areas represent the intersection volumes between the monomers and the shell.

the three possible cases which are expressed by the inequalities:

$$r < d_{ij} + r_m \text{ and } r + dr > d_{ij} + r_m \quad (\text{II.1.1a})$$

$$r < d_{ij} - r_m \text{ and } r + dr > d_{ij} - r_m \quad (\text{II.1.1b})$$

$$r > d_{ij} - r_m \text{ and } r + dr < d_{ij} + r_m \quad (\text{II.1.1c})$$

where  $d_{ij}$  is the distance between the  $i^{\text{th}}$  and  $j^{\text{th}}$  monomers. Case 1, as expressed in Equation II.1.1(a), corresponds to the intersection with monomer 5, Case 2 (Equation II.1.1(b)) corresponds to the intersection with monomer 7 and Case 3 (Equation II.1.1(c)) corresponds to the intersection with monomer 6. Equation II.1.1 refers to the general expression of the different cases. When applied to Figure II.6, the subscript  $i$  on Equation II.1.1 is  $i = 1$ . The volume of intersection between

two spheres of radius  $r_1$  and  $r_2$  whose centers are separated by a distance  $d_{12}$  is given by:

$$V_{int}(r_1, r_2, d_{12}) = \pi(r_1 + r_2 - d_{12})^2 \frac{d_{12}^2 + 2d_{12}r_2 - 3r_2^2 + 2d_{12}r_1 + 6r_2r_1 - 3r_1^2}{12d_{12}} \quad (\text{II.1.2})$$

The volume of intersection in each case is then expressed as:

$$V_1(r, r_m, d_{ij}) = \frac{4}{3}\pi r_m^3 - V_{int}(r, r_m, d_{ij}) \quad (\text{II.1.3a})$$

$$V_2(r, r_m, d_{ij}) = V_{int}(r + dr, r_m, d_{ij}) \quad (\text{II.1.3b})$$

$$V_3(r, r_m, d_{ij}) = V_{int}(r + dr, r_m, d_{ij}) - V_{int}(r, r_m, d_{ij}) \quad (\text{II.1.3c})$$

where the subscripts  $_1$ ,  $_2$  and  $_3$  refer to the different cases. In the general case, the fraction of occupied volume at distance  $r$  from the  $i^{\text{th}}$  monomer is expressed as:

$$f_{i,occ}(r) = \frac{1}{V_{shell}(r)} \sum_{\substack{j=1 \\ j \neq i}}^{j=N_m} \begin{cases} V_1(r, r_m, d_{ij}), & \text{if } r < d_{ij} + r_m \text{ and } r + dr > d_{ij} + r_m \\ V_2(r, r_m, d_{ij}), & \text{if } r < d_{ij} - r_m \text{ and } r + dr > d_{ij} - r_m \\ V_3(r, r_m, d_{ij}), & \text{if } r > d_{ij} - r_m \text{ and } r + dr < d_{ij} + r_m \\ 0, & \text{otherwise} \end{cases} \quad (\text{II.1.4})$$

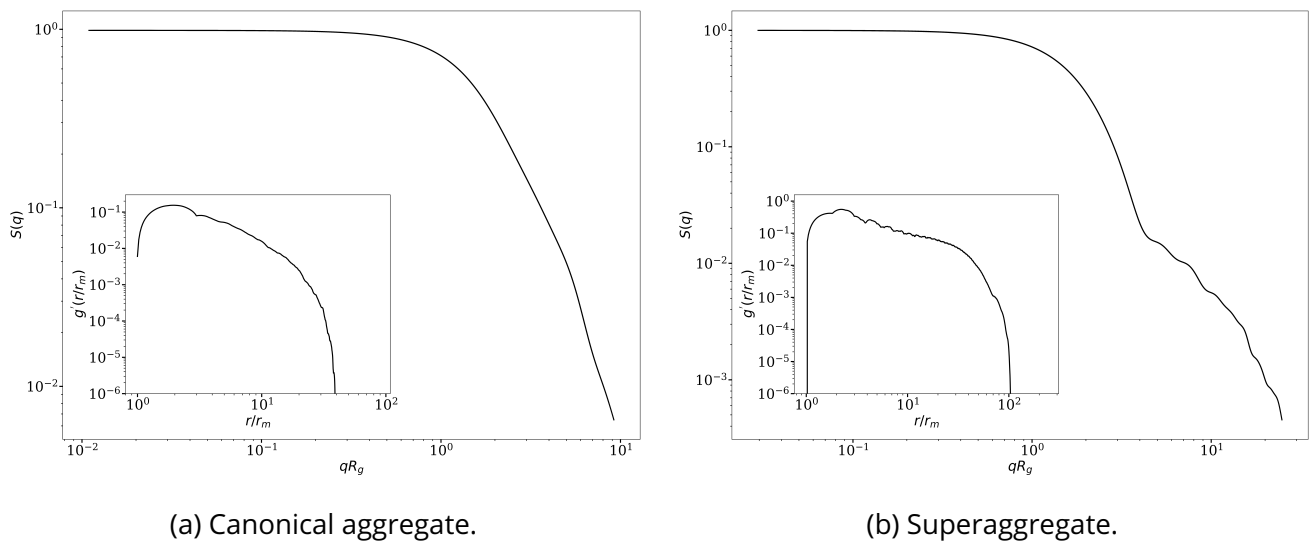
where  $V_{shell}$  is the volume of the shell such as  $V_{shell} = 4/3\pi((r + dr)^3 - r^3)$ . By computing this fraction over a range from  $r = r_m$  to  $r \gg R_g$ , the function describing the fraction of space occupied by monomers as a function of the distance from one monomer center is obtained. This function is then computed again by changing the shell center to another monomer center. The average of all these calculations gives the auto-correlation function such as:

$$g'(r) = \frac{1}{N_m} \sum_{i=1}^{i=N_m} f_{i,occ}(r) \quad (\text{II.1.5})$$

The structure factor is then computed such as:

$$S(q) = \frac{1}{N_m V_m} \left( 1 + 4\pi \int_{r=r_m}^{r \gg R_g} \frac{\sin(qr)}{qr} g'(r) r^2 dr \right) \quad (\text{II.1.6})$$

where  $V_m = 4/3\pi r_m^3$  is the volume occupied by a monomer. This equation slightly differs from Equation I.2.38 because our algorithm does not take into account the auto-correlation of the monomers with themselves. Hence, the density auto-correlation function  $g$  is unknown. Nevertheless, for monodisperse spherical monomers, this neglected contribution results in the added term in the parenthesis of Equation II.1.6, while the conversion from the auto-correlation function to the density auto-correlation function is achieved by the normalization by the volume of the aggregate.



(a) Canonical aggregate.

(b) Superaggregate.

Figure II.7: Structure factors  $S(q)$  and auto-correlation function  $g'(r/r_m)$  of the canonical aggregate and of the superaggregate.

Figure II.7 presents the structure factors  $S(q)$  of the canonical aggregate on subfigure (a) and of the superaggregate on subfigure (b). The insets in these subfigures represent the auto-correlation functions  $g'(r/r_m)$  of their respective aggregates. As in Equation I.2.39, two regimes can be identified to describe the evolution of the structure factor in the reciprocal space. The Guinier regime when  $qR_g < 1$  and corresponding to Equation I.2.39(a) is present in both the canonical aggregate structure factor (Figure II.7(a)) and the superaggregate structure factor (Figure II.7(b)). On the other hand, differences appear in the power law regimes (Equation I.2.39(b);  $qR_g > 1$ ) of these two aggregates. The canonical aggregate exhibits the expected single power-law dependence, while the superaggregate exhibits two distinct power-law regimes. This dual power-law dependence according to the length scale in the reciprocal space is characteristic of

superaggregates [151].

### Comparison between RDG-FA and STMM over canonical aggregates and superaggregate

In the RDG-FA theory, the differential scattering cross-sections are computed using the previously retrieved structure factor. Hence, considering the structural differences between the two considered aggregates, it is expected that the radiative properties will be affected. As described in Section I.2.4, the RDG-FA theory does not account for the coupling of the scattered fields by individual monomers. This justifies the use of the STM method to study the effects of this coupling by comparison with the results obtained with the RDG-FA theory, as the STM method accounts for this interdependence.

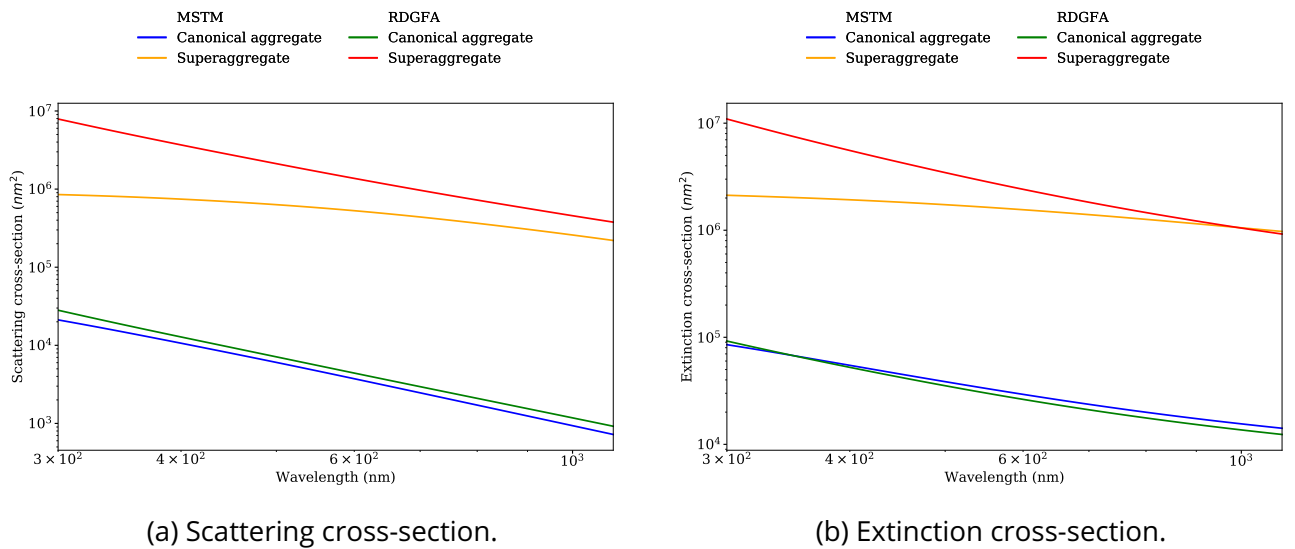


Figure II.8: Scattering and extinction cross-sections of the canonical aggregate and of the superaggregate.

Figure II.8 presents the scattering and extinction cross-sections of the canonical aggregate and of the superaggregate, computed with the RDG-FA theory and the MSTM code on the wavelength range  $\lambda = 300 - 1100$  nm. The cross-sections of the canonical aggregate computed with the RDG-FA theory are in overall good agreement with those computed with the MSTM code, especially considering the extinction cross-sections. The scattering cross-sections of the canonical aggregate computed with the RDG-FA theory are systematically higher than those computed with the STM method. Larger discrepancies are found in the cross-sections of the superaggre-

gate when computed with the RDG-FA theory and the MSTM code. Indeed, the RDG-FA theory overestimates the scattering cross-sections by almost one order of magnitude in the UV part of the spectrum. As the wavelength increases, the agreement of the scattering cross-sections computed with both these methods improves. The extinction cross-sections follow a similar pattern, where the curves are largely separated in the UV part of the spectrum and eventually overlap in the IR part. The departure of the curves at shorter wavelengths might result from a stronger coupling of the scattered field by the monomers. Indeed, the Rayleigh-Debye-Gans approximation might not hold as strongly in these conditions. This coupling might also be dependent on the morphology of the aggregate, as these discrepancies are not as present when considering the canonical aggregate. Because the radiative properties are computed for only one realization of each type of aggregate, the standard deviation could not be computed. Hence, it should be considered that the computed radiative properties might be in agreement within their respective standard deviations, especially considering the canonical aggregate.

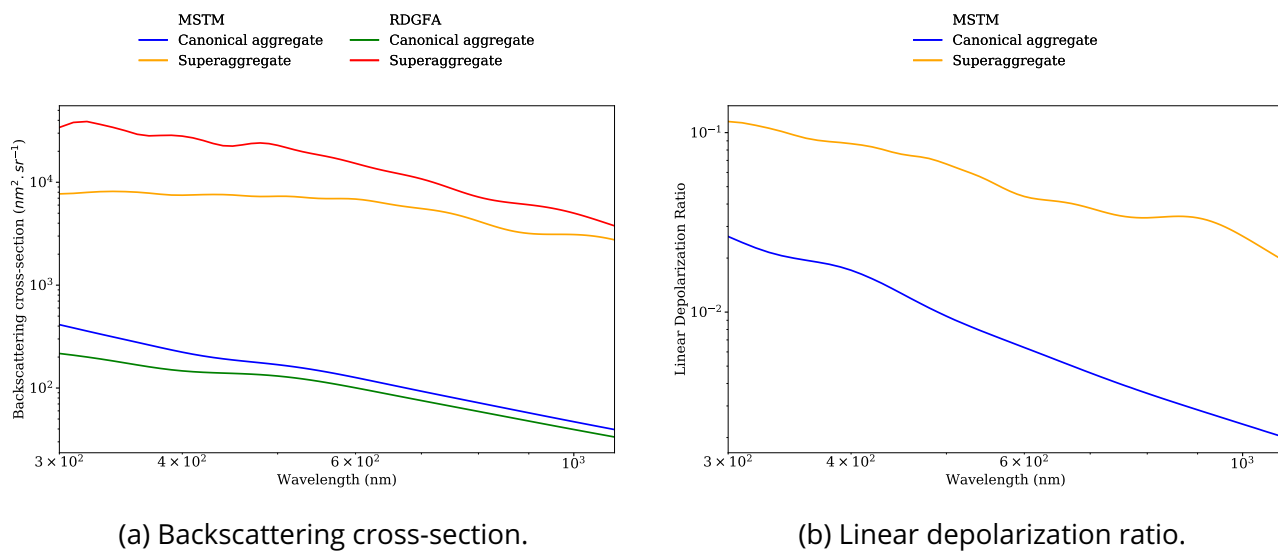


Figure II.9: Backscattering cross-sections and linear depolarization ratio of the canonical aggregate and of the superaggregate.

Figure II.9 presents the wavelength dependence of the backscattering cross-sections and of the LDR of the two considered aggregates. The backscattering cross-sections presented in Figure II.9(a) follow trends similar to those of the scattering cross-sections. Indeed, the backscattering cross-sections computed with the different methods are in poor agreement in the UV part of

the spectrum, and are progressively converging as the wavelength increases. In contrast to the scattering cross-sections, the backscattering cross-sections of the canonical aggregate computed with the MSTM code are larger than those computed with the RDG-FA theory. Larger discrepancies are also observable in the UV part of the spectrum. For the superaggregate, the RDG-FA theory still overestimates the backscattering cross-sections by almost one order of magnitude at short wavelengths and down to a factor of  $\approx 1.5$  at larger wavelengths.

Because the RDG-FA theory does not allow to compute the LDR, Figure II.9(b) only presents the LDRs computed with the MSTM code. However, it should be noted that the RDG-FA computation have been undertaken while considering its standard formulation, and that depolarization models have been developed in order to extend the RDG-FA theory and account for depolarization [152]. This incapacity of the standard RDG-FA theory to compute the LDR comes from the fact that this technique ignores the coupling of the monomers scattered fields. Hence, the values of the LDR computed with the MSTM code can be used as a proxy to qualitatively evaluate this coupling. The LDRs of the superaggregate are found to be up to one order of magnitude higher than the LDRs of the canonical aggregate. In order investigate the source of the discrepancies between the RDG-FA results and the MSTM results, Figure II.10 presents the Rayleigh-Debye-Gans approximation criterion as a function of wavelength.

Considering the results presented in Figure II.10, it appears that the Rayleigh-Debye-Gans approximation criterion  $2x_m|m_o - 1| \ll 1$  is verified over the whole wavelength range. However, this criterion rapidly approaches the value of 1 as the wavelength decreases, and the criterion is only approximately verified. This feature may explains the larger discrepancies between the radiative properties using the RDF-FA and the MSTM code in the UV range, as the criterion does not hold strongly. Tables II.2 and II.3 present the radiative properties of the canonical and superaggregates respectively, computed with the RDG-FA theory and the MSTM code at three different wavelengths, namely  $\lambda = 355, 532$  and  $1064$  nm. As in Figures II.8 and II.9, the radiative properties of the canonical aggregate computed with the RDG-FA theory and the STM method are in overall good agreement. The largest discrepancies are found in the backscattering cross-sections, and in consequence in the lidar ratios. As for the superaggregate, the comparison between the radiative

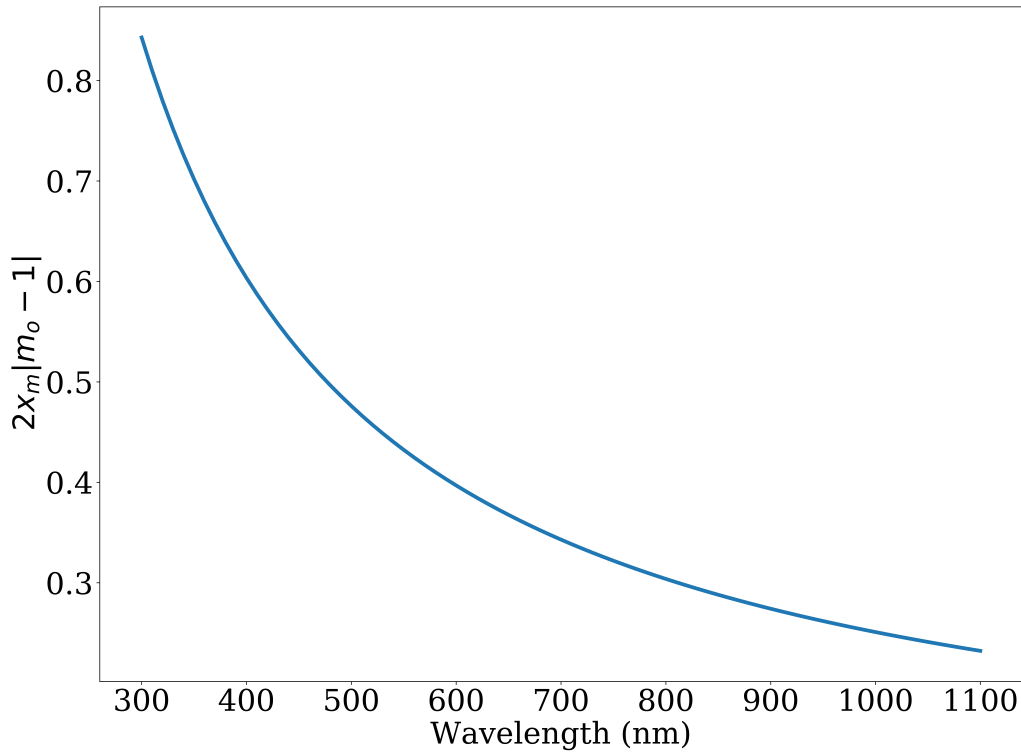


Figure II.10: Rayleigh-Debye-Gans approximation criterion as a function of wavelength. As a reminder, the size of the size parameter  $x_m$  is defined such as  $x_m = 2\pi r_m/\lambda$  and the optical index is computed following the wavelength dependent relationship presented in [7].

properties with the RDG-FA theory and the STM method shows much larger discrepancies.

Overall, the radiative properties of the canonical aggregate computed with the MSTM code are within the standard deviations of the radiative properties computed in Subsection II.1.2 for the same micro-physical parameters (*i.e.*  $r_m = 20$  nm and  $N_m = 90$ ). The RDG-FA theory provides accurate results of the extinction cross-section, a slight overestimation of the scattering cross-section and a slight underestimation of the backscattering cross-section. The radiative properties of the superaggregate computed with these two methods show much larger discrepancies. Considering that the MSTM code accounts for the coupling of the scattered fields, we may consider that this method provides more accurate results than those computed with the RDG-FA theory. Hence, the RDG-FA theory should be used with care when considering superaggregates. The radiative properties of the superaggregate are found to be  $\approx 1 - 2$  order of magnitude larger than those of the canonical aggregate.

Method	RDG-FA			STM			
	$\lambda$ (nm)	355	532	1064	355	532	1064
$C_{ext}(\text{nm}^2)$		65725	31834	12789	66105	35030	14602
$C_{sca}(\text{nm}^2)$		17610	6046	1003	14277	5140	791
$C_{abs}(\text{nm}^2)$		48115	25788	11786	51828	29890	16811
$\omega_0$		0.268	0.190	0.078	0.216	0.147	0.05
$dC_{bac}(\text{nm}^2.\text{sr}^{-1})$		171	122	35	287	156	42
$LR$		383	261	361	230	225	348
$\delta_p$		0	0	0	0.020	0.008	0.002
$g_0$		0.62	0.48	0.27	0.64	0.53	0.31

Table II.2: Radiative properties of the canonical aggregate.

Method	RDG-FA			STM			
	$\lambda$ (nm)	355	532	1064	355	532	1064
$C_{ext}(\text{nm}^2)$		$7.2902 \times 10^6$	$3.0461 \times 10^6$	962849	$2.0133 \times 10^6$	$1.6732 \times 10^6$	$1.0012 \times 10^6$
$C_{sca}(\text{nm}^2)$		$5.0048 \times 10^6$	$1.8213 \times 10^6$	403007	794770	597570	232920
$C_{abs}(\text{nm}^2)$		$2.2855 \times 10^6$	$1.2249 \times 10^6$	559842	$1.2185 \times 10^6$	$1.0756 \times 10^6$	768280
$\omega_0$		0.687	0.598	0.419	0.395	0.357	0.233
$dC_{bac}(\text{nm}^2.\text{sr}^{-1})$		30400	19670	4188	8068	7127	2936
$LR$		240	155	230	250	235	341
$\delta_p$		0	0	0	0.095	0.059	0.022
$g_0$		0.79	0.75	0.73	0.90	0.85	0.78

Table II.3: Radiative properties of the superaggregate.

## II.2 Evaluation of the Linear Depolarization Ratio of soot fractal aggregates

In this section the method and results of the measurement of the LDR of soot particles are presented. The particles under study are in suspension in ambient air, and the LDR is measured in the exact backscattering direction. This measurement is coupled with TEM observations of the emitted particles and with a numerical study. The numerical study aims at evaluating the morphological parameters and optical index which would ensure the lowest discrepancies with the measurements. Two morphological models are considered, with aggregates composed of either monodisperse or polydisperse monomers in point contact. The methods and results presented in this section have been published in the reference [2], which stems from a collaboration with the Institute of Light and Matter (ILM) in Lyon, France (CNRS Mixed Research Unit ILM UMR 5306). The ILM team developed an unique the experimental set-up for the laboratory evaluation of the LDR of particles. Hence, only a short, non-exhaustive description of the methods of the backscattering experiment is provided in Appendix C, but the reader is invited to read the article from Miffre et al. [153] for more detailed specifications.

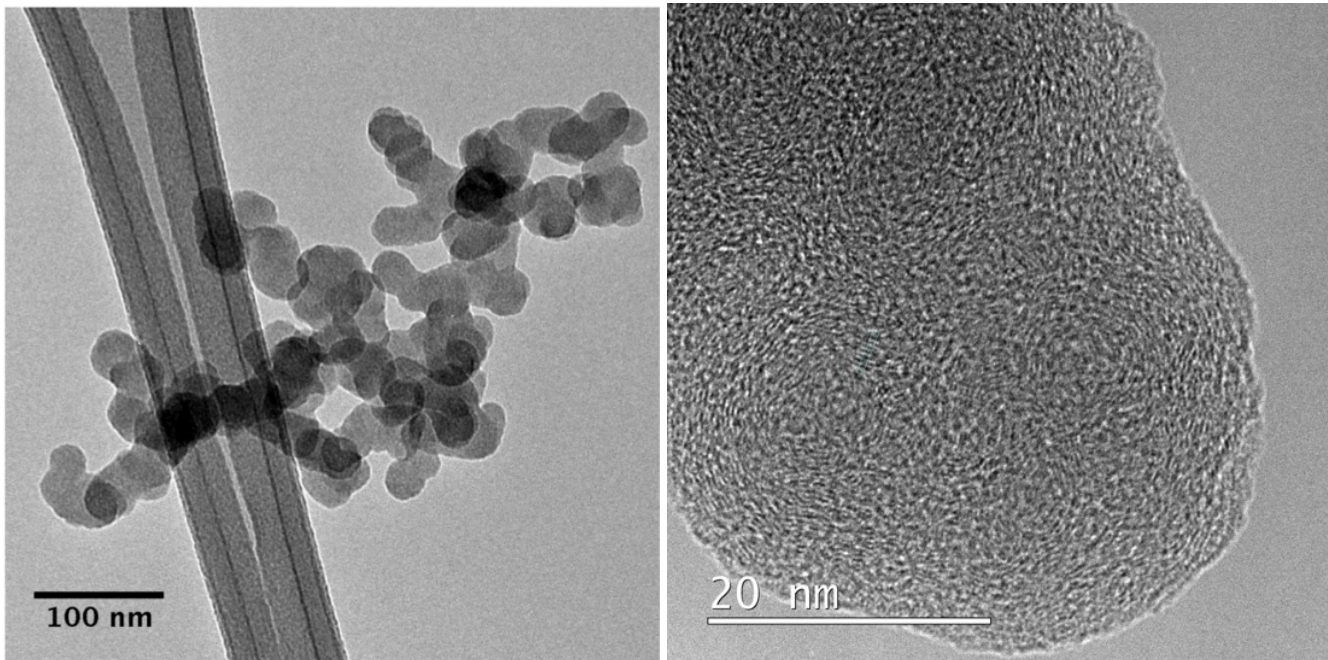
### II.2.1 Characterization of soot emitted from a kerosene pool-fire and experimental results

For the purpose of this study, a small-scale kerosene pool fire has been designed, which consists in a round container of kerosene with a diameter of 50 mm and 20 mm height. Such an experimental set-up enables the production of a constant soot emission from a defined volume of fuel. Following theoretical knowledge about liquid pool fire, the pool fire heat release rate and burning duration are evaluated for a kerosene burning rate  $m'' = 0.039 \text{ kg}\cdot\text{m}^{-2}\cdot\text{s}^{-1}$ . In this study, JET A-1 (NATO code F-35) kerosene was used. Thus, the heat release rate is estimated at 5 kW for a burning duration of 30 seconds. The flame height is comprised between 35 cm and 55 cm estimated from the Heskestad and Thomas method [154, 155]. The light backscattering measure-

ments were carried out starting a few seconds after ignition and during the steady burning time of the pool fire combustion.

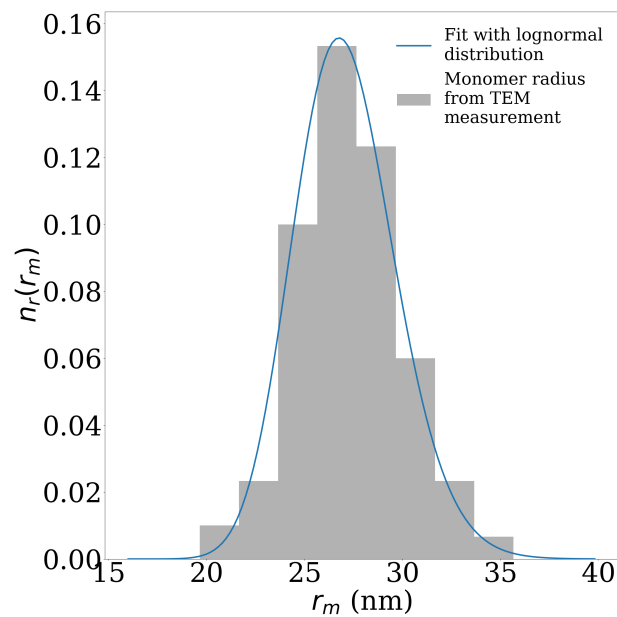
Soot particles emitted from the small-scale kerosene pool fire have been analyzed by Transmission Electron Microscopy (TEM), as shown in Figure II.11(a). Particles have been captured and transferred on TEM grids covered by a porous carbon film in order to observe suspended aggregates. The TEM grids were placed at the laser height (i.e. 30 cm above the recipient base), and approximately 3 cm off the axis formed by the container center and the laser beam. The Zeiss LIBRA 200 microscope is equipped with an in-column filter to achieve filtered images and operates at 200 kV. No degradation of the soot structure has been observed during the light backscattering experiment. Typical aggregates, as illustrated in Figure II.11(a), are composed of several tens of monomers with narrow size dispersion. These monomers exhibit a degree of non-sphericity and overlapping. Figure II.11(b) presents a zoomed-in view of a monomer sampled during this experiment. Disordered inclusions are present within this monomer, with concentric graphitic layers on the outer area. Due to restraints imposed by the process of particles sampling, the monomer radius reported here represents radii averaged over several TEM grids at different sampling locations in the pool fire. Analysis of the TEM image allows the retrieval of the monomer radius size distribution, as displayed in Figure II.11(c). To characterize this size distribution, the lognormal size distribution defined in Equation I.1.5(c) is used. Using a non-linear regression method, the monomer radius size distribution is found to be characterized by a mean radius of  $R_m = 27$  nm and a standard deviation of  $\sigma_m = 1.1$ . The monomer mean radius value is relatively large compared with soot produced by laminar diffusion flames but remains consistent with previous results obtained from soot emitted by pool fires [64, 156].

Following the methodology described in Appendix C, the measurement of the ratios  $[F_{22}/F_{11}]_{lab}$  and the evaluation of the LDRs was achieved the wavelengths  $\lambda = 355$  nm and  $\lambda = 532$  nm simultaneously. The methodology used for the retrieval of these quantities is described in reference [2] and [153]. The values of the ratio  $[F_{22}/F_{11}]_{lab}$  and of the LDRs are presented in Table II.4. The LDRs are found equal to  $\delta_{lab} = 11.7 \pm 2.3\%$  at wavelength  $\lambda = 355$  nm and to  $\delta_{lab} = 8.7 \pm 2.1\%$  at wavelength  $\lambda = 532$  nm.



(a) High resolution TEM image of a soot aggregate.

(b) High resolution TEM image of a monomer.



(c) Monomer radius size distribution.

Figure II.11: High resolution TEM image of a soot aggregate generated from the JET A-1 pool fire (a), of a monomer (b) and corresponding monomer radius size distribution (c). In order to represent this distribution, 151 monomers have been characterized.

$\lambda$ (nm)	$[F_{22}(\pi)/F_{11}(\pi)]_{lab}$	$\delta_{lab}$ (%)
355	$0.79 \pm 0.03$	$11.7 \pm 2.3$
532	$0.84 \pm 0.03$	$8.7 \pm 2.1$

Table II.4: Evaluation of the ratio  $[F_{22}(\pi)/F_{11}(\pi)]_{lab}$  and the LDR  $\delta_{lab}$  of soot particles emitted from a JET A-1 pool fire.

## II.2.2 Methods for the numerical evaluation of the LDR

In order to provide further interpretations of the measurements of the LDRs of these soot particles, a numerical study has been undertaken. This numerical study consists in generating ensembles of soot aggregates with varying morphology and optical index, and in computing their radiative properties. The parameters which result in the lowest discrepancy between the numerical and the experimental LDR are identified. By comparison with the available data from the literature and with the TEM observations, this allows to provide insights on the validity of the hypothesis of the morphological model and on its potential shortcomings.

Several ensembles of aggregates have been generated. The morphological models considered for the generation of these ensembles are those presented in Sections II.1.2 and II.1.3, corresponding to aggregates composed of monodisperse and polydisperse monomers respectively. As a reminder, the monomer radius size distribution of the aggregates composed of polydisperse monomers is defined in Equation I.1.5(b). In both case, the FracVAL TCCA code has been used for the generation of the aggregates. All aggregates are generated with a fractal dimension of  $D_f = 1.8$  and a fractal prefactor  $k_f = 1.3$ . Several ensembles are generated for both morphological models. Each ensemble contains fifty aggregate realizations, which will allow the computation of the average LDR and its standard deviation afterwards. The variable micro-physical parameters of the ensembles are the number of monomers  $N_m$  and the monomer radius  $r_m$  (mean geometrical monomer radius  $R_m$  for the polydisperse case). Ensembles are created for monomer number  $N_m \in [20, 200]$  with steps  $\Delta N_m = 20$ , and with radius  $r_m \in [10, 30]$  nm with steps  $\Delta r_m = 2.5$  nm ( $R_m \in [10, 30]$  nm and  $\Delta R_m = 2.5$  nm respectively for the polydisperse case). In the polydisperse case, the monomer radius standard deviation is set to  $\sigma_m = 1.1$ . To summarize, Figure II.12 presents two examples of aggregates generated with a monodisperse (II.12(a))

and a polydisperse (II.12(b)) monomer radius distribution, both with a number of monomers of  $N_m = 100$ . In Figure II.12(c) is also represented the monomer radius distribution of the aggregates generated with the FracVAL code, using the previously defined parameters.

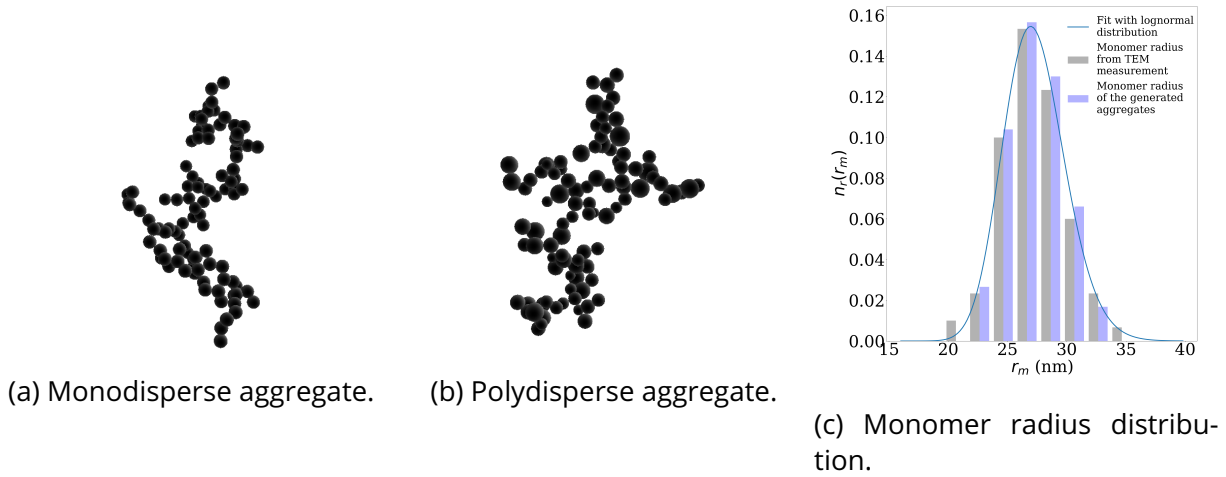


Figure II.12: Examples of generated aggregate with a monodisperse size distribution (a) and a polydisperse size distribution (b). For the polydisperse case, the TEM-observed size distribution (in grey) is compared with the one computed from the numerically-generated aggregates (in blue).

As in Sections II.1.2 and II.1.3, the MSTM code is used for the computation of the radiative properties. For both shape models, the orientation-averaged ratio  $[F_{22}/F_{11}]_{num}$  of each individual aggregate is computed. Results are then averaged according to the set of morphological parameters used in the generation of the aggregates. Hence, in this numerical study, we report results of ensembles of aggregates with same morphological parameters and the associated numerical standard deviations. In order to compute the scattering matrix of the generated aggregates, the complex refractive index is needed. As described in Section I.1.3, a wide range of complex refractive indices of soot particles are reported in the literature, and the optical index of the particles generated under the conditions of the experiment described in Section II.2.1 is unknown. In order to cover the range of possible indices, several values of the optical index are used during the computations:  $m_o = 1.16 + i0.71$ ,  $m_o = 1.61 + i0.74$ ,  $m_o = 1.68 + i0.93$ ,  $m_o = 1.81 + i0.76$  [51],  $m_o = 2.15 + i0.8$  [152] and  $m_o = 2.65 + i1.32$  [9]. These indices are used for both the UV and the VIS computations. The choice of these values is motivated by an already existing study [152] aiming, among other things, at studying the impact of the optical index on the depolarization ratio.

All computations are operated within the random orientation settings. Indeed, as the interacting particles are observed in ambient air and in the close vicinity of the pool-fire, the airflow resulting from the combustion process most probably prevents the particles from keeping a preferred orientation during the measurement.

### II.2.3 Numerical results

Figure II.13 presents the results of the numerical modelling of the ratio  $[F_{22}(\pi)/F_{11}(\pi)]_{num}$  for aggregates composed of monodisperse monomers, together with the corresponding LDR values derived from Equation C.1. In the following, the angle dependency of the scattering matrix elements  $F_{11}$  and  $F_{22}$  is implied, as the ratio is exclusively evaluated in the backscattering direction. These numerical results show several trends across all subfigures. First, smaller ratios can be observed as the monomer radius increases, which implies that soot fractal aggregates with large monomers produce larger LDRs at both wavelengths. A wavelength dependence of the ratio can also be observed. Indeed, at constant morphological parameters and refractive index, the LDR at 532 nm wavelength is lower than at 355 nm. This is consistent with the trends reported above in Section II.1.2. The modification of the optical index also induces large variations of the ratio  $[F_{22}/F_{11}]_{num}$  and consequently of the LDR. Both real part and imaginary part increase induce larger LDR. Finally, in some cases, a dependence on the number of monomers can be observed. Aggregates with a number of monomers under 80 show a decrease in the ratio  $[F_{22}/F_{11}]_{num}$  with increasing monomer number. In the other cases, the variation is less significant. These numerical results are consistent with results present in the literature as in [139, 157]. The numerical computation presented in this section allows for a comparison of the different radiative properties between monodisperse aggregates and polydisperse aggregates. Because such a comparison is not the primary objective of this study, this analysis is presented in Appendix B.

The numerical results for the ensembles of aggregates formed by polydisperse monomers are presented in Figure II.14. As in the monodisperse case, the ratio  $[F_{22}/F_{11}]_{num}$  decreases with increasing optical index, monomer radius and number of monomers. Compared with the monodisperse results presented in Figure II.13, the results for the polydisperse case present slightly lower

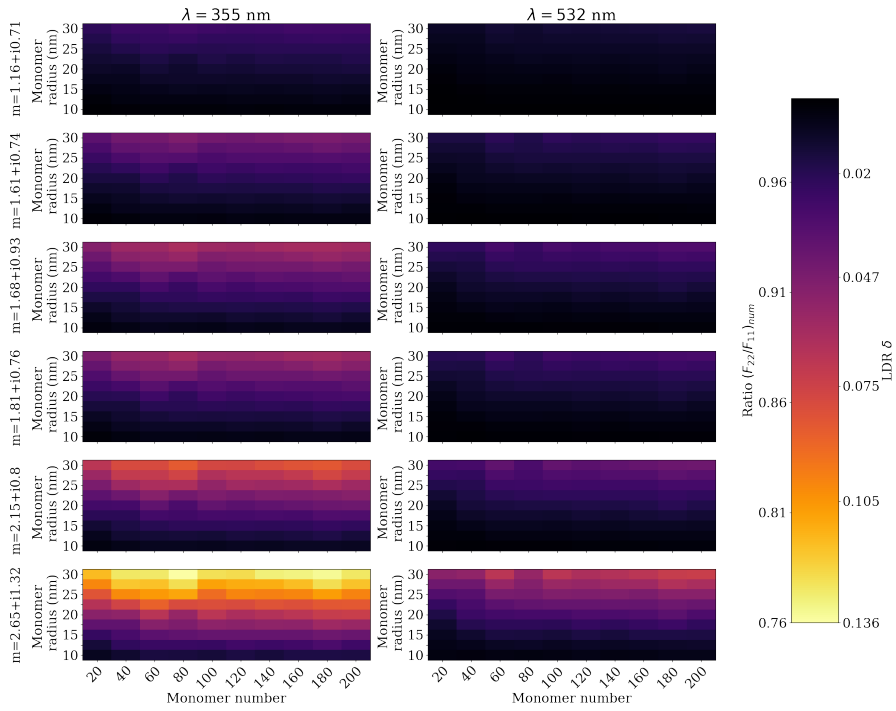


Figure II.13: Numerical results of the ratio  $[F_{22}/F_{11}]_{num}$  and the LDR for ensembles of aggregates formed by monodisperse monomers. The columns of subplots refers to different wavelengths, while the rows refer to different refractive indices. Inside the figures themselves, the x-axis represents variable monomer number, and the y-axis represents variable monomer radius. The colour scale indicates variation in the numerically computed ratio  $[F_{22}/F_{11}]_{num}$  and LDR.

$[F_{22}/F_{11}]_{num}$  values (i.e. higher LDRs). In [152], a slight decrease of the LDR with polydispersity is reported. However, the authors used a normal monomer radius distribution function, in comparison with the lognormal function used in this study, which could explain the discrepancy between our results. This is further supported by the results presented in [158] using a lognormal distribution. Polydisperse results also present an almost monotonic decrease of the ratio  $[F_{22}/F_{11}]_{num}$  with the monomer number, in contrast to the monodisperse results where more variability is present. This smoothing effect can be attributed to the polydispersity of the monomer radii.

In order to assess the discrepancies between the laboratory-measured  $[F_{22}/F_{11}]_{lab}$  and the numerically-computed  $[F_{22}/F_{11}]_{num}$  ratios, the percent disagreement  $\kappa$  is introduced and defined as:

$$\kappa = 100 \frac{[F_{22}/F_{11}]_{num} - [F_{22}/F_{11}]_{lab}}{[F_{22}/F_{11}]_{lab}} \quad (\text{II.2.1})$$

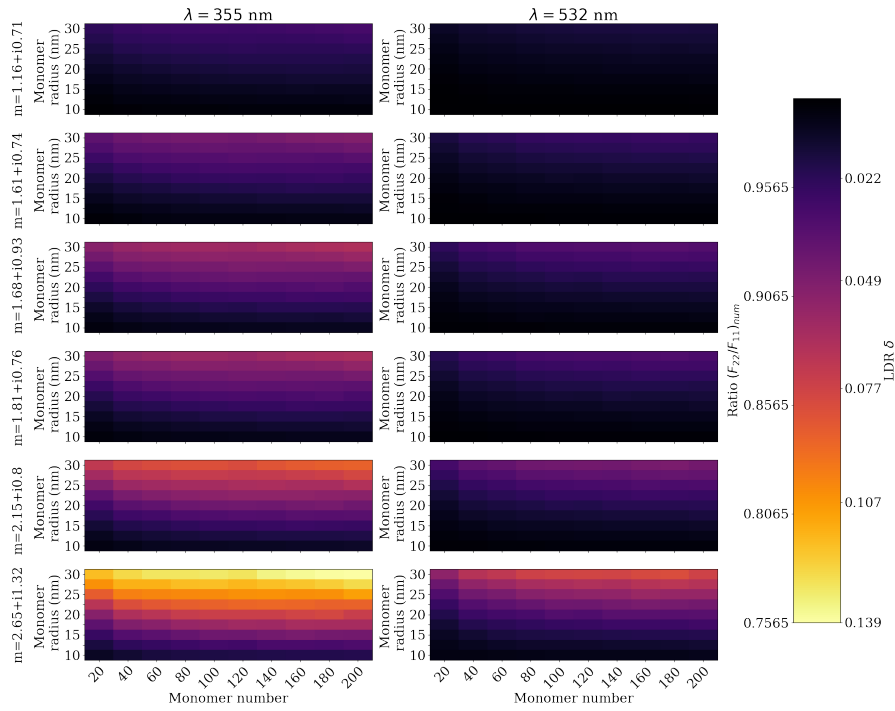
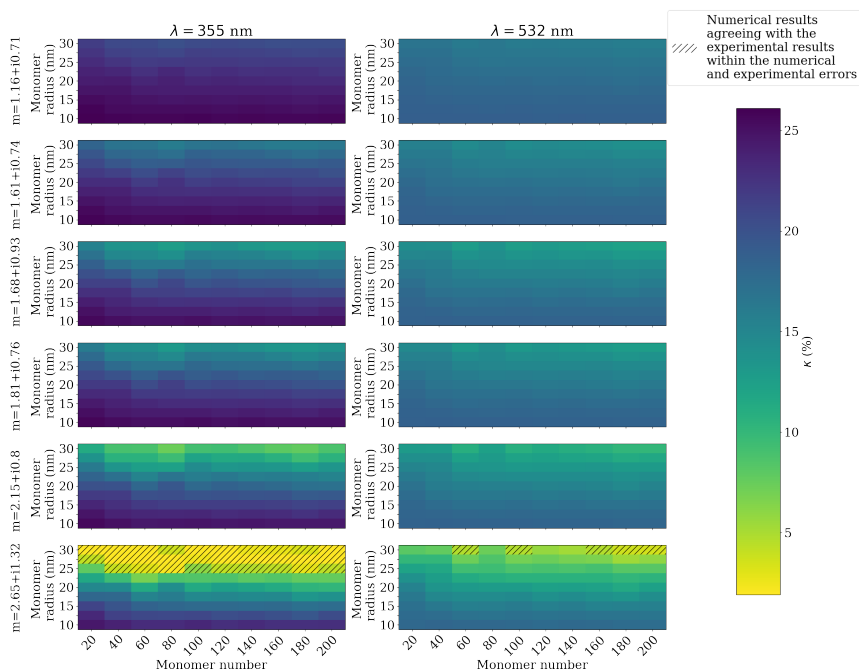


Figure II.14: Numerical results of the ratio  $[F_{22}/F_{11}]_{num}$  and LDR for ensembles of aggregates formed by polydisperse monomers. The colour scale and overall organization of the figure is identical to Figure II.13.

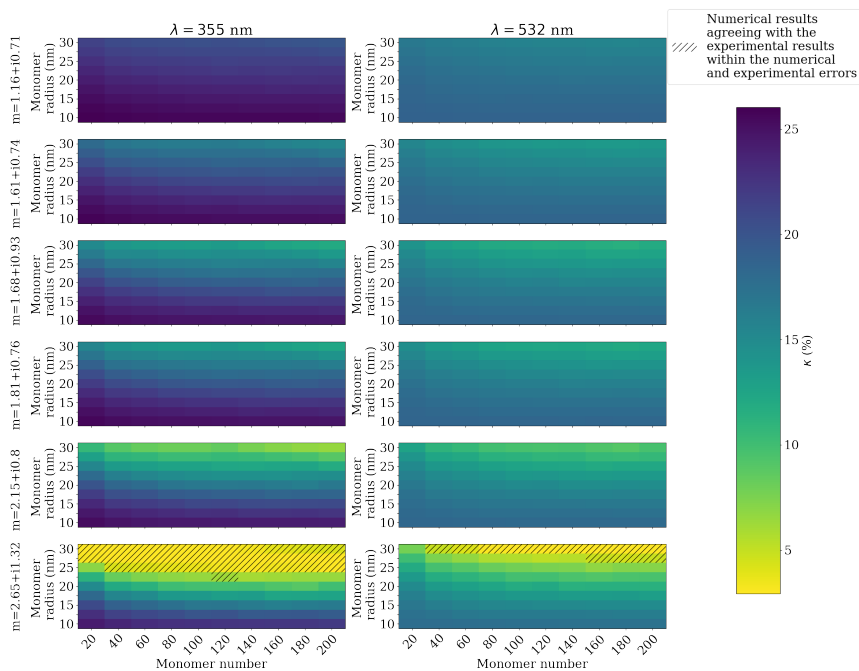
In Figure II.15(a), the percent disagreement between the numerical and experimental results is represented, in the case of monodisperse aggregates. The dashed area represents the range of parameters (i.e. complex refractive index, monomer radius, monomer number) which reproduces the experimental results within the numerical standard deviation and the experimental uncertainties. At 355 nm wavelength, one main range of agreement can be observed. Using a complex refractive index of  $m_o = 2.65 + i1.32$ , the soot aggregates with monomer radius  $r_m \geq 25$  nm show good agreement, with the number of monomers within  $N_m \in [20, 200]$ . At 532 nm wavelength, the results noticeably differ. Indeed, the range of parameters that reproduces the laboratory experimental results is more reduced; only the computation using a complex refractive index of  $m_o = 2.65 + i1.32$ , with monomer radius  $r_m = 30$  nm and monomer number  $N_m = 60, 100$  and within  $N_m \in [160, 200]$  is able to reproduce the experimental results. As stated in Appendix C, the ratio  $[F_{22}/F_{11}]_{lab}$  has been experimentally evaluated simultaneously at 355 nm and 532 nm wavelengths. This indicates that a unique ensemble of soot aggregates is responsible for the

observed ratios  $[F_{22}/F_{11}]_{lab}$  and LDRs. Hence, it is expected that the agreeing numerical results should have the same morphological parameters at both wavelengths. The range of agreement of the morphological parameters (i.e.  $N_m$  and  $r_m$ ) can then be reduced by considering only those which coincide at both 355 nm and 532 nm wavelengths. Hence, the ensembles of monomer radius  $r_m = 30$  nm and monomer number  $N_m = 60, 100$  and within  $N_m \in [160, 200]$  are the only ensembles reproducing the experimental results.

Likewise, the  $\kappa$ -values for the polydisperse aggregates results are presented in Figure II.15(b). Results are similar to those observed in the monodisperse case at 355 nm wavelength, but present differences at 532 nm wavelength. At 355 nm wavelength, results are in agreement for ensembles of monomer radius  $R_m \geq 25$  nm and with monomer number within  $N_m \in [20, 200]$  with a refractive index of  $m_o = 2.65 + i1.32$ . At 532 nm wavelength, the lesser variability in the results induced by the polydispersity causes a clearer range of agreement. For a refractive index of  $m_o = 2.65 + i1.32$ , ensembles with monomer radius  $R_m = 30$  nm and monomer number  $N_m \in [40, 200]$  are in agreement, as for ensembles with  $R_m = 27.5$  nm and  $N_m \in [160, 200]$ .



(a) Monodisperse aggregates



(b) Polydisperse aggregates

Figure II.15: Relative discrepancy  $\kappa$  between the laboratory and numerical experiments for monodisperse (a) and polydisperse (b) aggregates (colour scale, with better agreement as the value approaches 0). The columns of subplots refers to different wavelengths, while the rows refer to different refractive indices. Inside the figures themselves, the x-axis represents variable monomer number, and the y-axis represents variable monomer radius.

This numerical study has allowed to identify several ensembles whose backscattering properties are in agreement with the laboratory results. The monomer radius of these ensembles is consistent with results from the TEM-measurements. The number of monomers is also in a realistic range. Although the numerical results coincide with the experimental results in these cases, the refractive index used remains unusually large. Indeed, this optical index corresponds to spark-generated soot [9], which microstructure is composed almost exclusively of amorphous (or disordered) carbon [4]. In comparison, the soot aggregates emitted during our experiment exhibit a hybrid structure of mostly amorphous carbon, with some concentric graphitic layers with amorphous inclusions, as presented in Figure II.11(b). Considering that the introduction of monomer radius polydispersity did not significantly improve the agreement between the numerical and experimental results, this strongly suggests that the morphological models used in this study are in need of further refinement in order to better interpret the laboratory experimental measurements. Several morphological effects can be considered in order to do so. Particle overlapping and necking effects (i.e. supplementary material at the monomers surface) could produce significant changes of the lidar depolarization ratio. As described in [152], particle overlapping has an effect similar to a decrease in monomer number, while necking produces a scaling effect on the LDR in the forward direction. Still, interrogation remains whether these morphological parameters also produce similar results in the backward scattering direction, and in which proportion. To account for these specific morphological effects, the STM method cannot be used for the scattering properties computation. Hence, methods with higher computational cost are required, such as DDA methods. Spheroidal monomers can also be considered in order to better replicate soot morphology. Wu et al. [159] investigated the effects of both prolate and oblate spheroid monomers on the scattering properties of soot aggregates, and showed a decrease in the  $F_{22}/F_{11}$  ratio in the backward scattering direction. This morphology type also requires DDA calculations, as the STM method cannot be used for spheroidal monomers currently.

## Conclusion and considerations for the characterization of soot particles using lidar instruments

In this chapter, the radiative properties of soot aggregates have been computed and among them, the linear depolarization ratio has been experimentally evaluated. Increasingly complex morphological models have been used to describe the aggregates structure. Aggregates composed of monodisperse monomers are first considered, and polydispersity is then introduced. A specific case of study on an superaggregate is also presented and compared with a monodisperse aggregate. This superaggregate can be described as an unusually large aggregate formed by the clustering of several "canonical" aggregates, and which presents several fractal dimensions at different length scale. In all cases except the one corresponding to the superaggregate, ensembles with the same sets of morphological parameters have been generated. This allows for the computation of the standard deviations of the radiative properties along with the radiative properties themselves.

The radiative properties are computed on several wavelength ranges, either on a spectrum ranging from  $\lambda \in [300, 1100]$  nm in order to address emerging supercontinuum lidar technologies, or on the more conventional set of wavelengths  $\lambda = 355, 532, 1064$  nm, which correspond to Nd:YAG lasers frequency tripled, doubled and fundamental wavelengths respectively. To compute the radiative properties, two methods are used throughout this chapter. The STM method is predominantly used, as this method is adequate to compute the radiative properties of objects which are composed of spherical primary particles in point contact. The RDG-FA theory is also used and its performances are assessed on canonical and superaggregates by comparison with the results obtained with the STM method.

Throughout this chapter, emphasis has been put on the radiative properties that are the most relevant to lidar applications. The generation of ensembles of different morphological parameters has allowed to study the effects of the variations of these parameters on the radiative properties. It has been observed that the radius of the monomers is the morphological property inducing the largest impact on all radiative properties, while the number of monomers is found to

be moderately impactful and the fractal dimension only induces small variations. When comparing the results obtained with the STM method and with the RDG-FA theory, it has been observed that the latter does produce fairly accurate results when considering canonical aggregates, but is inherently unable to account for coupling effects. Hence, the LDR cannot be retrieved using the RDG-FA theory. Moreover, the accuracy of the RDG-FA theory decreases at smaller wavelengths and when considering superaggregates.

The linear depolarization ratio of soot particles has been thoroughly investigated within this chapter. Numerical results have shown a strong dependence of this parameter on the radius of monomers and on the optical index. The LDR of soot particles has also been experimentally evaluated. To our knowledge, this is the first experimental evaluation of the LDR of soot particles in ambient air and in the backscattering direction. The obtained values of the LDR, *i.e.*  $\delta_{lab} = 11.7 \pm 2.3 \%$  ( $\lambda = 355 \text{ nm}$ ) and  $\delta_{lab} = 8.7 \pm 2.1 \%$  ( $\lambda = 532 \text{ nm}$ ), are compared with numerical results for both polydisperse and monodisperse aggregates. Although the numerical results do reproduce the experimental results, they do so only for an optical index that correspond to amorphous carbon. This suggests that the morphological models used may not be entirely representative of the particles emitted during the experiment, and that more complex morphological features might need to be accounted for.

Hence, an argument can be made that a refinement of the morphological models is needed, which would eventually result in a more accurate evaluation of the radiative properties. This would require extensive TEM observations to investigate the degree of overlapping, necking or of any other complex morphological feature. The computation of the radiative properties of particles of such morphologies would then require a method that allows to account for these complex features. The DDA is an appropriate method to that end, but is computationally intensive. In lidar applications, the received signal is related to the backscattered radiation within a volume, and when considering soot particles, an assumption of a preferred orientation of the particles seems ill-advised. This implies that orientation averaged computations of distributions of particles are needed, which further increase the computational cost of DDA calculations. Hence, considering the additional TEM investigation, morphological model development and computational cost

needed for increasing the accuracy of the numerical results, only the methods presented in this chapter will be used in the latter investigations presented in this thesis.

One of the objectives of this thesis is to model lidar signals that would be acquired on soot particles. This modeling process stems from its use in the assessment of the feasibility of the characterization of soot particles by means of lidar measurements. The retrieval of soot morphological parameters through lidar measurements is a complex process, as the number of unknowns is potentially greater than the number of measurable quantities. Prior sensitivity studies are required in order to describe in which magnitude a retrieval of soot morphological properties is possible, taking into account instrumental noise, polydispersion of any of the morphological parameters inside the measurement volume, and range dependent quantities. Still, the results presented in this chapter show promising outlooks for lidar microphysical parameter inversion, specifically for the retrieval of the monomer radius. Knowledge of this morphological parameter could provide a first assessment of the LR values, likely allowing the use of an inverse algorithm in order to retrieve both backscattering and extinction coefficient profiles.

While the values of the computed lidar cross-sections and LDR are in good agreement with other modeled values found in the literature [160, 161], the LR values presented here are much higher than those usually used in lidar inversion methods [162]. Several factors can explain this discrepancy. As the interacting particles are part of a volume formed by the laser pulse divergence and length, soot can be mixed with other aerosols during lidar measurements, as in smoke. A second influencing factor could be the ageing status of the soot particles, as the atmospheric processing of these aerosols change their radiative properties. Considering the fractal models used in this chapter, the numerical results of this thesis are more relevant to freshly emitted soot aggregates (as opposed to atmospheric soot particles), *i.e.* uncoated soot aerosols not yet influenced by ageing processes, although the morphological models are still in need of refinement.

As expressed in Section 1.3, the computation of the light-matter interaction term of lidar signals in the single scattering approximation  $U_{SS}$  only requires the extinction and backscattering cross-sections, and eventually the polarized counterpart of the latter in the case of polarization-resolved lidars. Hence, the cross-sections presented in this section can be used as they stand for the

modeling of single scattering lidar signals. However, multiple scattering effects may contribute to the acquired lidar signal, as described in Section I.3.4. Consequently, a sound modeling of lidar signals requires to account for this contribution. In order to do so, a lidar signal simulation code has been developed, and is presented in the following chapter.

## **Chapter III**

# **Stochastic method for the simulation of polarization-resolved lidar signals accounting for multiple scattering**

### **Introduction**

As described in Section I.3.4, several methods allow to simulate lidar signals accounting for multiple scattering. Among these methods, those based on Monte-Carlo algorithm require few approximations and are fairly adaptable to different scattering media. In this chapter, a program based on the Monte-Carlo method is described.

This program is based on the work from Starkov et al. [135] and Kerscher et al. [163]. A publicly available version of the program described in [164] has been used as the basis of the work. However, this publicly available version does not include the description of the polarization. Hence, the architecture of the aforementioned program is used as the backbone for the code presented in this thesis, but has been heavily modified in order to include the description of polarization. Moreover, a parallelization procedure has been implemented in order to fasten the computations on computer architecture supporting multithreading. This parallel computing implementation uses the Message Passing Interface (MPI) standard.

Hence, this chapter presents a description of the methods and techniques used in the development lidar signal simulation code. A general description of the Monte-Carlo method is first given, with a listing of the input parameters and a general overview of the code architecture. This first subsection also provides a brief description of all the steps and techniques used within this code. The second section of this chapter provides a more detailed description of each of the methods used within the program. The third section of this chapter presents comparative investigations which aim to assess the validity of the results obtained with this program.

## **III.1 Description of the Monte-Carlo simulation program**

### **III.1.1 General presentation**

Monte-Carlo methods are a broad set of numerical, stochastic methods. They allow for the estimation of integrals by making use of the law of large numbers (LLN) and of the central limit theorem (CLT). Hence, Monte-Carlo methods consist in conceiving a numerical experiment within which a random variable is subject to various transformations. These transformations are devised by sampling probability density functions (PDF) based on the physical processes at stakes. By repeating this experiment a large number of times, the CLT indicates that the results of these experiments are normally distributed, which allows for an error estimation, while the LLN indicates that the mean of this distribution approaches the expected value of the integral the experiment is based upon.

In order to simulate lidar signals using a Monte-Carlo method, the emitted pulse is described as a collection of corpuscular objects, which will be hereby called photons. The processes of propagation of these pseudo photons within a scattering medium and the phenomena of scattering and of absorption are described as a sequence of stochastic events based on the radiative properties of the scattering medium. This transport theoretical approach is thoroughly detailed in the reference [135] and in the references therein, and leads to the formulation of the lidar problem as an integral.

In this section, an overall description of the program is given and its general architecture is

presented. The work undertaken in this thesis has consisted in implementing the description of polarization within the program. In order to do so, the photons are described using several vectors and quantities allowing to track their position, direction of propagation, and plane of polarization. As such, this program can be categorized as an Euler Monte-Carlo code [165]. Moreover, the photons polarization state is also tracked using a Stokes vector as defined by Equation I.2.6.

As aforementioned, the principle of the Monte-Carlo simulation is to simulate the propagation, absorption and scattering of photons within a scattering medium and while considering a lidar geometry. Nevertheless, this standard approach is highly inefficient as it is associated with large computational time. This can be envisioned following simple considerations. Considering only the first order of scattering (*i.e.* single scattering), the probability of a photon being scattered rather than absorbed is determined by the albedo of the scattering medium. Moreover, the probability of a photon being scattered in the direction of the lidar instrument (*i.e.* the backward direction) is determined by the phase function. Hence, taking as an example the radiative properties of polydisperse aggregates as presented in Section II.1.3 at  $\lambda = 355$  nm, a first approximation gives a probability of a photon being scattered in the backward direction of  $\mathcal{P}_{bac} \approx 0.01\%<sup>1</sup>$ . This implies that only one photon in one hundred thousands will actually contribute to the output signal.

To reduce the computational cost of the calculation, three variance reduction techniques are implemented, namely peel-off scattering [166, 167, 168], scattering splitting [164] and absorption weighting [169]. These techniques are triggered at different steps of the program, the latter one being used in complement to the first two. As such, the peel-off scattering technique and the scattering splitting technique are described in dedicated subsections (*i.e.* Subsection III.2.4 and Subsection III.2.6 respectively), while absorption weighting is presented throughout this section.

---

<sup>1</sup>This value is obtained following the probabilities given in [24], with an elementary solid angle of  $d\Omega = 2\pi(1 - \cos(d\theta))$  sr, with  $d\theta = 0.5^\circ$ . The value of the phase function is approximated to  $a_1(\pi) = 0.2$  and the value of the single scattering albedo is  $\omega_0 = 0.232$ .

### III.1.2 Architecture

The general architecture of the program is presented in Figure III.1. Two main loops are constituting this program; (i) the primary loop takes as inputs user-defined parameters (*e.g.* lidar instrumental characteristics, scattering medium geometry) and returns the output signal and variance; (ii) the secondary loop contains the functions simulating the light-matter interaction processes. An important feature of the Monte-Carlo code is the presence of this secondary loop, which is a direct result of the scattering splitting variance reduction technique. As this technique is described in Section III.2.6, only a brief description is hereby given. At each iteration of the main loop, a photon referred to as the primary photon is initialized. In the secondary loop, this primary photon can undergo splitting, resulting in two secondary photons which can in turn be split at the next iteration. This results in an increasingly large number of secondary photons being tracked, all originating from the same primary photon. This ensemble of secondary photons is referred to as a photon family, and their interactions are iteratively accounted for in the secondary loop.

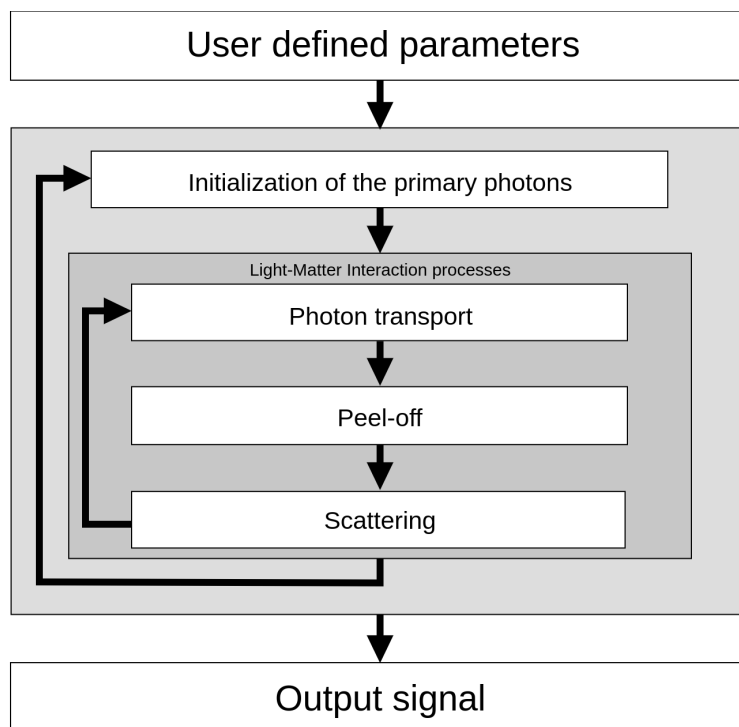


Figure III.1: Simplified schematic of the program architecture.

### III.1.3 Problem geometry and input parameters

The simulations undertaken in this program take place within the framework of lidar instruments. As such, the geometries of the instrument and of the scattering medium need to be accounted for. Both monostatic and bistatic lidar configurations can be modeled, with arbitrary surface of collection, Field-Of-View (FOV), laser divergence and pulse duration. The scattering medium is modeled as a succession of plane slabs, with definite thicknesses along the vertical axis (*i.e.*  $\hat{e}_z$ ) and infinite widths along the horizontal axes (*i.e.*  $\hat{e}_x$  and  $\hat{e}_y$ ). This geometry is schematically represented on Figure III.2. However, this program does not allow the modeling of irregularly shaped interfaces between two scattering media, or continuous variation of the radiative properties of a slab.

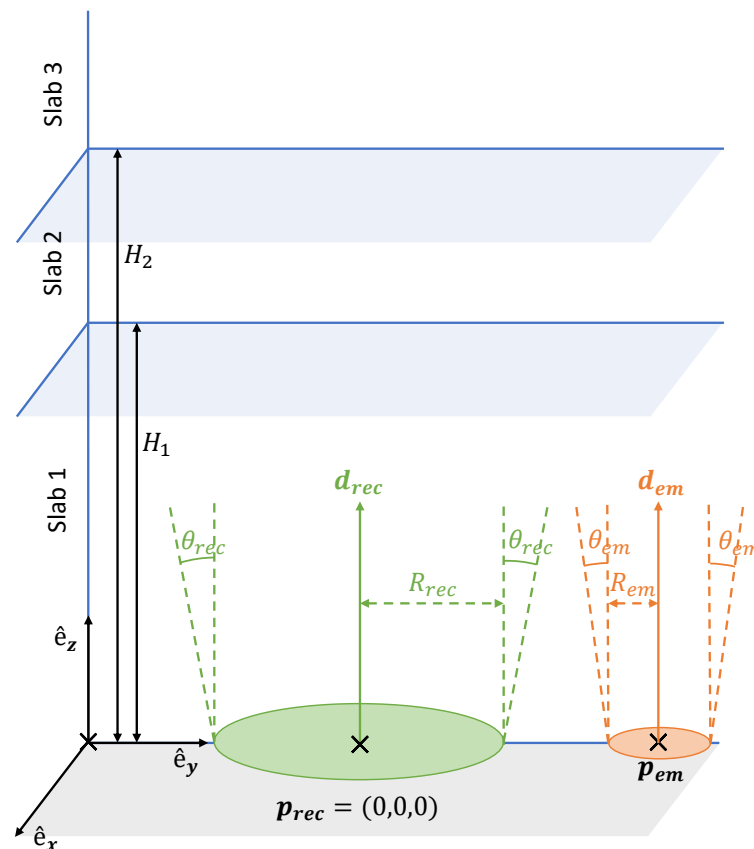


Figure III.2: Simplified schematic of the lidar geometry within the program.

As shown on Figure III.2, the lidar emitter and receiver are modeled as discs of radii  $R_{em}$  and

$R_{rec}$  respectively. The position of the center of the emitter disc is defined by the vector  $\mathbf{p}_{em}$ , while the position of the receiver disc center is placed at the coordinate  $\mathbf{p}_{rec} = (0 \ 0 \ 0)$ . The half-angle divergence of the laser beam is defined by the angle  $\theta_{em}$  and the receiver half-angle FOV by the angle  $\theta_{rec}$ . The height of each slab is characterized by the parameter  $H_i$ , which defines the height of the  $i^{\text{th}}$  slab upper bound. These parameters are defined by the user prior to the program launch. All the input parameters are presented in Table III.1.

In addition to these input parameters, input files containing the scattering matrix of the scattering medium must be provided for each slab. These scattering matrices, in association with the array containing the slabs single scattering albedo and the one containing the slabs extinction coefficients, allow for the description of the slabs radiative properties. Hence, an inhomogeneous medium can be modeled by a succession of slabs of different radiative properties. Because these radiative properties and scattering matrices have been computed within Chapter II when considering soot particles, this code will eventually allow the simulation of lidar signals over soot particles accounting for multiple scattering. A number of the input parameters presented in Table III.1 are related to methods which have not yet been presented, and thus will be described in the following section and subsections therein.

Emitter parameters			Scattering medium parameters				
Name	Description	Symbol	Unit	Name	Description	Symbol	Unit
Laser divergence	Divergence of the laser beam (half angle)	$\theta_{em}$	mrad	Number of slabs	Number of slabs with different parameters composing the scattering medium	$N_{slab}$	
Collimator aperture	Aperture of the laser collimator. The surface of emission is represented as a disc.	$R_{em}$	km	Slabs upper bound distance	Array containing the distance to the receiver of each slab upper plane. The length of the array is $N_{slab} - 1$ , the last slab being infinitely thick.	$H_{slab}$	km
Pulse spatial width	Spatial width of the emitted pulse in km. The pulse is square-shaped. This parameters is expressed as the product between light speed in the vacuum $c_0$ with the pulse temporal width $\tau_0$ .	$L_{em}$	km	Extinction efficient	Array containing the extinction coefficients of the slabs. The length of the array is $N_{slab}$ . Setting any slab extinction coefficient to 0 prevents any interactions from happening within the corresponding slab.	$\alpha$	$\text{km}^{-1}$
Emitter position	Position of the center of the disc of emission.	$\mathbf{p}_{em}$	km	Albedo	Array containing the single scattering albedos of the slabs. The length of the array is $N_{slab}$ .	$\omega_0$	
Stokes vector	Stokes vector of the primary photons.	$\mathbf{I}_{em}$		Scattering matrix file name	Array containing the path and filenames of each slabs scattering matrix. The length of the array is $N_{slab}$ .		
				Scattering matrix resolution	Number of angles in the scattering matrix.		
Receiver parameters			Output parameters				
Receiver Field of View	Receiver Field Of View (half angle)	$\theta_{rec}$	mrad	Minimum length	Minimum path length of the photons whose contributions are accounted for.	$t_{min}$	km
Receiver radius	Radius of the receiver. The surface of reception is described as a disc.	$R_{rec}$	km	Maximum length	Maximum path length of the photons whose contributions are accounted for.	$t_{max}$	km
Receiver direction	Direction of the receiver axis. In the current version of this program, this vector is necessarily vertical, i.e. along $\hat{e}_z$ with null components along $\hat{e}_x$ and $\hat{e}_y$ .	$\mathbf{d}_{rec}$		Length step	Path length step between each output contribution. This parameter is analog to twice the lidar spatial resolution.	$\Delta t$	km
Monte-Carlo parameters			Monte-Carlo parameters				
Number of primary photons	Number of primary photons generated in the primary loop.	$N_{ph}$		Cone angle	Half-angle of the cone in which the scattering splitting technique is triggered.	$\theta_{cone}$	mrad
Scattering splitting phase function angle	The scattering phase function is split at this angle into the forward and backward phase functions.	$\theta_{split}$	$^\circ$	Cone radius	Radius of the cone at the receiver height within which the scattering splitting technique is triggered.	$R_{cone}$	km
Scattering splitting receiver angle	Maximum angle between the current photon direction and the current photon position for the scattering splitting to happen.	$\zeta$	$^\circ$	Number of scattering orders	Maximum number of scattering orders.	$j_{max}$	

Table III.1: List of the input parameters of the Monte-Carlo program.

## III.2 Methods and variance reduction techniques

### III.2.1 Initialization

In the lidar signal simulation program, a single photon is launched at each primary loop iteration. Each photon has associated quantities which need to be initialized, namely its position, direction and reference vectors, its Stokes vector and its initial path length. Table III.2 presents the different quantities used in this subsection. Figure III.3 presents the architecture of the photon initialization step. Several iterators are presented in this table and in this figure. These iterators are used as subscripts in order to track the different photons within the program. The iterator  $i$  tracks the number of primary photons that have been launched. It is used as a stopping condition of the program if its value exceeds the maximum number of primary photons  $N_{ph}$ . As these primary photons might undergo splitting during the following steps of the program, the iterator  $k$  is used to track the number of photons within a photon family. The last iterator  $j$  tracks the number of scattering events undergone by a photon. This allows to track separately the contribution of each scattering order to the output signal. During the initialization step, only one photon is included within the photon family and no scattering event has yet been undergone by this photon. Hence, at this step, the last two iterators  $j$  and  $k$  take the value  $k = 1$  and  $j = 0$  respectively. In order to ease the notation, these last two iterators are suppressed from the subscripts in this subsection.

Name	Description	Symbol
Position vector	Vector allowing to track a photon position.	$\mathbf{p}_i = (p_x \quad p_y \quad p_z)$
Propagation direction vector	Vector defining the direction of propagation of a photon.	$\mathbf{d}_i = (d_x \quad d_y \quad d_z)$
Reference vector	Vector allowing to track the plane in which the Stokes vector $\mathbf{I}$ is defined.	$\boldsymbol{\rho}_i = (\rho_{i,x} \quad \rho_{i,y} \quad \rho_{i,z})$
Stokes vector	Stokes vector of the tracked photon.	$\mathbf{I}_i = [I_i \quad Q_i \quad U_i \quad V_i]^T$
Path length	Distance traveled by the photon.	$t_i$
Iterator integers	Iterators for the tracking of the number of launched primary photons, of the number of undergone scattering events and of the current photon within the photon family.	$i, j, k$

Table III.2: List of the defining parameters of a photon in the Monte-Carlo code.

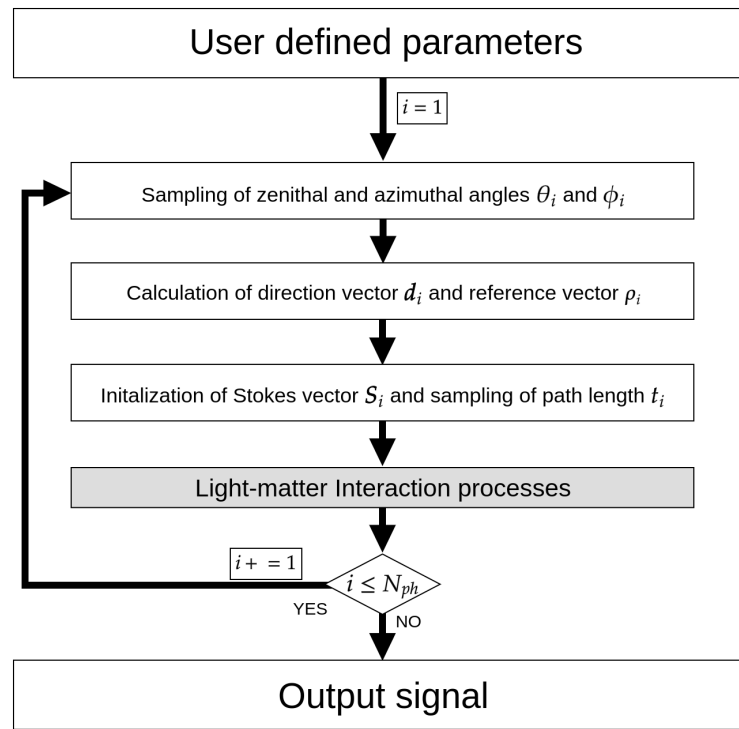


Figure III.3: Architecture of the photon initialization process.

As presented in Figure III.3, the first step of the photon initialization process consists in sampling the initial zenithal angle  $\theta_i$  and azimuthal angle  $\phi_i$ . As the emitter divergence is finite and defined by the input parameter  $\theta_{em}$ , the zenithal angle is bounded by this input parameter. On the other hand, the azimuthal angle is chosen randomly between 0 and  $2\pi$ . Numerically, these angles are sampled using the formulae :

$$\begin{aligned}\theta_i &= \eta_0 \theta_{em} \\ \phi_i &= 2\pi \eta_0\end{aligned}\tag{III.2.1}$$

where  $\eta_0$  is a generated pseudo-random number within the uniform law over  $\eta_0 \in [0, 1]$ . The direction vector  $\mathbf{d}_i$  and the reference vector  $\boldsymbol{\rho}_i$  are then calculated using Rodrigues' rotation formula. First, the primary photon reference vector  $\boldsymbol{\rho}_i$  is obtained by rotating the reference vector  $\boldsymbol{\rho}_{em}$  along the direction vector  $\mathbf{d}_{em}$  by the azimuthal angle  $\phi_i$ . This operation is expressed as :

$$\boldsymbol{\rho}_i = \boldsymbol{\rho}_{em} \cos(\phi_i) + (\mathbf{d}_{em} \times \boldsymbol{\rho}_{em}) \sin(\phi_i) + \mathbf{d}_{em} (\mathbf{d}_{em} \cdot \boldsymbol{\rho}_{em}) (1 - \cos(\phi_i))\tag{III.2.2}$$

where  $\mathbf{d}_{em} = (0 \ 0 \ 1)$  is the emitter direction vector and  $\boldsymbol{\rho}_{em} = (0 \ 1 \ 0)$  is the emitter reference vector. Then, the emitter direction vector  $\mathbf{d}_{em}$  is rotated along the primary photon reference vector  $\boldsymbol{\rho}_i$  by the zenithal angle  $\theta_i$ , resulting in the primary photon direction vector  $\mathbf{d}_i$  as :

$$\mathbf{d}_i = \mathbf{d}_{em} \cos(\theta_i) + (\boldsymbol{\rho}_i \times \mathbf{d}_{em}) \sin(\theta_i) + \boldsymbol{\rho}_i (\boldsymbol{\rho}_i \cdot \mathbf{d}_{em}) (1 - \cos(\theta_i)) \quad (\text{III.2.3})$$

Note that the third term of these equations is null during the photon initialization process. However, these formulae will also be used in the later steps of this program. Hence, the full expression of these formulae are hereby presented.

The position  $\mathbf{p}_i$  of the emitted primary photon is randomly chosen within the disc of radius  $R_{em}$  and of center defined by the position vector  $\mathbf{p}_{em}$ . The disc itself is placed in the plane formed by the vectors  $\hat{\mathbf{e}}_x$  and  $\hat{\mathbf{e}}_y$ .

The primary photon Stokes vector is initialized with :

$$\mathbf{I}_i = \mathbf{I}_{em} \quad (\text{III.2.4})$$

Finally, the initial path length of the primary photon is calculated with :

$$t_i = \eta_0 L_{em} \quad (\text{III.2.5})$$

where  $\eta_0$  is another generated pseudo-random number. This initial path length parameter can be envisioned as a mean to assign a position of the photon within the emitted pulse of length  $L_{em}$ . As such, Equation III.2.5 implies that a square-shape model is used to describe the emitted pulse. During the transport step described in the following subsection, the path length of the photon will be updated according to the traveled distance. Moreover, during the output signal computation step, this quantity will be used to compute the range-dependent signal. Because the photon always travels at the same speed, and because several scattering events may occur consequently, the use of this updated quantity will eventually allow to simulate the signal stretching effect which was described in subsection I.3.4.

### III.2.2 Photon transport method

The purpose of the transport step is to modify the initial position vector  $\mathbf{p}_{i,j,k}$  of a photon into its new position vector  $\mathbf{p}'_{i,j,k}$  by propagating it through the scattering medium following its direction vector  $\mathbf{d}_{i,j,k}$ , taking into account the extinction coefficient of each slab. In the following, the subscripts  $i$ ,  $j$  and  $k$  are also implied in order to lighten the notation. The superscript ' indicates the quantities that are modified during the transport step. Figures III.4 and III.5 present a schematic view of the transport process and its architecture respectively. Table III.3 presents the parameters that are used within this process.

Name	Description	Symbol
Current photon position vector	Position vector of the current photon	$\mathbf{p}$
Current photon direction vector	Direction vector of the current photon	$\mathbf{d}$
Transported photon position vector	Position vector of the transported photon	$\mathbf{p}'$
Transport path length	Path length of the photon during the transport procedure	$\Delta l$
Optical depth	Optical depth of the photon during the transport procedure	$\tau_i$
Slab height	Height of a slab	$H$
Extinction coefficient	Extinction coefficient of a slab	$\alpha$
Subscript integers	Integer subscripts designating within which slab the photon is. The $si$ subscript indicates the initial slab of the current photon, the $s$ subscript indicates the different slabs in which the photon is transported and the $sf$ subscript indicates the final slab where the photon is stopped.	$si, s, sf$

Table III.3: List of the parameters used in the transport step.

Figure III.4 presents a schematic view of the transport process. In this example, the current photon position is defined by the vector  $\mathbf{p}$  and its direction by the vector  $\mathbf{d}$ . Both of these vectors are within the plane formed by the vectors  $\hat{e}_y$  and  $\hat{e}_z$  in order to simplify the visualization. During the transport process, the photon position is moved upward if  $d_z > 0$ , as in Figure III.4, or downward if  $d_z < 0$  by a distance  $\Delta l$  along the direction vector  $\mathbf{d}$ . The gray crosses represent the intersection points between each slab boundary plane and the photon path during the transport process.

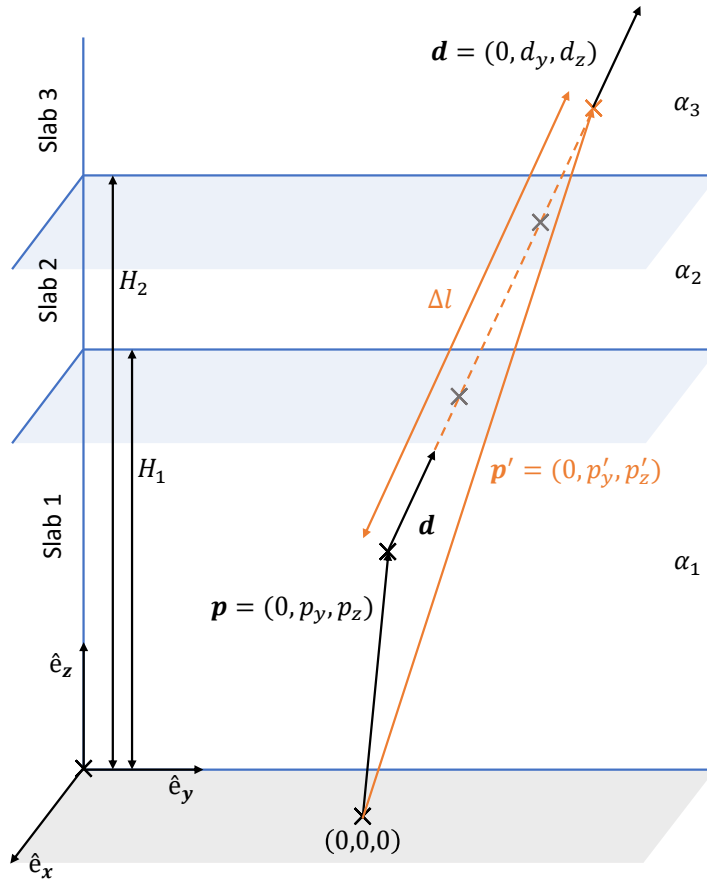


Figure III.4: Schematic view of the photon transport process.

As presented on Figure III.5, the transport process starts by sampling a random number  $\tau_i \in [0, +\infty[$ . This parameter  $\tau_i$  represents the optical depth between the initial position of the photon and its final position that will be later determined. The probability density function (PDF)  $f_{\Delta l}$  of either an absorption event or a scattering event occurring after a transport distance  $\Delta l$  can be expressed as [170]:

$$f_{\Delta l}(\Delta l) = \alpha(r) \exp\left(-\int_0^{\Delta l} \alpha(r) dr\right) \quad (\text{III.2.6})$$

The corresponding cumulative distribution function  $F_{\Delta l}$  is then expressed and sampled such as :

$$F_{\Delta l}(\Delta l) = \eta_0 = \exp\left(-\int_0^{\Delta l} \alpha(r) dr\right) \quad (\text{III.2.7})$$

If the scattering medium is made of only one slab, if the current photon is traveling upward and is within the last slab ( $d_z > 0$  and  $si = N_{slab}$ ) or downward and within the first slab ( $d_z < 0$  and

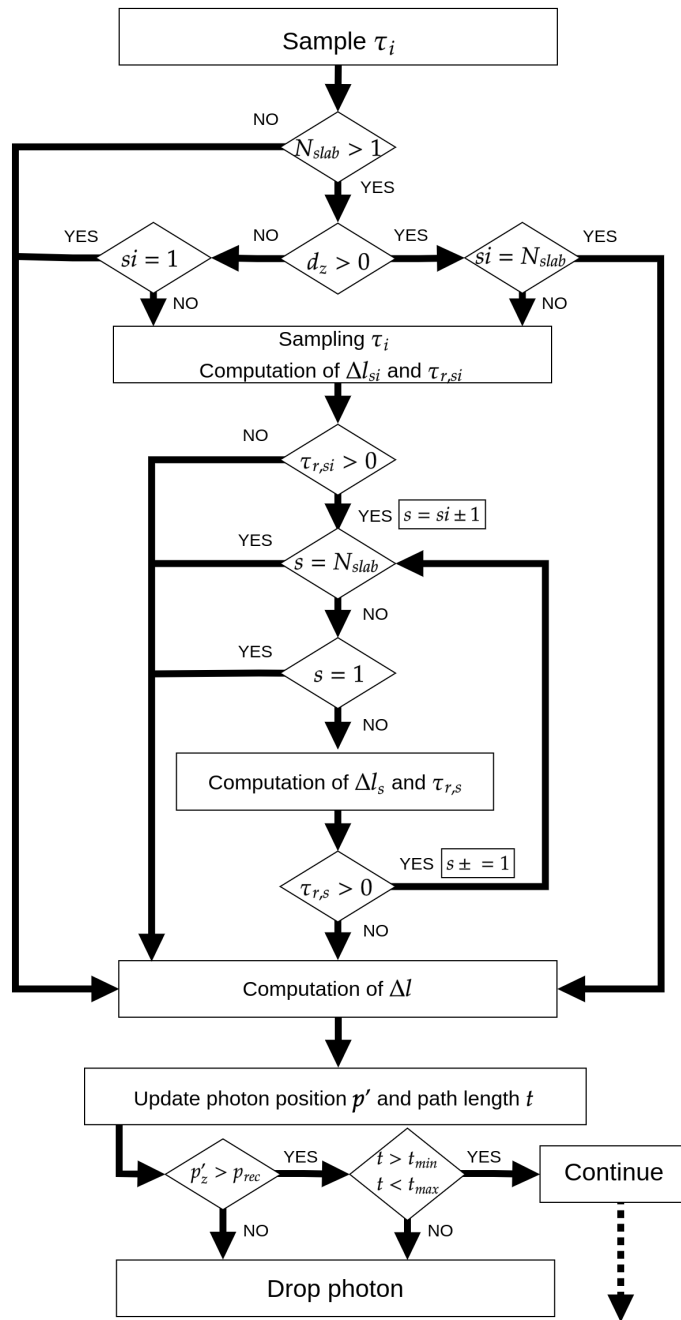


Figure III.5: Architecture of the photon transport process.

$s_i = 1$ ), then the photon initial and final positions are necessarily within the same slab. Hence, in these cases, the determination of the distance traveled by the photon simply consists in solving the following equation :

$$\Delta l = \frac{-\ln(\eta_0)}{\alpha_{s_i}} = \frac{\tau_i}{\alpha_{s_i}} \quad (\text{III.2.8})$$

where the subscript  $s_i$  indicates in which slab the initial photon is located. However, several slabs

with variable extinction coefficients can also be modeled. Such geometries requires to iteratively solve Equation III.2.7. As such, the parameter  $\tau_i$  is computed by generating a pseudo-random number within the uniform law over  $\eta_0 \in [0, 1]$  such as :

$$\tau_i = -\ln(\eta_0) \quad (\text{III.2.9})$$

In this general case, several slabs with different extinction coefficients are considered, and the sampled optical depth  $\tau_i$  might result in the transition of a photon from one slab to another. Hence, an iterative process is implemented in order to compute the optical depth along the photon direction vector from one slab to the next. As such, after finding within which slab  $si$  the current photon is located, the distance between this position and the intersection point between the next encountered slab upper plane ( $si$  if  $d_z > 0$ ;  $si - 1$  if  $d_z < 0$ ) and the direction half-line is computed as :

$$\begin{aligned} \Delta l_{si} &= \left| \frac{H_{si} - p_z}{d_z} \right| & \text{if } d_z > 0 \\ \Delta l_{si} &= \left| \frac{p_z - H_{si-1}}{d_z} \right| & \text{if } d_z < 0 \end{aligned} \quad (\text{III.2.10})$$

Following this step, the optical depth between the photon initial position and the intersection point with the next slab is obtained by inverting Equation III.2.8. This optical depth, noted  $\tau_{si}$ , is subtracted to the sampled optical depth  $\tau_i$  such as

$$\tau_{r,si} = \tau_i - \tau_{si} \quad (\text{III.2.11})$$

The quantity  $\tau_{r,si}$  represents the "rest" of the optical depth that needs to be accounted for in order to compute the final position of the photon after its transport. It is used as a condition to determine whether the process should continue within the next slab. Indeed, the condition  $\tau_{r,si} < 0$  indicates that the optical depth from the photon initial position to the next intersection is higher than the sampled optical depth. Hence, the final position of the photon must lie within the current slab, and the travel distance is computed using Equation III.2.8.

Otherwise, the condition  $\tau_{r,si} > 0$  indicates that the process should continue provided that

the first or last slab is not reached. Because the optical depth now needs to be computed from one intersection to the next, the general expression when computing  $\Delta l_s$  is given by :

$$\Delta l_s = \left| \frac{H_s - H_{s-1}}{d_z} \right| \quad (\text{III.2.12})$$

where the subscript  $s$  is updated to correspond to the slab whose the optical depth is computed. The rest of the optical depth is then computed as :

$$\tau_{r,s} = \tau_{r,s\pm 1} - \tau_s \quad \text{for} \quad d_z = \mp |d_z| \quad (\text{III.2.13})$$

These steps are repeated until the condition  $\tau_{r,s} < 0$  is verified. After these steps, the distance between the intersection point and the photon final position is :

$$\Delta l_{s=sf} = \frac{\tau_{r,s\pm 1}}{\alpha_{s=sf}} \quad \text{for} \quad d_z = \mp |d_z| \quad (\text{III.2.14})$$

where the subscript  $sf$  refers to the final slab within which the photon is transported. The total traveled distance is then obtained with :

$$\Delta l = \sum_{s=s_i}^{s_f} \Delta l_s \quad (\text{III.2.15})$$

This procedure allows to compute the distance traveled by a photon for a sampled optical depth  $\tau_i$ . Nevertheless, two other cases must also be considered. If  $d_z > 0$  and the iterative process reaches the last slab, then Equation III.2.14 is directly used to compute the last segment distance verifying the condition  $\tau_{r,s} = 0$ . Secondly, if  $d_z < 0$  and the first slab is reached, Equation III.2.14 is also directly used.

Knowing the distance  $\Delta l$ , the new position vector is obtained with :

$$\mathbf{p}' = \mathbf{p} + \mathbf{d}\Delta l \quad (\text{III.2.16})$$

and the new photon path length  $t'$  is incremented as :

$$t' = t + \Delta l \quad (\text{III.2.17})$$

The updated photon position  $p'$  and path length  $t'$  are also used to determine whether the calculation for the current photon is dropped. Indeed, if  $p'_z < p_{rec,z}$ , or if  $t' > t_{max}$ , the current photon will no longer be tracked within the program.

### III.2.3 Absorption and the notion of weight

The direct approach to the simulation of the absorption process in the Monte-Carlo method is to generate a pseudo-random number and to compare it with the single scattering albedo  $\omega_0$  of the current slab [169]. Indeed, the probability of a scattering event during the light matter interaction process is given by  $\mathcal{P}_{sca} = C_{sca}/C_{ext} = \omega_0$  while the probability of absorption is given by  $\mathcal{P}_{abs} = C_{abs}/C_{ext} = 1 - \omega_0$ . Hence, if  $\eta_0 < \omega_0$ , a scattering event is taking place, otherwise an absorption event happens and the current photon propagation is terminated. When considering a scattering medium with a low albedo, as it is the case for soot particles, this approach can result in reduced computational time due to a large proportion of photon being absorbed. However, this also implies that these terminated photons do not contribute to the return signal, consequently producing results with a high associated variance. Hence, this approach results in a major inefficiency, due to some photon paths being calculated although they ultimately do not contribute to the signal.

Hence, the absorption weighting variance reduction technique is implemented. Two types of absorption weighting are considered; (i) discrete absorption weighting and (ii) continuous absorption weighting [169]. In this program, the discrete absorption weighting technique is used after each transport step, while the continuous absorption weighting is only used during the peel-off scattering step. As such, continuous absorption weighting will be described in Subsection III.2.4.

Nevertheless, these two variance reduction techniques, as well as those that will be presented in the following sections, all introduce the notion of a weight associated to each photon. This

weight is initially equal to 1 when the primary photon is initialized, and it is updated each time a variance reduction technique is used. The updated value depends on the specific variance reduction technique that is used. The techniques presented in this thesis all rely on implementing some form of bias in the probability distribution. The purpose of the weight is then to counterbalance these biases. During the output signal computation, each photon contribution to the signal is weighted by this parameter. This part will be described in Subsection III.2.7.

In order to provide an example of the computation of a photon weight, discrete absorption weighting is hereby described. This variance reduction technique consists of completely removing the possibility of absorption, and hence preventing photons from being prematurely terminated. This allows to keep track of photons that would have been absorbed and that might eventually contribute to the returned signal. The general computation of the weight associated with the introduction of a bias is formulated as :

$$q = \frac{\mathcal{P}_{unbiased}}{\mathcal{P}_{biased}} \quad (\text{III.2.18})$$

where  $q$  is the weight,  $\mathcal{P}_{unbiased}$  is the probability of the unbiased event that should have happened and  $\mathcal{P}_{biased}$  is the probability of the biased event that did happen. In the discrete absorption weighting technique, the aim is to make absorption events impossible, so that only scattering events ever happen. Hence, the probability of the unbiased event is the probability of scattering, and the probability of the biased event is equal to one. The weight is then computed as :

$$q_{daw} = \mathcal{P}_{sca} = \omega_0 \quad (\text{III.2.19})$$

where the subscript *daw* indicates that this weight is associated with the use of the discrete absorption weighting technique.

As aforementioned, the discrete absorption weighting technique is triggered after each transport step in order to ensure that a scattering event will take place. Using this variance reduction technique, the probability of a photon being scattered in the direction of the receiver after a single event can be computed. Using the same example and approximation as in Subsection III.1.1,

this probability is now approximately equal to  $\mathcal{P}_{bac} \approx 0.05\%$  for soot aggregates. This probability is  $1/\omega_0$  times the original one. Nevertheless, because the photons contributions are weighted by  $q_{daw} = \omega_0$ , the output signal remains unbiased.

### III.2.4 Peel-off scattering

Peel-off scattering is a variance reduction technique which is implemented in order to further increase the probability of a photon contributing to the lidar signal. It consists in calculating the contribution to the signal of each photon after its transport and before the next scattering event takes place [167]. It can be envisioned as a forced scattering event toward the receiver. This section describes the different steps and cases of the peel-off scattering technique.

In the lidar framework, the output signal is determined by the contributions of the photons that are within the FOV of the receiver. Hence, this condition must be verified in order to proceed to the peel-off scattering step. Considering a receiver disc within the plane formed by the vectors  $\hat{e}_x$  and  $\hat{e}_y$  and a FOV axis  $\mathbf{d}_{rec}$  whose components are null along these two unit vectors, this condition is expressed as :

$$\sqrt{p_x^2 + p_y^2} \leq R_{rec} + \tan(\theta_{rec})p_z \quad (\text{III.2.20})$$

If this condition is verified, a received photon is created. This photon can be envisioned as the virtual particle that would result from a forced scattering event of the current photon toward the receiver. This virtual photon is only considered within the peel-off scattering step and is not tracked in the later iterations of the program.

Two cases can then be considered. In the peel-off case, a random location is sampled within the receiver area. A scattering event is then simulated with the outgoing direction vector passing through the initial photon position and the receiver location. Nevertheless, if the direction of propagation along the axis  $\hat{e}_z$  is negative  $d_z < 0$  and if the intersection point between the direction vector and the receiver plane is within the receiver area, then no sampling of a receiver point is needed, and a forced forward scattering event is simulated. This scenario is hereby re-

ferred to as the regular case. The received photon is then transported from its initial position to the receiver location. During this transport step a continuous absorption weighting technique is implemented in order to counterbalance the forced transportation from one location to another. Moreover, a weight modification is also attributed in order to account for the scattering event that has been forced into a specific direction. The received photon Stokes vector is then rotated so that its reference vector coincides with the reference vector of the primary photon of the corresponding family.

This procedure eventually allows to compute the contributions of photons to the output signal, which will be described in Section III.2.7. In the rest of this section, the different steps needed to achieve the peel-off variance reduction technique are described. Figure III.6 presents the architecture of this step, and Table III.4 summarizes the main quantities that will be used within this step.

Name	Description	Symbol
Photon position vector	Position vector of the current photon	$\mathbf{p}$
Photon direction vector	Direction vector of the current photon	$\mathbf{d}$
Photon reference vector	Reference vector of the current photon	$\boldsymbol{\rho}$
Photon path length	Path length of the current photon	$t$
Scattering angle	Scattering angle in the rotation procedure	$\theta$
Azimutal angle	Azimutal angle in the rotation procedure	$\phi$
Optical depth	Optical depth during the transport procedure	$\tau$
Stokes vector	Stokes vector of the current photon	$\mathbf{I}$
Subscripts	Subscripts indicating which photon the current quantity is referring to. The $r$ subscript references the received photon, the $w$ subscript references a weighted quantity and the $f$ subscript indicates the final quantity whose contribution will be added to the global contribution.	$r, w, f$

Table III.4: List of the parameters used in the peel-off scattering process.

In the peel-off case, the first step is to choose a random location in the area formed by the intersection of the receiver area and the disc formed by the cone with apex at the position  $\mathbf{p}$ , height  $p_z$ , axis along  $-\hat{\mathbf{e}}_z$  and aperture  $2\theta_{rec}$ . This location is the final position of the photon before its contribution is computed, and it is noted  $\mathbf{p}_r$ . In order to sample this point, several cases are considered :

- (i) The cone base area is within the receiver area : In this case, a point is chosen randomly

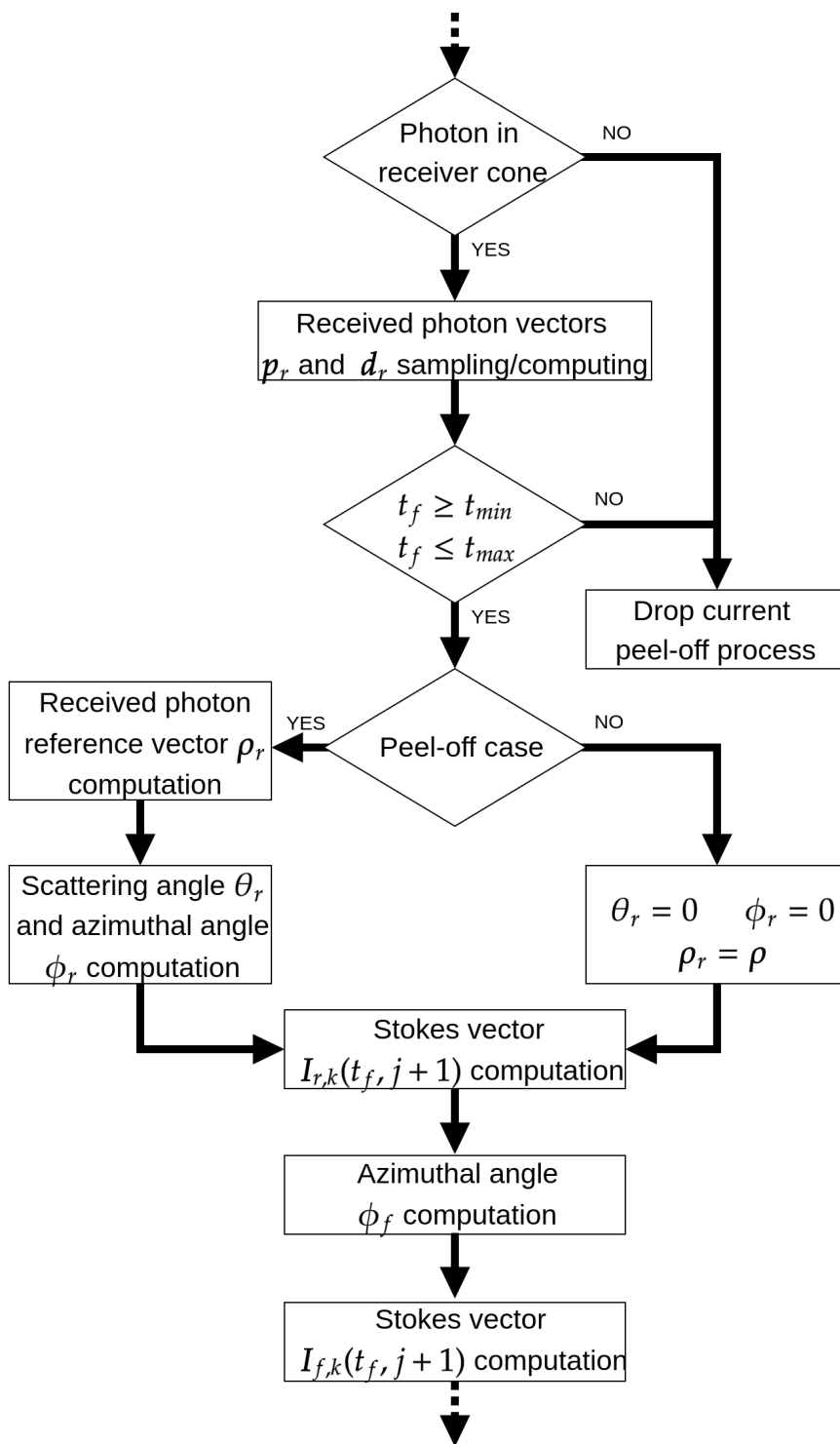


Figure III.6: Architecture of the peel-off scattering process.

within the cone base area.

(ii) The receiver area is within the cone base area : In this case, a point is chosen randomly within the receiver area.

(iii) The receiver area and cone base area do not fully overlap and the condition  $\sqrt{p_x^2 + p_y^2} < \max(R_{rec}, \tan(\theta_{rec})p_z)$  is verified : A rejection method is used. This condition essentially verifies whether the overlapping areas between the receiver disc and the cone base is large enough for this rejection technique to be efficient. Indeed, this rejection technique consists of sampling a random point which is located within the cone base area. If this point is not inside the receiver area, then another point is sampled until this condition is satisfied.

(iv) The receiver area and cone base area do not fully overlap and the condition  $\sqrt{p_x^2 + p_y^2} > \max(R_{rec}, \tan(\theta_{rec})p_z)$  is verified : A point is sampled within the overlapping areas. First, the intersection points  $p_1$  and  $p_2$  between the two areas perimeters are found, and the minimum and maximum values of  $p_{r,x}$  are determined. A random position  $p_{r,x}$  is then chosen with  $p_{r,x} \in [p_{r,x_{min}}, p_{r,x_{max}}]$ . Knowing the position along the x axis, the equations of the circles of the receiver area and cone base area are then solved. The minimum value along the y axis is then determined as  $y_{min} = \max(\min(y_{rec}), \min(y_{cone}))$  and maximum value as  $y_{max} = \min(\max(y_{rec}), \max(y_{cone}))$ . A random position is then chosen along the y axis with  $p_{r,y} \in [p_{r,y_{min}}, p_{r,y_{max}}]$ .

Although the rejection technique would be sufficient by itself, the last sampling method has been implemented in order to reduce the computation time for very small overlapping areas. In the regular case, all of these steps are not necessary, and the received photon position is taken as the intersection between the current photon direction vector and the receiver area.

Knowing the position of the received photon, its path length  $t$  can be calculated as :

$$t_f = t + |\mathbf{p}_r - \mathbf{p}| \quad (\text{III.2.21})$$

This path length is then used to verify whether the photon path length is within the user-defined range of the output signal. This is expressed by the inequalities :

$$t_f \geq t_{min} \quad (\text{III.2.22a})$$

$$t_f \leq t_{max} \quad (\text{III.2.22b})$$

If any of these inequalities is not verified, then the peel-off step is dropped and the calculation proceeds to the next step of the program. Moreover, if the inequality from Equation III.2.22 is not verified, the current photon path is terminated from the program, and it will not be subject to any additional transport or scattering processes.

In the peel-off case, the newly created received photon direction and reference vectors are needed. These vectors are hereby noted  $\mathbf{d}_r$  and  $\boldsymbol{\rho}_r$ . Several steps are required in order to achieve these computations. In this thesis, the procedure described by Peest et al. [167] has been implemented. As such, the vector  $\mathbf{d}_r$  is expressed as :

$$\mathbf{d}_r = \frac{\mathbf{p}_r - \mathbf{p}}{|\mathbf{p}_r - \mathbf{p}|} \quad (\text{III.2.23})$$

The received reference vector is expressed as :

$$\boldsymbol{\rho}_r = \frac{\mathbf{d} \times \mathbf{d}_r}{|\mathbf{d} \times \mathbf{d}_r|} \quad (\text{III.2.24})$$

In order to compute the modification of the Stokes vector due to these changes of direction and reference vector, the received photon scattering angle  $\theta_r$  and azimuthal angle  $\phi_r$  are needed. The former is obtained by the scalar product between the original direction vector and the received photon direction vector as :

$$\cos(\theta_r) = \mathbf{d} \cdot \mathbf{d}_r \quad (\text{III.2.25})$$

The cosine and sine of the azimuthal angle are obtained through the following formulae :

$$\begin{aligned} \cos(\phi_r) &= \boldsymbol{\rho} \cdot \boldsymbol{\rho}_r \\ \sin(\phi_r) &= |\boldsymbol{\rho} \times \boldsymbol{\rho}_r| \end{aligned} \quad (\text{III.2.26})$$

As the photon is transported from its original position to the receiver without any form of sampling, the contribution of the extinction between these two points is taken into account. Continuous absorption weighting is used in order to correct this bias. Essentially, it consists in computing

the probability that a photon would indeed be transported along the path between the initial photon position  $\mathbf{p}$  and the received photon position  $\mathbf{p}_r$ . As such, this probability involves the use of the extinction coefficients, as both absorption or scattering events could be sampled along this path in the standard approach. Although extinction is the simulated process, this technique is hereby referred to as continuous absorption weighting due to the use of this terminology in the literature [167, 169], and in order to contrast with the discrete absorption weighting technique previously introduced. Indeed, the discrete absorption weighting is only triggered at discrete path lengths (*i.e.* after the transport process), while the continuous absorption weighting technique occurs throughout the forced photon transport during this peel-off process. The weight modification associated with continuous absorption weighting is expressed as :

$$q_{caw} = \exp(-\tau_r) \quad (\text{III.2.27})$$

where  $\tau_r$  is the optical depth between the initial photon position  $\mathbf{p}$  and the received photon position  $\mathbf{p}_r$ , computed along the direction  $\mathbf{d}_r$ .

The process of peel-off scattering also introduces a weight modification, as a forced scattering event has been simulated in the direction of the receiver. Following Equation III.2.18, the biased event probability is here  $\mathcal{P}_{biased} = 1$ . Hence, this weight is expressed as :

$$q_{PO} = \frac{\pi R_{rec}^2}{|\mathbf{p}_r - \mathbf{p}|^2} f_{pol}(\theta_r, \phi_r) \quad (\text{III.2.28})$$

where  $f_{pol}$  is the polarized phase function at angles  $\theta_r$  and  $\phi_r$ . This quantity will be further detailed in subsection III.2.5. Moreover, the fractional term of the equation above accounts for for the  $A/r^2$  term of the lidar equation (see Equation I.3.2).

Knowing the rotation angles and the weight modifications, the received Stokes vector is expressed as the product of the initial Stokes vector with the rotation matrix  $\mathbf{R}(\phi)$  such as :

$$\begin{aligned} \mathbf{I}_{r,k}(t_f, j+1) &= q_{caw} q_{PO} \frac{\tilde{\mathbf{F}}(\theta_r)}{C_{pol} f_{pol}(\theta_r, \phi_r)} \mathbf{R}(\phi_r) \mathbf{I}_k(t, j) \\ &= \exp(-\tau_r) \frac{\pi R_{rec}^2}{|\mathbf{p}_r - \mathbf{p}|^2} \frac{\tilde{\mathbf{F}}(\theta_r)}{C_{pol}} \mathbf{R}(\phi_r) \mathbf{I}_k(t, j) \end{aligned} \quad (\text{III.2.29})$$

where  $C_{pol}$  is a normalization constant that will also be described in subsection III.2.5. The above equation introduces the rotation matrix  $\mathbf{R}(\phi_r)$ , which expresses the outgoing Stokes vector when the scattering plane is rotated by an angle  $\phi_r$ . Moreover, the scattering order  $j$  of the Stokes vector  $\mathbf{I}$  has been added within the parenthesis in order to emphasize that it is incremented during the peel-off process. The fractional term  $1/(C_{pol}f_{pol})$  is used in order to ensure that the first element of the product of the scattering matrix  $\tilde{\mathbf{F}}$  with the initial Stokes vector  $\mathbf{I}$  remains unchanged. The rotation matrix  $\mathbf{R}(\phi_r)$  is expressed as :

$$\mathbf{R}(\phi) = \begin{bmatrix} 1 & 0 & 0 & 0 \\ 0 & \cos(2\phi) & \sin(2\phi) & 0 \\ 0 & -\sin(2\phi) & \cos(2\phi) & 0 \\ 0 & 0 & 0 & 1 \end{bmatrix} \quad (\text{III.2.30})$$

Note that in the regular case, *i.e.* when the initial photon is within the receiver FOV and its direction vector is intersecting with the receiver area, both zenithal and azimuthal angles are null ( $\theta_r = 0$  and  $\phi_r = 0$ ). Hence the rotation matrix  $\mathbf{R}(\phi_r)$  becomes an identity matrix.

Finally, the computation of the contribution of the photon to the receiver requires one last rotation, so that the received photon reference vector coincides with the reference vector of the primary photon of its family. The cosine and sine of the rotation angle  $\phi_f$  are obtained with :

$$\begin{aligned} \cos(\phi_f) &= \boldsymbol{\rho}_r \cdot \boldsymbol{\rho}_i \\ \sin(\phi_f) &= (\boldsymbol{\rho}_r \times \boldsymbol{\rho}_i) \cdot \mathbf{d}_r \end{aligned} \quad (\text{III.2.31})$$

As a reminder,  $\boldsymbol{\rho}_i$  is the reference vector of the primary photon of the current photon family, and is initialized following the procedure described in Section III.2.1. In the regular case,  $\boldsymbol{\rho}_r$  is the unchanged reference vector  $\boldsymbol{\rho}$  of the current photon.

And the final Stokes vector  $\mathbf{S}_f$  is obtained with :

$$\mathbf{I}_{f,k}(t_f, j+1) = \mathbf{R}(\phi_f) \mathbf{I}_{r,k}(t_f, j+1) \quad (\text{III.2.32})$$

The final Stokes vector  $\mathbf{I}_{f,k}(t_f, j + 1)$  of each received photon is saved and stored in memory. These Stokes vectors will be later used in Subsection III.2.7 in order to compute the lidar signal. Note that this peel-off step does not prevent any future interaction of the current photon, except if the inequality from Equation III.2.22 is not verified in which case the calculations for the current photon are terminated entirely.

### III.2.5 Angle sampling method

In the peel-off scattering technique, the scattering events are forced to a specific direction. However, the standard approach to the simulation of scattering events is to sample the scattering angle and azimuthal angle following a probability density function (PDF) based on the radiative properties of the scattering medium.

This PDF is given by the phase function. In the unpolarized case, the phase function is described by the element  $a_1$  of the normalized scattering matrix. However, in the polarized case, the phase function depends on the polarization state of the incident light. Indeed, the scattered Stokes vector is expressed as :

$$\mathbf{I}_{sca}(\theta_{sca}, \phi_{sca}) = \tilde{\mathbf{F}}(\theta_{sca}) \mathbf{R}(\phi_{sca}) \mathbf{I}_{inc} \quad (\text{III.2.33})$$

where  $\theta_{sca}$  and  $\phi_{sca}$  are the scattering and azimuthal angles respectively. In the following, the subscript  $sca$  is implied when applied to the angles in order to lighten the notation. Considering the first element of the Stokes vector and developing Equation III.2.33 gives :

$$I_{sca}(\theta, \phi) = I_{inc} a_1(\theta) + b_1(\theta) (Q_{inc} \cos(2\phi) + U_{inc} \sin(2\phi)) \quad (\text{III.2.34})$$

The polarized phase function is proportional to the ratio of the scattered intensity over the incident intensity [167]. Hence, it is defined as :

$$\begin{aligned}
f_{pol}(\theta, \phi) &= \frac{1}{C_{pol}} \left[ a_1(\theta) + b_1(\theta) \left( \frac{Q}{I} \cos(2\phi) + \frac{U}{I} \sin(2\phi) \right) \right] \\
&= \frac{1}{C_{pol}} [a_1(\theta) + \gamma(\phi)b_1(\theta)]
\end{aligned} \tag{III.2.35}$$

with  $\gamma(\phi)$  being defined as :

$$\gamma(\phi) = \left( \frac{Q}{I} \cos(2\phi) + \frac{U}{I} \sin(2\phi) \right) \tag{III.2.36}$$

and  $C_{pol}$  being a normalization constant such as :

$$\begin{aligned}
C_{pol} &= \int_0^{2\pi} \int_0^\pi [a_1(\theta) + \gamma(\phi)b_1(\theta)] \sin(\theta) d\theta d\phi \\
&= 2\pi \int_0^\pi a_1(\theta) \sin(\theta) d\theta
\end{aligned} \tag{III.2.37}$$

Considering Equation I.2.22, the normalization constant is then  $C_{pol} = 4\pi$ . The polarized phase function can then be considered as a PDF. Several methods can be implemented in order to sample the angles from this PDF, such as rejection sampling [165, 171, 172], inverse cumulative distribution function (CDF) methods [172], and tabulated methods [167, 172, 173, 174, 175]. Rejection sampling might be the easiest method to implement, but is rather inefficient when considering phase functions with large peaks [172]. The inverse CDF methods are very efficient, but they require the knowledge of the analytical form of the inverse of the CDF of the considered PDF [172]. Hence, a tabulated method, *i.e.* a method based on lookup tables, is implemented within the program hereby described.

When considering polarization, a conditional probability technique must first be implemented. The polarized phase function is expressed as a joint PDF of the marginal PDF of  $\phi$  with a conditional PDF of  $\theta$  such as :

$$f_{pol}(\theta, \phi) = f_\varphi(\phi) f_{\Theta|\varphi}(\theta|\phi) \tag{III.2.38}$$

where  $f_\varphi(\phi)$  is the marginal PDF and  $f_{\Theta|\varphi}(\theta|\phi)$  is the conditional PDF. Using this technique, an azimuthal angle can be first sampled from the marginal PDF, and then used to compute the con-

ditional PDF and to sample the scattering angle from it. The marginal PDF can be computed as :

$$\begin{aligned} f_{\varphi}(\phi) &= \int_0^{\pi} f_{pol}(\theta, \phi) \sin(\theta) d\theta = \frac{1}{4\pi} \left[ \int_0^{\pi} a_1(\theta) \sin(\theta) d\theta + \gamma(\phi) \int_0^{\pi} b_1(\theta) \sin(\theta) d\theta \right] \\ &= \frac{1}{2\pi} \left[ 1 + \left( \frac{Q}{I} \cos(2\phi) + \frac{U}{I} \sin(2\phi) \right) \bar{b}_1 \right] \end{aligned} \quad (\text{III.2.39})$$

where  $\bar{b}_1 = 1/2 \int_0^{\pi} b_1 \sin(\theta) d\theta$ . Equation III.2.39 can be further simplified by changing the reference frame of the incident Stokes vector so that the element  $U$  of the incident Stokes vector is null. This is achieved by computing the angle  $\Psi$  as :

$$\Psi = \frac{1}{2} \arctan \left( \frac{U}{Q} \right) \quad (\text{III.2.40})$$

The incident Stokes vector is then rotated such as :

$$\mathbf{I}^* = \mathbf{R}(\Psi) \mathbf{I} \quad (\text{III.2.41})$$

where the superscript  $*$  indicates that the incident Stokes vector has been rotated. Equation III.2.39 then becomes :

$$f_{\varphi}(\phi^*) = \frac{1}{2\pi} \left[ 1 + \frac{Q^*}{I^*} \bar{b}_1 \cos(2\phi^*) \right] \quad (\text{III.2.42})$$

where  $\phi^*$  is the azimuthal angle taking into account the already considered rotation by the angle  $\Psi$ , such as  $\phi = \phi^* + \Psi$ . The CDF of this marginal PDF can then be computed analytically such as :

$$F_{\varphi}(\phi^*) = \frac{1}{2\pi} \int_0^{\phi^* \leq 2\pi} \left[ 1 + \frac{Q^*}{I^*} \bar{b}_1 \cos(2\phi^{*'}) \right] d\phi^{*' } = \frac{1}{2\pi} \left[ \phi^* + \frac{1}{2} \frac{Q^*}{I^*} \bar{b}_1 \sin(2\phi^*) \right] \quad (\text{III.2.43})$$

A uniform pseudo-random number  $\eta_0 \in [0, 1]$  is then generated, and the azimuthal angle  $\phi$  is sampled by solving the equation :

$$4\pi\eta_0 = \left[ 2\phi^* + \frac{Q^*}{I^*} \bar{b}_1 \sin(2\phi^*) \right] \quad (\text{III.2.44})$$

Equation III.2.44 can be put under the form of the Kepler's equation such as :

$$M = E - e \sin(E) \quad (\text{III.2.45})$$

with  $M = 4\pi\eta_0$ ,  $E = 2\phi^*$  and  $e = -\bar{b}_1 Q^*/I^*$ . The Newton-Raphson iteration method is then used in order to compute the value of  $\phi^*$ . This method consists of iteratively computing the parameter  $E_n$  until the difference between two iterations is below a certain threshold,  $n$  being the index of the current iteration. This iteration process is expressed as :

$$E_{n+1} = E_n + \frac{M - E_n + e \sin(E_n)}{1 - e \cos(E_n)} \quad (\text{III.2.46})$$

In the program presented in this thesis, the relative convergence criterion is set to  $10^{-6}$ , and  $E_0 = M$ . Finally, the angle  $\phi$  is computed as :

$$\phi = \frac{E_{nf}}{2} + \Psi \quad (\text{III.2.47})$$

where  $E_{nf}$  is the last value obtained by the iteration process of Equation III.2.46 before the convergence criterion is triggered. Once an azimuthal angle  $\phi$  has been sampled, the conditional PDF  $f_{\Theta|\varphi}(\theta|\phi)$  can be computed. It is expressed as :

$$f_{\Theta|\varphi}(\theta|\phi) = \frac{a_1(\theta) + \gamma(\phi)b_1(\theta)}{C_{\Theta|\varphi}(\phi)} \quad (\text{III.2.48})$$

where  $C_{\Theta|\varphi}(\phi)$  is a normalization factor. It is computed as :

$$C_{\Theta|\varphi}(\phi) = \int_0^\pi [a_1(\theta') + \gamma(\phi)b_1(\theta')] \sin(\theta') d\theta' = 2 + 2\gamma(\phi)\bar{b}_1 \quad (\text{III.2.49})$$

The conditional CDF is then expressed as :

$$\begin{aligned} F_{\Theta|\varphi}(\theta|\phi) &= \frac{1}{C_{\Theta|\varphi}(\phi)} \int_0^{\theta \leq \pi} \left[ a_1(\theta') + \gamma(\phi)b_1(\theta') \right] \sin(\theta') d\theta' \\ &= \frac{1}{C_{\Theta|\varphi}(\phi)} \left[ \int_0^{\theta \leq \pi} a_1(\theta') \sin(\theta') d\theta' + \gamma(\phi) \int_0^{\theta \leq \pi} b_1(\theta') \sin(\theta') d\theta' \right] \end{aligned} \quad (\text{III.2.50})$$

Proceeding to a change of variable such as  $\mu = \cos(\theta)$ , Equation III.2.50 becomes :

$$F_{\mu|\varphi}(\mu|\phi) = \frac{1}{1 + \gamma(\phi)\bar{b}_1} \left[ \frac{1}{2} \int_{\mu \geq -1}^1 a_1(\mu') d\mu' + \gamma(\phi) \frac{1}{2} \int_{\mu \geq -1}^1 b_1(\mu') d\mu' \right] \quad (\text{III.2.51})$$

A uniform pseudo-random number  $\eta_0 \in [0, 1]$  is generated, and substituted with  $F_{\mu|\varphi}(\mu|\phi)$  in Equation III.2.51. Then, the determination of the scattering angle requires to solve this equation. However, in the general case, the elements of the scattering matrix are only known at discrete values of  $\theta$ , and the number  $\eta_0$  might not correspond to one of these discrete values. Hence, a method needs to be implemented in order to compute the integrals of Equation III.2.51, so that intermediate values of  $\theta$  are accounted for. In order to do so, the scattering matrix elements are expressed using a Piecewise Linear Approximation (PLA). As such, such as the sampling the cosine of the scattering angle consists in solving the quadratic equation :

$$\begin{aligned} 0 &= \frac{1}{2} (\alpha_k + \gamma(\phi)\iota_k) \mu^2 + (\beta_k + \gamma(\phi)\zeta_k) \mu - \frac{1}{2} (\alpha_k + \gamma(\phi)\iota_k) \mu_k^2 - (\beta_k + \gamma(\phi)\zeta_k) \mu_k \\ &\quad + 2(1 + \gamma(\phi)\bar{b}_1)(\eta_0 - F_{\mu|\varphi}(\mu_k|\phi)) \end{aligned} \quad (\text{III.2.52})$$

where  $k$  is an iterator that indicates which value of the discrete scattering matrix is referred to, and for which the corresponding discrete cosine of the scattering angle  $\mu_k$  is the closest inferior to  $\mu$ . Note that the iterator  $k$  differs from the one presented in Table III.2.  $\alpha_k$  and  $\beta_k$  are the PLA coefficients of the scattering matrix element  $a_1$ ,  $\iota_k$  and  $\zeta_k$  are the PLA coefficients of the element  $(a_1)_k$ , and  $\iota_k$  and  $\zeta_k$  are the PLA coefficients of the element  $(b_1)_k$ . Note that the coefficients  $\alpha$  and  $\beta$  used here differ from the extinction and backscattering coefficients defined in Section I.3, while

$\zeta_k$  differs from the angle described in Table III.1.

Finally the scattering angle is found by means of the following formula :

$$\theta = \arccos(\mu) \quad (\text{III.2.53})$$

The procedure described in this section allows to sample the scattering angle and azimuthal angle when considering any scattering medium composed of randomly oriented particles, with any polarization state of the incident light. The following section is dedicated to the description of the next steps of the scattering process, and also introduces the scattering splitting variance reduction technique.

### III.2.6 Scattering and scattering splitting

In Section III.2.4, the peel-off scattering technique was introduced. After being subject to a stochastic transport step, the contribution of the current photon to the the received signal is computed analytically. However, this semi-analytical approach only allows to compute the contribution at first order of scattering. In order to account for the contribution of multiple scattering, an additional step must be undertaken. This additional step consists in the sampling of new direction of propagation for the current photon. This new direction is sampled according to the scattering matrix of the interacting medium, as this matrix can be used in order to construct a probability density function expressing the probability of photon being scattered in a specific direction, as described in Section III.2.5. As such, this step is referred to as the scattering step.

The aim of this scattering step is to modify the direction of propagation  $\mathbf{d}_{i,j,k}$  of the current photon into a new direction vector  $\mathbf{d}_{i,j+1,k}$ . Consequently, the reference vector  $\boldsymbol{\rho}_{i,j,k}$  and Stokes vector  $\mathbf{I}_{i,j,k}$  must also be modified accordingly. Within this step, the scattering splitting variance reduction technique can also be triggered. In this case, two photons are created, one that is referenced with the subscripts  $i, j + 1, k$  and that is scattered in the forward direction, and one referenced with the subscripts  $i, j + 1, k + 1$  and that is scattered in the backward direction. In order to lighten the notation, a different set of subscripts and superscripts is used. The outcoming

vectors are represented by the superscript  $'$ , while in the scattering splitting case the forward scattered photon is denoted by the superscript  $FW$  and the backward scattered photon by the superscript  $BW$ . Table III.5 summarizes the different quantities used during the scattering step, and Figure III.7 presents a schematic view of the architecture of the scattering step.

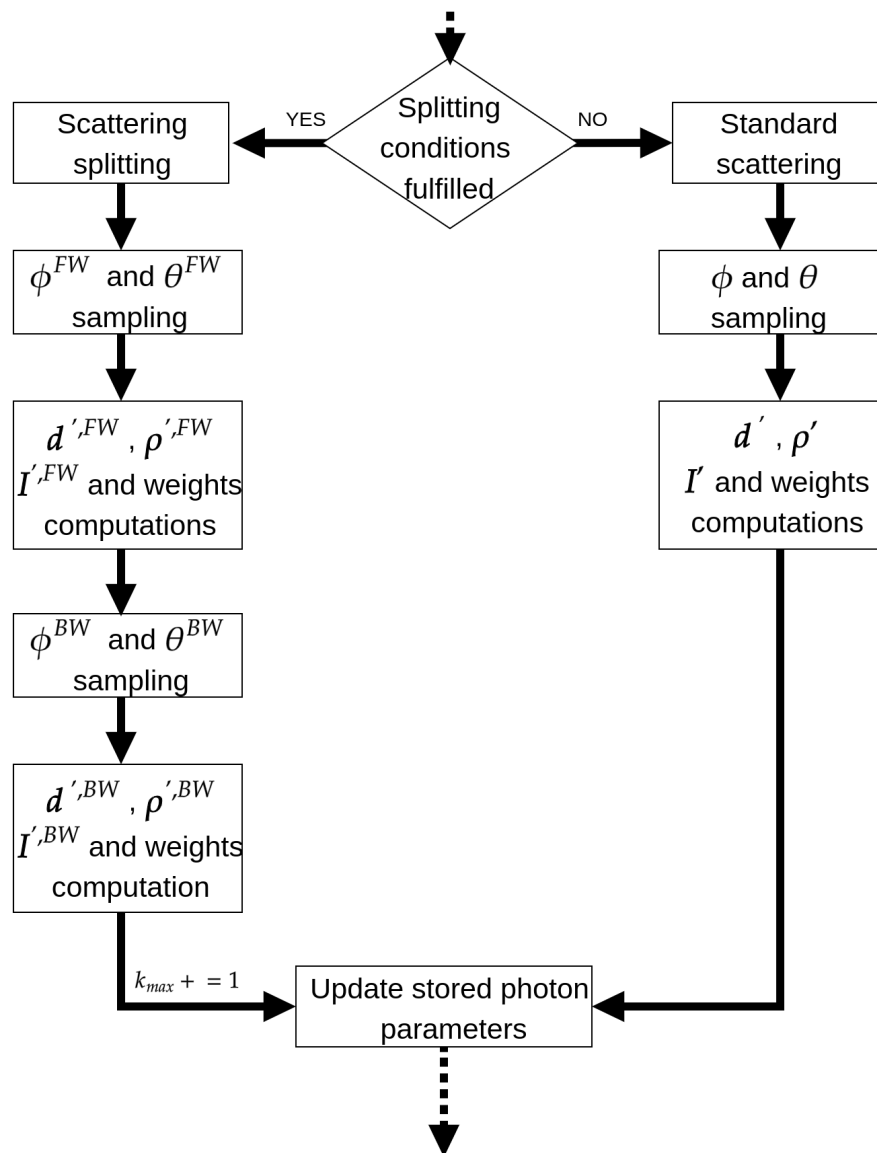


Figure III.7: Schematic view of the architecture of the scattering step.

The first step of the scattering process is to determine whether the scattering splitting variance reduction technique is triggered. Several conditions need to be verified in order to do so. They

Name	Description	Symbol
Photon position vector	Position vector of the current photon	$\mathbf{p}$
Photon direction vector	Direction vector of the current photon	$\mathbf{d}$
Photon reference vector	Reference vector of the current photon	$\boldsymbol{\rho}$
Scattering plane rotation angle	Angle between the current reference vector and the reference vector lying in the scattering plane	$\Psi$
Scattering angle	Scattering angle of the current rotation	$\theta$
Azimuthal angle	Azimuthal angle of the current rotation	$\phi$
Cumulative distribution function	Cumulative distribution function used to sample either the scattering angle or the azimuthal angle	$F$
Polarized phase function	Polarized phase function of the current scattering event	$f_{pol}$
Stokes vector	Stokes vector of the current photon	$\mathbf{I}$
Weight factor	Weight factor associated with the current scattering event	$q$
Cone angle	Angle of the cone at the receiver for the scattering splitting	$\theta_{cone}$
Scattering splitting phase function angle	The scattering phase function is split at this angle into the forward and backward phase functions.	$\theta_{split}$
Cone radius	Radius of the code at the receiver for the scattering splitting	$R_{cone}$
Scattering splitting receiver angle	Maximum angle between the current photon direction and the current photon position for the scattering to happen.	$\zeta$
Superscripts	Superscripts indicating which quantity is currently used. The ' superscript indicates the rotated quantity. The * superscript indicates a quantity whose associated reference vector lies in the scattering plane, $FW$ stands for forward and $BW$ for backward	$'$ , $*$ , $FW$ , $BW$
Subscripts	Subscripts providing information on the current quantity. The subscript $daw$ stands for discrete absorption weighting and $ssw$ for scattering splitting weighting	$daw$ , $ssw$

Table III.5: List of the parameters used in the scattering and scattering splitting process.

are expressed as :

$$\sqrt{p_x^2 + p_y^2} < \tan(\theta_{cone})p_z + R_{cone} \quad (III.2.54a)$$

$$\frac{\mathbf{p} \cdot \mathbf{d}}{|\mathbf{p}| |\mathbf{d}|} > \cos(\zeta) \quad (III.2.54b)$$

where  $\zeta$  is the maximal angle between the current photon position vector  $\mathbf{p}$  and the direction vector  $\mathbf{d}$  that would prevent the the triggering of the scattering splitting technique. The first of these conditions verifies whether the photon position is within a cone whose apex position on the horizontal plane is the same as the receiver disc center, of radius  $R_{cone}$  at  $p_{rec,z} = 0$  and of half-angle  $\theta_{cone}$ . Schematically, this cone encompasses the cone formed by the receiver FOV when  $\theta_{cone} > \theta_{rec}$ . The second condition verifies whether the angle between the current photon position vector and the direction vector is lower than the angle  $\zeta$ , e.g. with  $\zeta = 90^\circ$  this conditions verifies if the photon is moving closer to the receiver. Both of these conditions need to be verified in order

to trigger the scattering splitting variance reduction technique. These conditions are introduced because this technique necessitates a large amount of computational power, as two photons are created each time it is employed. As such, the three parameters  $R_{cone}$ ,  $\theta_{cone}$  and  $\zeta$  can be tuned in order to increase or decrease the probability of this technique being triggered.

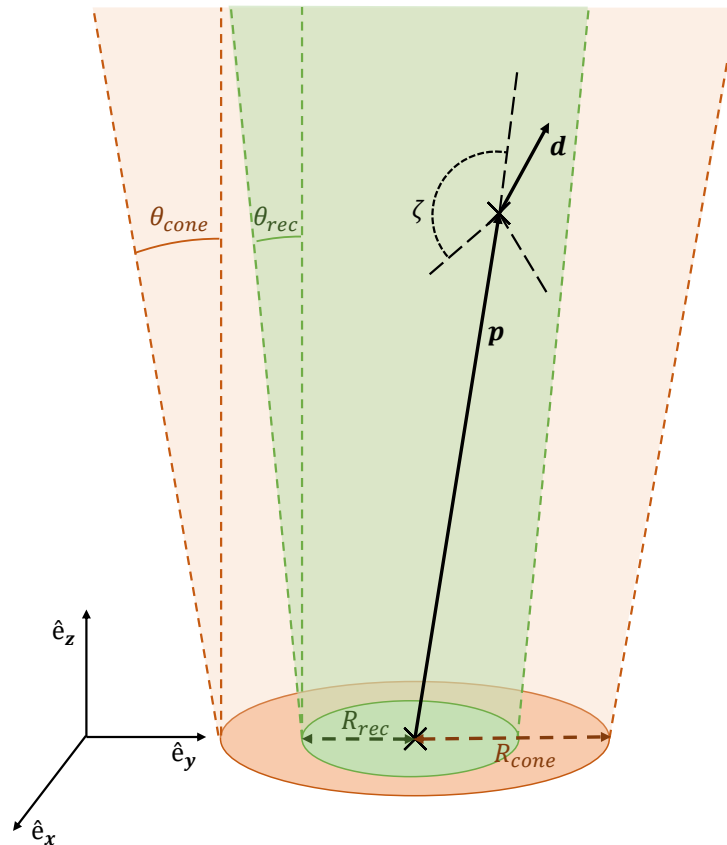


Figure III.8: Schematic view of the triggering conditions of the scattering splitting technique. The receiver FOV is represented in green and the scattering splitting cone is represented in orange. On this figure, the photon is located within the scattering splitting cone, hence verifying the condition from Equation III.2.54(a). Moreover, the angle between the photon position vector  $\mathbf{p}$  and the direction vector  $\mathbf{d}$  is lower than the angle  $\zeta$ , verifying the condition from Equation III.2.54(b). Hence, in this example, both conditions are verified and the scattering splitting technique is triggered.

In the case of standard scattering, *i.e.* when the scattering splitting variance reduction technique is not triggered, several steps lead to the modification of the current photon vectors. First, a scattering angle  $\theta$  and an azimuthal angle  $\phi$  are sampled following the procedure described in Subsection III.2.5. The new direction vector  $\mathbf{d}'$  and rotation vector  $\boldsymbol{\rho}'$  are then obtained by adapting

the rotation formulae described in Equations III.2.2 and III.2.3 such as :

$$\boldsymbol{\rho}' = \boldsymbol{\rho} \cos(\phi) + (\mathbf{d} \times \boldsymbol{\rho}) \sin(\phi) + \mathbf{d}(\mathbf{d} \cdot \boldsymbol{\rho})(1 - \cos(\phi)) \quad (\text{III.2.55a})$$

$$\mathbf{d}' = \mathbf{d} \cos(\theta) + (\boldsymbol{\rho}' \times \mathbf{d}) \sin(\theta) + \boldsymbol{\rho}'(\boldsymbol{\rho}' \cdot \mathbf{d})(1 - \cos(\theta)) \quad (\text{III.2.55b})$$

And the outgoing Stokes vector is computed as :

$$\mathbf{I}'(\theta, \phi) = q_{daw} \frac{1}{C_{pol} f_{pol}(\theta, \phi)} \tilde{\mathbf{F}}(\theta) \mathbf{R}(\phi) \mathbf{I} \quad (\text{III.2.56})$$

The fractional term in the Equation above is implemented in order to ensure that the intensity of the scattered photon remains unchanged except for the modification due to the weight associated with the discrete absorption weighting technique, as described in Subsection III.2.3.

In this standard approach to the scattering process, the number of photons remains unchanged, and the scattering order  $j$  of the scattered photon is incremented by one such as  $j' = j + 1$ . In the scattering splitting case, several modifications need to be implemented in the procedure allowing to sample the angles  $\theta$  and  $\phi$ . Indeed, the aim of this technique is to use modified PDFs in order to scatter two photons, one that is scattered with a scattering angle in the interval  $\theta \in [0, \theta_{split}]$  and which is hereby referred to as the forward photon (superscript  $FW$ ), and another in the interval  $\theta \in ]\theta_{split}, \pi]$  and which is referred to as the backward photon (superscript  $BW$ ). This variance reduction technique serves several purposes. First, one can envision that the trajectories of the primary photons before the first event will be mostly similar. Indeed, these primary photons are emitted within the cone restrained by the laser divergence  $\theta_{em}$ , which in most cases is fairly low. Hence, the differences between the primary photons trajectory arise from a different sampling of their transported lengths. The scattering splitting variance reduction technique hence allows to compute the trajectories of two photons after the first scattering event, by only computing the first transport process once. Moreover, the phase function of large particles often presents a large forward peak. Because the sampling of the scattering angle is based on this phase function, this implies that most of the photons which would be scattered following a standard sampling process would be directed in the near-forward direction. The scattering split-

ting technique allows to increase the probability that photons are scattered in other directions, which can be of potential importance when computing the lidar signals.

Hence, in order to implement the scattering splitting technique, several modifications of the sampling procedure are needed. In the following, the superscripts  $FW$  and  $BW$  are used to differentiate the forward and backward PDFs, CDFs and normalization constants. These superscripts are not used for the differentiation of the generated random numbers and sampled angles as it would considerably burden up the notation, but the reader is reminded that these quantities may differ between the two cases. The first step is then to modify the scattering PDF defined in Equation III.2.35 so that only forward or backward angles can be sampled. Two new PDFs are then created such as :

$$f_{pol}^{FW} = \frac{1}{C_{pol}^{FW}} [a_1(\theta) + \gamma(\phi)b_1(\theta)] \quad (III.2.57a)$$

$$f_{pol}^{BW} = \frac{1}{C_{pol}^{BW}} [a_1(\theta) + \gamma(\phi)b_1(\theta)] \quad (III.2.57b)$$

where the normalization constants  $C_{pol}^{FW}$  and  $C_{pol}^{BW}$  are defined such as :

$$C_{pol}^{FW} = 2\pi \int_0^{\theta_{split}} a_1(\theta) \sin(\theta) d\theta = 4\pi(\bar{a}_1)^{FW} \quad (III.2.58a)$$

$$C_{pol}^{BW} = 2\pi \int_0^{\pi-\theta_{split}} a_1(\theta) \sin(\theta) d\theta = 4\pi(\bar{a}_1)^{BW} \quad (III.2.58b)$$

where  $(\bar{a}_1)^{FW} = (1/2) \int_0^{\theta_{split}} a_1(\theta) \sin(\theta) d\theta$  and  $(\bar{a}_1)^{BW} = (1/2) \int_0^{\pi-\theta_{split}} a_1(\theta) \sin(\theta) d\theta$ . Following this step, the conditional probability technique presented in Subsection III.2.5 remains mostly unchanged. For the sampling of the azimuthal angle  $\phi$ , the integral bounds in the computation of the marginal PDFs as described in Equation III.2.39 are changed. The marginal PDFs are then computed as :

$$f_{\varphi}(\phi^*)^{FW} = \frac{1}{2\pi} \left[ 1 + \frac{Q^*}{I^*} \frac{(\bar{b}_1)^{FW}}{(\bar{a}_1)^{FW}} \cos(2\phi^*) \right] \quad (III.2.59a)$$

$$f_{\varphi}(\phi^*)^{BW} = \frac{1}{2\pi} \left[ 1 + \frac{Q^*}{I^*} \frac{(\bar{b}_1)^{BW}}{(\bar{a}_1)^{BW}} \cos(2\phi^*) \right] \quad (III.2.59b)$$

where the quantities  $(\bar{a}_1)^{FW}$  and  $(\bar{a}_1)^{BW}$  have been introduced when compared to Equation III.2.42 due to the different integration intervals when using the standard sampling technique and the scattering sampling technique. The corresponding CDFs are :

$$F_{\varphi}(\phi^*)^{FW} = \frac{1}{2\pi} \left[ \phi^* + \frac{Q^*}{2I^*} \frac{(\bar{b}_1)^{FW}}{(\bar{a}_1)^{FW}} \sin(2\phi^*) \right] \quad (\text{III.2.60a})$$

$$F_{\varphi}(\phi^*)^{BW} = \frac{1}{2\pi} \left[ \phi^* + \frac{Q^*}{2I^*} \frac{(\bar{b}_1)^{BW}}{(\bar{a}_1)^{BW}} \sin(2\phi^*) \right] \quad (\text{III.2.60b})$$

The azimuthal angle can then be sampled by generating a pseudo-random number and solving the Kepler's equation (*i.e.* Equation III.2.45) as described in Subsection III.2.5.

Following the same framework, the conditional PDFs are then computed as :

$$f_{\Theta|\varphi}^{FW}(\theta|\phi) = \frac{a_1(\theta) + \gamma(\phi)b_1(\theta)}{C_{\Theta|\varphi}^{FW}(\phi)} \quad (\text{III.2.61a})$$

$$f_{\Theta|\varphi}^{BW}(\theta|\phi) = \frac{a_1(\theta) + \gamma(\phi)b_1(\theta)}{C_{\Theta|\varphi}^{BW}(\phi)} \quad (\text{III.2.61b})$$

with constants  $C_{\Theta|\varphi}^{FW}$  and  $C_{\Theta|\varphi}^{BW}$  such as :

$$C_{\Theta|\varphi}^{FW}(\phi) = \int_0^{\theta_{split}} \left[ a_1(\theta') + \gamma(\phi)b_1(\theta') \right] \sin(\theta') d\theta' = 2(\bar{a}_1)^{FW} + 2\gamma(\phi)(\bar{b}_1)^{FW} \quad (\text{III.2.62a})$$

$$C_{\Theta|\varphi}^{BW}(\phi) = \int_0^{\pi-\theta_{split}} \left[ a_1(\theta') + \gamma(\phi)b_1(\theta') \right] \sin(\theta') d\theta' = 2(\bar{a}_1)^{BW} + 2\gamma(\phi)(\bar{b}_1)^{BW} \quad (\text{III.2.62b})$$

And the CDFs are computed following the change of variable  $\mu = \cos(\theta)$  such as :

$$F_{\mu|\varphi}^{FW}(\mu|\phi) = \frac{1}{(\bar{a}_1)^{FW} + \gamma(\phi)(\bar{b}_1)^{FW}} \left[ -\frac{1}{2} \int_1^{\mu \geq \mu_{split}} a_1(\mu') d\mu' - \frac{1}{2} \int_1^{\mu \geq \mu_{split}} \gamma b_1(\mu') d\mu' \right] \quad (\text{III.2.63a})$$

$$F_{\mu|\varphi}^{BW}(\mu|\phi) = \frac{1}{(\bar{a}_1)^{BW} + \gamma(\phi)(\bar{b}_1)^{BW}} \left[ -\frac{1}{2} \int_1^{\mu \geq -\mu_{split}} a_1(\mu') d\mu' - \frac{1}{2} \int_1^{\mu \geq -\mu_{split}} \gamma b_1(\mu') d\mu' \right] \quad (\text{III.2.63b})$$

where  $\mu_{split} = \cos(\theta_{split})$ . Following this definition of the CDFs, the same PLA is used and two random numbers are generated, one for each photon. Hence, within the integrals of Equations III.2.63b(a) and (b), the scattering elements  $a_1(\mu')$  and  $b_1(\mu')$  are replaced by their linear interpo-

lations. These equations are then expressed as quadratic equations such as :

$$0 = \frac{1}{2} (\alpha_k + \gamma(\phi)\iota_k) \mu^2 + (\beta_k + \gamma(\phi)\zeta_k) \mu - \frac{1}{2} (\alpha_k + \gamma(\phi)\iota_k) \mu_k^2 - (\beta_k + \gamma(\phi)\zeta_k) \mu_k + 2 [(\bar{a}_1)^{FW} + \gamma(\phi)(\bar{b}_1)^{FW}] (\eta_0 - F_{\mu|\varphi}^{FW}(\mu_k|\phi)) \quad (\text{III.2.64a})$$

$$0 = \frac{1}{2} (\alpha_k + \gamma(\phi)\iota_k) \mu^2 + (\beta_k + \gamma(\phi)\zeta_k) \mu - \frac{1}{2} (\alpha_k + \gamma(\phi)\iota_k) \mu_k^2 - (\beta_k + \gamma(\phi)\zeta_k) \mu_k + 2 [(\bar{a}_1)^{BW} + \gamma(\phi)(\bar{b}_1)^{BW}] (\eta_0 - F_{\mu|\varphi}^{BW}(\mu_k|\phi)) \quad (\text{III.2.64b})$$

In the procedure described above, the cosine of the forward scattering angle is sampled in the interval  $\mu \in [\mu_{split}, 1]$ , and the cosine of the backward scattering angle in  $\mu \in [-\mu_{split}, 1]$ . However, the aim of the backward photon is to be scattered with a cosine of the scattering angle in the interval  $\mu \in [-1, \mu_{split}]$ . Hence, in order to address this issue, the scattering angles are computed as :

$$\theta^{FW} = \arccos(\mu^{FW}) \quad (\text{III.2.65a})$$

$$\theta^{BW} = \arccos(-\mu^{BW}) \quad (\text{III.2.65b})$$

where the superscripts have been introduced to emphasize that these angles are different. Knowing the scattering angle and the azimuthal angle, the reference and direction vectors of both forward and backward photons can be computed using Equation III.2.55. However, when considering the Stokes vector, the scattering splitting variance reduction technique introduces biases that need to be accounted for by weight modifications. For the forward photon, this weight is expressed as :

$$q_{ssw}^{FW} = \frac{f_\varphi(\phi) f_{\Theta|\varphi}(\theta, \phi)}{f_\varphi^{FW}(\phi) f_{\Theta|\varphi}^{FW}(\theta, \phi)} = \frac{1 + (Q^*/I^*)\bar{b}_1 \cos(2\phi^*)}{1 + (Q^*/I^*)((\bar{b}_1)^{FW}/(\bar{a}_1)^{FW}) \cos(2\phi^*)} \frac{(\bar{a}_1)^{FW} + \gamma(\phi)(\bar{b}_1)^{FW}}{1 + \gamma(\phi)\bar{b}_1} \quad (\text{III.2.66})$$

The computation of the weight of the backward photon also needs to account for the change of

sign of the cosine, which gives :

$$\begin{aligned}
q_{ssw}^{BW} &= \frac{f_{\varphi}(\phi) f_{\Theta|\varphi}(\theta|\phi)}{f_{\varphi}^{BW}(\phi) f_{\Theta|\varphi}^{BW}(\pi - \theta|\phi)} \\
&= \frac{1 + (Q^*/I^*) \bar{b}_1 \cos(2\phi^*)}{1 + (Q^*/I^*) ((\bar{b}_1)^{BW} / (\bar{a}_1)^{BW}) \cos(2\phi^*)} \\
&\quad \times \frac{(\bar{a}_1)^{BW} + \gamma(\phi) (\bar{b}_1)^{BW}}{1 + \gamma(\phi) \bar{b}_1} \frac{a_1(\theta) + \gamma(\phi) b_1(\theta)}{a_1(\pi - \theta) + \gamma(\phi) b_1(\pi - \theta)}
\end{aligned} \tag{III.2.67}$$

Finally, the scattered Stokes vectors are computed such as :

$$\mathbf{I}',^{FW}(\theta^{FW}, \phi^{FW}) = q_{daw} q_{ssw}^{FW} \frac{\tilde{\mathbf{F}}(\theta^{FW})}{C_{pol} f_{pol}(\theta^{FW}, \phi^{FW})} \mathbf{R}(\phi^{FW}) \mathbf{I} \tag{III.2.68a}$$

$$\mathbf{I}',^{BW}(\theta^{FW}, \phi^{FW}) = q_{daw} q_{ssw}^{BW} \frac{\tilde{\mathbf{F}}(\theta^{BW})}{C_{pol} f_{pol}(\theta^{BW}, \phi^{BW})} \mathbf{R}(\phi^{BW}) \mathbf{I} \tag{III.2.68b}$$

Following the scattering step, the number of photons within the family  $k_{max}$  is either kept the same or increased by one when the scattering splitting technique happens. The newly scattered photons is then subject to transport, peel-off and scattering until a stopping condition is triggered. Two stopping conditions are considered; (i) if the scattering order  $j$  is equal to  $j_{max} - 1$ , then the current light-matter interaction loop stops after each photon of the current family has been subject to the peel-off scattering step; (ii) if the first element of the Stokes vector passes below a certain threshold  $I_{i,j,k} < \varepsilon$ , then the current photon is terminated and no longer tracked within the program.

### III.2.7 Return signal calculation

Within the peel-off scattering technique, the contribution of the received photon  $\mathbf{I}_{f,k}(t_f, j)$  is calculated. Each of these contributions are defined at a length  $t_f$ . However, the lidar signal is the time-averaged power within a certain time step  $\Delta t$ . In order to simulate this process, a sequence

of discrete path lengths is created such as :

$$t_l = t_{l-1} + \Delta t \quad \text{for} \quad \left\{ l \in \mathbb{N} \mid 1 \leq l \leq \frac{t_{max} - t_{min}}{\Delta t} \right\} \quad (\text{III.2.69})$$

where  $t_0 = t_{min}$ , and  $t_{max}$ ,  $t_{min}$  and  $\Delta t$  are input parameters as described in Table III.1. After each iteration of the light-matter interaction loop, these contributions  $\mathbf{I}_{f,k}(t_f, j)$  are summed over the different photons within the photon family and according to their path lengths. This can be expressed as :

$$\mathbf{I}_f(t_l, j) = \sum_{k=1}^{k=k_{max}} \begin{cases} \mathbf{I}_{f,k}(t_f, j), & \text{if } t_l < t_f < t_{l+1} \\ 0, & \text{otherwise} \end{cases} \quad (\text{III.2.70})$$

This allows to save the contribution of each photon family. The output Stokes vectors are then computed as :

$$\mathbf{I}(t_l) = \frac{1}{N_{ph}} \sum_{i=1}^{N_{ph}} \sum_{j=1}^{j_{max}} \mathbf{I}_f(t_l, j) \quad (\text{III.2.71a})$$

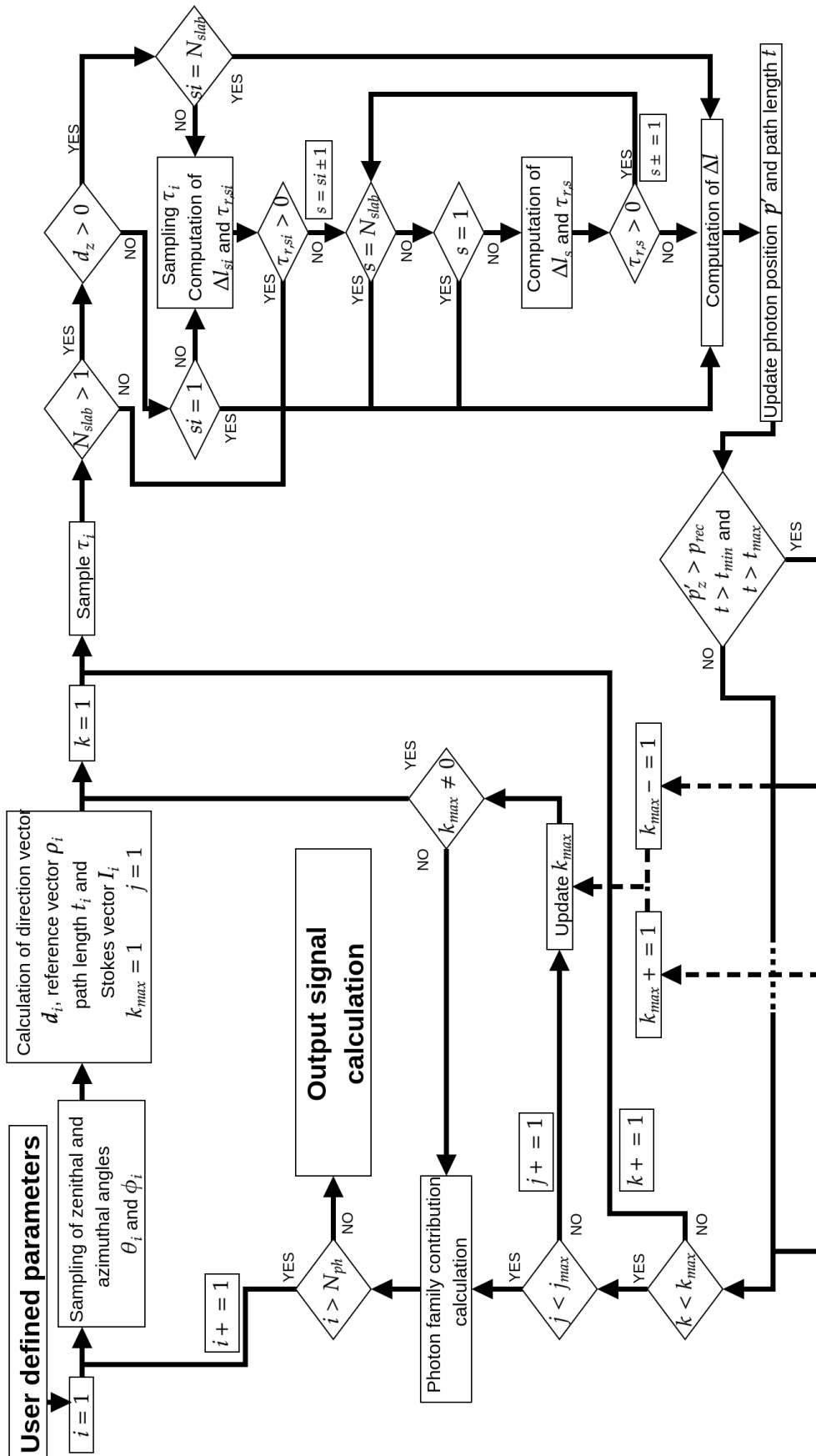
$$\mathbf{I}(t_l, j) = \frac{1}{N_{ph}} \sum_{i=1}^{N_{ph}} \mathbf{I}_f(t_l, j) \quad (\text{III.2.71b})$$

The standard deviations are then calculated as :

$$\sigma_v(t_l) = \sqrt{\frac{1}{N_{ph} - 1} \sum_{i=1}^{i=N_{ph}} \left[ \left( \sum_{j=1}^{j_{max}} (\mathbf{I}(t_l, j))_v \right)^2 - (\mathbf{I}(t_l))_v^2 \right]} \quad (\text{III.2.72a})$$

$$\sigma_v(t_l, j) = \sqrt{\frac{1}{N_{ph} - 1} \sum_{i=1}^{i=N_{ph}} (\mathbf{I}(t_l, j))_v^2 - (\mathbf{I}(t_l))_v^2} \quad (\text{III.2.72b})$$

where  $v = I, Q, U, V$  indicates which element of the Stokes vector is referred to (e.g.  $(\mathbf{I}(t_l, j))_Q = Q(t_l, j)$ ). The computation of the output Stokes vectors and of their associated standard deviations concludes the program. Figure III.9 presents a complete view of the architecture of the program and of the different steps within. Section III.3 presents the procedures undertaken in order to assess the validity of the results obtained with this program.



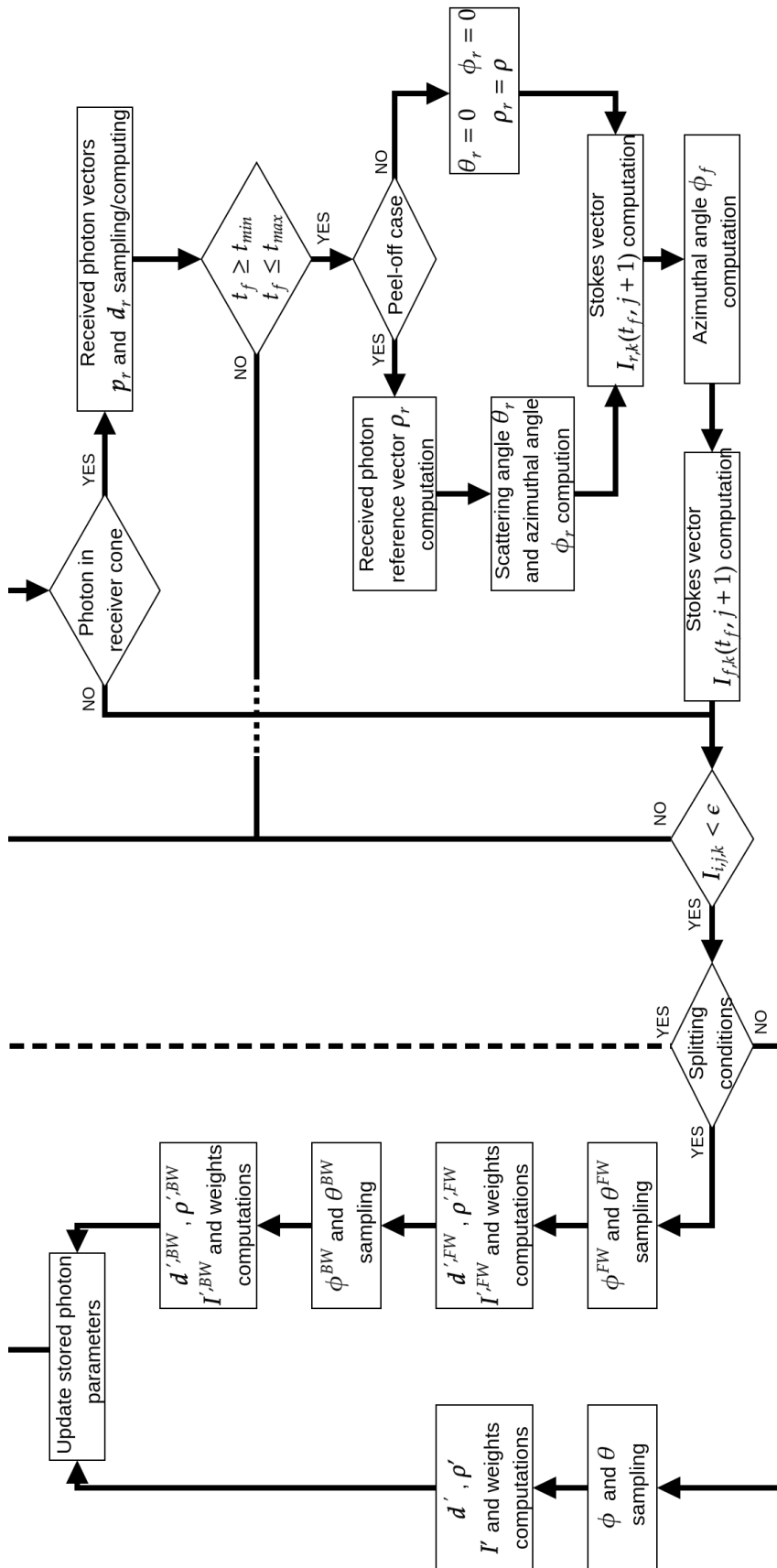


Figure III.9: Complete architecture of the lidar signal simulation program. In this figure, the dotted lines are used to indicate unjoined intersecting paths. The dashed lines indicate instructions relative to the parameters  $k_{r,max}$  and that are only triggered at the next scattering order.

### III.3 Program validation

This section presents the approaches that have been undertaken in order to validate the lidar signal simulation program. In Subsection III.3.1, the intensity scattered by a particle is computed analytically and compared with the intensity computed using the method presented in Section III.1. This allows to validate individually the angle sampling method presented in Subsection III.2.5 and the scattering splitting method presented in Subsection III.2.6. Subsection III.3.2 presents results obtained with the lidar signal simulation program, while only considering the first order of scattering. These signals are compared with the single scattering lidar equation (see Equation I.3.2). In the lidar signal simulation program, the lidar signal at the first order of scattering is not influenced by the angle sampling method and by the scattering splitting technique. Hence, this comparison allows to validate the transport method, as well as the peel-off technique and the continuous absorption weighting technique. Finally, Subsection III.3.3 presents the comparison between quantities derived from lidar signals simulated with this program to results that have been presented in the literature. This attempt at reproducing previously published results has been undertaken using the data available in the corresponding articles, and allows for a qualitative evaluation of the program results validity.

#### III.3.1 Validation of the angle sampling method

In order to proceed to the validation of the angle sampling method, and in a second time to the scattering splitting variance reduction technique, the corresponding parts of the program have been isolated<sup>2</sup>.

For the purpose of this validation procedure, two types of particles are considered. The first corresponds to Rayleigh scatterers, *i.e.* particles or molecules whose size parameters verify  $x_m = 2\pi r_m/\lambda \ll 1$ . The normalized scattering matrix of such particles is expressed as :

<sup>2</sup>Specifically, the functions corresponding to the angle sampling, the scattering splitting, and the computation of the scattered Stokes vectors and of the weights have been rewritten in Python. This has been done for test purposes at first, and has been kept in order to simplify the analysis of the data hereby presented. Nevertheless, the calculations undergone within the Python script are strictly identical to those of the main program.

$$\tilde{\mathbf{F}}(\theta) = \frac{3}{4} \begin{bmatrix} \cos^2(\theta) + 1 & \cos^2(\theta) - 1 & 0 & 0 \\ \cos^2(\theta) - 1 & \cos^2(\theta) + 1 & 0 & 0 \\ 0 & 0 & 2 \cos(\theta) & 0 \\ 0 & 0 & 0 & 2 \cos(\theta) \end{bmatrix} \quad (\text{III.3.1})$$

The second case is taken from the work of [176], and corresponds to polydisperse water droplets. Specifically, the scattering matrix of the first case of reference [176] is used. The particles size distribution is expressed as a Gamma distribution such as [177] :

$$n_s(r_m) = \frac{1}{R_{eff}} \frac{1}{(\gamma_r - 1)!} \left( \frac{r_m}{R_{eff}} \right)^{\gamma_r - 1} \exp\left(-\frac{r_m}{R_{eff}}\right) \quad (\text{III.3.2})$$

where  $R_{eff}$  is the effective radius and  $\gamma_r$  is the shape parameter of the distribution. In the case considered here,  $R_{eff} = 8 \mu\text{m}$  and  $\gamma_r = 6$ . The normalized scattering matrix corresponding to this distribution of spherical particles is computed using the PyMieScatt library [178] with an optical index of  $m_o = 1.3337 + i1.5 \cdot 10^{-9}$  at  $\lambda = 532 \text{ nm}$ . The normalized scattering matrices are computed from  $R_{min} = 1 \mu\text{m}$  to  $R_{max} = 20 \mu\text{m}$ , with a step of  $\Delta R = 0.02 \mu\text{m}$  and with an angular resolution of  $\Delta\theta = 0.25^\circ$ . These matrices are then averaged according to the size distribution presented in Equation III.3.2.

The sampling methods presented in this thesis results in angles that have been sampled over a continuous range. In order to analyze the results, the sampled Stokes vectors are summed in a matrix, whose rows correspond to the scattering angle and columns to the azimuthal angle. The dimension of this matrix is  $[4 \times N_\theta \times N_\phi]$ , where  $N_\theta$  and  $N_\phi$  are the numbers of discrete scattering angle and azimuthal angle respectively. The elements of this matrix are computed such as :

$$\mathbf{I}_{l,m} = \frac{1}{N_{ph}} \sum_{i=1}^{N_{ph}} \begin{cases} \mathbf{I}'(\theta, \phi) & \text{if } \theta_l < \theta < \theta_{l+1} \text{ and } \phi_m < \phi < \phi_{m+1} \\ 0 & \text{otherwise} \end{cases} \quad (\text{III.3.3})$$

where the subscripts  $l$  and  $m$  indicate the row and column of the matrix, corresponding to the angles  $\theta_l = (l - 1)\Delta\theta$  and  $\phi_m = (m - 1)\Delta\phi$  respectively,  $N_{ph}$  is the number of samples, equivalent

to a number of launched photons, and  $\mathbf{I}'(\theta, \phi)$  is the Stokes vectors sampled at the angles  $\theta$  and  $\phi$  and computed as in Equation III.2.56 taking  $q_{daw} = 1$ . In the calculation presented in this section, the number of samples has been set to  $N_{ph} = 10^7$ . When the scattering splitting technique is applied, Equation III.3.3 becomes :

$$\mathbf{I}_{l,m}^s = \frac{1}{N_{ph}} \sum_{i=1}^{N_{ph}} \begin{cases} \mathbf{I}',FW(\theta^{FW}, \phi^{FW}) & \text{if } \theta_l < \theta^{FW} < \theta_{l+1} \text{ and } \phi_m < \phi^{FW} < \phi_{m+1} \\ \mathbf{I}',BW(\theta^{BW}, \phi^{BW}) & \text{if } \theta_l < \theta^{BW} < \theta_{l+1} \text{ and } \phi_m < \phi^{BW} < \phi_{m+1} \\ 0 & \text{otherwise} \end{cases} \quad (\text{III.3.4})$$

where the superscript  $s$  indicates that the scattering splitting technique is used and  $\mathbf{I}',FW$  and  $\mathbf{I}',BW$  are computed as in Equation III.2.68 with  $q_{daw} = 1$ . In the results presented in this section, the scattering splitting angle has been set to either  $\theta_{split} = 30^\circ, 90^\circ$  or  $150^\circ$ . These three values are chosen for a comparison purpose, as one might expect variations in the obtained results depending on the scattering matrix of the scatterers and on this scattering splitting angle.

A corresponding Stokes vector can then computed analytically such as :

$$\mathbf{I}_{l,m}^t = \frac{1}{4\pi} \mathbf{F}(\theta_l) \mathbf{R}(\phi_m) \mathbf{I} \sin(\theta_l) \Delta\theta \Delta\phi \quad (\text{III.3.5})$$

where the superscript  $t$  indicates that this Stokes vector is tabulated using the analytical expression of the analytical expression of the Rayleigh scattering matrix. In the following, the Stokes vectors resulting from the Monte-Carlo calculation are referred to as the sampled Stokes vector, while those stemming from Equation III.3.5 are referred to as the tabulated Stokes vectors. When considering the first element of this Stokes vector, Equation III.3.5 becomes :

$$\begin{aligned} I_{l,m}^t &= \frac{1}{4\pi} [a_1(\theta_l)I + a_2(\theta_l) (Q \cos(2\phi_m) + U \sin(2\phi_m))] \sin(\theta_l) \Delta\theta \Delta\phi \\ &= f_{pol}(\theta_l, \phi_m) \sin(\theta_l) \Delta\theta \Delta\phi \end{aligned} \quad (\text{III.3.6})$$

Equation III.3.6 is then equivalent to the probability of scattering within the solid angle  $d\Omega = \sin(\theta_l) \Delta\theta \Delta\phi$  [24].

Figure III.10 presents the first element of the sampled Stokes vector, calculated using the stan-

standard angle sampling method, using the scattering splitting technique with three different splitting angles  $\theta_{split}$  and the first element of the tabulated Stokes vector. The incident light is considered linearly and horizontally polarized (*i.e.*  $\mathbf{I} = [1 \quad 1 \quad 0 \quad 0]^T$ ). These results have been averaged over the azimuthal angle.

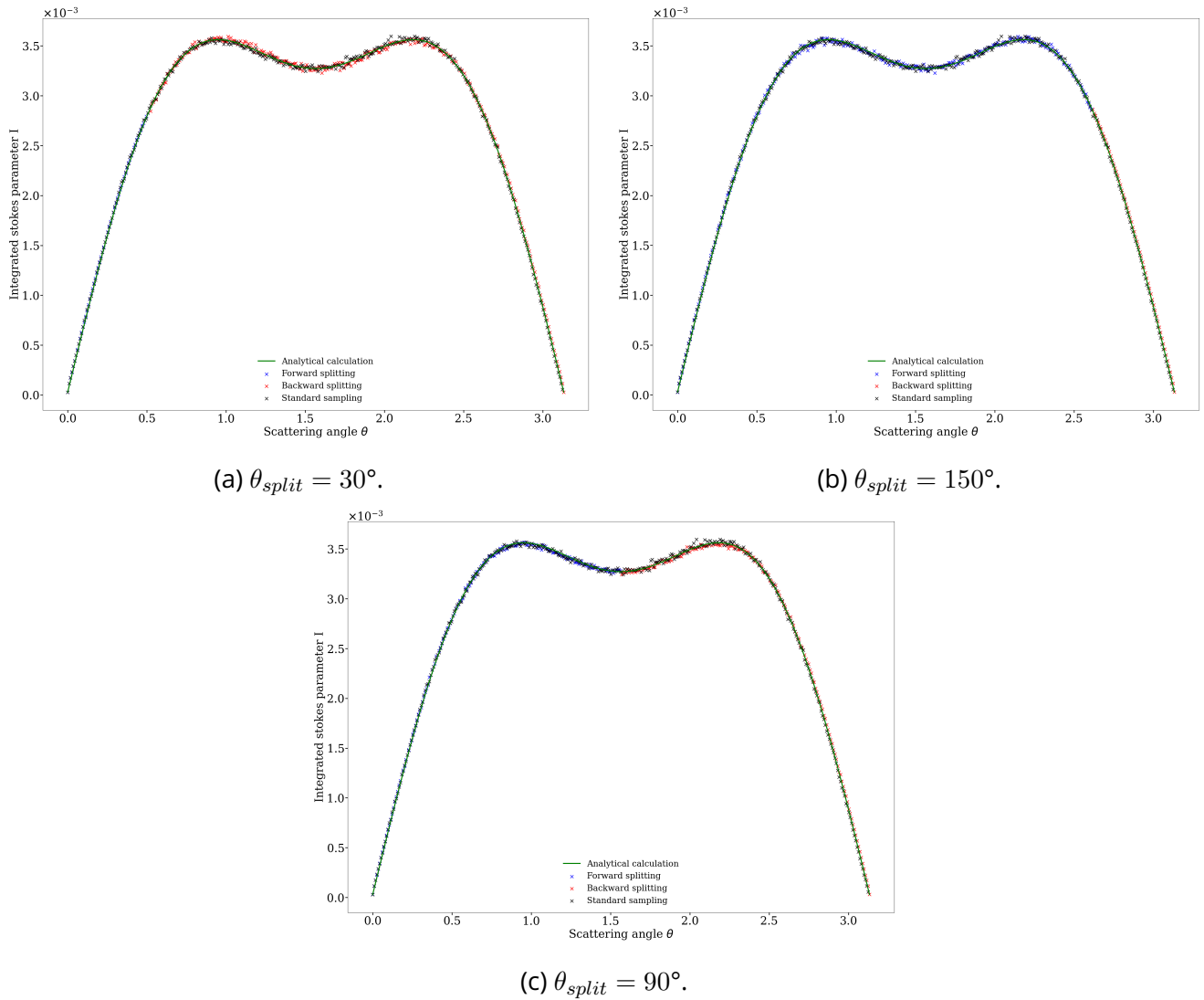


Figure III.10: First element of the Stokes vector scattered by Rayleigh scatterers and averaged over the azimuthal angles. Results are either calculated analytically (green line), using the standard angle sampling method (black crosses) or using the scattering splitting technique for different scattering splitting angles (blue and red crosses).

Overall, Figure III.10 shows that the results computed with either the standard sampling method or the scattering splitting technique are in good agreement with the tabulated counterpart. The use of the scattering splitting technique does not seem to improve the agreement between the

sampled values and the tabulated Stokes vector when averaged over the azimuthal angle. In order to investigate the influence of the azimuthal angle, the percent disagreement  $\kappa$  is defined as :

$$\kappa_\nu = 100 \frac{(\mathbf{I}^s)_\nu - (\mathbf{I}^t)_\nu}{|(\mathbf{I}^t)_\nu|} \quad (\text{III.3.7})$$

where the subscript  $\nu$  indicates which element of the Stokes vector is referred to, *i.e.*  $\nu = I, Q$ . When fully considering the azimuthal angle dependence, Figure III.11 present the values of tabulated first element of the Stokes vector  $I^t$ , which are used as the reference values in the computation of the percent disagreements. Figures III.12 present this percent disagreement when computed with the either the standard sampling technique or with the scattering splitting technique using the three different scattering splitting angles.

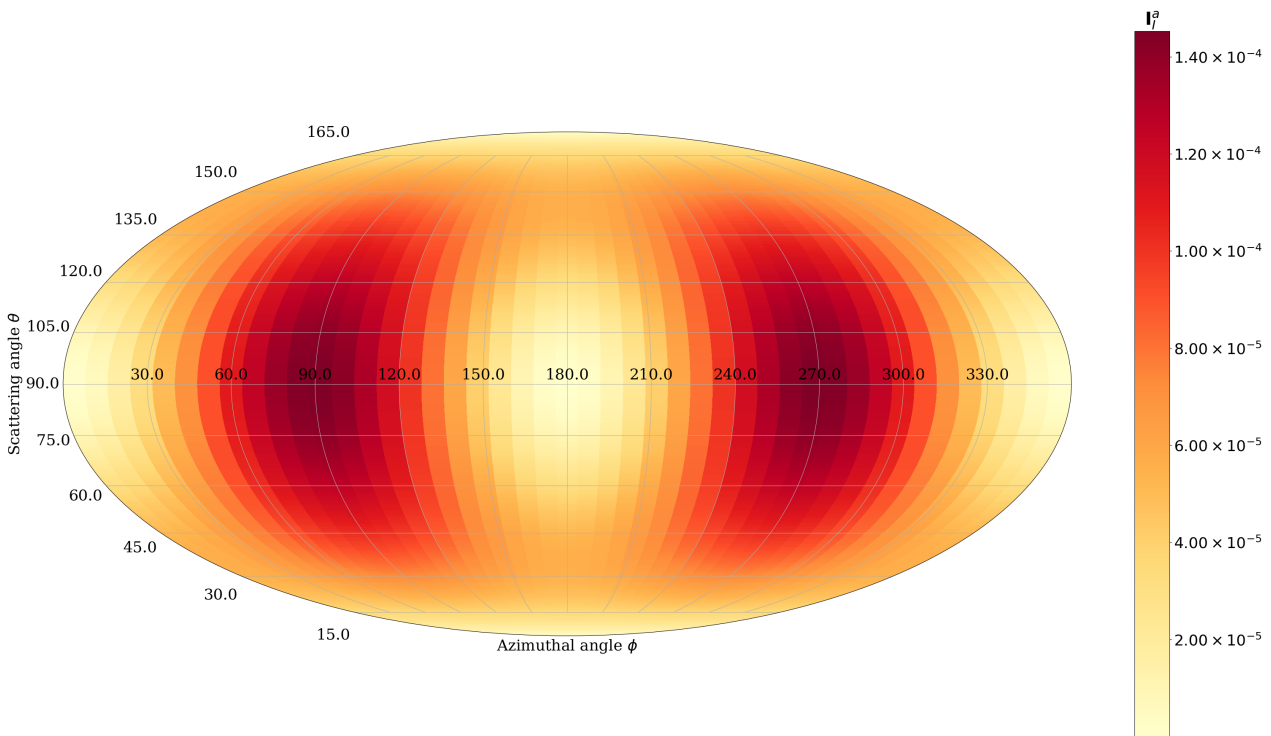


Figure III.11: First element of the tabulated Stokes vector scattered by Rayleigh scatterers as a function of the scattering angle  $\theta$  and of the azimuthal angle  $\phi$ . Results are computed for an azimuthal angle step of  $\Delta\phi = 4^\circ$  and a scattering angle step  $\Delta\theta = 0.5^\circ$ .

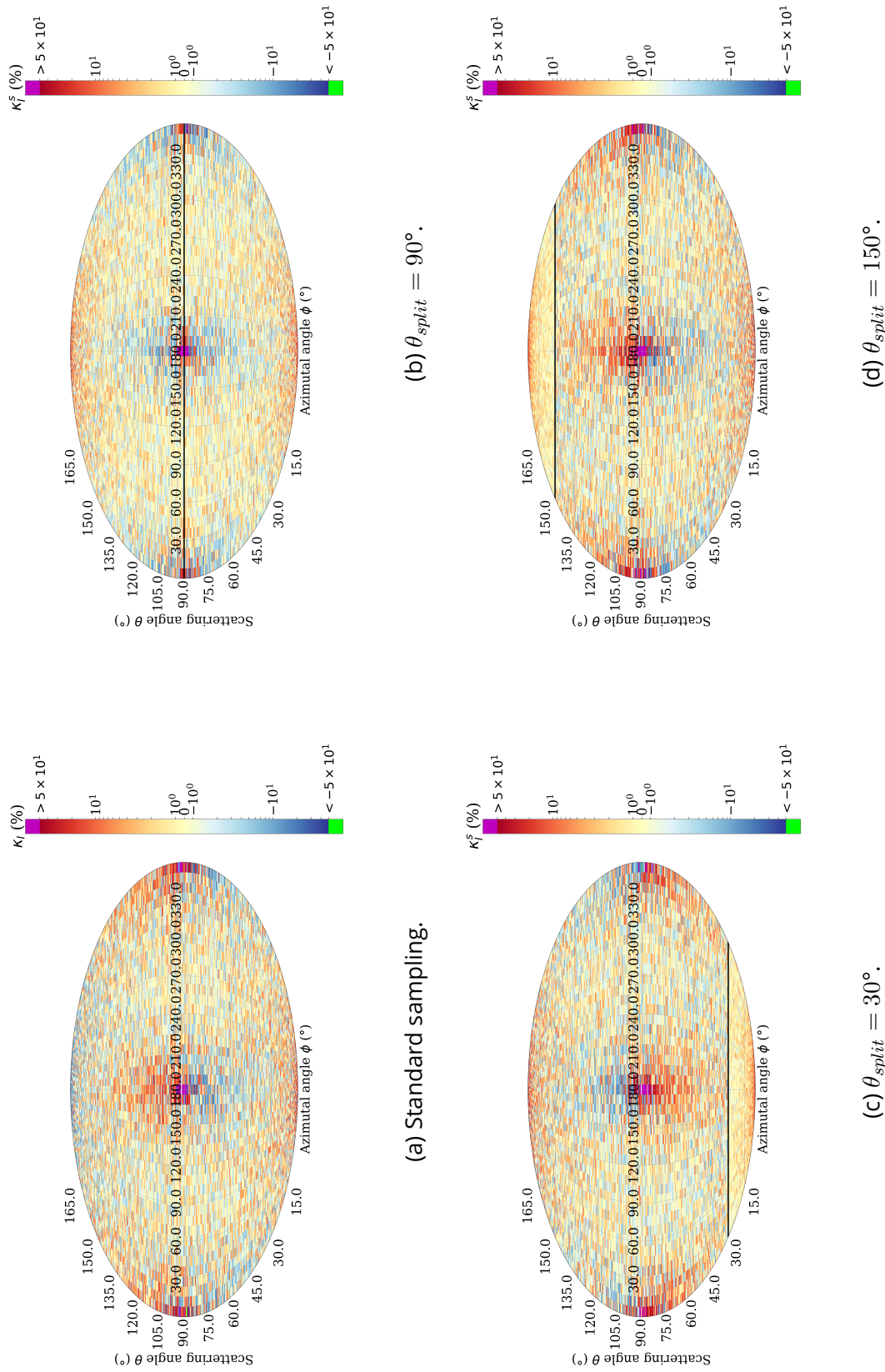


Figure III.12: Percent disagreements of the sampled first element of the Stokes vector scattered by Rayleigh scatterers as a function of the scattering angle  $\theta$  and of the azimuthal angle  $\phi$ . Results are computed for an azimuthal angle step of  $\Delta\phi = 4^\circ$  and a scattering angle step  $\Delta\theta = 0.5^\circ$ . The black lines on subfigures (b), (c) and (d) mark the scattering splitting angle.

Figure III.12 shows that larger discrepancies are present between the sampled values and the tabulated values when fully accounting for the azimuthal angle dependence. However, the use of the scattering splitting technique reduces the percent disagreement, as shown by comparing Figures III.12(b), (c) and (d) with Figure III.12(a). Better agreement is especially obtained within the smallest hemisphere such as when  $\theta < 30^\circ$  with  $\theta_{split} = 30^\circ$  (Subfigure III.12(c)) or when  $\theta > 150^\circ$  when  $\theta_{split} = 150^\circ$  (Subfigure III.12(d)). Several regions of these figures show particularly high values of the percent disagreement with  $|\kappa_I| > 50\%$ . Comparing with Figure III.11, it appears that these regions correspond to the values of the tabulated first element of the Stokes vector approaching  $I^t \approx 0$ . Hence, these larger discrepancies can be interpreted using Equation III.3.7, as small differences between the sampled and the tabulated values may result in large percent disagreements. The same comparison process can be applied to the second element of the scattered Stokes vector, and is presented on Figures III.13, III.14 and III.15.

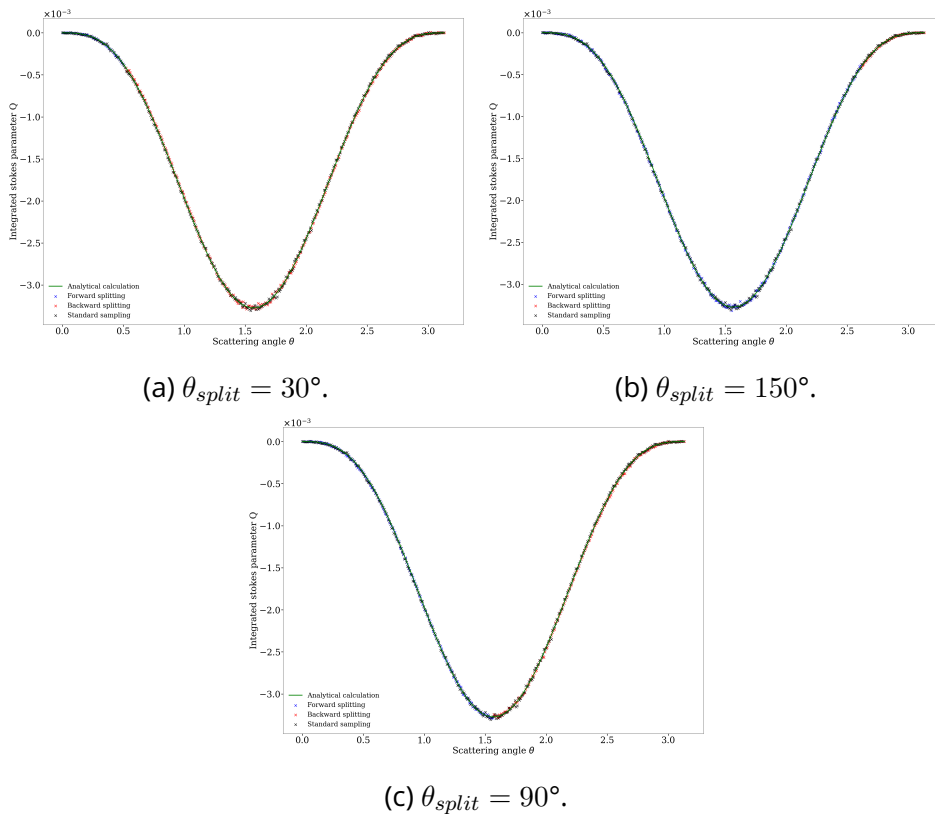


Figure III.13: Second element of the Stokes vector scattered by Rayleigh scatterers and averaged over the azimuthal angles. Results are either calculated analytically (green line), using the standard angle sampling method (black crosses) or using the scattering splitting technique for different scattering splitting angles (blue and red crosses).

Considering Figure III.13, the sampled values of the  $\phi$ -averaged second element of the Stokes vector also seem in agreement with the tabulated Stokes vector values. However, when considering the azimuthal angle dependence as in Figure III.15, larger discrepancies are observable. Indeed, these results present features that are similar to those presented in Figure III.12. As such, large percent disagreement are found in the regions where the second element of the tabulated Stokes vector is found close to 0 (see Figure III.14 for comparison), and the scattering splitting technique reduces the percent disagreement, especially in the smallest hemispheres when  $\theta_{split} \neq 90^\circ$ .

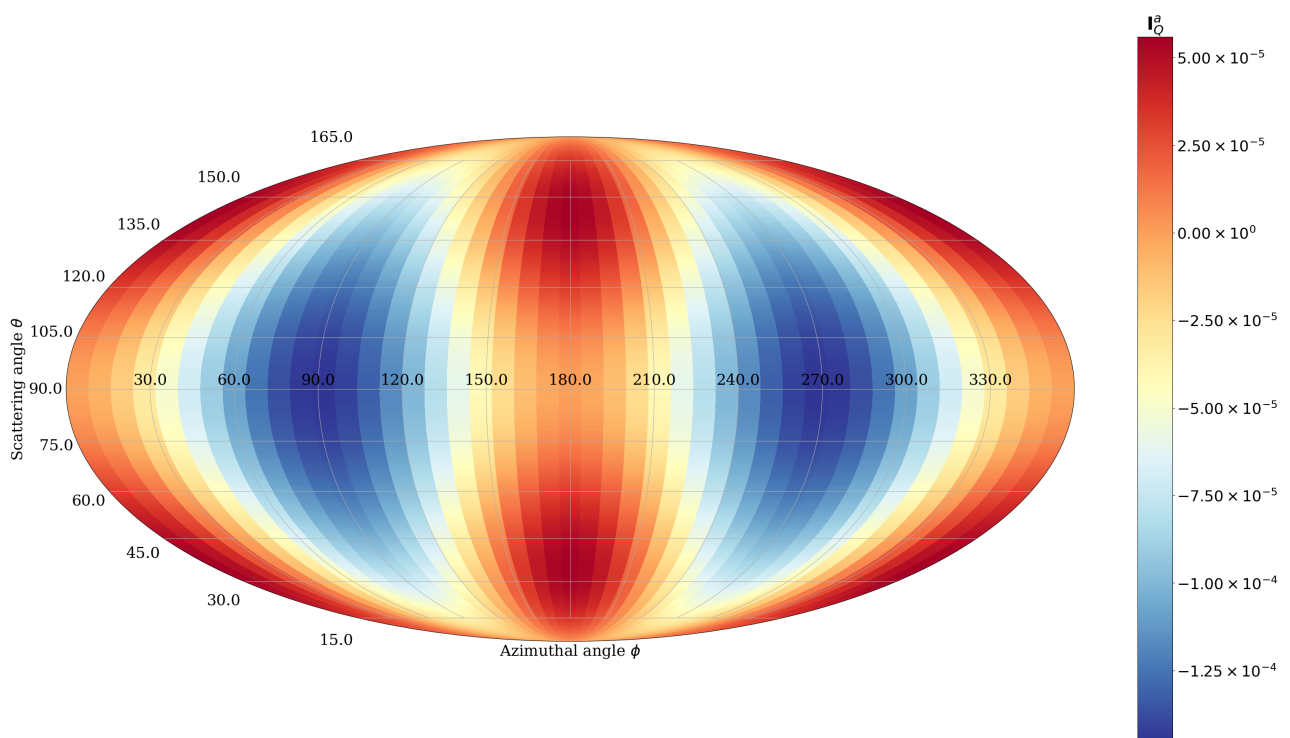
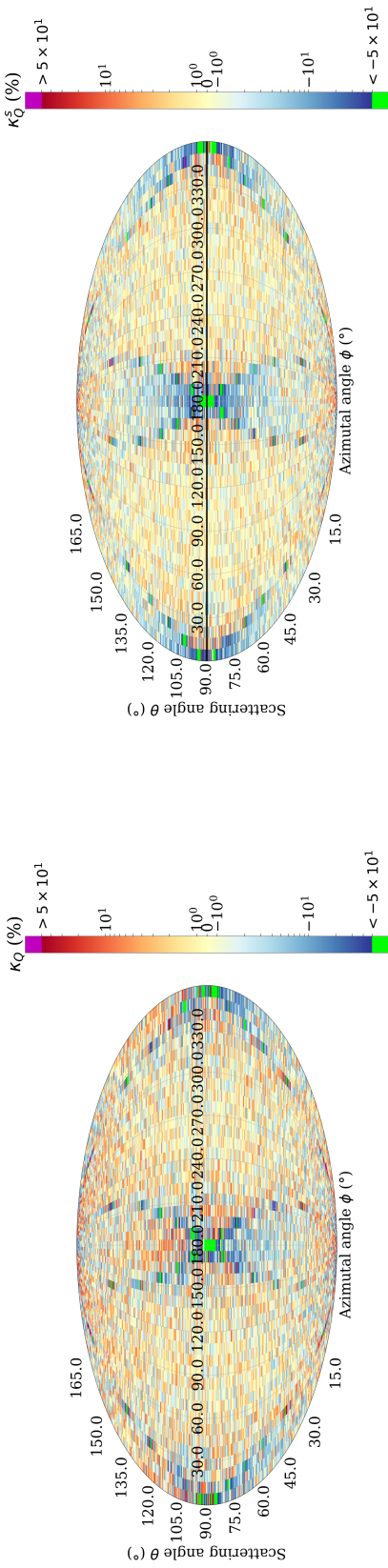
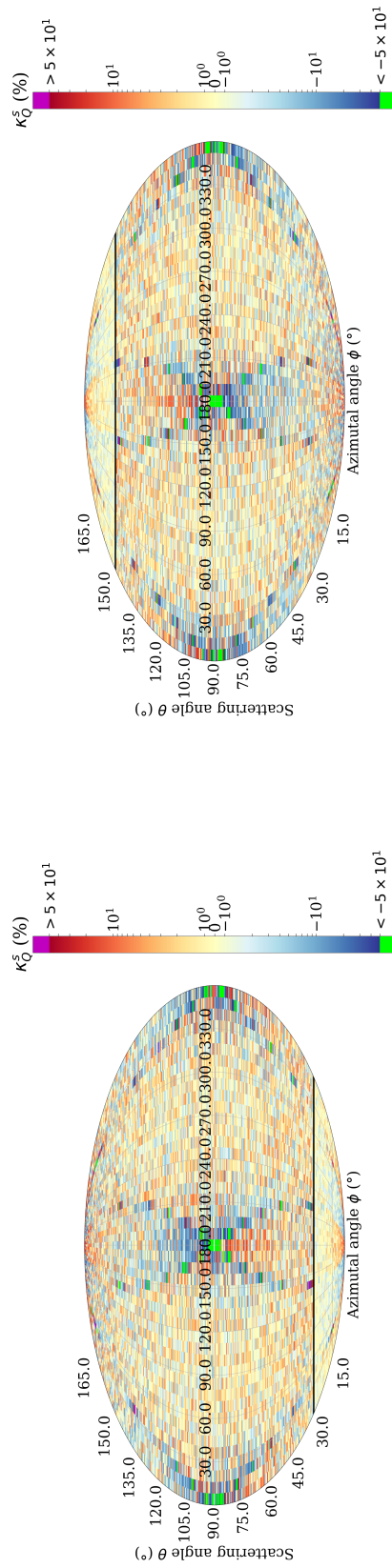


Figure III.14: Second element of the tabulated Stokes vector scattered by Rayleigh scatterers as a function of the scattering angle  $\theta$  and of the azimuthal angle  $\phi$ . Results are computed for an azimuthal angle step of  $\Delta\phi = 4^\circ$  and a scattering angle step  $\Delta\theta = 0.5^\circ$ .



(a) Standard sampling.

(b)  $\theta_{split} = 90^\circ$ .



(c)  $\theta_{split} = 30^\circ$ .

(d)  $\theta_{split} = 150^\circ$ .

Figure III.15: Percent disagreements of the sampled second element of the Stokes vector scattered by Rayleigh scatterers as a function of the scattering angle  $\theta$  and of the azimuthal angle  $\phi$ . Results are computed for an azimuthal angle step of  $\Delta\phi = 4^\circ$  and a scattering angle step  $\Delta\theta = 0.5^\circ$ . The black lines on subfigures (b), (c) and (d) mark the scattering splitting angle.

This comparison procedure is now applied to the second case, using the scattering matrix of the spherical particle distribution described at the beginning of this subsection. Results are presented on Figures III.16, III.17 and III.18 when considering the first element of the Stokes vector.

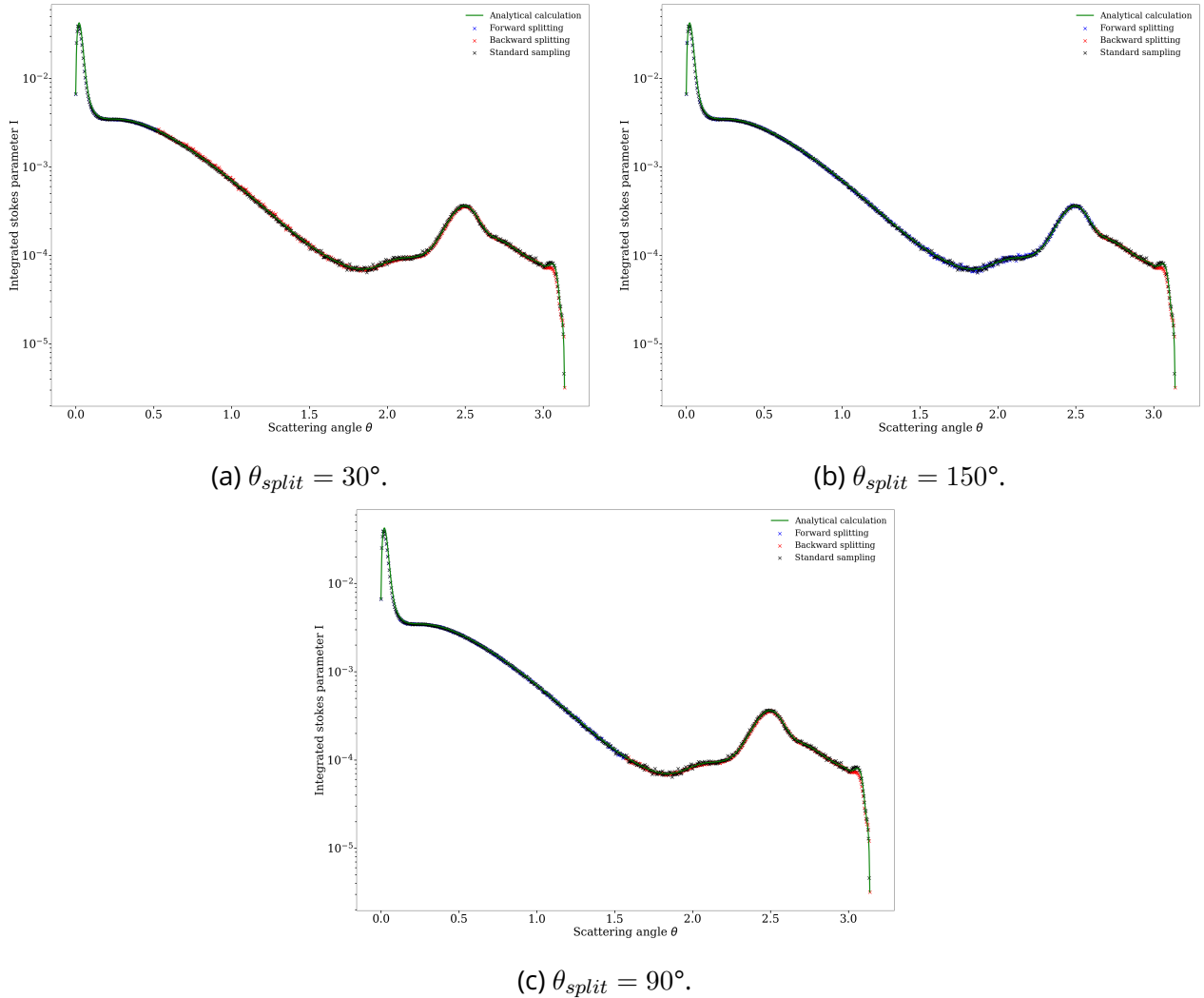
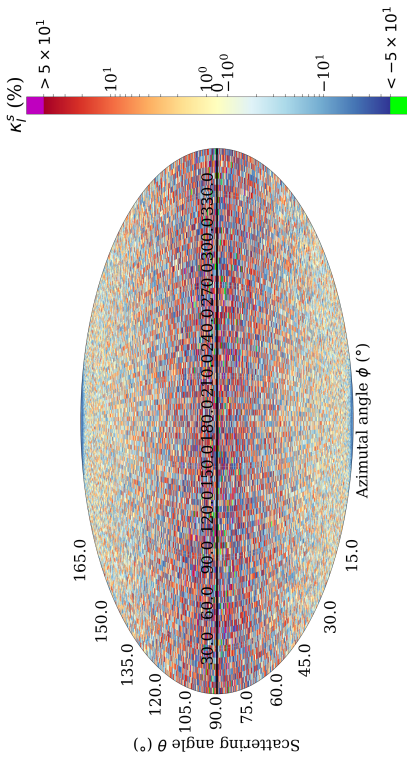
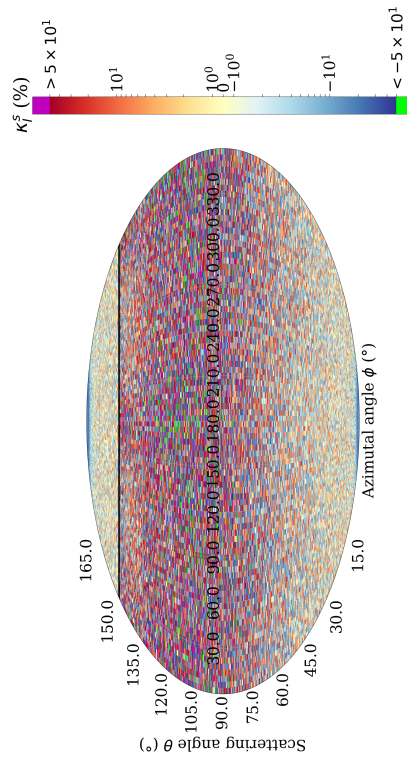


Figure III.16: First element of the Stokes vector scattered by spherical particles and averaged over the azimuthal angles. Results are either calculated analytically (green line), using the standard angle sampling method (black crosses) or using the scattering splitting technique for different scattering splitting angles (blue and red crosses).



(a) Standard sampling.

(b)  $\theta_{split} = 90^\circ$ .



(c)  $\theta_{split} = 30^\circ$ .

(d)  $\theta_{split} = 150^\circ$ .

Figure III.17: Percent disagreements of the sampled first element of the Stokes vector scattered by spherical particles as a function of the scattering angle  $\theta$  and of the azimuthal angle  $\phi$ . Results are computed for an azimuthal angle step of  $\Delta\phi = 2^\circ$  and a scattering angle step  $\Delta\theta = 0.25^\circ$ . The black lines on subfigures (b), (c) and (d) mark the scattering splitting angle.

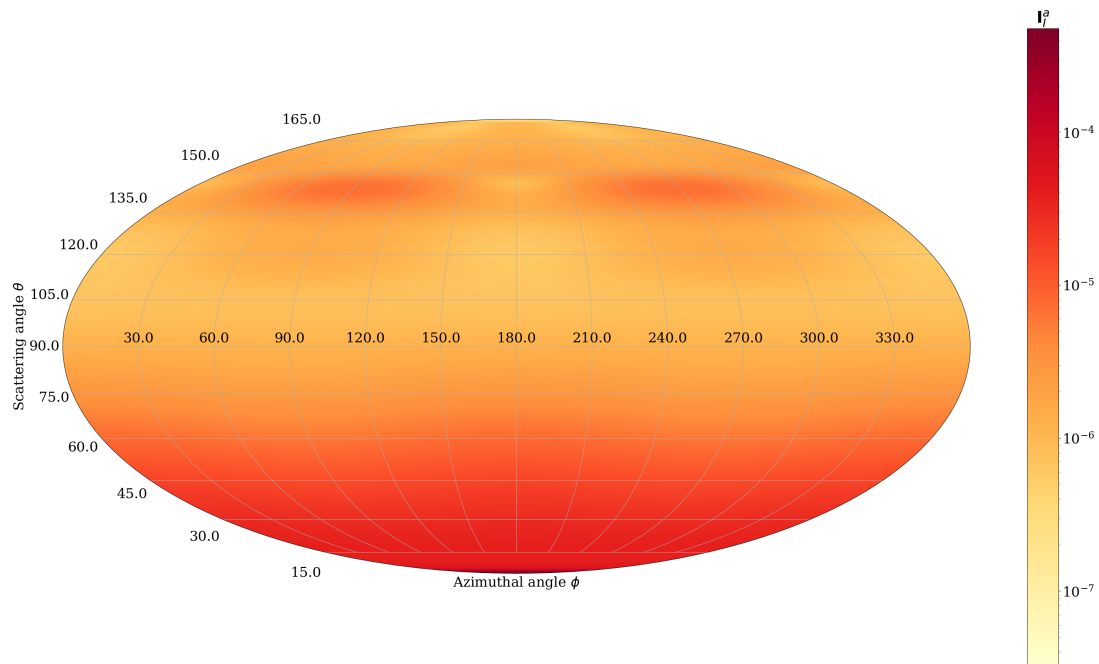


Figure III.18: First element of the tabulated Stokes vector scattered by spherical particles as a function of the scattering angle  $\theta$  and of the azimuthal angle  $\phi$ . Results are computed for an azimuthal angle step of  $\Delta\phi = 2^\circ$  and a scattering angle step  $\Delta\theta = 0.25^\circ$ .

As in the Rayleigh scatterers case, good agreement is found when considering the  $\phi$ -averaged first element of the Stokes vector as shown on Figure III.16. However, the sampling of the backward splitted photon seems slightly under-evaluated at  $\theta \approx 3.1$  rad, near the exact-backscattering direction. This under-evaluation is most likely due to the scattering splitting method for the backward photons, and to the computation of the associated weight as expressed in Section III.2.6 and Equation III.2.67. This weight computation has indeed a larger number of sources of error, which can arise from the computation of the integrated quantities  $(\overline{a_1})^{BW}$ ,  $(\overline{b_1})^{BW}$  and  $\overline{b_1}$  or from the linear interpolation used for the computation of the scattering matrix elements in the last fractional term of this equation.

Now considering the percent disagreement, it appears that this parameter increases rapidly when increasing the scattering angle in the standard sampling case, as seen in Figure III.17(a). Comparing with Figure III.18, this behavior can be interpreted by the rapidly decreasing values of the first element of the tabulated Stokes vector. Indeed, in contrast with Rayleigh scatterers, the scattering pattern of spherical particles present a large forward peak, which induce an under-

sampling of the large scattering angles. However, the scattering splitting technique improves the agreement between the sampled and tabulated values, as seen on Figures III.17(b), (c) and (d). This behavior can be interpreted by the method used to sample scattering angles when using the scattering splitting technique. As described in Section III.2.6, the scattering angle is first sampled within the forward hemisphere before being transferred to the backward hemisphere. Because a large forward peak is present, a larger number of photons are sampled in the near-backscattering region, hence reducing the percent disagreement. Finally, the second element of the Stokes vector is considered, and the corresponding results are presented on Figures III.19, III.20 and III.21.

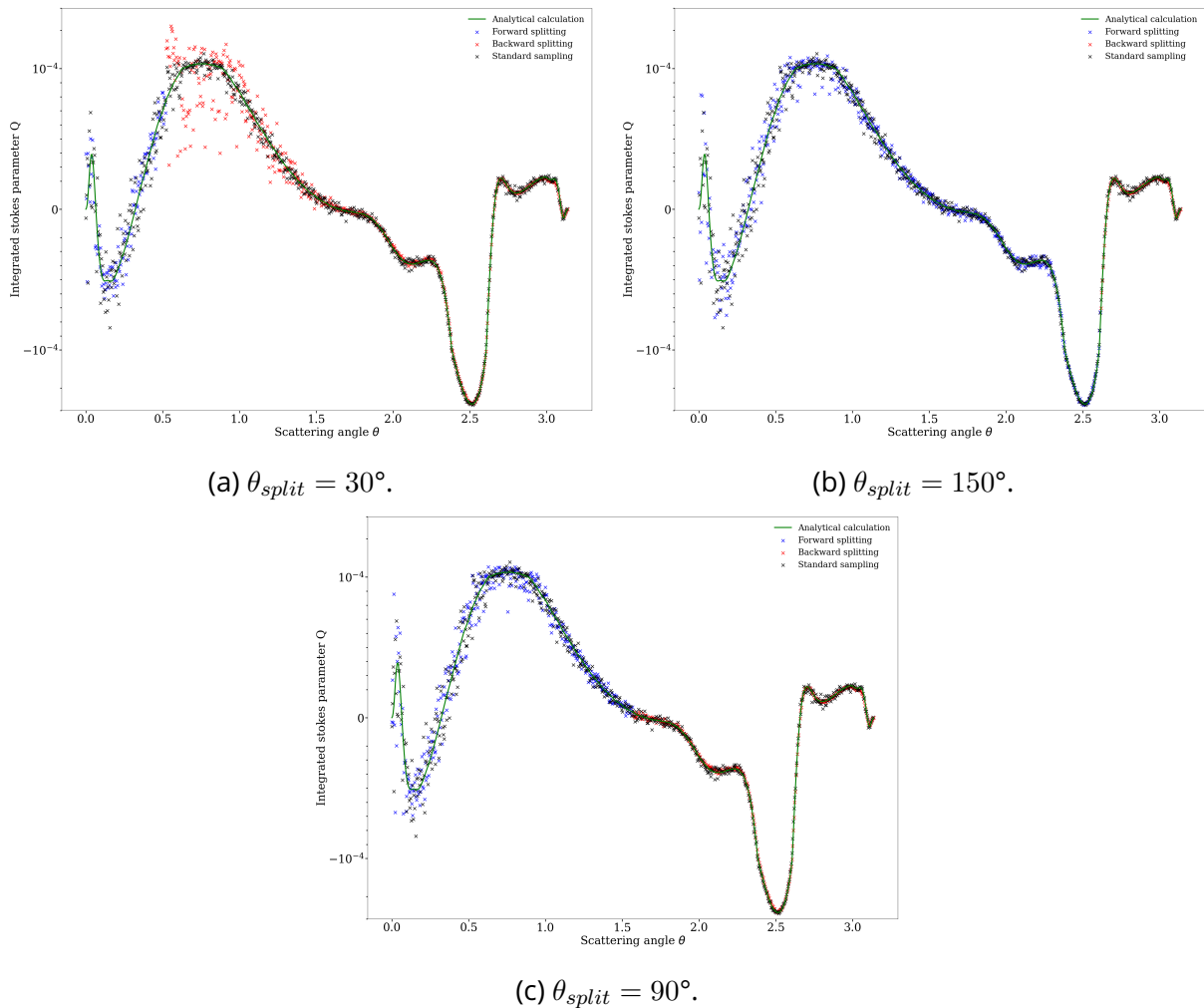


Figure III.19: Second element of the sampled Stokes vector scattered by spherical particles and averaged over the azimuthal angles. Results are either calculated analytically (green line), using the standard angle sampling method (black crosses) or using the scattering splitting technique for different scattering splitting angles (blue and red crosses).

Figure III.19 shows a good agreement between the sampled  $\phi$ -averaged second elements of the Stokes vector for scattering angles larger than  $\theta \approx \pi/2$ , but rather poor agreement in the forward direction, especially for the backward splitted photons when the scattering splitting technique is applied with  $\theta_{split} = 30^\circ$  (see Subfigure III.19(a)). However, the source of these discrepancies is rather easily identifiable. Indeed, according to Equation III.2.68 and considering unit weights, the second element of the Stokes vector is computed as :

$$Q^{sca} = \frac{b_1(\theta)I + a_2(\theta)Q \cos(2\phi)}{a_1(\theta) + \gamma(\phi)b_1(\theta)} \quad (III.3.8)$$

In the equation above, it appears that the range of values of  $Q^{sca}$  potentially being sampled at one scattering angle  $\theta$  for different azimuthal angles  $\phi$  depends on the relative differences between  $|b_1(\theta)|$  and  $|a_2(\theta)|$ . If  $|a_2(\theta)| \gg |b_1(\theta)|$  and  $|a_1(\theta)| \gg |b_1(\theta)|$ , then Equation III.3.8 can be approximated as :

$$Q^{sca} \approx \frac{a_2(\theta)}{a_1(\theta)} Q \cos(2\phi) \quad (III.3.9)$$

This results in an unstable summation of the second elements of the scattered Stokes vector, especially when considering the low scattering angle step that has been considered. These two conditions (*i.e.*  $|a_2(\theta)| \gg |b_1(\theta)|$  and  $|a_1(\theta)| \gg |b_1(\theta)|$ ) are verified in the forward hemisphere when considering the spherical particles distribution but are not when considering the Rayleigh scatterers. This  $\cos(2\phi)$  dependence can also be observed on Figure III.20, where the forward hemisphere follows this dependence while the backward hemisphere does not. Moreover, the second elements of the Stokes vector for the forward scattered photon when  $\theta_{split} = 30^\circ$  appear in better agreement than those sampled with the standard angle sampling method. This is most likely due to the larger number of photons being sampled within the range  $\theta \in [0, \theta_{split}]$ .

The larger discrepancies of the sampled backward photon  $\phi$ -averaged parameter  $Q$  can also be explained by considering the probability of a photon being sampled in this region. Indeed, as described in Section III.2.6, the scattering angle is first sampled within the range  $\theta \in [0, \pi - \theta_{split}]$  before being transformed into the range  $\theta \in [\theta_{split}, \pi]$ . This implies that the probability of a backward photon being scattered at the angle  $\theta$  is actually the probability of it being scattered at

the angle  $\pi - \theta$ . Because the phase function of the spherical particles presents a large forward peak, this implies that the probability of a backward photon being scattered at an angle close to  $\theta_{split}$  is rather low. Combined with the interpretation for the instability in the forward hemisphere described above, this under-sampling of backward photons close to  $\theta_{split}$  results in even larger discrepancies.

Finally, when considering the azimuthal angle dependence, Figure III.21 presents the same features as Figure III.17. Indeed, the percent disagreement increases when the values of the tabulated second element of the Stokes vector approach 0. Moreover, smaller percent disagreements are found when the scattering splitting technique is applied. However, comparing Subfigure III.21(c) with Subfigure III.21(a), it also appears that larger discrepancies are present at angles  $\theta \approx \theta_{split}$  in the backward hemisphere when using the scattering splitting angle with  $\theta_{split} = 30^\circ$ . This behavior can also be explained following the previously detailed interpretation of the disagreement between the  $\phi$ -averaged values shown on Figure III.19(a).

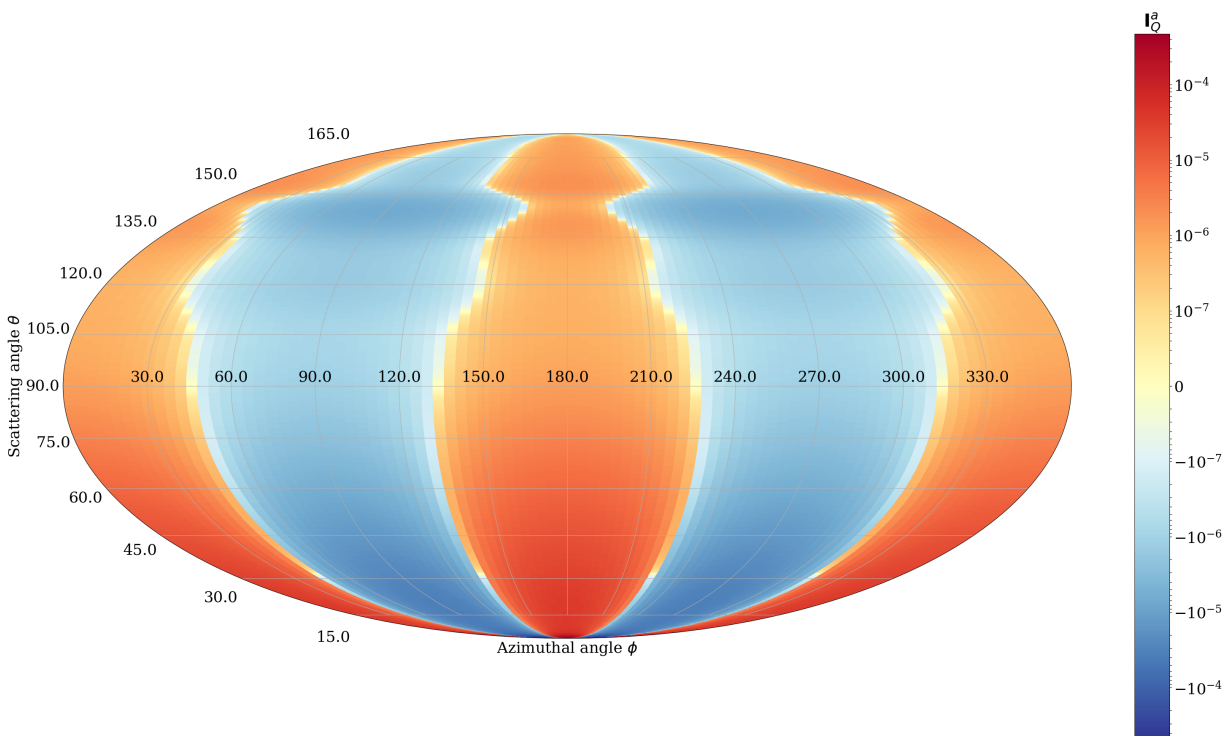


Figure III.20: Second element of the tabulated Stokes vector scattered by spherical particles as a function of the scattering angle  $\theta$  and of the azimuthal angle  $\phi$ . Results are computed for an azimuthal angle step of  $\Delta\phi = 2^\circ$  and a scattering angle step  $\Delta\theta = 0.25^\circ$ .

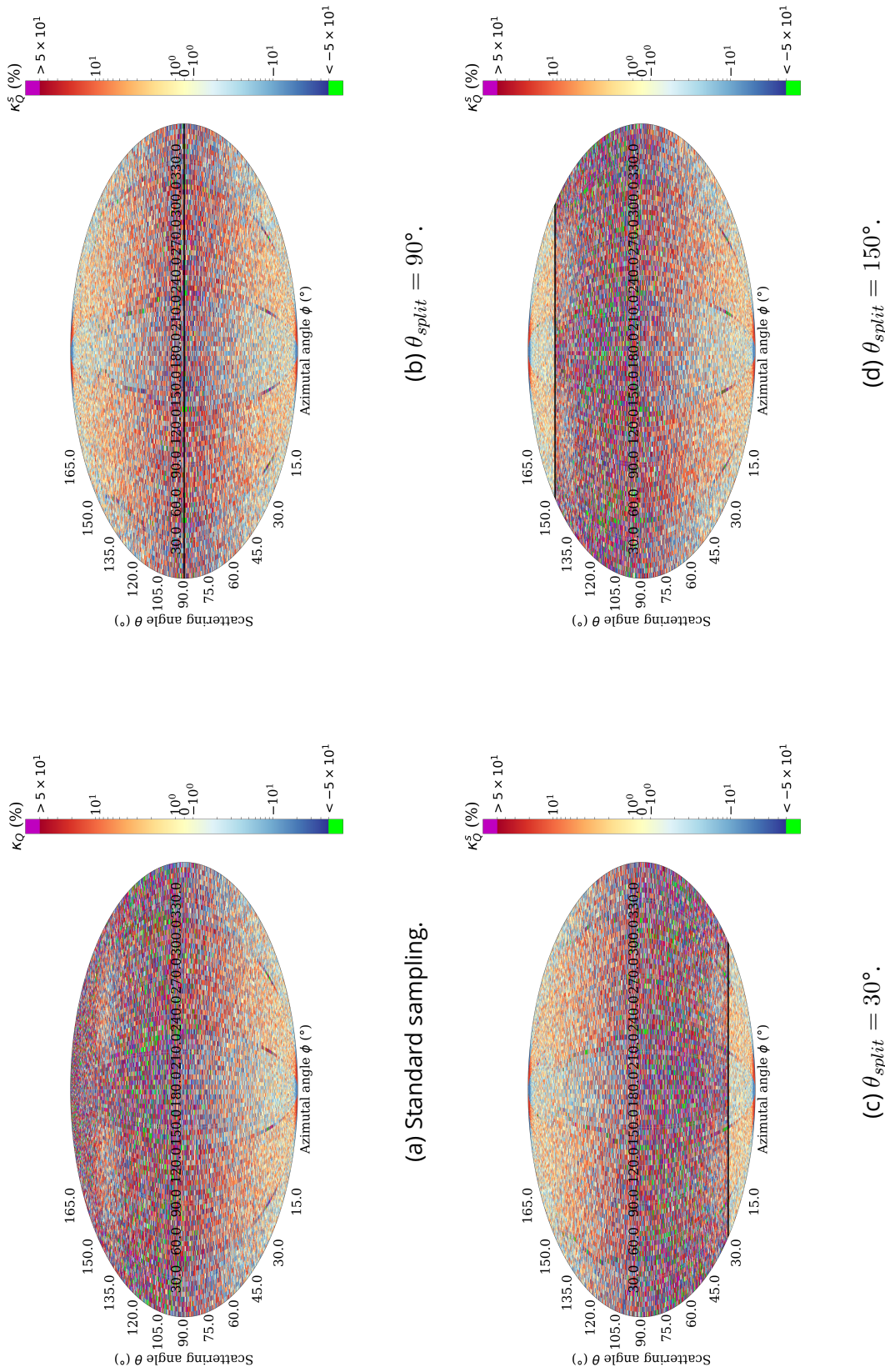


Figure III.21: Percent disagreements of the sampled second element of the Stokes vector scattered by spherical particles as a function of the scattering angle  $\theta$  and of the azimuthal angle  $\phi$ . Results are computed for an azimuthal angle step of  $\Delta\phi = 2^\circ$  and a scattering angle step  $\Delta\theta = 0.25^\circ$ . The black lines on subfigures (b), (c) and (d) mark the scattering splitting angle.

Overall, both the standard angle sampling method and the scattering splitting technique result in a good agreement with the tabulated Stokes vector when considering  $\phi$ -average values. The scattering splitting technique also allows to reduce the discrepancies when considering the azimuthal angle dependent quantities. However, care must be taken when choosing the scattering splitting angle, as it can result in larger instabilities depending on the scattering matrix of the considered particles. Indeed, in the simulations undertaken in this section, it appears that the angle  $\theta_{split} = 30^\circ$  is particularly ill-suited as it induces larger errors at scattering angles near  $\theta \approx \theta_{split}$ .

### III.3.2 Comparison with the single scattering lidar equation

In this subsection, the output signal of the Monte-Carlo program at first order of scattering is compared with the analytical expression of the lidar signal in the single scattering approximation. This analytical expression, described in Equation I.3.2, is slightly modified in order to only consider the terms that are accounted for in the Monte-Carlo lidar signal simulation program. As such, in this section, the analytical single scattering lidar signal is expressed as :

$$I(r, \lambda) = \frac{A}{r^2} \beta(r, \lambda) \exp \left( -2 \int_{r_b}^r \alpha(r', \lambda) dr' \right) \quad (\text{III.3.10})$$

where  $r_b$  is the distance between the cloud base and the receiver. This expression of the lidar signal is compared with the output signal obtained using the Monte-Carlo program, while only considering the first order of scattering. Two cases are considered for the simulation of the scattering medium. The first is identical to the spherical particles case of the previous subsection, and corresponds to the "Case 1" from the reference [176]. As such, the scattering medium is composed of three slabs. The second slab radiative properties are computed following the method described in Section III.3.1 and in reference [176], and the slab lower boundary is located at 700 km from the receiver. The cloud geometric thickness is  $H_c = 1$  km, and the optical depth between its lower boundary and its upper boundary is  $\tau = 20$ . The first and last slabs are simulated as a non-interacting medium, with a null optical depth.

The second considered case also stems from the reference [176], and is meant to reproduce

the "Case 12" of this reference. The methodology used for the computation of the radiative properties of the scattering medium is the same as in the previous subsection. As such, Equation III.3.2 is used in order to compute the size distribution of the particles, using  $R_{eff} = 3 \mu\text{m}$  and  $\gamma_r = 6$ , and the radiative properties are then computed at each radius step and averaged appropriately. Three slabs also compose the scattering medium, the first and last slabs preventing any interaction. However in this case, the lower boundary of the second slab is placed at a distance of 700 m of the receiver, with a cloud geometric thickness of  $H_c = 1 \text{ km}$ . The optical depth of this second slab is  $\tau = 10$ .

These two cases allow to compare results when considering two different scattering media. Moreover, the first case aims to simulate a geometry relevant to space-based lidar systems, the scattering medium being situated at 700 km from the instrument. In contrast, the distance from the scattering medium to the instrument in the second case is more relevant to ground-based lidar systems. In these two cases, the receiver radius has been set to  $R_{rec} = \sqrt{1 \cdot 10^{-6} / \pi} \text{ km}$ , so that the receiver area is equal to  $A = 1 \text{ m}^2$ . The emitter divergence is set to  $\theta_{em} = 0.02 \text{ mrad}$  and its collimator aperture to  $R_{em} = 1.5 \text{ mm}$ . These last two quantities are parametrized as such in order to ensure that all emitted photons are within the receiver FOV during the computation of the first order of scattering. Because the pulse length is not accounted for in Equation III.3.10, two values of the length of the emitted pulse are used, *i.e.* either  $L_{em} = 12 \text{ m}$  or  $L_{em} = 1 \text{ mm}$ . The results obtained with the first and second size distributions are presented on Figures III.22 and III.23 respectively. Subfigures on the left-hand side correspond to the pulse length  $L_{em} = 12 \text{ m}$  while those on the right-hand side correspond to the pulse length  $L_{em} = 1 \text{ mm}$ . The path length step  $\Delta t$  for the output signal computation is set to  $\Delta t = 10 \text{ m}$ , so that the range step on the presented figures is  $\Delta r = 5 \text{ m}$ .  $N_{ph} = 1 \cdot 10^8$  primary photons are emitted.

Overall, Figures III.22 and III.23 show a good agreement between Monte-Carlo results and the analytical expression from Equation III.3.10. The effect of the pulse length  $L_{em}$  can be observed by comparing the left-hand side subfigures with the right-hand side subfigures. Indeed, when  $L_{em} = 12 \text{ m}$  (left subfigures), the Monte-Carlo signal shows at first an increase of the signal that is not accounted for in the analytical calculations and that is not present for  $L_{em} = 1 \text{ mm}$ . Consider-

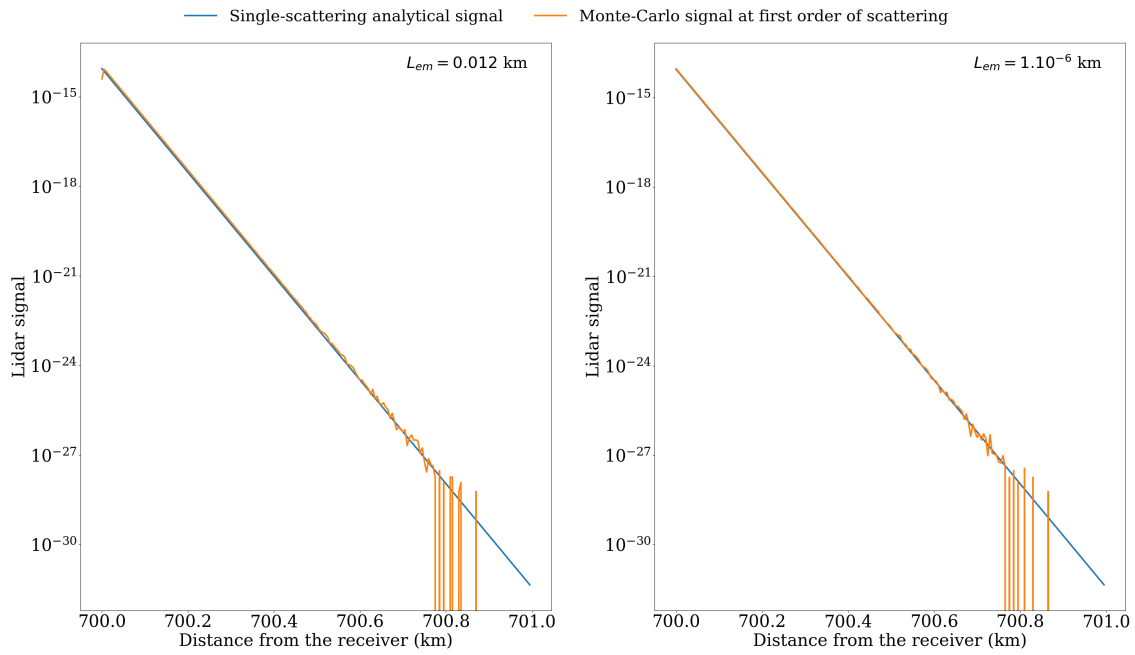


Figure III.22: First case of validation between the output signal of the Monte-Carlo program at first order of scattering and the single scattering lidar equation.

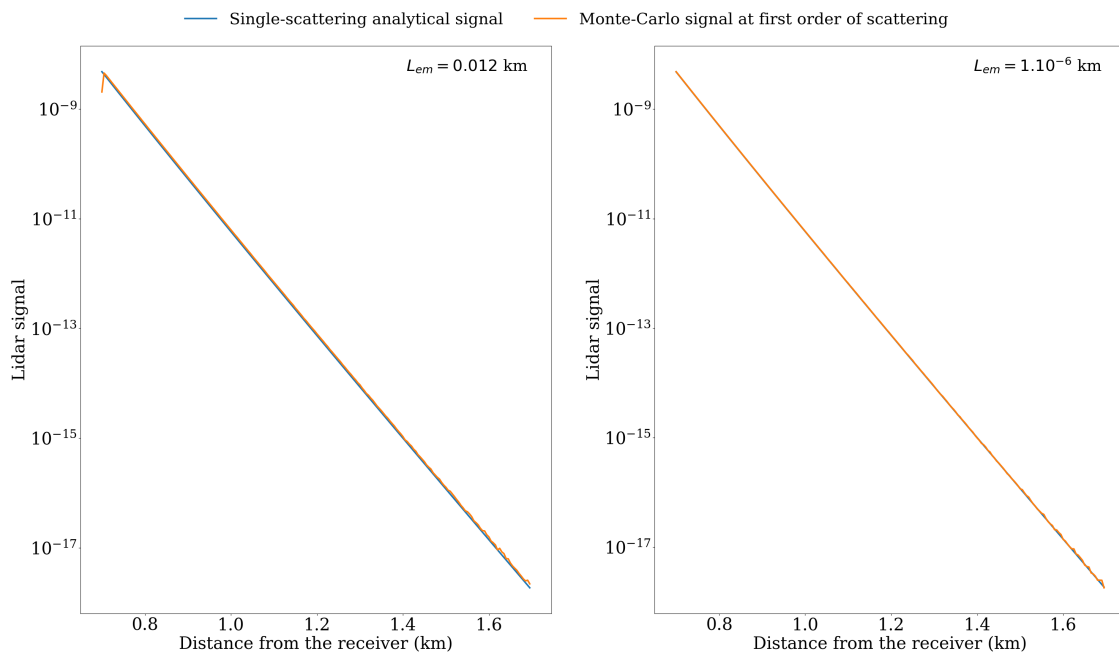


Figure III.23: Second case of validation between the output signal of the Monte-Carlo program at first order of scattering and the single scattering lidar equation.

ing Equation III.2.5 and that  $L_{em} > \Delta t$ , this feature can be explained by the fact that some of the primary photons are initialized with a path length  $\Delta_i > \Delta t$ . However, all of these photon positions

are still initialized on the emitter disc. Hence, some of these photons that should be contributing to the bin corresponding to the lower boundary of the scattering medium are actually contributing to the next bin. This induces an underestimation of the first bin and an overestimation of the following bins. This effect is suppressed by reducing the pulse length, as presented on the right-hand subfigures, which show a better agreement with the analytical computations.

Considering Figure III.22, it can be observed that the agreement progressively deteriorates with increasing distance from the receiver, until some discontinuities appear. The same deterioration can be observed on Figure III.23 to a lesser degree. This effect can be explained by the rather large optical depths that are considered in these simulations (*i.e.*  $\tau = 20$  for Figure III.22 and  $\tau = 10$  for Figure III.23). As described in Subsection III.2.2, the transport length of the photons is driven by the extinction properties of the medium, and consequently by its optical depth. Hence, for large optical depths, very few photons are transported in the outer regions of the scattering medium, inducing an instability of the output signal and eventually discontinuities. Nevertheless, when considering the distance range corresponding to optical depth  $\tau < 7 - 10$  with  $L_{em} = 1$  mm, the relative error between the Monte-Carlo results and the analytical expression is found to be less than 7%.

### III.3.3 Inter-comparison with available data from the literature

This section presents a direct comparison between the results presented in reference [176] and those obtained with the code previously described. Hence, the radiative properties and lidar geometry for twelve of the fourteen cases of reference [176] are simulated, and an attempt to reproduce the results is made. The two missing cases correspond to the cases 8 and 9. Indeed, these two cases simulate broken clouds that are not accounted for in the program presented here. Table III.6 presents the varying parameters between the different cases (which is a reproduction of Table 1 of reference [176]), while Table III.7 presents the parameters that are kept constant for all the simulations. Note that some cases stemming from this reference have already been used in the previous section. As such, the radiative properties of the scattering medium are computed following the same method as the one referring to spherical particles described in Subsection

## III.3.1.

Case	Wavelength $\lambda$ (nm)	Cloud base/ receiver distance $r_b$ (km)	$R_e$ ( $\mu\text{m}$ )	$\gamma$	$\tau$	$\theta_{rec}$ (mrad)
1	532	700	4	6	20	0.13
2	532	700	8	16	8	0.13
3	532	700	8	6	8	0.13
4	1064	700	8	6	8	0.13
5	1064	700	4	25	8	0.13
6	532	700	4	6	8	1.3
7	532	700	4	6	8	0.04
10	1064	0.7	4	6	8	12
11	532	0.7	8	6	16	12
12	532	0.7	3	6	10	16
13	532	0.7	8	6	16	0.5
14	1064	0.7	4	6	8	6

Table III.6: Variable parameters between the different simulated cases. This table is a reproduction of Table 1 of reference [176].

$\theta_{em}$ (mrad)	$R_{em}$ (cm)	$L_{em}$ (m)	$\mathbf{I}_{em}$	$R_{rec}$ (m)	$\Delta t$ (m)	$N_{ph}$	$\theta_{split}$ ( $^\circ$ )	$\zeta$ ( $^\circ$ )	$\theta_{cone}$ (mrad)	$R_{cone}$ (cm)	$j_{max}$
0.02	1.5	12	$[1 \ 1 \ 0 \ 0]^T$	$\sqrt{1/\pi}$	10	$1.10^8$	90	90	$1.05\theta_{rec}$	1.5	10

Table III.7: Constant parameters for all the simulations.

The article from Hu et al. [176] introduces two quantities; (i) the accumulated single scattering fraction  $A_S(r)$  and (ii) the accumulated depolarization ratio  $\delta_{acc}(r)$ . The former is expressed as :

$$A_S(r) = \frac{\int_{r_b}^r I(r', 1) dr'}{\int_{r_b}^r I(r') dr'} \quad (\text{III.3.11})$$

where  $I(r', 1)$  is the output contribution of the first element of the Stokes vector at first order of scattering, and  $I(r')$  is the total contribution of the first element of the Stokes vector (see Equations (III.2.71(a) and (b))). The accumulated depolarization ratio is computed as :

$$\delta_{acc}(r) = \frac{\int_{r_b}^r (I(r') - Q(r')) dr'}{\int_{r_b}^r (I(r') + Q(r')) dr'} \quad (\text{III.3.12})$$

In reference [176], a functional relationship is found between these two quantities. This rela-

relationship is expressed as :

$$A_s = 0.999 - 3.906\delta_{acc} + 6.263\delta_{acc}^2 - 3.554\delta_{acc}^3 \quad (\text{III.3.13})$$

Within reference [176], it is stated that hundreds of scenarios were modeled with extinction coefficients ranging from  $\alpha = 1 \text{ km}^{-1}$  to  $\alpha = 100 \text{ km}^{-1}$ , with a cloud geometric thickness ranging from  $H_c = 0.2 \text{ km}$  to  $H_c = 1 \text{ km}$ . In the simulations undertaken in this thesis, only clouds with geometric thickness of either  $H_c = 1 \text{ km}$  or  $H_c = 0.2 \text{ km}$  have been considered. Because the modeled interacting medium consists of only one homogeneous slab, the extinction coefficients are parametrized such as  $\alpha = \tau/H_c$ .

Figures III.24 present the accumulated single scattering fraction as a function of the accumulated depolarization ratio for the cases 1 through 7 and 10 through 14 respectively. Moreover, Tables III.8 and III.9 present the root mean square error (RMSE) between the simulation results and Equation III.3.13.

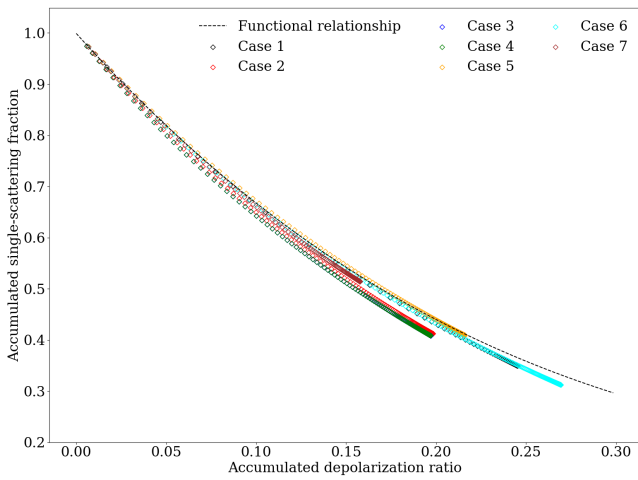
Case	1	2	3	4	5	6	7	10	11	12	13	14
RMSE	0.073	0.076	0.078	0.078	0.071	0.073	0.071	0.077	0.084	0.074	0.104	0.084

Table III.8: Root mean square error of the simulations with geometric thickness  $H_c = 1.0 \text{ km}$ .

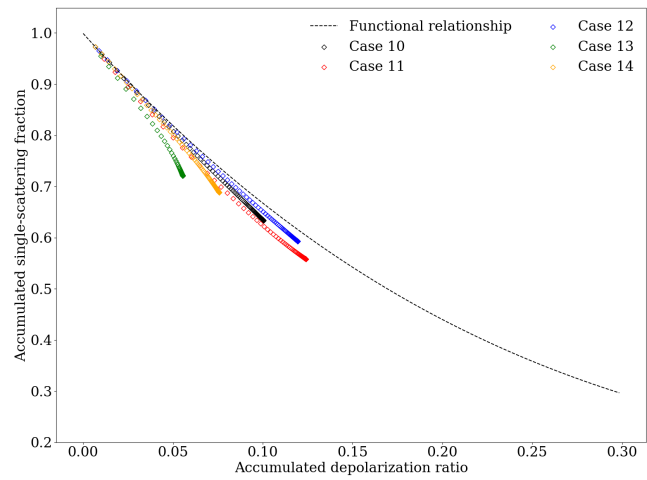
Case	1	2	3	4	5	6	7	10	11	12	13	14
RMSE	0.073	0.077	0.077	0.077	0.072	0.073	0.071	0.071	0.079	0.071	0.084	0.071

Table III.9: Root mean square error of the simulations with geometric thickness  $H_c = 0.2 \text{ km}$ .

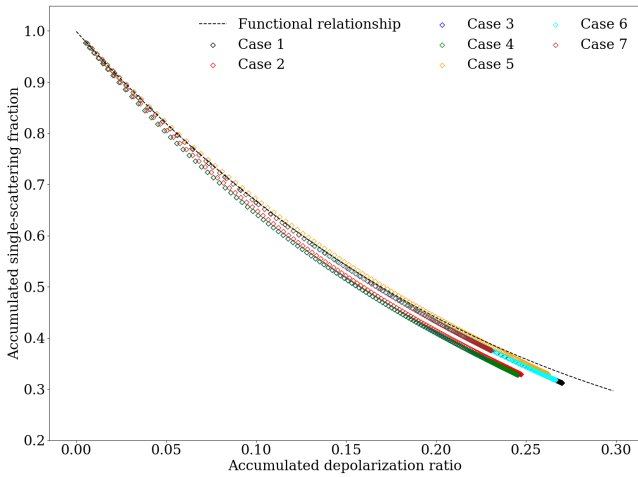
Overall, the results presented on Figures III.24(a) and (c) follow the functional relationship presented in [176] and expressed in Equation III.3.13. Considering the space-based geometry simulations (subfigures (a) and (c)), the results from cases 2, 3 and 4 show a slight deviation from the functional relationship (the results from case 3 are superimposed with those of case 4), while the other cases follow it more closely. This is also expressed by the RMSE values presented on Tables III.8 and III.9. Indeed higher values of the RMSE are found for these three cases. However, when compared to Figure 1 of reference [176], the results presented here do not show the same maximum values of the accumulated depolarization ratio and the same minimum values of the



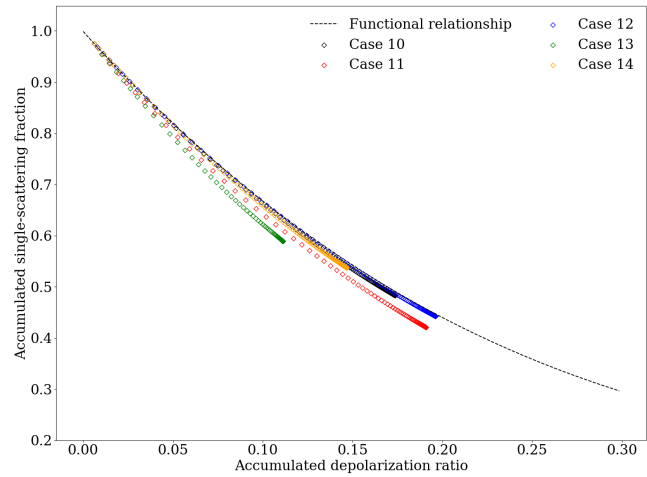
(a) Spaced-based lidar geometry.  $H_c = 1$  km.



(b) Ground-based lidar geometry.  $H_c = 1$  km.



(c) Spaced-based lidar geometry.  $H_c = 0.2$  km.



(d) Ground-based lidar geometry.  $H_c = 0.2$  km.

Figure III.24: Accumulated single scattering fraction as a function of the accumulated depolarization ratio. For more clarity, the results have been separated into four subfigures, *i.e.* the first row (Subfigures (a) and (b)) are relevant to results acquired with a cloud of geometric thickness  $H_c = 1$  km, while the second row (Subfigures (c) and (d)) for a cloud with  $H_c = 0.2$  km. The first column (Subfigures (a) and (c)) presents results acquired for a space-based lidar geometry (cases 1-7) and the second column (subfigures (b) and (d)) for a ground-based lidar geometry (cases 10-14). The dashed line represents the functional relationship expressed in Equation III.3.13.

accumulated single scattering fraction. Indeed, case 1 on Figure III.24(c) reaches an accumulated depolarization ratio of  $\approx 0.27$  with an accumulated single scattering fraction of  $\approx 0.30$ , while in the reference these values are  $\approx 0.41$  and  $\approx 0.2$  respectively. When considering the ground-based lidar geometry (subfigures (b) and (d)), results also follow the functional relationship, except for the case 13 and the case 11 to a lesser extent as highlighted by their higher RMSE values. Due

to the congested presentation of Figure 1 of reference [176], the direct comparison between the cases is made difficult. However, on this figure, results from the case 13 also show deviation from the functional relationship.

Comparing the results obtained with a cloud geometric thickness of  $H_c = 1$  km (subfigures (a) and (b)) with those obtained with  $H_c = 0.2$  km (subfigures (c) and (d)), the ground-based geometry results follow more closely the functional relationship when  $H_c = 0.2$  km. Indeed, comparing Table III.8 and Table III.9, lower RMSE values are found when reducing the cloud geometric thickness in the ground-based cases. Moreover, all cases except for the case 6 are reaching higher values of the accumulated depolarization ratio with lower cloud geometric thickness. This behavior may be explained by the higher extinction coefficients induced by a reduction of the geometric thickness, as the optical depth is kept constant. Indeed, a larger extinction coefficient would reduce the transport length along the direction parallel to the cloud boundaries, increasing the probability of a photon being subject to another scattering event while still being within the receiver FOV, and hence contributing to the received signal through the peel-off scattering technique. Following this interpretation, this effect would be particularly marked for small footprint of the FOV, *i.e.* for small receiver FOV or short cloud base/receiver distance.

The differences observed between the results presented here and those of reference [176] may be explained by the differences between the Monte-Carlo programs themselves, as the reference results stem from the Monte-Carlo scheme described in [179]. Moreover, some simulation parameters are not presented within reference [176], such as the pulse length  $L_{em}$ , the number of emitted photons  $N_{ph}$  or the receiver radius  $R_{rec}$ . Furthermore, there is no indication of which cloud geometric thickness is considered in the results presented in Figure 1 of reference [176].

## Conclusion

In this chapter, the lidar signal simulation program has been thoroughly described within Section III.1. Each of the different steps of this algorithm have been presented in dedicated subsections, namely the initialization step in Subsection III.2.1, the transport step in Subsection III.2.2 and the

scattering step in Subsections III.2.4, III.2.5 and III.2.6. In these latest three subsections, care has been taken to introduce the underlying mathematical developments introduced by the variance reduction techniques. Each of these variance reduction techniques, namely absorption weighting (continuous and discrete), peel-off scattering and scattering splitting, introduces a weight modification resulting from the biasing of the associated probability density functions.

Several methods have been used to assess the performance of the program. An investigation of the angle sampling method and of the scattering splitting variance reduction technique has yielded results showing a good agreement between these methods and the analytical computation of the Stokes vector elements. However, it has also highlighted the limits of the scattering splitting technique. Indeed, depending on the scattering matrix of the scatterers, the choice of the scattering splitting angle may result in large discrepancies. Several simulations have also been undertaken to compare the signals resulting from the Monte-Carlo program with the analytical expression of the single scattering lidar equation. This comparison showed that these two methods are in agreement, provided that the pulse length is lower than the output signal spatial resolution. Several quantities resulting from the output signal of the simulation program have also been compared with a functional relationship stemming from the literature [176]. These quantities follow this functional relationship, but some discrepancies have been found when compared to the results presented in this reference. These discrepancies may be explained by differences in the simulation parameters or in the simulation programs themselves.

Several improvements of this program can be considered. Indeed, the plane-parallel homogeneous slabs description of the scattering medium may be improved by considering more complex boundary geometries (*e.g.* using cells rather than slabs). Moreover, stretch methods can be used in order to artificially increase the path length of photons, which would increase the efficiency of the program for large optical depths [180]. The angle sampling method may also be improved by introducing a Gibbs sampling method [172], and the peel-off scattering method may be extended so that the calculated peeled-off photon contribution includes several orders of scattering and several photon interactions in the vicinity of the original event [168].

Nevertheless, the Monte-Carlo lidar signal simulation program still allows to model a variety

of lidar instruments and scattering medium geometries and compositions, for an optical depth of  $\tau < 7 - 10$  depending on the simulation parameters. Within this range, this program allows to simulate lidar signals acquired on scattering media composed of soot particles, the radiative properties of which have been presented in Chapter II. Hence, the following chapter reports investigations of the impact of multiple scattering on lidar signals, using the previously described methodology for the computation of radiative properties and lidar signals simulated by means of this program.



## **Chapter IV**

# **Impact of multiple scattering on lidar signals for a scattering medium composed of soot particles**

### **Introduction**

In Chapter II, several methods used for the computation of the radiative properties of soot fractal aggregates have been presented. These radiative properties have been computed while considering aggregates of various morphologies. However, these radiative properties alone do not allow for the simulation of multiply-scattered lidar signals in the case of optically dense scattering media. Consequently, a more refined numerical model has been developed. This numerical model has been presented and thoroughly described in Chapter III, and consists in a Monte-Carlo scheme. Hence, in this chapter, the model presented in Chapter III is used in combination with the radiative properties resulting from the methodology presented in Chapter II. This allows to simulate lidar signals including multiple scattering measured from dense soot plumes, and to study the potential impacts of multiple scattering on this signal and the ensuing signal-dependent quantities.

Two main approaches are undertaken in this chapter in order to study these impacts. In the

first section, numerical experiments aiming to model plumes composed of soot fractal aggregates are presented. During the computation of the radiative properties, several optical indices are considered. Moreover, during the simulation of the lidar signals, several different concentration profiles are modeled. This allows for the investigation of the potential impacts of multiple scattering in multiple scenarios. The second section of this chapter presents results obtained during these simulations, as well as an evaluation of the multiple scattering correction factors. The third section of this chapter also makes use of these simulations, but its purpose is to investigate the possibility to derive phenomenological relationships that would be useful in lidar signals analysis.

The second approach consists in evaluating the multiple scattering contribution to experimental lidar signals acquired on soot particles emitted from a pool fire. This study is presented in the fourth section of this chapter. It consists in using the extinction coefficient profile resulting from the inversion of the experimental lidar signal as an input parameter for the simulation, while the medium scattering matrix is simulated using the same aggregate model and same optical index as those used during the signal inversion. This approach allows to investigate if an experimental lidar signal may have been impacted by multiple scattering. Because the signal inversion procedure makes use of the single-scattering approximation, this also allows to assess whether this approximation is verified.

## IV.1 Radiative properties and plume model

In Section II.1.3, the methodology for the computation of the radiative properties of soot fractal aggregates with polydisperse monomers has been presented. The same methodology is used in this section in order to provide the radiative properties necessary to proceed to the lidar signal simulations. The radiative properties are evaluated at three different wavelengths, *i.e.*  $\lambda = 355$  nm,  $\lambda = 532$  nm and  $\lambda = 1064$  nm, which correspond to Nd:YAG laser frequency tripled, doubled and main emission wavelengths respectively. As described in Section I.1.3, the optical index of soot particles depends on several properties, such as the nature of the fuel and the combustion

conditions. For these reasons, three optical indices have been considered, (i)  $m_o = 1.55 + i0.86$  [8]; (ii)  $m_o = 2.68 + i1.32$  [9] and (iii) the wavelength-dependent dispersion law from Chang and Charalampopoulos [7]. The first two optical indices are kept constant at all three wavelengths, while in the third case, the value of the optical index is calculated at each wavelength. The indices from Bescond et al. [8] and from Chang and Charalampopoulos [7] are chosen in order to provide results relevant to a variety of soot materials, which have proven to present a large optical index variability. However, the index from Schnaiter et al. [9] is relevant to spark-generated soot, but is considered in this study to address the results obtained during Section II.2.2, where this index allowed to reproduce the experimentally evaluated LDR of soot particles emitted from a kerosene pool fire.

The morphological parameters of the soot aggregates are also kept identical to those presented in Section II.1.3. Hence, an ensemble of one hundred aggregates is generated using the FracVAL code [80], with a monomer mean geometrical radius  $R_m = 20$  nm, monomer radius standard deviation  $\sigma_m = 1.1$ , fractal dimension  $D_f = 1.8$ , fractal prefactor  $k_f = 1.3$  and number of monomers  $N_m = 100$ . Tables IV.1, IV.2 and IV.3 present the radiative properties of these particles, when computed using the MSTM code and using the three previously mentioned optical indices.

$\lambda$ (nm)	355	532	1064
$m_o$	$1.55 + i0.86$	$1.55 + i0.86$	$1.55 + i0.86$
$C_{ext}$ (nm <sup>2</sup> )	$86214 \pm 743$	$56714 \pm 551$	$26753 \pm 262$
$C_{sca}$ (nm <sup>2</sup> )	$18519 \pm 532$	$7597 \pm 298$	$1157 \pm 46$
$C_{abs}$ (nm <sup>2</sup> )	$67695 \pm 587$	$49117 \pm 380$	$22596 \pm 226$
$\omega_0$	$0.215 \pm 0.005$	$0.134 \pm 0.004$	$0.043 \pm 0.001$
$dC_{bac}$ (nm <sup>2</sup> .sr <sup>-1</sup> )	$365 \pm 35$	$221 \pm 21$	$60 \pm 6$
$LR$ (sr)	$238 \pm 22$	$259 \pm 25$	$448 \pm 47$
$\delta_p$	$0.025 \pm 0.003$	$0.011 \pm 0.002$	$0.003 \pm 0.001$
$g_0$	$0.668 \pm 0.020$	$0.552 \pm 0.021$	$0.330 \pm 0.021$

Table IV.1: Radiative properties of the modeled soot aggregates with polydisperse monomers, computed with Bescond et al. [8] optical index.

As expressed in Chapter III, the lidar signal simulation code requires the specification of the scattering medium radiative properties, *i.e.* the scattering matrix, single scattering albedo and extinction coefficient, as well as their respective spatial variations along the optical path. In each Monte-Carlo simulation, a single wavelength and a single fractal aggregate model are used.

$\lambda$ (nm)	355	532	1064
$m_o$	$2.68 + i1.32$	$2.68 + i1.32$	$2.68 + i1.321$
$C_{ext}(\text{nm}^2)$	$119951 \pm 1774$	$64152 \pm 1296$	$22228 \pm 368$
$C_{sca}(\text{nm}^2)$	$52456 \pm 1382$	$20917 \pm 902$	$2829 \pm 128$
$C_{abs}(\text{nm}^2)$	$67495 \pm 711$	$43235 \pm 522$	$19399 \pm 263$
$\omega_0$	$0.437 \pm 0.006$	$0.326 \pm 0.008$	$0.127 \pm 0.004$
$dC_{bac}(\text{nm}^2.\text{sr}^{-1})$	$1132 \pm 119$	$634 \pm 65$	$151 \pm 17$
$LR$ (sr)	$107 \pm 11$	$102 \pm 10$	$149 \pm 16$
$\delta_p$	$0.070 \pm 0.008$	$0.031 \pm 0.004$	$0.006 \pm 0.002$
$g_0$	$0.654 \pm 0.020$	$0.539 \pm 0.021$	$0.321 \pm 0.022$

Table IV.2: Radiative properties of the modeled soot aggregates with polydisperse monomers, computed with Schnaiter et al. [9] optical index.

$\lambda$ (nm)	355	532	1064
$m_o$	$1.663 + i0.715$	$1.732 + i0.600$	$1.819 + i0.591$
$C_{ext}(\text{nm}^2)$	$74978 \pm 763$	$40071 \pm 501$	$16574 \pm 184$
$C_{sca}(\text{nm}^2)$	$17434 \pm 551$	$6419 \pm 274$	$997 \pm 41$
$C_{abs}(\text{nm}^2)$	$57544 \pm 473$	$33652 \pm 291$	$15578 \pm 151$
$\omega_0$	$0.232 \pm 0.006$	$0.160 \pm 0.005$	$0.060 \pm 0.002$
$dC_{bac}(\text{nm}^2.\text{sr}^{-1})$	$349 \pm 34$	$191 \pm 19$	$53 \pm 6$
$LR$ (sr)	$217 \pm 21$	$212 \pm 21$	$319 \pm 33$
$\delta_p$	$0.022 \pm 0.003$	$0.009 \pm 0.001$	$0.002 \pm 0.001$
$g_0$	$0.663 \pm 0.020$	$0.534 \pm 0.021$	$0.320 \pm 0.021$

Table IV.3: Radiative properties of the modeled soot aggregates with polydisperse monomers, computed with Chang and Charalampopoulos [7] dispersion law.

Hence, the spatial variation of the scattering medium radiative properties is only caused by the plume model. The scattering medium is modeled as being composed exclusively of freshly emitted soot particles. In order to represent the spatial distribution of freshly emitted particles, a gaussian plume model is used. The particle number concentration profile  $n_p$  is then expressed as :

$$n_p(r) = n_0 e^{-\frac{1}{2} \left( \frac{r-r_c}{\sigma_r} \right)^2} \quad (\text{IV.1.1})$$

where  $n_p(r)$  is the particle number concentration as a function of the distance to the receiver  $r$ ,  $n_0$  is the particle number concentration at the profile maximum,  $r_c$  is the profile center and  $\sigma_r$  is the standard deviation. This standard deviation also allows to determine the full width at half maximum (FWHM) of the particle number concentration profile such as  $\text{FWHM} = 2\sqrt{2 \ln 2} \sigma_r$ . In

all simulations, the parameters  $r_c$  and  $\sigma_r$  are set to  $r_c = 1.15$  km and  $\sigma_r = 0.0375$  km. The cloud optical depth can then be calculated using the formula :

$$\tau(r, \lambda) = \int_{r_0}^r n_p(r') C_{ext}(\lambda) dr' \quad (IV.1.2)$$

where  $r_0 = r_c - 4\sigma_r = 1$  km. Note that this expression of the optical depth uses the single scattering approximation. As such, the values of the optical depth are hereby only used in order to differentiate between different concentration profiles.

In the calculations hereby presented, the particle number distribution constant  $n_0$  is parametrized so that a predefined value of the cloud optical depth  $\tau(r_{max}) = \tau_{max}$  is obtained, with  $r_{max} = r_c + 4\sigma_r = 1.3$  km. This allows to study a range of clouds with comparable optical depth at different wavelengths. Ten values of the optical depth are used, ranging from  $\tau_{max} = 1$  to  $\tau_{max} = 10$ , with a step of  $\Delta\tau = 1$ . Knowing this optical depth, the particle number distribution constant  $n_0$  can be retrieved as :

$$n_0 = \frac{\tau_{max}}{C_{ext}} \frac{1}{\sigma_r \sqrt{2\pi}} \quad (IV.1.3)$$

Hence, ten different particle number concentration profiles are modeled for each of the three wavelengths with varying constants  $n_0$ , these constants being parametrized so that Equation IV.1.2 verifies the predefined optical depths  $\tau_{max}$ . Because the Monte-Carlo simulations cannot account for a continuous variation of the interacting medium radiative properties, sets of discrete slabs are created for each of these profiles. Each slab except for the first one is 1.2 m thick (*i.e.*  $H_s - H_{s-1} = 1.2$  m). The first slab upper plane is set to  $H_1 = 1$  km, and its radiative properties are parametrized such as no interactions are simulated within it. Equations IV.1.1 and I.3.5(b) are then used in order to compute the extinction coefficient of every other slab.

Several other parameters are needed to run the Monte-Carlo simulations. These parameters are summarized in Table IV.4 and their respective values are presented. The parameters presented in this table are kept constant for each simulation, with the exception of the receiver Field-Of-View (FOV). The simulations are performed for a FOV value of either  $\theta_{rec} = 0.5$  mrad (half-

angle) or  $\theta_{rec} = 5$  mrad (half-angle). These angles have been chosen in order to address the wide range of receiver FOV of ground based lidar instruments such as the Polly<sup>XT</sup> lidar (Dual FOV; 1 mrad and 2.2 mrad full angle) [122] or the Multiple-Field-of-view Multiple-Scattering Polarization Lidar (MFMSPL; 8 channels with a FOV of 10 mrad full angle each; total FOV 70 mrad full angle) [123].

Emitter parameters		Receiver parameters	
Parameter	Value	Parameter	Value
$\theta_{em}$	0.1 mrad	$R_{rec}$	0.1 m
$R_{em}$	0.045 m	$\mathbf{d}_{rec}$	$[0 \ 0 \ 1]^T$
$L_{em}$	3.6 m	<b>Output parameters</b>	
$\mathbf{p}_{em}$	$[0 \ 0 \ 0]^T$	$t_{min}$	2.0 km
$\mathbf{d}_{em}$	$[0 \ 0 \ 1]^T$	$t_{max}$	2.6 km
$\mathbf{I}_{em}$	$[1 \ 1 \ 0 \ 0]^T$	$\Delta t$	1.2 m
<b>Monte-Carlo parameters</b>			
$N_{ph}$	$10^9$	$\theta_{cone}$	$1.15\theta_{rec}$
$\theta_{split}$	$90^\circ$	$R_{cone}$	0.1 m
$\zeta$	$90^\circ$	$j_{max}$	10

Table IV.4: List of the input parameters of the Monte-Carlo program.

Moreover, in this chapter, the notations of the Monte-Carlo total lidar signal  $\mathbf{I}(t_l)$  and of the scatter-order dependent signal  $\mathbf{I}(t_l, j)$  are modified. The Monte-Carlo total lidar signal  $\mathbf{I}(t_l)$  is noted  $P_{MS}(r)$ , where  $r$  defines the distance to the receiver and  $P_{MS}$  is referred to as the multiply-scattered lidar signal. Moreover, the lidar signal at first order of scattering  $\mathbf{I}(t_l, j)$  is noted  $P_1(r)$ . Finally, the polarization-resolved multiply-scattered signals are expressed as :

$$P_{MS,\parallel}(r) = (1/2)(I(t_l) + Q(t_l)) \quad (\text{IV.1.4a})$$

$$P_{MS,\perp}(r) = (1/2)(I(t_l) - Q(t_l)) \quad (\text{IV.1.4b})$$

These notations are used throughout this chapter, and allow to unify the notion of path length  $t$  of the Monte-Carlo scheme with the notion of range  $r$  of lidar instruments, and to express the output of the Monte-Carlo scheme in the framework of lidar instruments as described in Section I.3.

## IV.2 Multiply-scattered lidar signals and correction factors

In this section, the multiply-scattered signals resulting from the lidar signal simulation code are presented and compared to the single-scattering lidar equation presented in Equation III.3.10. The multiple scattering correction factor from Platt [133] is also computed using Equation I.3.13. This allows for the computation of a corrected attenuated backscattering function  $U_{corr}$  as in Equation I.3.12, and of the corrected signal  $P_{corr}$  such as :

$$\begin{aligned} P_{corr}(r) &= \frac{A}{r^2} U_{corr}(r) \\ &= \frac{A}{r^2} \beta(r) \exp\left(-2\eta(r) \int_0^r \alpha(r') dr'\right) \end{aligned} \quad (IV.2.1)$$

Figure IV.1 presents results obtained with the optical index from Bescond et al. [8] at wavelength  $\lambda = 532$  nm with a receiver FOV half-angle  $\theta_{rec} = 5$  mrad and maximal optical depth  $\tau_{max} = 5$ . The multiply-scattered lidar signal  $P_{MS}(r)$  resulting from the simulation code, the single-scattering lidar signal  $P_{SS}(r)$ , the corrected lidar signal  $P_{corr}(r)$  and the multiple scattering correction factors  $\eta(r)$  are represented on this figure.

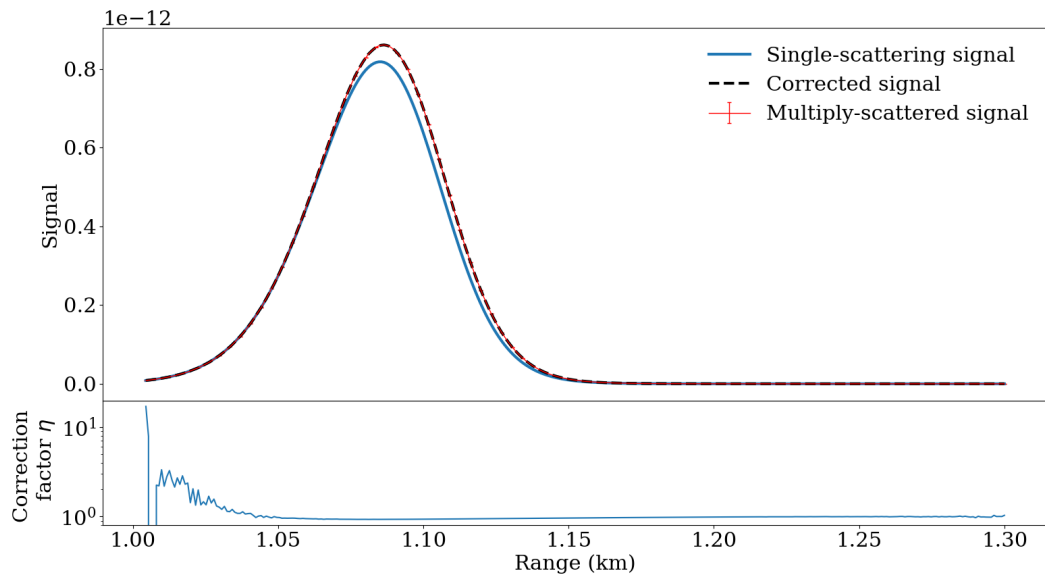


Figure IV.1: Multiply-scattered lidar signal  $P_{MS}(r)$  resulting from the simulation code, single-scattering lidar signal  $P_{SS}(r)$ , corrected lidar signal  $P_{corr}(r)$  and multiple scattering correction factors  $\eta(r)$  as a function of the distance from the receiver for the simulation undertaken with the optical index from Bescond et al. [8] at wavelength  $\lambda = 532$  nm with a receiver FOV half-angle  $\theta_{rec} = 5$  mrad and maximal optical depth  $\tau_{max} = 5$ .

Comparing the single-scattering signal and the multiply-scattered signal on Figure IV.1, it appears that the multiple scattering effect induces both the pulse stretching effect and the increase in backscattered power effect as previously described in Section I.3.4. Indeed, the multiply-scattered lidar signal reaches a higher maximum which is characteristic of an increase in backscattered power. Moreover, this maximum is reached at a larger distance from the receiver and the shape of the multiply-scattered lidar signal is wider than the single-scattering lidar signal, which allows to identify the pulse-stretching effect.

As expected, the computation of the correction factors  $\eta(r)$  results in a corrected signal in agreement with the multiply-scattered signal. However the evolution of the correction factor values with the range is unstable in the first few tens of meters. This instability can be explained by the considered cloud profile and the shortcomings of the Monte-Carlo lidar signal simulation code. In order to better illustrate this, Figure IV.2 presents the optical depth and the extinction coefficients of the modeled slabs using the same simulation parameters as in the previous figure.

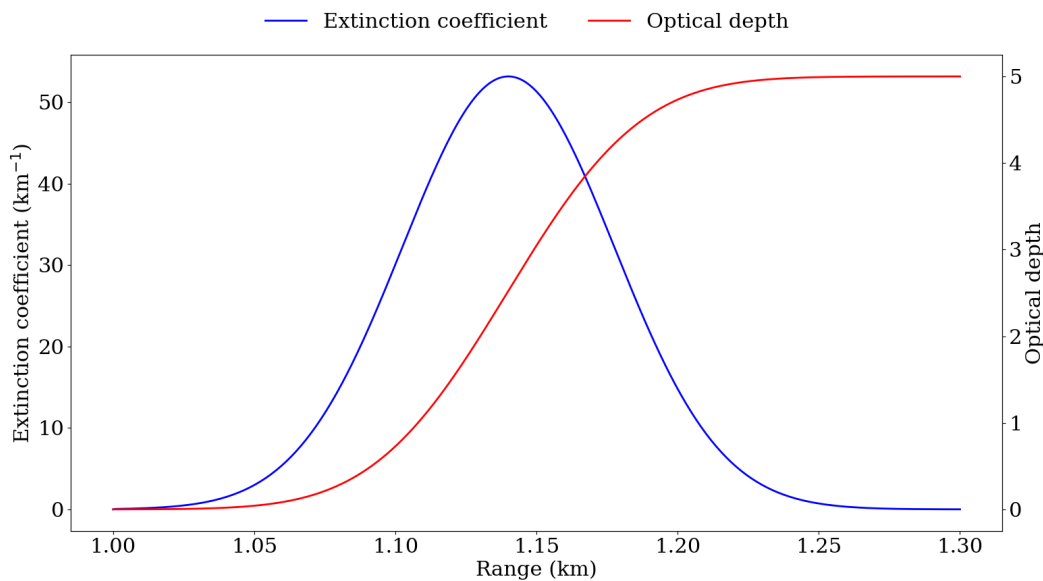


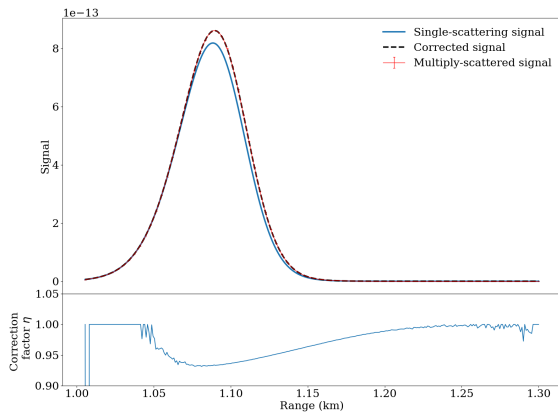
Figure IV.2: Optical depth and extinction coefficient as a function of the distance to the receiver.

As described in Section III.2.2, the extinction coefficients drive the transport step in the lidar signal simulation code. According to Figure IV.2, these extinction coefficients are fairly low in the first tens of meters of the modeled plume. Moreover, the path length step of the simulation is  $\Delta t = 1.2$  m as presented in Table IV.4. These two considerations allow to interpret the instability

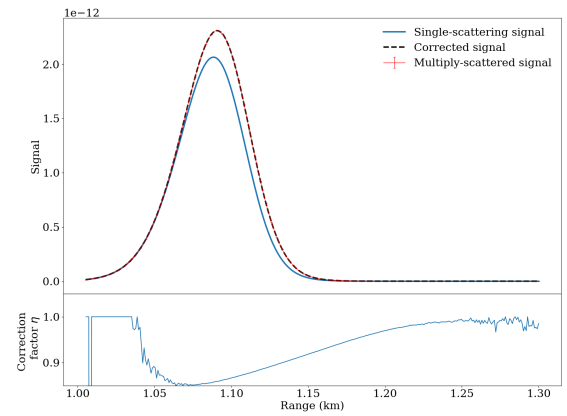
of the computed correction factors as the result of an under-sampling of interaction events in this range, which is further amplified by the low averaging step  $\Delta t$ . Furthermore, the pulse length  $L_{em}$  is larger than the path length step  $\Delta t$  by a factor 3. As previously mentioned in Section III.3.2, this effect also results in discrepancies between the single-scattering signals and Monte-Carlo signals, and consequently larger correction factors at short range.

In order to better ascertain the variation of the multiple scattering correction factors as a function of range, the following figures only account for the signals and the corresponding correction factors that are obtained with extinction coefficients  $\alpha(r) > 2 \text{ km}^{-1}$ . Moreover, the upper values of the correction factors are bounded to 1. Considering the large number of simulations undertaken (*i.e.* 180 different cases), only a selection is hereby presented.

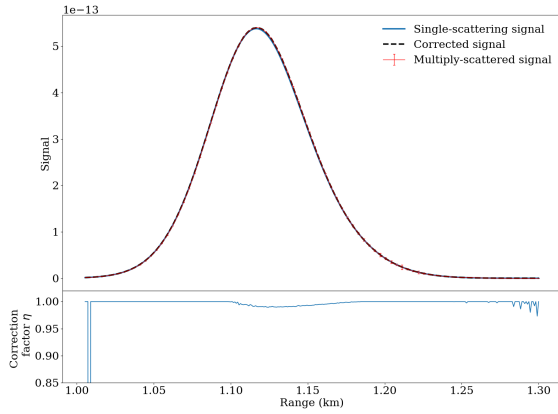
Figure IV.3 presents the results obtained for six different simulation cases. Subfigure IV.3(a) corresponds to the same case as Figure IV.1, but the dataset has been filtered following the conditions previously mentioned, allowing to show more clearly the evolution of the correction factor with range. Subfigure IV.3(b) corresponds to the simulation case with the same parameters as Subfigure IV.3(a), except for the optical index which is taken from Schnaiter et al. [9]. While Subfigure IV.3(a) shows a maximum signal of  $\approx 8.3 \cdot 10^{-13} \text{ km}^{-1}$  and correction factors as low as  $\approx 0.93$ , the results obtained with the optical index from Schnaiter et al. [9] as presented on Figure IV.3(b) show that the multiply-scattered signal presents a higher maximum ( $\approx 2.4 \cdot 10^{-12} \text{ km}^{-1}$ ), and that the correction factors values are lower ( $\approx 0.86$ ) than in the previous case. These differences can be attributed to the variation of the radiative properties induced by the change of optical index. Indeed, comparing Table IV.1 and Table IV.2, the backscattering cross-sections and single-scattering albedo computed with the optical index from Schnaiter et al. [9] are found higher than those computed with the index from Bescond et al. [8]. In the lidar signal simulation code, this results in a larger overall signal, and in a lesser attenuation of the contribution of photons during the discrete absorption weighting technique.



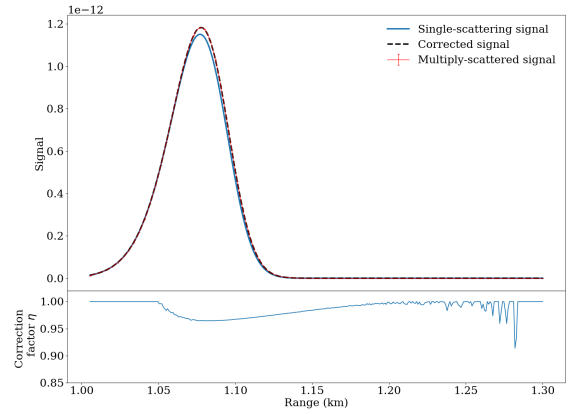
(a) Optical index from Bescond et al. [8], with the parameters  $\lambda = 532 \text{ nm}$ ,  $\tau_{max} = 5$ ,  $\theta_{rec} = 5 \text{ mrad}$ .



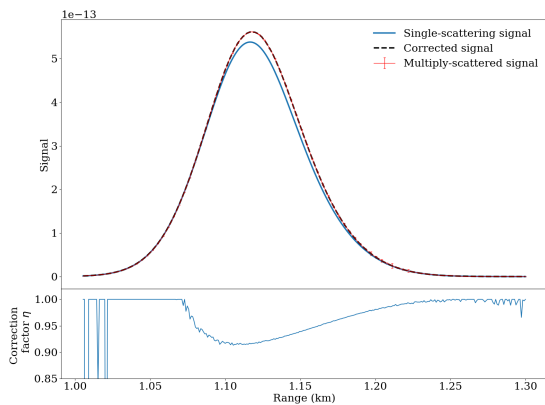
(b) Optical index from Schnaiter et al. [9], with the parameters  $\lambda = 532 \text{ nm}$ ,  $\tau_{max} = 5$ ,  $\theta_{rec} = 5 \text{ mrad}$ .



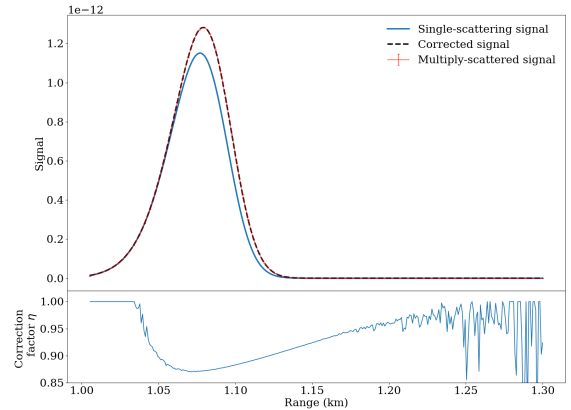
(c) Optical index from Chang and Charalampopoulos [7], with the parameters  $\lambda = 355 \text{ nm}$ ,  $\tau_{max} = 1$ ,  $\theta_{rec} = 0.5 \text{ mrad}$ .



(d) Optical index from Chang and Charalampopoulos [7], with the parameters  $\lambda = 355 \text{ nm}$ ,  $\tau_{max} = 10$ ,  $\theta_{rec} = 0.5 \text{ mrad}$ .



(e) Optical index from Chang and Charalampopoulos [7], with the parameters  $\lambda = 355 \text{ nm}$ ,  $\tau_{max} = 1$ ,  $\theta_{rec} = 5 \text{ mrad}$ .



(f) Optical index from Chang and Charalampopoulos [7], with the parameters  $\lambda = 355 \text{ nm}$ ,  $\tau_{max} = 10$ ,  $\theta_{rec} = 5 \text{ mrad}$ .

Figure IV.3: Multiply-scattered lidar signal  $P_{MS}(r)$  resulting from the simulation code, single-scattering lidar signal  $P_{SS}(r)$ , corrected lidar signal  $P_{corr}(r)$  and multiple scattering correction factors  $\eta(r)$  as a function of the distance from the receiver for several simulation cases.

Subfigures IV.3(c), (d), (e) and (f) present the results obtained for four different cases. All these subfigures are obtained using the dispersion law from Chang and Charalampopoulos [7] at wavelength  $\lambda = 355$  nm. However, Subfigures IV.3(c) and (e) correspond to simulations with a maximal optical depth  $\tau_{max} = 1$ , while Subfigures IV.3(d) and (f) correspond to a maximal optical depth of  $\tau_{max} = 10$ . Moreover, the results presented on the second row (*i.e.* Subfigures IV.3(c) and (d)) are computed using a receiver FOV half-angle  $\theta_{rec} = 0.5$  mrad, while the third row (*i.e.* Subfigures IV.3(e) and (f)) correspond to the simulation cases computed using  $\theta_{rec} = 5$  mrad.

Comparing Subfigures IV.3(c) and (d) with Subfigures IV.3(e) and (f), the increase of the receiver FOV induces lower correction factors. This is due to a higher fraction of the lidar signal being attributed to multiple scattering, as seen by the gap between the single-scattering signal and the multiply-scattered signal. This behavior is expected. Indeed, while scattering events at first scattering order are necessarily within the emitter cone, higher scattering order events can be located outside of it. Hence, increasing the receiver FOV increases the probability of a scattering event at scattering order higher than one being detected.

An increase of the plume maximal optical depth also induces an increase of multiple scattering, as seen by the comparison between the Subfigures IV.3(c) and (e) with IV.3(d) and (f). Indeed, while multiple scattering does not impact the results presented on Subfigure IV.3(c) ( $\eta > 0.99$  at all ranges), Subfigure IV.3(d) shows correction factors with a minimum value of  $\approx 0.96$ . The last two cases also present the same effect. The increase of optical depth also induces a modification of the range at which the signal maximum is attained and of the amplitude of this maximum. These two features are also expected. Indeed, the increase of maximal optical depth translates by an overall increase of the extinction coefficient within the modeled plume. This reduces the mean path length of the photon within the Monte-Carlo simulation, hence decreasing the range at which the signal maximum is attained and increasing the probability of a scattering event at scattering order  $> 1$  being detected. Moreover, this also induces a decrease of the width of the signal.

The multiple scattering correction factors presented on Subfigures IV.3(d) and IV.3(f) are found unstable in the farther region of the plume. Considering the high maximal optical depth of this

medium ( $\tau_{max} = 10$ ), this behavior may be explained by a lack of photons reaching the outer range of the modeled plume, as was previously mentioned in Subsection III.3.2. This further supports the need for the implementation of a stretch variance-reduction technique within the simulation program.

Now, considering a polarization-resolved signal, the parallel and perpendicular single-scattering signals can be expressed as :

$$P_{SS,i}(r) = \frac{A}{r^2} \beta_i(r) \exp(-2\tau(r)) \quad (\text{IV.2.2})$$

where the subscript  $i$  indicates whether the  $\parallel$ -polarization or  $\perp$ -polarization is considered,  $\beta_{\parallel}(r) = (1/2)n_p(r)(F_{11}(\pi) + F_{22}(\pi))$  and  $\beta_{\perp}(r) = (1/2)n_p(r)(F_{11}(\pi) - F_{22}(\pi))$ . Correction factors  $\eta_{\parallel}$  and  $\eta_{\perp}$  can then be expressed by modifying Equation I.3.13 such as :

$$\eta_i(r) = 1 - \frac{1}{2\tau} \log \left( \frac{P_{MS,i}(r)}{P_{SS,i}(r)} \right) \quad (\text{IV.2.3})$$

And the corrected polarization-resolved signals are expressed as :

$$P_{corr,i}(r) = \frac{A}{r^2} \beta_i(r) \exp(-2\eta_i(r)\tau(r)) \quad (\text{IV.2.4})$$

Figures IV.4 and IV.5 present examples of simulated polarization-resolved lidar signals. These results correspond to the simulation case undertaken with the optical index from Schnaiter et al. [9] at  $\lambda = 532$  nm and with a maximal optical depth  $\tau_{max} = 5$ .

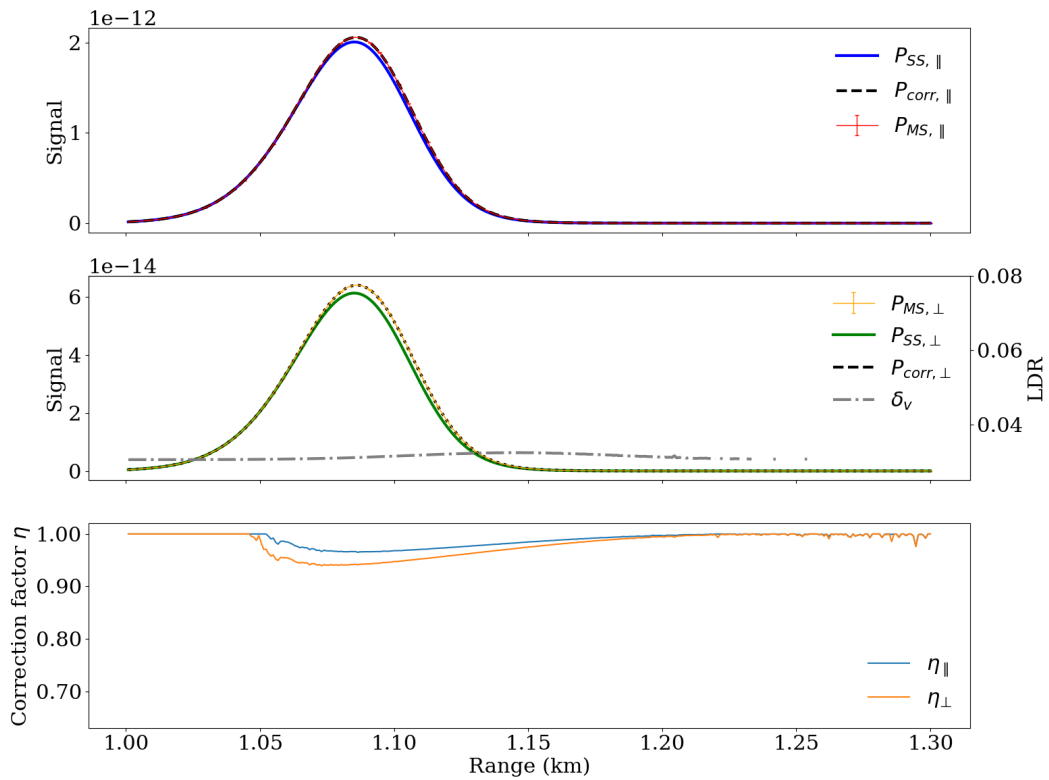


Figure IV.4: Polarization-resolved lidar signals, LDR and multiple scattering factors as a function of the distance from the receiver with a receiver FOV of  $\theta_{rec} = 0.5$  mrad.

Figures IV.4 and IV.5 present the results obtained while considering a receiver FOV  $\theta_{rec} = 0.5$  mrad and  $\theta_{rec} = 5$  mrad respectively. As expected, the corrected signals also reproduce the Monte-Carlo results whether the  $\parallel$ -polarization or the  $\perp$ -polarization is considered. The correction factor for the  $\perp$ -polarization  $\eta_{\perp}$  is also found lower than the parallel correction factor  $\eta_{\parallel}$ . Moreover, the increase of the receiver FOV  $\theta_{rec}$  induces a larger difference between these two correction factors. This results in a larger increase of the linear depolarization ratio, as the LDR is the ratio between the  $\parallel$ -polarized signal and the  $\perp$ -polarized signal (see Equation I.3.11).

Overall, the multiple scattering correction factors introduced by Platt [133] allow to reproduce the Monte-Carlo results. However, it has been observed that the variation of these correction factors with range can be unstable at the boundaries of the scattering medium. This supports the need to improve the lidar signal simulation code by introducing a stretch variance-reduction technique, as previously mentioned in Section III.3. The use of these correction factors as presented here is fairly limited. Indeed, their computation requires the knowledge of the multiply-

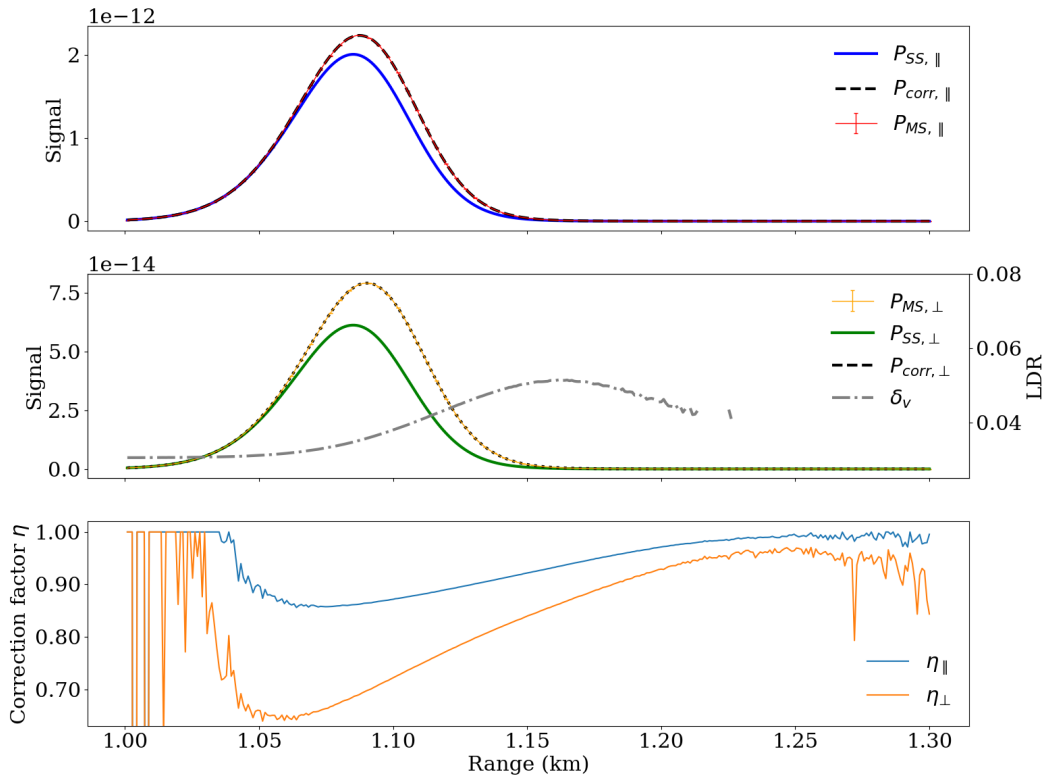


Figure IV.5: Polarization-resolved lidar signals, LDR and multiple scattering factors as a function of the distance from the receiver with a receiver FOV of  $\theta_{rec} = 5$  mrad.

scattered lidar signal and of the range-dependent variation of both backscattering coefficients and extinction coefficients. While the signal is the measurable quantity of the lidar experiment, the backscattering and extinction coefficients are obtained using an inversion algorithm which may use the single-scattering approximation, and hence be prone to errors.

### IV.3 Phenomenological relationships

In this section, an attempt is made to determine phenomenological relationships between different quantities extracted from the simulated signals. In particular, the evolution of the LDR and of the multiple scattering fraction (MSF) with varying optical depth is investigated. The LDR is expressed using Equation I.3.11 using the polarization-resolved multiply-scattered signals  $P_{MS,||}$  and  $P_{MS,\perp}$ , while the MSF is expressed as :

$$MSF(r) = \frac{P_{MS}(r) - P_1(r)}{P_1(r)} \quad (IV.3.1)$$

Using this expression of the MSF, the multiple scattering correction factor presented in Equation I.3.13 can be computed as :

$$\eta = 1 + \frac{1}{2\tau} \log(1 - MSF) \quad (IV.3.2)$$

The results presented in this section stem from simulations that are identical to those presented in the previous sections. For a reliable results analysis, several precautions have been taken. The only reported data points are those for which the computed relative errors on the MSF and on the LDR are below 10% and those for which the received signal  $P_{MS}(r)$  is greater than 1% of the corresponding signal maximum. Moreover, the only presented values of the MSF are those higher than 1%. Figure IV.6 presents the evolution of the MSF and of the LDR as a function of the plume optical depth, at wavelength  $\lambda = 355$  nm (Subfigure IV.6(a)),  $\lambda = 532$  nm (Subfigure IV.6(b)) and  $\lambda = 1064$  nm (Subfigure IV.6(c)), when considering soot aggregates whose radiative properties have been computed using the optical index dispersion law from Chang and Charalampopoulos [7].

Overall, both the MSF and the volume LDR present increasing values with larger optical depths. The increase in MSF can be attributed to the increasing interaction event probability as the particle number concentration increases. The slight increase of LDR can be also attributed to the increased MSF. Moreover, larger values of the MSF and LDR are observed with a larger FOV. For larger values of the FOV, the probability of a multiply scattered photon contributing to the return signal increases, while the single-scattering contribution remains unchanged, the laser divergence being smaller than the FOV as seen in Table IV.4.

In all simulation cases with low optical depth, both MSF and LDR are decreasing after reaching a maximum. This behavior can be interpreted by an insufficient number of scattering events in the section of the cloud located after the maximum of particle number concentration. Because the phase functions of the soot aggregates are largely peaked forward, photons scattered in the

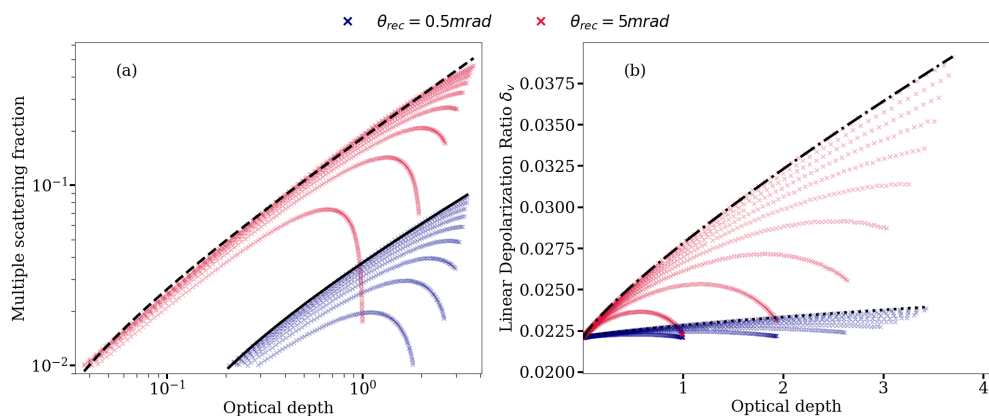
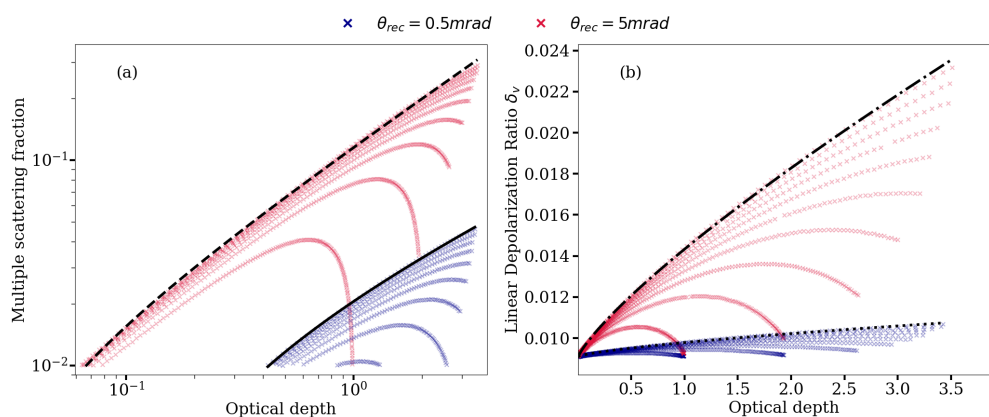
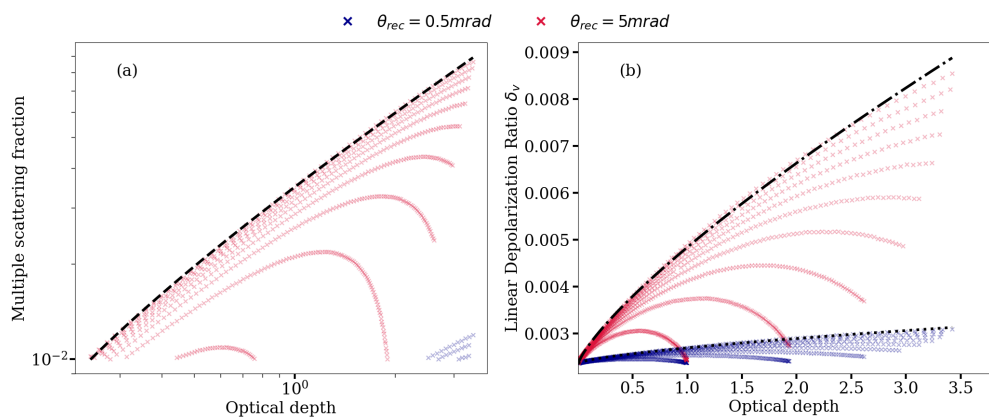
(a)  $\lambda = 355$  nm(b)  $\lambda = 532$  nm(c)  $\lambda = 1064$  nm

Figure IV.6: MSF and LDR as a function of the soot plume optical depth. The full lines and dashed lines represent fitted functions for the evolution of the MSF with optical depth using a FOV of  $\theta_{rec} = 0.5$  mrad and  $\theta_{rec} = 5$  mrad respectively. Similarly, the dotted and dash-dotted lines represent fitted functions for the evolution of the LDR with optical depth using a FOV of  $\theta_{rec} = 0.5$  mrad and  $\theta_{rec} = 5$  mrad respectively.

first half of the profile are mostly scattered in the direction of the second half, where their scattering probability decreases. Because these photons are not necessarily scattered in the exact forward direction ( $\theta_{sca} = 0$ ), the next scattering event undergone by these photons can be located outside of the receiver FOV. The distance between two successive events being driven by the scattering medium extinction coefficient, a decrease in the density of the medium induces a longer transport distance. Since the single scattering signal is not affected by this effect, the emitter divergence being largely smaller than the receiver FOV, this induces a decrease of the multiple scattering fraction, and consequently of the volume LDR.

In order to provide an evaluation of the relationship of the MSF and of the LDR with optical depth, the datasets corresponding to the simulation with optical depth at maximum range  $\tau_{max} = 10$  have been fitted using two functions. On Figure IV.6, the full lines and dashed lines are obtained using a least square regression of the aforementioned MSF data sets. Similarly, the dotted and dash-dot lines of Figure IV.6 are obtained through a regression analysis of the LDRs obtained in the simulations with  $\tau_{max} = 10$ . During all these regression analyses, the target function is a power law function such as :

$$MSF(\tau) = a + b\tau^c \quad (IV.3.3a)$$

$$\delta_v(\tau) = d + e\tau^f \quad (IV.3.3b)$$

where  $a$ ,  $b$  and  $c$  are the MSF regression coefficients and  $d$ ,  $e$  and  $f$  are the LDR regression coefficients. This regression analysis has not been undertaken on the MSF at  $\lambda = 1064$  nm due to a lack of data verifying the prerequisite conditions mentioned above. Table IV.5 presents the values of these regression coefficients.

Overall, the values of these coefficients reflect the trends observable on Figure IV.6. Larger values of the coefficients  $b$  and  $e$  are associated with a larger increase of the MSF and of the LDR respectively. The coefficients  $d$  can be envisioned as the single-scattering particular LDR  $\delta$ , and are in agreement with the values reported in Table IV.3. The parameters  $c$  and  $f$  express the overall

$\lambda$ (nm)	$\theta_{rec}$ (mrad)	$a$	$b$	$c$	$d$	$e$	$f$
355	0.5	$-6.33 \cdot 10^{-3}$	$4.35 \cdot 10^{-2}$	$6.32 \cdot 10^{-1}$	$2.21 \cdot 10^{-2}$	$7.59 \cdot 10^{-4}$	$7.27 \cdot 10^{-1}$
355	5	$-6.27 \cdot 10^{-3}$	$1.90 \cdot 10^{-1}$	$7.62 \cdot 10^{-1}$	$2.21 \cdot 10^{-2}$	$5.77 \cdot 10^{-3}$	$8.31 \cdot 10^{-1}$
532	0.5	$-8.01 \cdot 10^{-3}$	$2.85 \cdot 10^{-2}$	$5.67 \cdot 10^{-1}$	$9.09 \cdot 10^{-3}$	$6.91 \cdot 10^{-4}$	$7.04 \cdot 10^{-1}$
532	5	$-5.22 \cdot 10^{-3}$	$1.20 \cdot 10^{-1}$	$7.63 \cdot 10^{-1}$	$9.05 \cdot 10^{-3}$	$5.28 \cdot 10^{-3}$	$8.06 \cdot 10^{-1}$
1064	0.5	-	-	-	$2.36 \cdot 10^{-3}$	$3.30 \cdot 10^{-4}$	$6.84 \cdot 10^{-1}$
1064	5	$-4.79 \cdot 10^{-3}$	$3.96 \cdot 10^{-2}$	$7.01 \cdot 10^{-1}$	$2.34 \cdot 10^{-3}$	$2.50 \cdot 10^{-3}$	$7.82 \cdot 10^{-1}$

Table IV.5: Coefficients of the regression analyses for the simulations undertaken with soot particles whose optical index is taken from Chang and Charalampopoulos [7].

bends of the curves. Indeed, the rate of increase of both the MSF and the LDR decreases with larger optical depth. This feature is expressed by the parameters  $c$  and  $f$ , which are found lower than 1 in all cases. Considering the simulations undertaken with the other two optical indices, the values of the regression parameters are presented in Tables IV.6 and IV.7.

$\lambda$ (nm)	$\theta_{rec}$ (mrad)	$a$	$b$	$c$	$d$	$e$	$f$
355	0.5	$-6.68 \cdot 10^{-3}$	$4.14 \cdot 10^{-2}$	$6.21 \cdot 10^{-1}$	$2.44 \cdot 10^{-2}$	$6.88 \cdot 10^{-4}$	$7.19 \cdot 10^{-1}$
355	5	$-5.81 \cdot 10^{-3}$	$1.78 \cdot 10^{-1}$	$7.68 \cdot 10^{-1}$	$2.43 \cdot 10^{-2}$	$5.21 \cdot 10^{-3}$	$8.22 \cdot 10^{-1}$
532	0.5	$-8.80 \cdot 10^{-3}$	$2.61 \cdot 10^{-2}$	$5.02 \cdot 10^{-1}$	$1.12 \cdot 10^{-2}$	$5.73 \cdot 10^{-4}$	$6.94 \cdot 10^{-1}$
532	5	$-4.78 \cdot 10^{-3}$	$1.03 \cdot 10^{-1}$	$7.64 \cdot 10^{-1}$	$1.11 \cdot 10^{-2}$	$4.35 \cdot 10^{-3}$	$7.91 \cdot 10^{-1}$
1064	0.5	-	-	-	$2.78 \cdot 10^{-3}$	$2.39 \cdot 10^{-4}$	$6.77 \cdot 10^{-1}$
1064	5	$-5.24 \cdot 10^{-3}$	$3.07 \cdot 10^{-2}$	$6.66 \cdot 10^{-1}$	$2.76 \cdot 10^{-3}$	$1.82 \cdot 10^{-3}$	$7.65 \cdot 10^{-1}$

Table IV.6: Coefficients of the regression analyses for the simulation undertaken with soot particles whose optical index is taken from Bescond et al. [8].

$\lambda$ (nm)	$\theta_{rec}$ (mrad)	$a$	$b$	$c$	$d$	$e$	$f$
355	0.5	$-5.59 \cdot 10^{-3}$	$7.20 \cdot 10^{-2}$	$6.90 \cdot 10^{-1}$	$6.98 \cdot 10^{-2}$	$1.51 \cdot 10^{-3}$	$8.18 \cdot 10^{-1}$
355	5	$-9.25 \cdot 10^{-3}$	$3.07 \cdot 10^{-1}$	$7.26 \cdot 10^{-1}$	$7.00 \cdot 10^{-2}$	$1.14 \cdot 10^{-2}$	$9.68 \cdot 10^{-1}$
532	0.5	$-6.23 \cdot 10^{-3}$	$4.66 \cdot 10^{-2}$	$6.41 \cdot 10^{-1}$	$3.05 \cdot 10^{-2}$	$1.46 \cdot 10^{-3}$	$7.53 \cdot 10^{-1}$
532	5	$-6.56 \cdot 10^{-3}$	$2.19 \cdot 10^{-1}$	$7.52 \cdot 10^{-1}$	$3.05 \cdot 10^{-2}$	$1.12 \cdot 10^{-2}$	$8.93 \cdot 10^{-1}$
1064	0.5	$-1.43 \cdot 10^{-2}$	$2.54 \cdot 10^{-2}$	$3.59 \cdot 10^{-1}$	$6.87 \cdot 10^{-3}$	$7.03 \cdot 10^{-4}$	$6.97 \cdot 10^{-1}$
1064	5	$-4.74 \cdot 10^{-3}$	$7.56 \cdot 10^{-2}$	$7.45 \cdot 10^{-1}$	$6.83 \cdot 10^{-3}$	$5.40 \cdot 10^{-3}$	$8.03 \cdot 10^{-1}$

Table IV.7: Coefficients of the regression analyses for the simulation undertaken with soot particles whose optical index is taken from Schnaiter et al. [9].

The regression parameters resulting from the simulation undertaken with the optical index from Bescond et al. [8] and presented in Table IV.6 are similar to those presented in Table IV.5. Comparing the parameters  $b$ ,  $c$ ,  $e$  and  $f$  between these two cases, the use of the optical index from Bescond et al. [8] results in a slightly slower increase of both the MSF and the LDR with

increasing optical depth. This behavior may be explained by the lower single-scattering albedo in this case.

More differences appear when considering the results obtained using the optical index from Schnaiter et al. [9] as presented in Table IV.7. While the parameters  $c$  and  $f$  remain mostly unchanged, the parameters  $b$  and  $e$  increase by a factor  $\approx 2,3$  when compared to the results presented in Table IV.5. This indicates that the MSF and LDR of these aggregates present a steeper increase with increasing optical depth.

Using Equations IV.3.3(a) and (b), the MSF can be expressed as a function of the LDR such as :

$$MSF(\delta_v) = a + b \left( \frac{\delta_v - d}{e} \right)^{c/f} \quad (IV.3.4)$$

The evolution of the MSF with the LDR is presented on Figures IV.7, IV.8 and IV.9. These three figures pertain to the results obtained while considering soot aggregates whose radiative properties are computed using the dispersion law from Chang and Charalampopoulos [7] and the optical indices from Bescond et al. [8] and Schnaiter et al. [9] respectively.

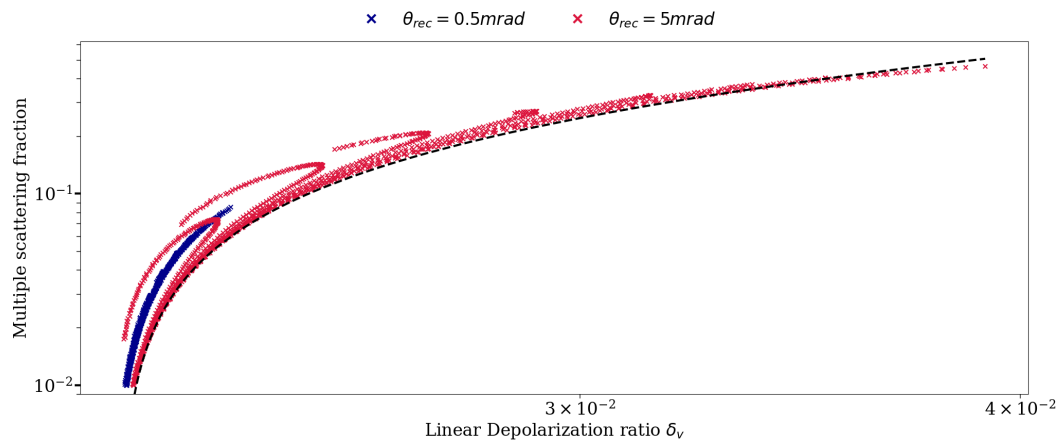
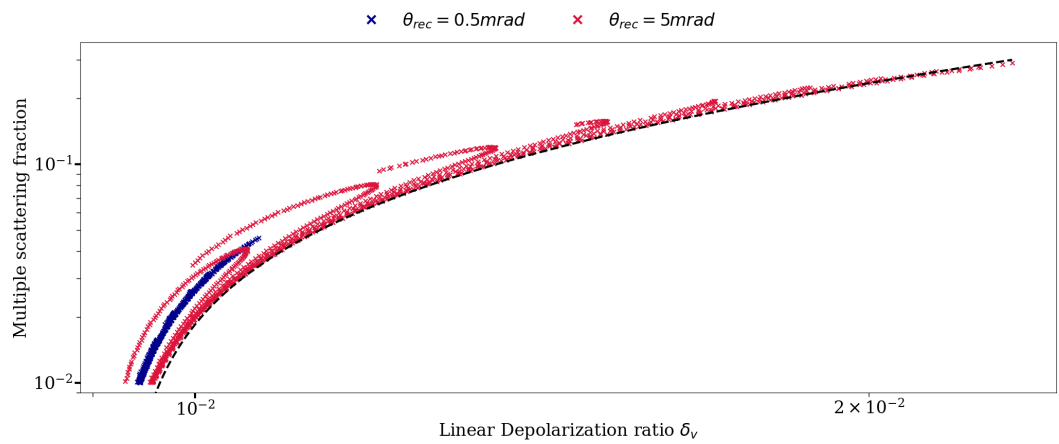
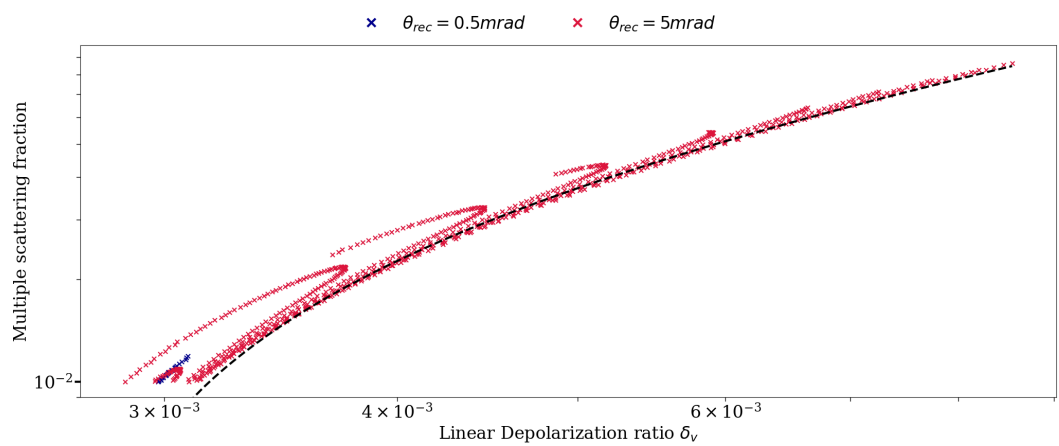
(a)  $\lambda = 355$  nm(b)  $\lambda = 532$  nm(c)  $\lambda = 1064$  nm

Figure IV.7: MSF as a function of the LDR. The dashed lines represent the MSFs resulting from the application of Equation IV.3.4 using the parameters presented in Table IV.5, computed using the dispersion law from Chang and Charalampopoulos [7].

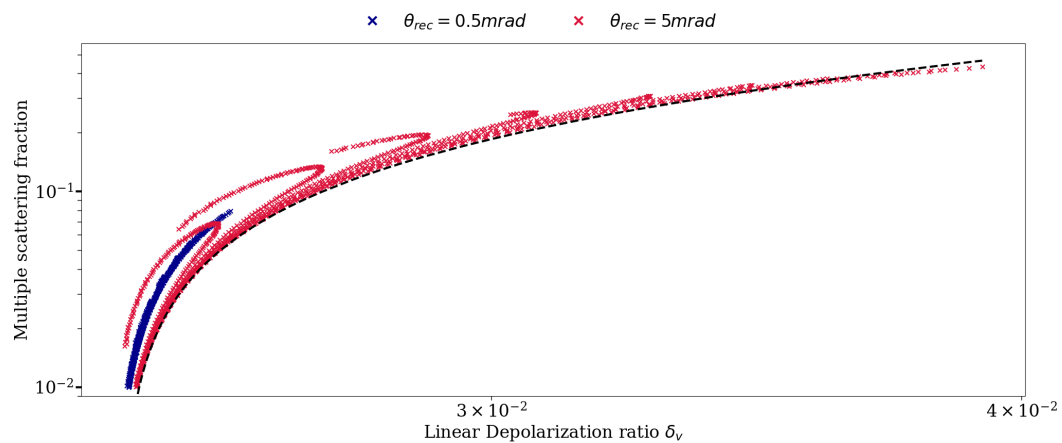
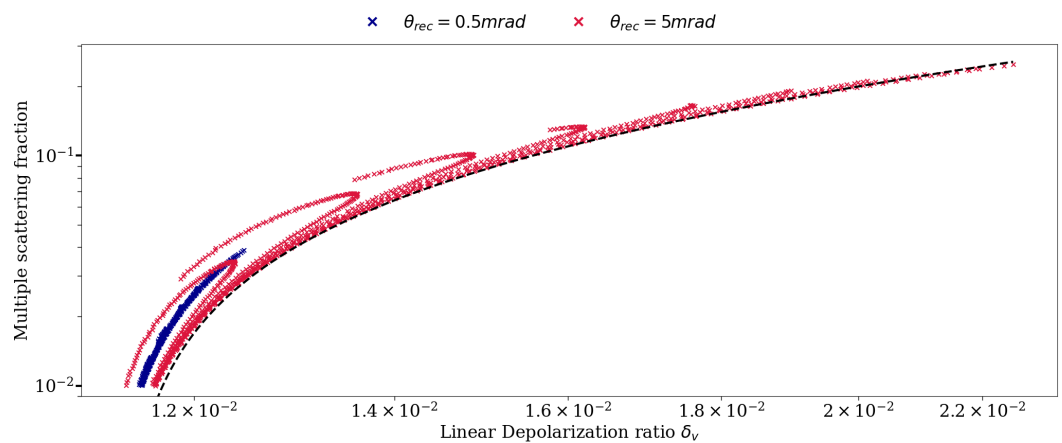
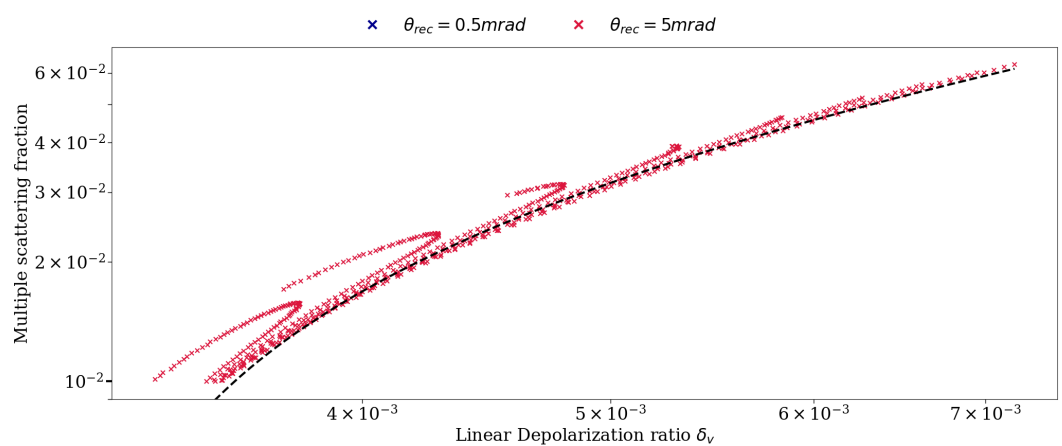
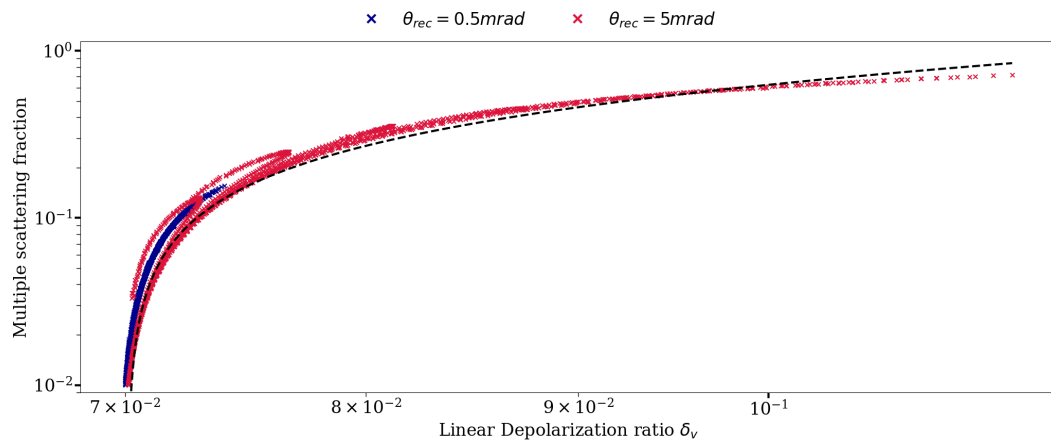
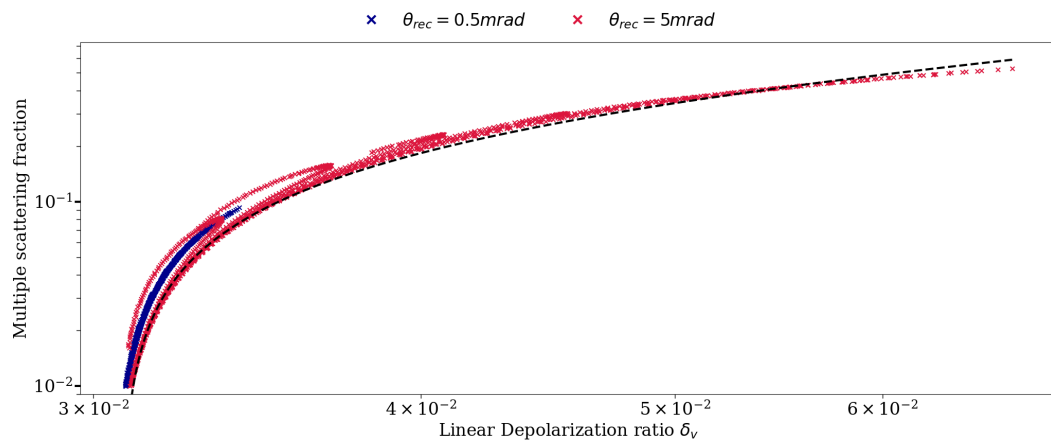
(a)  $\lambda = 355$  nm(b)  $\lambda = 532$  nm(c)  $\lambda = 1064$  nm

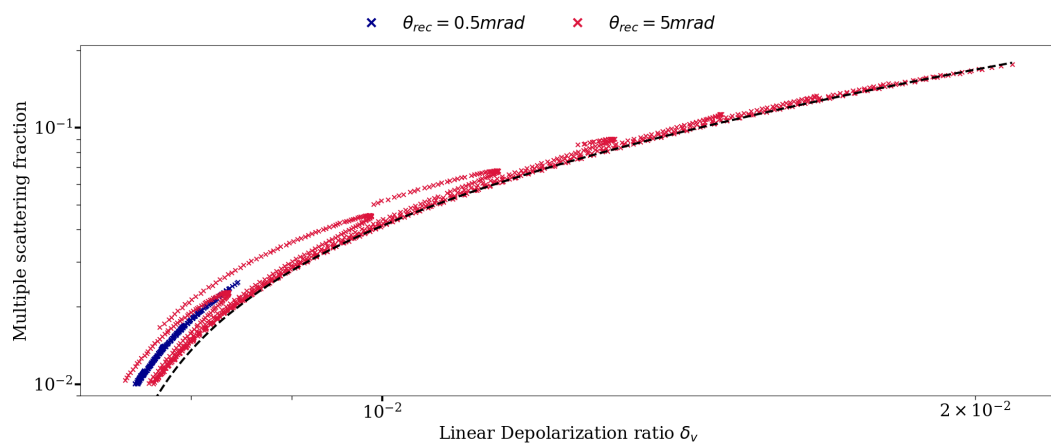
Figure IV.8: MSF as a function of the LDR. The dashed lines represent the MSFs resulting from the application of Equation IV.3.4 using the parameters presented in Table IV.6, computed using the optical index from Bescond et al. [8].



(a)  $\lambda = 355 \text{ nm}$



(b)  $\lambda = 532 \text{ nm}$



(c)  $\lambda = 1064 \text{ nm}$

Figure IV.9: MSF as a function of the LDR. The dashed lines represent the MSFs resulting from the application of Equation IV.3.4 using the parameters presented in Table IV.7, computed using the optical index from Schnaiter et al. [9].

Figures IV.7, IV.8 and IV.9 show that the evolution of the MSF with the LDR follows the relationship expressed in Equation IV.3.4. On these figures, Equation IV.3.4 is represented in dashed lines while using the parameters obtained for a receiver FOV of  $\theta_{rec} = 5$  mrad (see Tables IV.5, IV.6 and IV.7). Overall, these relationships express a minimum expected value of the MSF according to the simulated LDR. Indeed the MSF are almost always found higher than the ones expressed by the relationship for the same LDR value. On Figure IV.6, the MSF and LDR also show a decrease after attaining a maximum in some cases. This feature is also present on Figures IV.7, IV.8 and IV.9, but is conveyed here by the departure of the data points from the relationship curves.

Overall, these simulations allow to identify the impact of multiple scattering on the lidar signal measured in soot plumes. Indeed, these figures show that the multiple scattering can account for a non-negligible fraction of the return signal, from a few percent to several tens of percent according to the optical depth of the plume and according to the wavelength and optical index. Moreover, the LDR is also affected by multiple scattering effects, and can be subject to an increase by a factor two. However, the LDR remains low in the cases simulated with the optical index from Bescond et al. [8] and the dispersion law from Chang and Charalampopoulos [7], and its increase due to multiple scattering may not be discernible within experimental uncertainties. The cases simulated using the optical index from Schnaiter et al. [9] are presented here as a continuation of the results presented in Section II.2.3. In these cases, the LDR is found to reach values of  $\delta_v \approx 0.14$  at  $\lambda = 355$  nm with a multiple scattering fraction  $MSF \approx 0.65$  while using a monomer mean geometrical radius of  $R_m = 20$  nm. In Section II.2.3, such values of the LDR were only attained using the same optical index but with a monomer mean geometrical radius of  $R_m = 25 - 30$  nm. Although the experiment described in Section II.2 did not allow for the evaluation of either the plume optical depth profile or its concentration profile, these considerations lead to the possibility that multiple scattering effects may have occurred within this experiment.

In order to investigate the effect of the plume concentration profile, all the simulations described above have been undertaken once more, but considering a square concentration profile. As such, the interacting medium is modeled using three slabs. The first and last slabs are simulated with a null extinction coefficient, hence preventing the simulation of light-matter interaction

within these slabs. The second slab contains the modeled soot aggregates radiative properties, and its extinction coefficient is computed such as  $\alpha = \tau_{max}/(r_{max} - r_0)$ . Otherwise, all the simulation parameters described in Table IV.4 are kept identical, and the same radiative properties as those presented in Tables IV.1, IV.2 and IV.3 are used. Figure IV.10 presents a single example of the MSF as a function of the LDR for a square plume, at the wavelength  $\lambda = 532$  nm and considering soot aggregates whose radiative properties are computed using the dispersion law from Chang and Charalampopoulos [7].

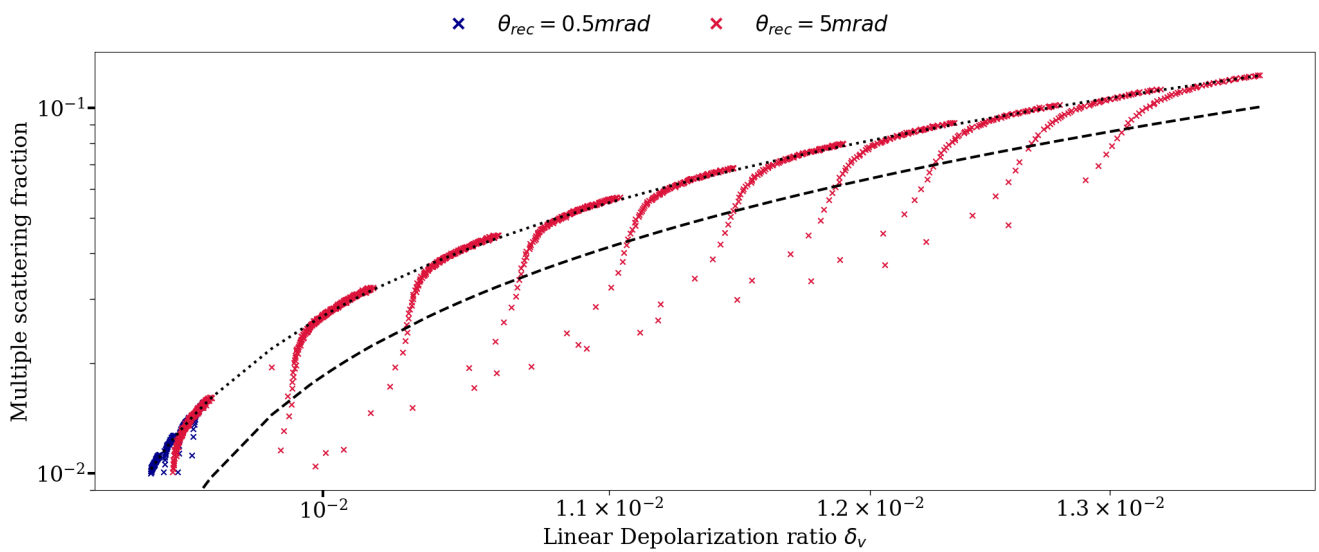


Figure IV.10: MSF as a function of the LDR using a square plume profile. The dashed line represents the MSFs resulting from the application of Equation IV.3.4 using the parameters presented in Table IV.5. The dotted line represents the results from a non-linear regression aiming to reproduce the observable trend.

Figure IV.10 shows that the use of Equation IV.3.4, *i.e.* the dashed line, with regression parameters stemming from a gaussian plume profile results in an underestimation of the MSF when applied to a square plume profile. This feature is also present in all the other simulation cases, but these cases are not presented here for the sake of brevity. These differences may be explained by differences in the multiple scattering effect itself during the simulations. Kahnert and Scheirer [181] make the distinction between two types of multiple scattering; (i) regular multiple scattering in which the photon path remains within the receiver FOV and is dominated by near-forward and near-backward scattering events and (ii) irregular multiple scattering in which the

photon path leads to the outside of the receiver FOV. Indeed, it can be envisioned that the differences between the two plume profiles may result in a larger proportion of irregular scattering within the square plume due to its constant extinction coefficient. However, the Monte-Carlo program does not provide the ability to distinguish between regular and irregular multiple scattering, which makes this interpretation hardly verifiable.

To express the relationship between the MSF and the LDR in the square profile case, Equation IV.3.4 is reformulated in order to reduce the number of parameters such as :

$$MSF(\delta_v) = a' + b'(\delta_v - d')^{c'} \quad (IV.3.5)$$

where by comparison with Equation IV.3.4, the new coefficients are expressed as  $a' = a$ ,  $b' = b/e^{c/f}$ ,  $d' = d$  and  $c' = c/f$ . This equation is then used to undertake a regression analysis, whose results are represented by the dotted line on Figure IV.10. Table IV.8 summarizes the values of the coefficients obtained through this regression analysis.

$\lambda(\text{nm})$	$m_0$	$a'$	$b'$	$c'$	$d'$
355	Bescond et al. [8]	$-9.82 \cdot 10^{-2}$	$1.14 \cdot 10^1$	$7.07 \cdot 10^{-1}$	$2.33 \cdot 10^{-2}$
355	Schnaiter et al. [9]	-1.41	4.00	$2.00 \cdot 10^{-1}$	$6.43 \cdot 10^{-2}$
355	Chang and Charalampopoulos [7]	$-8.94 \cdot 10^{-2}$	$1.14 \cdot 10^1$	$7.14 \cdot 10^{-1}$	$2.10 \cdot 10^{-2}$
532	Bescond et al. [8]	$-6.32 \cdot 10^{-2}$	$1.03 \cdot 10^1$	$7.85 \cdot 10^{-1}$	$9.69 \cdot 10^{-3}$
532	Schnaiter et al. [9]	$-3.03 \cdot 10^{-1}$	4.48	$5.08 \cdot 10^{-1}$	$2.56 \cdot 10^{-2}$
532	Chang and Charalampopoulos [7]	$-8.39 \cdot 10^{-2}$	9.25	$7.56 \cdot 10^{-1}$	$7.12 \cdot 10^{-3}$
1064	Bescond et al. [8], Schnaiter et al. [9] and Chang and Charalampopoulos [7]	-	-	-	-

Table IV.8: Parameters of the regression analysis for the simulations undertaken with a square profile, considering a receiver FOV  $\theta_{rec} = 5$  mrad.

The curve obtained through this regression analysis is found to accurately represent the evolution of the MSF with increasing LDR. However, this correspondence is only achieved after a first transition regime. This transition regime occurs in the lower region of the plume. In this region, single-scattering events account for the majority of the return signal. The proportion of the return signal due to multiple scattering then progressively increases, until reaching the regime which leads to the phenomenological relationship described by Equation IV.3.5. To visualize this contribution, Figure IV.11 presents the single-scattering and multiple scattering contributions to

the total signal as a function of range.

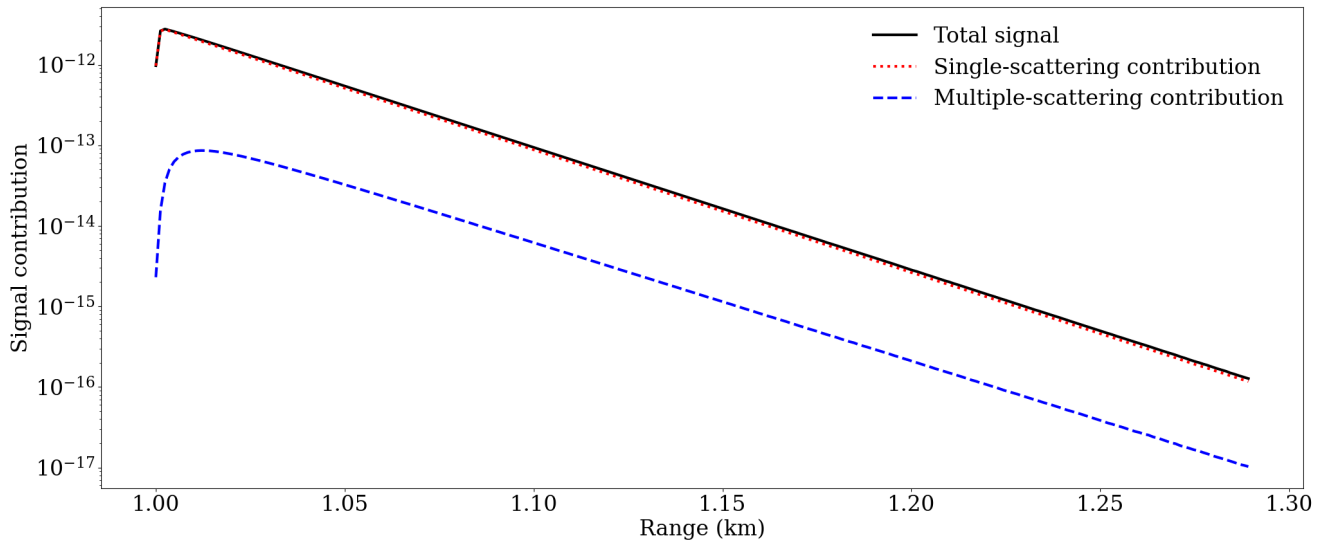


Figure IV.11: Single-scattering and multiple scattering contributions to the the total signal using a square plume profile. The scattering medium radiative properties have been computed using the dispersion law from Chang and Charalampopoulos [7], at  $\lambda = 532$  nm, and with a maximal optical depth  $\tau_{max} = 5$ .

The simulations presented in this section allow to determine phenomenological relationships, but their applicability remains limited. Indeed, although their formulations are common to all the considered cases, the equation parameters vary according to several parameters. In particular, a variation of the optical index induces large disparities. Moreover, the plume concentration profile also introduces variations in these parameters. Hence, in order to apply these relationships, a large number of *a priori* information about the interacting medium are needed, including the particles morphology, optical index and the plume concentration profile. Hence, larger scale sensitivity studies may be required in order to assess the influence of each parameter on the coefficients of these relationships. This could lead to a more general formulation that explicitly depends on variables such as the optical index or the plume optical depth.

Although no general formulations have been found, Monte-Carlo simulations can still be useful in more specific cases. Indeed, simulations may also be undertaken in order to analyze experimental lidar signals that have already been subject to inversion methods. This allows to use the inverted extinction coefficient profiles in order to model the interacting medium, allowing to

evaluate whether multiple scattering effects may have impacted the experimental signal. Such an analysis is presented in the following section.

## IV.4 Analysis of an experimental lidar signal through Monte-Carlo modeling

The experimental signal used in this section was acquired using the Colibri instrument [92, 124]. The experimental results and the methods used to achieve them are currently under review and should be presented in reference [182]. In this section, the objective is to use already inverted experimental lidar signals in order to proceed to Monte-Carlo simulations. As such, only the light scattering model, the modeled radiative properties and the inverted signals are presented, but the reader is invited to refer to the references above for more details on the measurement and inversion methods. The inverted extinction coefficients are used in order to produce a profile compatible with the Monte-Carlo lidar signal simulation program. The simulation undertaken using this profile then allows to evaluate the multiple scattering contribution to the signal, and hence whether multiple scattering effects may have influenced the inversion procedure.

To model the radiative properties of soot aggregates, the RDG-FA theory is used. Based on the TEM measurements presented in reference [182], the monomer mean geometrical radius is  $R_m = 23.8 \pm 0.4$  nm and the mean number of monomers is  $N_m = 100 \pm 10$ . For the purpose of the radiative properties calculation presented here, only the mean values are considered, and the monomer radius polydispersity is not accounted for. The fractal dimension is  $D_f = 1.7$  and the fractal prefactor is  $k_f = 2.2$ . The radiative properties are computed at the wavelength  $\lambda = 355.8$  nm, considering an optical index  $m_o = 1.66 + i0.76$ . This optical index corresponds to uncoated, freshly-emitted soot aggregates, and stems from the model proposed by Kelesidis et al. [183].

According to Equation 1.2.40, the structure factor is needed for the computation of the differential scattering cross-section. In this section, the structure factor is computed following the formulation from Dobbins and Megaridis [184]. As such, the structure factor is expressed as :

$$S(qR_g) = \begin{cases} \exp\left[-\frac{(qR_g)^2}{3}\right] & \text{if } (qR_g)^2 < \frac{3}{2}D_f \\ \left[\frac{3D_f}{2e(qR_g)^2}\right]^{\frac{D_f}{2}} & \text{if } (qR_g)^2 > \frac{3}{2}D_f \end{cases} \quad (\text{IV.4.1})$$

The scattering function  $F(m_o)$  and the absorption function  $E(m_o)$  are then computed following Equation I.2.35. The extinction cross-section can then be calculated using Equations I.2.17, I.2.33 and I.2.34. Finally, the scattering matrix is computed by adapting Equation I.2.40 in order to include the elements of the Rayleigh scattering matrix defined in Equation III.3.1 such as :

$$\mathbf{F}(\theta) = N_m^2 \frac{8\pi^4 R_m^6}{\lambda^4} F(m_o) S(\theta) \begin{bmatrix} 1 + \cos^2 \theta & \cos^2 \theta - 1 & 0 & 0 \\ \cos^2 \theta - 1 & 1 + \cos^2 \theta & 0 & 0 \\ 0 & 0 & 2 \cos(\theta) & 0 \\ 0 & 0 & 0 & 2 \cos(\theta) \end{bmatrix} \quad (\text{IV.4.2})$$

which, for  $\theta = \pi$ , verifies the formulation of the RDG-FA backscattering cross-section defined in Equation I.2.41. Table IV.9 presents the values of the extinction cross-section, of the backscattering cross-section and of the lidar ratio calculated following this method.

$C_{ext}(\text{nm}^2)$	$dC_{bac}(\text{nm}^2.\text{sr}^{-1})$	$LR(\text{sr})$
8303.3	637	130.4

Table IV.9: Radiative properties of the modeled soot aggregates using the RDG-FA theory.

The values obtained using this method and these parameters are well within the uncertainties of the values used in the inversion of the lidar signal presented in reference [182]. As such, the assumption is made that the radiative properties presented in Table IV.9 and that the scattering matrix computed following Equation IV.4.2 can be used in order to simulate this lidar signal using the Monte-Carlo program.

The following step consists in reproducing the experimental lidar signal extinction coefficient profile. In order to do so, the results of the lidar inversion method presented in [182] are used. These results consist in the backscattering and extinction coefficient profiles,  $\beta_{aer}(r)$  and  $\alpha_{aer}(r)$ , averaged over 4 ms. Figures IV.12 represent the inverted backscattering coefficient and extinction

coefficient profiles.

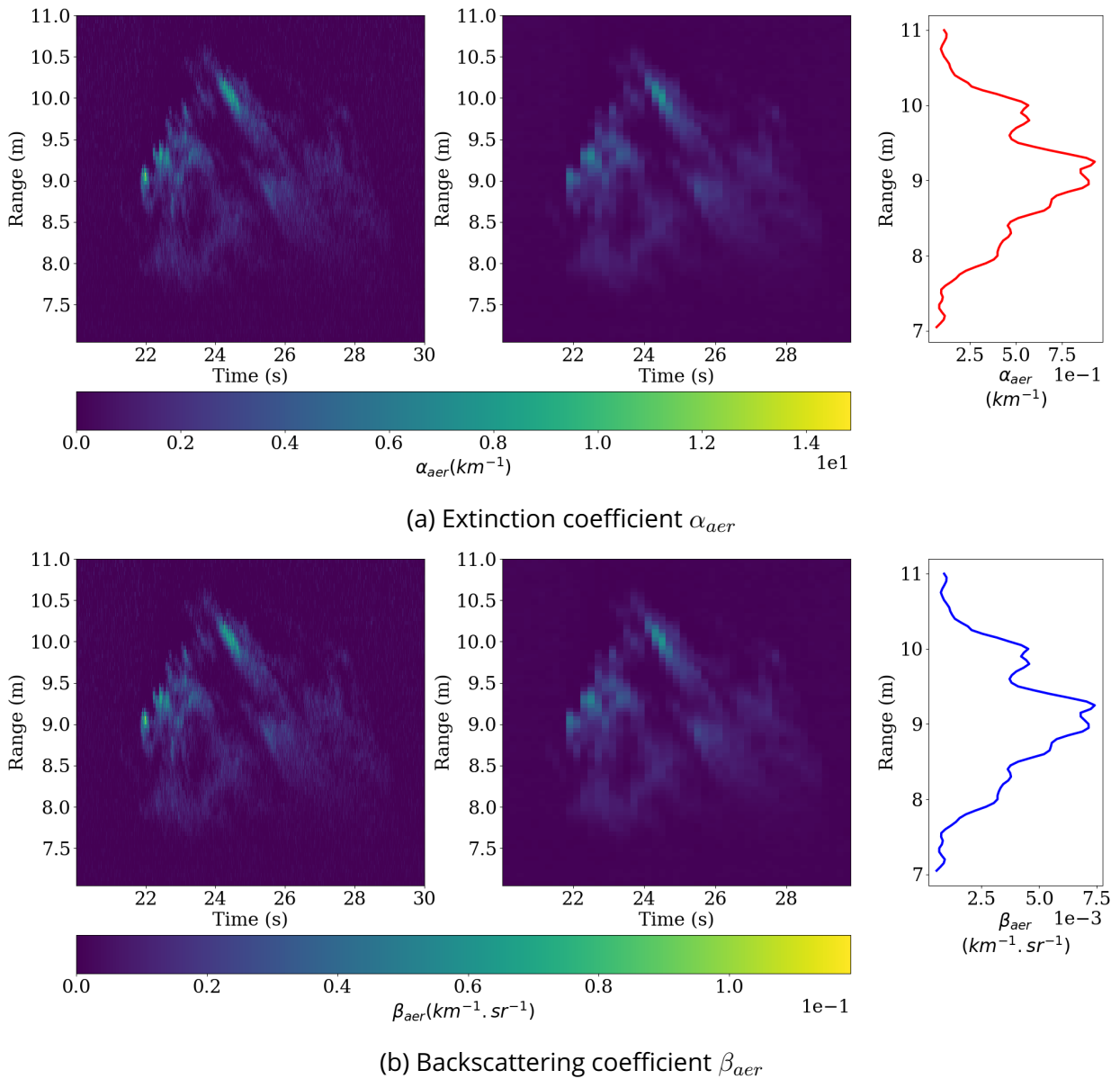


Figure IV.12: Extinction and backscattering coefficients resulting from the lidar inversion procedure. The left-hand side figures represent the profiles averaged over 4 ms, the central figures profiles are averaged over 200 ms, while the right-hand side figures represent the profile average over 10 s.

This figure highlights the presence of a smoke plume at a distance ranging from  $\approx 7$  m to  $\approx 11$  m of the lidar instrument. The left-hand side figures represent the extinction and backscattering profiles which stem directly from the lidar signal inversion procedure. As such, the time step between two profiles is of 4 ms. In order to reduce the number of profiles calculated in the Monte-Carlo program, these profiles have been averaged over 200 ms. These time-averaged profiles are

represented on the central figures. Moreover, the right-hand side figures represent the profiles averaged over the whole 10 s range.

The time-averaged extinction coefficient profiles can then be used in order to model the interacting medium within the Monte-Carlo program. However, several other parameters are needed in order to proceed to the simulations. In particular, the instrument geometry needs to be accounted for. Although the Colibri instrument presents a bi-static architecture, a monostatic lidar configuration is considered here as the Colibri instrument is designed in order to obtain a full overlap function at the distance of the plume (*i.e.*  $\approx 10$  m). Finally, the values of the instrument parameters as well as the Monte-Carlo parameters are presented in Table IV.10.

Emitter parameters		Receiver parameters	
Parameter	Value	Parameter	Value
$\theta_{em}$	0.5 mrad	$R_{rec}$	0.045 m
$R_{em}$	0.001 m	$\mathbf{d}_{rec}$	$[0\ 0\ 1]^T$
$L_{em}$	0.18 m	$\theta_{rec}$	1 mrad
$\mathbf{p}_{em}$	$[0\ 0\ 0]^T$	$t_{min}$	7 m
$\mathbf{d}_{em}$	$[0\ 0\ 1]^T$	$t_{max}$	11 m
$\mathbf{l}_{em}$	$[1\ 1\ 0\ 0]^T$	$\Delta t$	0.05 m
Monte-Carlo parameters			
$N_{ph}$	$10^9$	$\theta_{cone}$	$1.15\theta_{rec}$
$\theta_{split}$	$90^\circ$	$R_{cone}$	0.045 m
$\zeta$	$90^\circ$	$j_{max}$	3

Table IV.10: List of the input parameters of the Monte-Carlo program.

Figure IV.13 presents the MSF obtained from these simulations. The MSF shows identical features to the backscattering and extinction coefficients presented on Figure IV.12. The MSF is found higher in the region with larger extinction coefficients. However, the MSF presents very low values, under the tenth of percent. This behavior is expected considering the limited scale of the smoke plume. Although extinction coefficients up to  $7\text{ km}^{-1}$  are found within the time-averaged smoke plume (see Figure IV.12(a), right-hand side figure), the plume optical depth remains low due to its small scale. Hence, these simulations allow to provide evidence that, during this measurement campaign, the multiple scattering effect did not significantly influence the lidar signal. This analysis hence serves to confirm the single-scattering approximation that is used during the

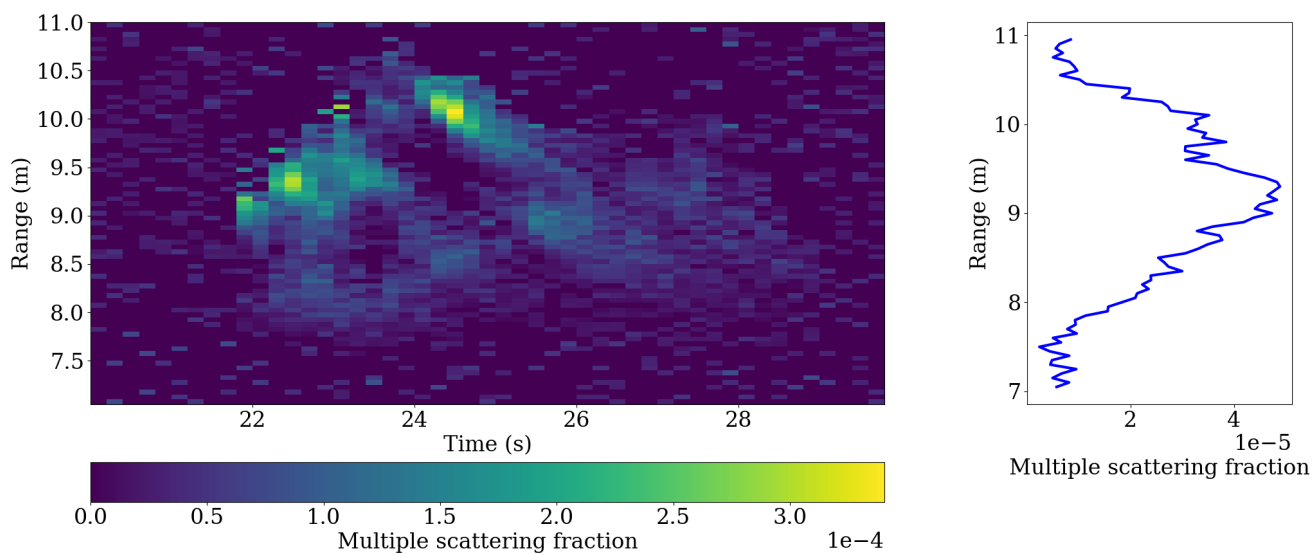


Figure IV.13: Multiple scattering fraction and time averaged multiple scattering fraction resulting from the Monte-Carlo simulation.

inversion of the lidar signal.

## Conclusion

This chapter is dedicated to the simulation of multiply-scattered lidar signals of soot particles using the Monte-Carlo program described in Chapter III. These simulations require to take into account the radiative properties of soot particles, which is achieved as part of Chapter II. As part of the computation of these radiative properties, several optical indices commonly used in the literature have been considered. Several investigations have been undertaken to study the influence of multiple scattering on these simulated lidar signals.

The first investigation has led to the computation of the multiple scattering correction factors introduced by Platt [133] for soot particles. The simulations undertaken have shown that this correction factor model does allow for the correction of the single-scattering signal in order to reproduce the results from the Monte-Carlo simulations. Moreover, shortcomings of the Monte-Carlo lidar signal simulation program have also been highlighted during this investigation. In particular, the need for a stretching variance reduction technique is evidenced by the observed instabilities in slabs with low extinction coefficients.

In the second investigation, the multiple scattering fraction and the linear depolarization ratio have been put under study. Specifically, the variations of these two parameters with the plume of optical depth follow relationships whose forms remain identical with different wavelengths, optical indices or receiver field-of-view. Moreover, the variation of the multiple scattering fraction with the linear depolarization ratio also follows a relationship whose formulation remains identical with a change of plume profile. However, any change of wavelength, optical index, receiver FOV or plume profile induces a modification of the coefficients of these relationships, hence reducing their applicability.

Finally, extinction coefficients stemming from the inversion of an experimental lidar signal have been used in order to assess the possible influence of multiple scattering within the soot plume. A negligible fraction of the numerical signal has been found to be due to multiple scattering effects. The procedure undertaken can be adapted to other signals acquired over soot particles, and hence allows to further refine the error estimation during lidar measurements and to assess whether the single-scattering approximation is verified.

Overall, it has been found within this chapter that multiple scattering only influences lidar signals in cases with large optical depth. This behavior is most likely due to the low single-scattering albedo of soot particles, which makes multiple scattering quite improbable. Moreover, the results remain strongly dependent on parameters such as the optical index or the plume profile, although some general formulations of the relationships between different quantities have been identified. Hence, larger scale sensitivity analyses would be required in order to evaluate the impact of each variable.

## **General conclusion and prospects**

The objective of this thesis has been to evaluate the impact of multiple scattering effects on polarization-resolved lidar signals measured on soot particle plumes. A numerical modeling approach has been undertaken in to assess this impact. However, such numerical studies require the knowledge of the scattering particles radiative properties, as well as a numerical model allowing to simulate the lidar signals themselves. As such, this thesis has been articulated according to these three axes: (i) the modeling of soot particles radiative properties, accounting for different types of morphologies; (ii) the development of a lidar signal simulation program, allowing to account for the signal polarization and for multiple scattering; (iii) the analysis of lidar signals when simulated with an interacting medium composed of soot particles. In the following paragraphs, a summary of the achievements relevant to these three axes is provided. This summary is also accompanied with perspectives and prospects that could provide further insights.

### **Soot particles radiative properties**

In this thesis, several studies have been undertaken in order to model the radiative properties of soot fractal aggregates. To model these radiative properties, the aggregate morphology is needed. As such, two different types of aggregate morphology have been studied. The first type of aggregate is referred to as standard aggregates and follows a fractal-like power-law relationship that links different morphological parameters, namely the fractal dimension, the fractal prefactor, the number of monomers, the monomer radius and the radius of gyration. The second type of aggregate put under study consists in a superaggregate. This type of aggregate can be envisioned as a particle resulting from the aggregation of several standard aggregates. As such,

it presents a larger number of monomers, and can present several distinct fractal dimensions at different length scales. Moreover, these two types of aggregates can be composed of either monodisperse monomers or polydisperse monomers. While the effect of polydispersity has been briefly put under study in the case of standard aggregates, it has not been considered for hybrid aggregates. Moreover, only one realization of superaggregate has been studied in this thesis, which did not allow to study the variability of its radiative properties. Hence, a first conceivable prospect would be to study the radiative properties of ensembles of superaggregates, the impact of monomer polydispersity on these radiative properties.

The first study presented in Section II.1.2 has consisted in generating ensembles of standard aggregates composed of monodisperse monomers and to study the resulting radiative properties over wavelengths ranging from  $\lambda = 300$  nm to  $\lambda = 1100$  nm. The radiative properties have been computed with the STM method using the MSTM code of Mackowski and Mishchenko [138], as this method provides accurate results when considering particle morphologies consisting in spheres in point-contact. This study has shown that a variation of the monomer radius could significantly alter the radiative properties of soot aggregates, with an increase of radius resulting in larger backscattering, scattering and extinction cross-sections, larger LDR and lower lidar ratio. An increase of the number of monomers has also shown to induce the same impacts although to a lesser degree. Finally, a variation of the fractal dimension only marginally alters the radiative properties when compared to other morphological parameters. The computation of the ensemble-averaged radiative properties has allowed to investigate the resulting standard deviations. Appendix A provides an evaluation of the standard deviation of the backscattering cross-sections of standard aggregates. A conclusion of this study is that ensembles containing  $\approx 50$  aggregate realizations may be sufficient in order to accurately assess the standard deviations and mean values of the radiative properties of soot aggregates, although a sensitivity study at a larger scale may be beneficial.

The second study presented in Section II.1.4 compares the radiative properties of a hybrid aggregate with those of a standard aggregate. These radiative properties are computed using both the STM method and the RDG-FA theory. In the latter case, an algorithm allowing to com-

pute the structure factor of soot aggregates has been developed. During this study, it has been observed that the results stemming from calculations using the RDG-FA theory with standard aggregates are in agreement with the STM results when considering the extinction cross-sections, but that the scattering cross-sections are slightly overestimated while the backscattering cross-sections are slightly underestimated. However, when considering hybrid aggregates, all three cross-sections are overestimated by the RDG-FA theory, especially at short wavelengths. Finally, the radiative properties of the hybrid aggregate are found to be  $\approx 1 - 2$  orders of magnitude larger than those of the canonical aggregate. However, as stated above, only one realization of hybrid aggregate has been put under study, which did not allow for the evaluation of the standard deviations of the radiative properties. Moreover, only monodisperse aggregates have been considered. Hence, further work can be achieved by studying ensembles of hybrid aggregates and by also studying the impact of monomer polydispersity on their radiative properties.

Considering the standard aggregates, the impacts of monomer polydispersity are briefly presented throughout Sections II.1.3 and II.2 and are studied in more details within Appendix B. This appendix presents a comparison between the radiative properties of standard aggregates with monodisperse monomers with those of standard aggregates with monomer radius following a log-normal size distribution with a standard deviation of  $\sigma_m = 1.1$ . The consideration of monomer polydispersity seems to induce an increase of the cross-sections and of the LDR and a decrease of the lidar ratio. However, only one type of monomer radius size distribution using a single standard deviation value has been used during this study. As such, a more comprehensive assessment of the impact of polydispersity could be achieved by the realization of sensitivity studies accounting for these parameters.

The last study that is related to the radiative properties of soot aggregates consists in the experimental evaluation of the LDR of soot particles in ambient air, freshly emitted from a kerosene pool fire. During this study, which is presented in Section II.2, the LDR of soot particles has been evaluated at  $\delta_{lab} = 11.7 \pm 2.3 \%$  at  $\lambda = 355 \text{ nm}$  and  $\delta_{lab} = 8.7 \pm 2.1 \%$  at  $\lambda = 532 \text{ nm}$ . A numerical study aiming to reproduce these results is also associated to these measurements. As such, both monodisperse and polydisperse aggregates have been considered, with the monomer ra-

dus  $r_m \in [10, 30]$  nm ( $R_m \in [10, 30]$  nm in the polydisperse case with  $\sigma_m = 1.1$ ) and the monomer number  $N_m \in [20, 200]$ . Moreover, several optical indices have been considered during the radiative properties computations, which have been undertaken using the MSTM code. A correspondence between the numerical results and the experimental results could only be achieved using an optical index of  $m_o = 2.65 + i1.32$ . As this optical index corresponds to spark-generated soot, this result suggests that the morphological model used during these computations may not be sufficiently refined. Hence, several other morphological features may need to be accounted for during the computation of soot particles radiative properties, such as necking or overlapping. Although no coating material has been observed within the TEM samples, this effect may also lead to an increase in LDR [185, 186] and to a variation of the material optical index.

Overall, the results obtained highlight the need for a better characterization of the soot particles morphology and optical index. This requires the development of numerical models allowing to simulate morphologies that account for complex features such as necking, overlapping and coating. Such morphologies would require DDA calculations to compute their radiative properties, hence considerably increasing the computational cost of such studies.

## Lidar signal simulation code

A Monte-Carlo code for the simulation of polarization-resolved lidar signals accounting for multiple scattering has been developed and is presented in Chapter III. As described in Sections III.1 and III.2, this code consists in simulating the transport and scattering of photons throughout an interacting medium, and in determining the resulting lidar signal by modeling the instrument geometry and computing the contribution of each photon to the signal. Several variance reduction techniques have been implemented in order to increase the computational efficiency of the program, namely absorption weighting (continuous and discrete), scattering splitting and peel-off scattering.

Validation procedures have been undertaken in order to assess the program performance. At first, the angle sampling method and the scattering splitting technique have been individually investigated within Section III.3.1. The scattering splitting technique increases the agreement

between the sampled Stokes vectors and the analytically derived ones. However, depending on the angle at which the phase function is split, large discrepancies can be observed. This indicates that care must be taken when choosing this scattering splitting angle.

A second validation procedure presented in Section III.3.2 has aimed at comparing the single-scattering signal obtained with the Monte-Carlo code with a single-scattering signal computed analytically. Results have shown a good agreement between these two methods. However, at large optical depth  $\tau > 7$ , the Monte-Carlo code has proven unable to provide a stable signal that resembles the analytical one. This behavior can be attributed to a lack of photons propagating within the outer regions of the cloud, resulting in few photons contributing to the received signal in these regions. In order to overcome this shortcoming of the code, a stretch variance reduction technique could be implemented in order to increase the path length of the simulated photons in regions with large extinction coefficients.

The last validation procedure consists in comparing results presented in the literature with those obtained using the code developed during this thesis. As such, several cases of water droplet clouds with various optical depths and distributions are simulated, while considering lidar instruments with different FOV and which are either ground-based or space-based. The reference from which stem the simulation cases, *i.e.* the article from Hu et al. [176], presents a relationship between the accumulated single-scattering fraction and the accumulated depolarization ratio. The results obtained using the Monte-Carlo code have been found to follow this relationship, but differences have been found when comparing these results case by case with those presented in reference [176]. The origins of these differences could not be identified, although they most likely stem from differences within the methods used for the computation of the lidar signals themselves.

Overall, the simulation code developed within this thesis allows to model polarization-resolved lidar signals using an interacting medium relevant to soot particles. Nevertheless, several features that could improve this program have been identified. First and foremost, stretch methods can provide means to increase the program accuracy in media with large optical depths by increasing the path lengths of photons, and in media with low optical depths by decreasing these

path lengths. The peel-off scattering method can also be extended in order to include the contributions of several scattering orders at the vicinity of each interaction event [168]. Finally, the interacting medium geometry can also be improved by modeling cells rather than slabs or by implementing the continuous variations of the radiative properties within one slab.

## **Simulated lidar signals**

The final chapter of this thesis combines the methodology presented in Chapter II for the computation of soot particles radiative properties with the simulation code described in Chapter III to simulate polarization-resolved lidar signals accounting for multiple scattering. As presented in Section IV.2, the use of the multiple scattering correction factors introduced by Platt [133] accurately correct the single-scattering signal as expected. The values of these correction factors have been found to vary strongly according to the optical index of the interacting particles and according to the optical depth of the smoke plume. Hence, multiple scattering has been found to induce an increase of the backscattered power and of the LDR in lidar signals simulated with scattering medium composed of soot particles. However, this investigation has also highlighted the need of refinement of the Monte-Carlo program by a introducing stretch variance reduction technique.

In Section IV.3, phenomenological relationships are derived from the evolutions of the multiple scattering fraction and of the LDR with increasing plume optical depth. All simulation cases are found to follow relationships of the same form, although the coefficients of the relationships strongly depend on the optical index of the particles and on the wavelength. Moreover, the evolution of the multiple scattering fraction according to the LDR has also been found to follow a relationship, whose form remains identical whether the interacting plume follows a square concentration profile or a gaussian concentration profile. Hence it appears that a formulation of this relationship could be extended in order to directly include parameters relevant to the radiative properties of the particles or of the plume profile. Such an endeavor would require a large scale sensitivity analysis.

Section IV.4 presents simulated lidar signals which have been modeled in order to reproduce

an experimental lidar signal. This signal has been acquired using a kerosene pool fire as the source of the soot particles. The RDG-FA theory has been used in order to model the particles scattering matrix and radiative properties, and using the extinction coefficients that have been inverted from the experimental signal. The simulations undertaken using these parameters have shown that the contribution of multiple scattering effects is limited, and accounts for less than 0.1 % of the lidar signal. Although multiple scattering effects do not seem to impact the lidar signal in this particular case, such an analysis still allows to refine the error estimation during the inversion process by confirming the single-scattering approximation validity. Still, a larger number of experimental polarization-resolved lidar signals would be useful in order to assess if the impact of multiple scattering found during the numerical simulations can be experimentally verified.



## Appendix A

# Standard deviation of the backscattering cross-sections of aggregates composed of monodisperse monomers

In this appendix, the standard deviations of the backscattering cross-sections are represented , considering the simulation parameters and results presented in Section II.1.2. The standard deviations are presented under their relative formulation, which are expressed as :

$$\begin{aligned}\sigma_{bac,rel}(N_a) &= 100 \frac{\sigma_{bac}(N_a)}{\langle C_{bac} \rangle_{N_a}} \\ &= 100 \frac{\sqrt{\frac{\sum_{i=1}^{N_a} (C_{bac,i} - \langle C_{bac} \rangle_{N_a})^2}{N_a}}}{\langle C_{bac} \rangle_{N_a}}\end{aligned}\tag{A.1}$$

where :

$$\langle C_{bac} \rangle_{N_a} = \frac{1}{N_a} \sum_{i=1}^{N_a} C_{bac,i}\tag{A.2}$$

where  $C_{bac,i}$  is the backscattering cross-section of the  $i^{\text{th}}$  aggregate realization, and  $N_a$  is the number of aggregate realization considered in the averaging, *i.e.* the number of aggregate in the ensemble. The dependencies on the micro-physical parameters  $N_m$ ,  $r_m$  and  $D_f$  are implied in the the two equations above. Figures A.1 to A.3 present the relative standard deviation of the backscattering cross-sections, for all the considered sets of micro-physical parameters.

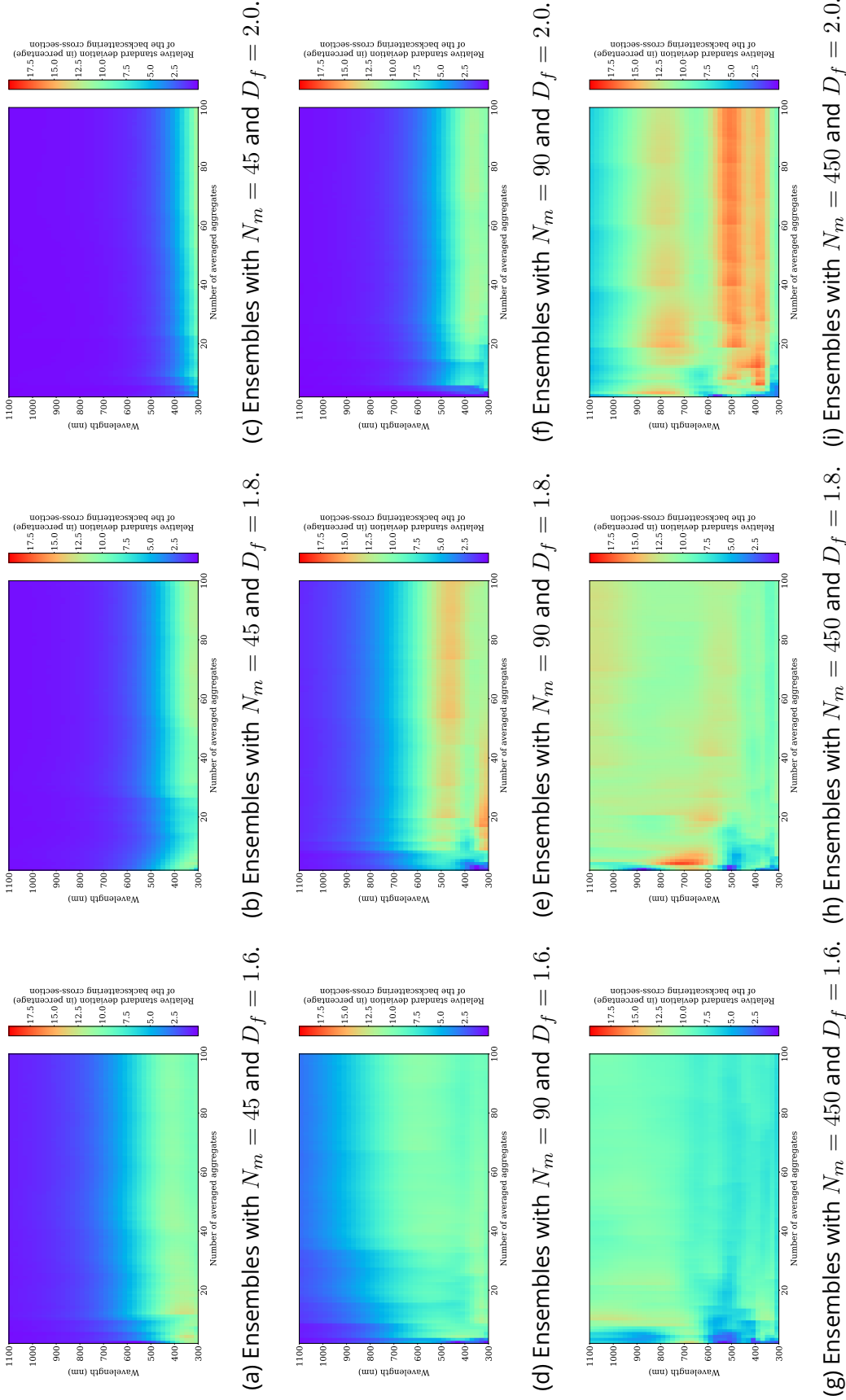


Figure A.1: Relative standard deviation of the backscattering cross-section, for aggregates with monodisperse monomers and with  $r_m = 10$  nm.

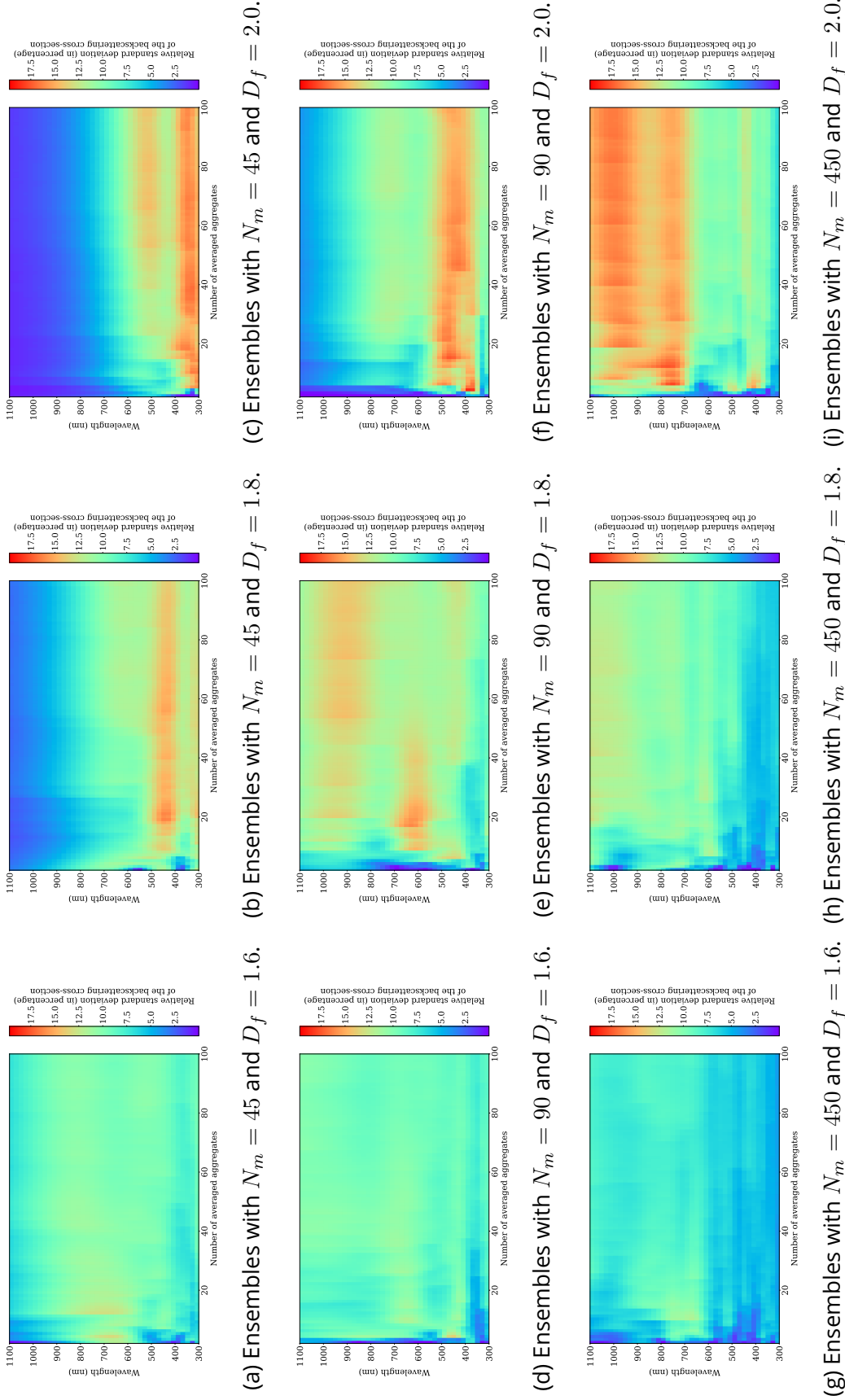
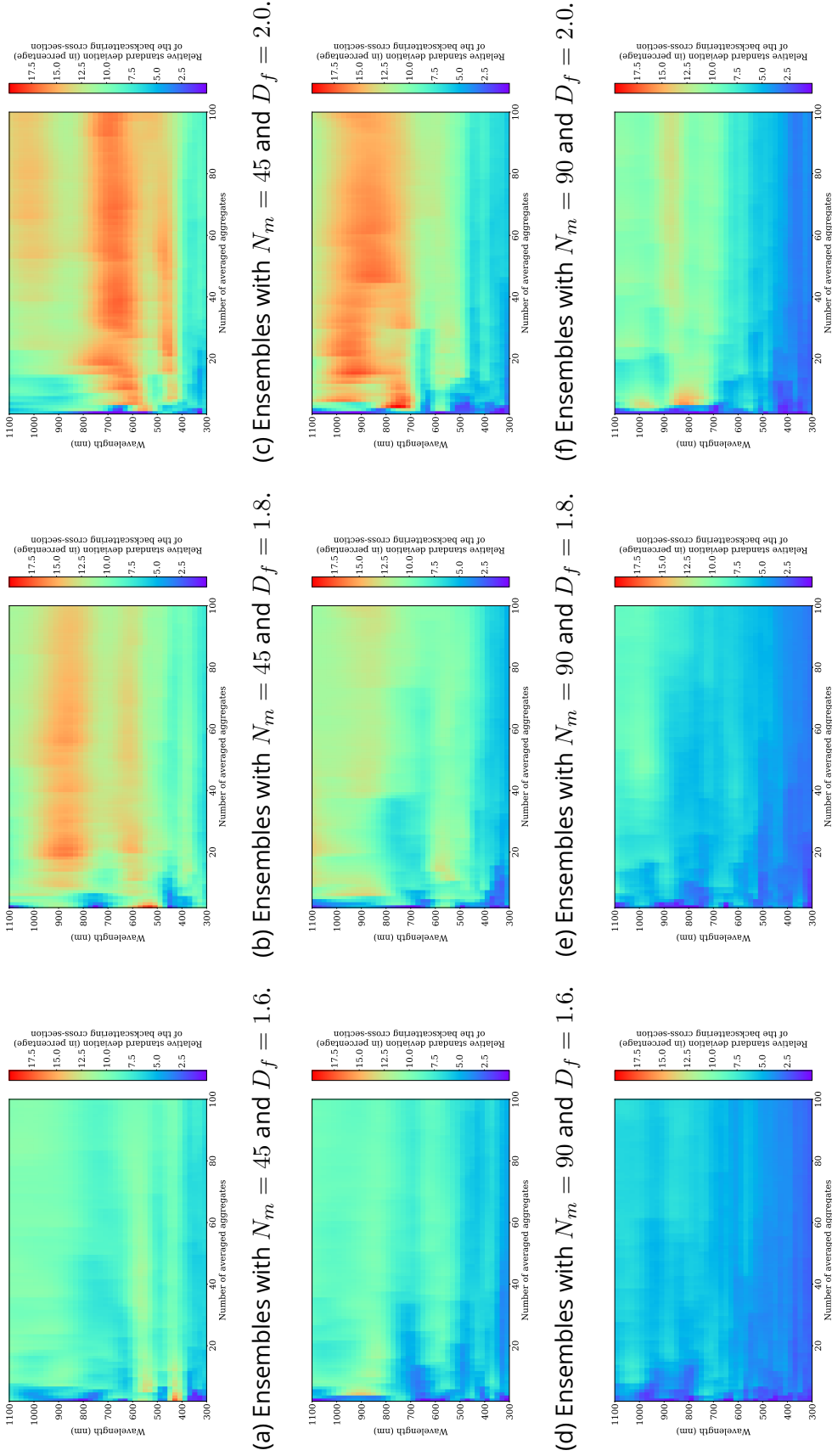


Figure A.2: Relative standard deviation of the backscattering cross-section, for aggregates with monodisperse monomers and with  $r_m = 20$  nm.



(a) Ensembles with  $N_m = 45$  and  $D_f = 1.6$ . (b) Ensembles with  $N_m = 45$  and  $D_f = 1.8$ . (c) Ensembles with  $N_m = 45$  and  $D_f = 2.0$ .

(d) Ensembles with  $N_m = 90$  and  $D_f = 1.6$ . (e) Ensembles with  $N_m = 90$  and  $D_f = 1.8$ . (f) Ensembles with  $N_m = 90$  and  $D_f = 2.0$ .

(g) Ensembles with  $N_m = 450$  and  $D_f = 1.6$ . (h) Ensembles with  $N_m = 450$  and  $D_f = 1.8$ . (i) Ensembles with  $N_m = 450$  and  $D_f = 2.0$ .

Figure A.3: Relative standard deviation of the backscattering cross-section, for aggregates with monodisperse monomers and with  $r_m = 40$  nm.

Figures A.1 to A.3 show that the relative standard deviation are found within  $\sigma_{bac,rel} \in [0, 20]\%$ . For ensembles with a monomer radius  $r_m = 10$  nm (Figure A.1), a larger number of monomers induces an overall increase of the standard deviation  $\sigma_{bac,rel}$ . Ensembles with  $r_m = 10$  nm and  $N_m = 450$  (subfigures A.1(g), (h) and (i)) also show an increase of  $\sigma_{bac,rel}$  with increasing fractal dimension. Ensembles with  $r_m = 20$  nm and  $r_m = 40$  nm also present this fractal dimension dependency. However, a larger number of monomers induces an overall decrease of  $\sigma_{bac,rel}$  for ensembles with  $r_m = 40$  nm and for ensembles with  $r_m = 20$  nm and  $D_f = 1.6$  or  $D_f = 1.8$ . In all cases, increasing the monomer radius also seems to induce a shift of the features to larger wavelengths. Because the standard deviation  $\sigma_{bac}(N_a)$  explicitly depends on the average value for the number of aggregates  $\langle C_{bac} \rangle_{N_a}$ , and because the relative standard deviation is the ratio between these two quantities, the investigation of the impact of the number of aggregates remains difficult. Hence, an alternative formulation of the relative standard deviation is proposed such as :

$$\begin{aligned}
 \sigma'_{bac,rel}(N_a) &= 100 \frac{\sigma'_{bac}(N_a)}{\langle C_{bac} \rangle_{100}} \\
 &= 100 \frac{\sqrt{\frac{\sum_{i=1}^{N_a} (C_{bac,i} - \langle C_{bac} \rangle_{100})^2}{N_a}}}{\langle C_{bac} \rangle_{100}}
 \end{aligned} \tag{A.3}$$

When compared with Equation A.1, this alternative formulation replaces every instance of the average backscattering cross-section  $\langle C_{bac} \rangle_{N_a}$  with its value for the largest considered ensemble, *i.e.* with a number of aggregates  $N_a = 100$ . This allows to reduce the number of sources of variation of the standard deviation. Indeed, the backscattering cross-sections of each aggregate realization  $C_{bac,i}$  is the only source of variation in this formulation. Figures A.4 to A.6 present the results obtained with this alternative formulation.

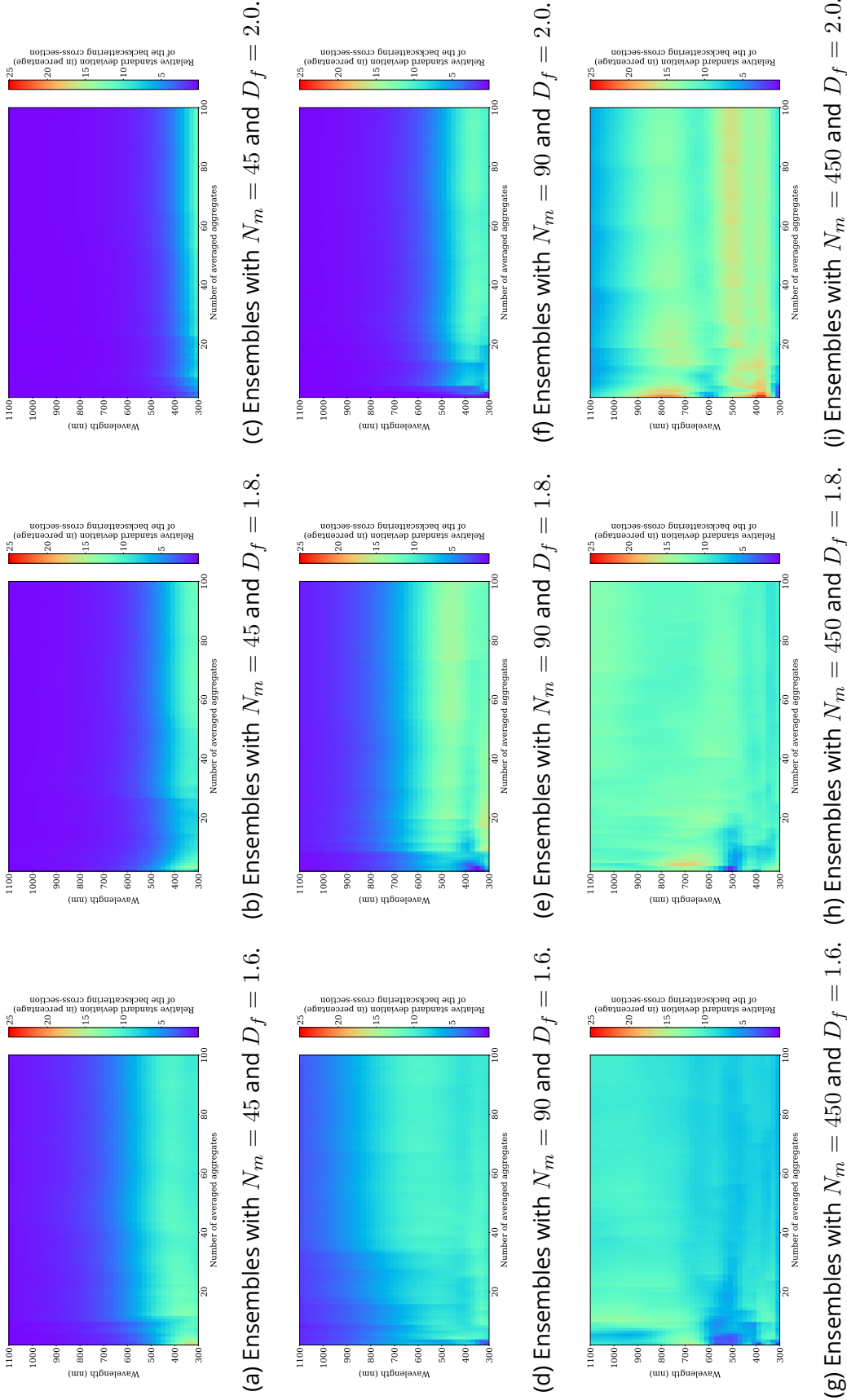


Figure A.4: Relative standard deviation of the backscattering cross-section, for aggregates with monodisperse monomers and with  $r_m = 10$  nm and using the alternative formulation.

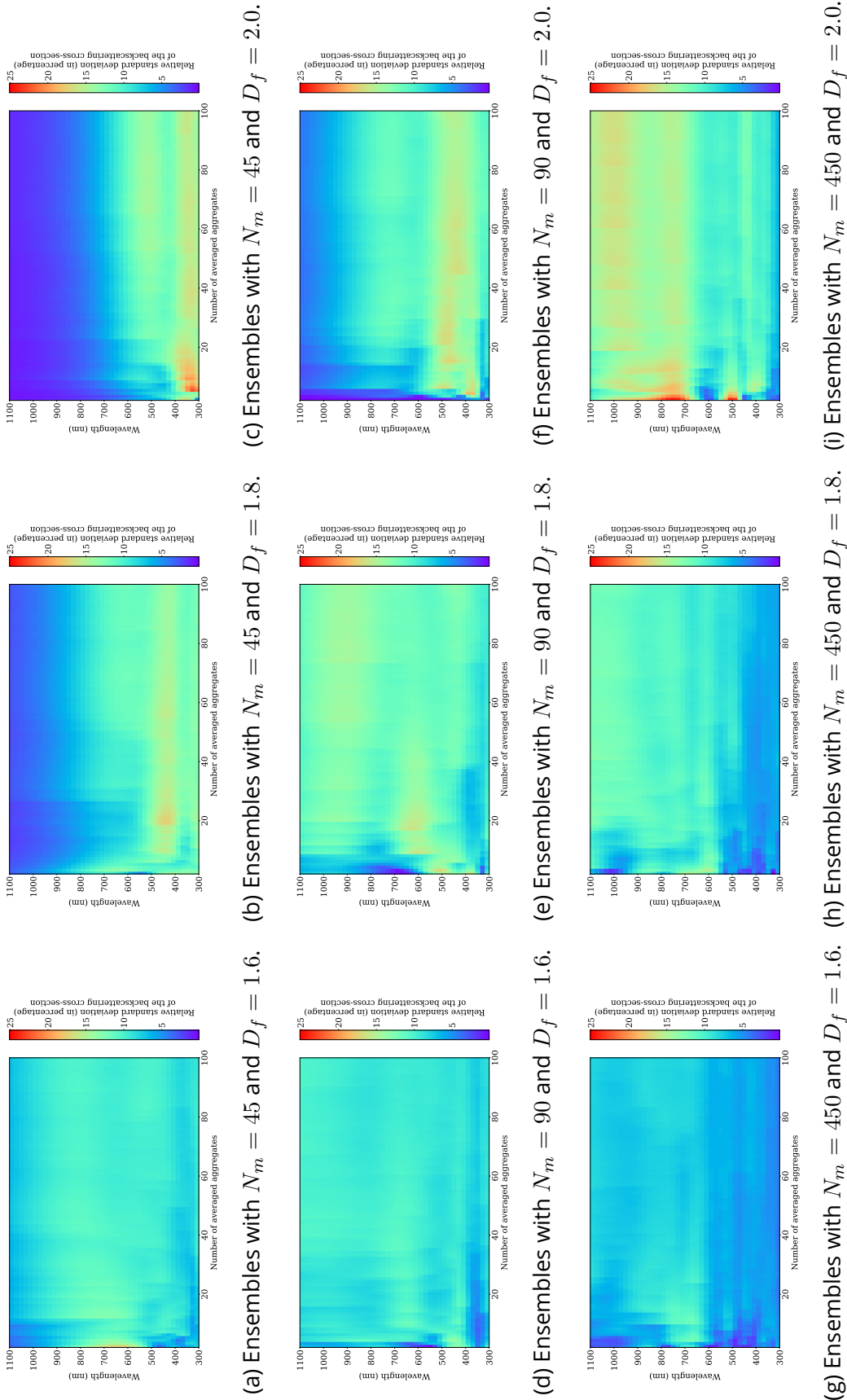


Figure A.5: Relative standard deviation of the backscattering cross-section, for aggregates with monodisperse monomers and with  $r_m = 20$  nm and using the alternative formulation.

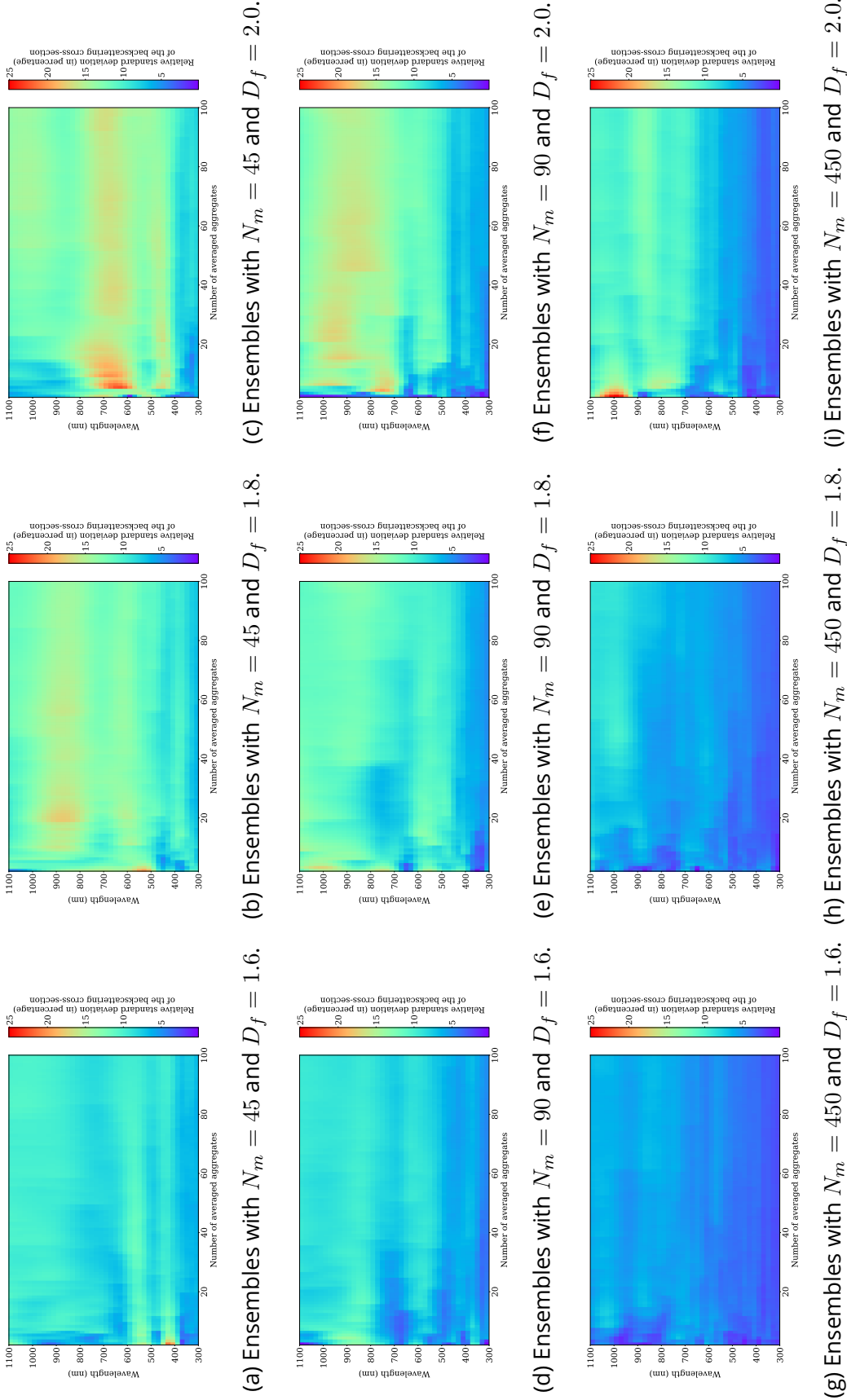


Figure A.6: Relative standard deviation of the backscattering cross-section, for aggregates with monodisperse monomers and with  $r_m = 40$  nm and using the alternative formulation.

Overall, these figures present the same features as Figures A.1 to A.3. However, Figures A.4 to A.6 highlight that, when considering a low number of aggregates, the estimation of the backscattering-cross section may be subject to error. To illustrate this, one may compare the results presented on Figure A.2(i) and A.5(i), which correspond to ensembles with the micro-physical parameters  $r_m = 20$  nm,  $N_m = 450$  and  $D_f = 2.0$ . On Figure A.5(i), and at the wavelengths around  $\lambda \approx 500$  nm and from  $\lambda = 700$  nm to  $\lambda = 900$  nm, the standard deviation is found close to 25% before decreasing. In contrast, A.2(i) presents the inverse feature, with a very low standard deviation rapidly increasing as the number of aggregates increases. This indicates that the average of the backscattering cross-section over the first few aggregate realizations resulted in either a large underestimation or overestimation.

Overall, Figures A.4, A.5 and A.6 show that the change of the number of aggregates per ensemble can induce large variation of the standard deviation at first, and possibly a strong overestimation or underestimation of the backscattering cross-section. However, these variation are less present for number of aggregates  $N_a > 20 - 50$  depending on the ensemble micro-physical parameters. This supports the need to consider ensemble-averaged quantities when investigating the radiative properties of soot aggregates. Moreover, the number of aggregates  $N_a = 50$  appears to be a reasonable compromise between the representativity of the average backscattering cross-section (and associated standard deviation) and the computational cost.



## Appendix B

# Comparison between the radiative properties of aggregates composed of monodisperse and polydisperse monomers and impact of the optical index

This appendix presents the comparison between the radiative properties of aggregates composed of monodisperse monomers with those of aggregates composed of polydisperse monomers. The results presented in this appendix stem from the numerical calculations presented in Section II.2. Hence, all simulation parameters are identical to those previously presented. While only the depolarization ratio  $\delta_p$  was presented in Section II.2, this appendix also includes results concerning the extinction cross-section  $C_{ext}$ , the scattering cross-section  $C_{sca}$ , the backscattering cross-section  $C_{bac}$ , the single-scattering albedo  $\omega_0$  and the lidar ratio. The figures presented in this appendix, *i.e.* Figures B.1 to Figures B.6, are based on the model from Figure II.13. Hence, on these figures the columns of subplots refer to different wavelengths, while the rows refer to different refractive indices. Inside the figures themselves, the x-axis represents variable monomer number, and the y-axis represents variable monomer radius. The color scale indicates variation in the represented quantity, *i.e.*  $C_{ext}$  on Figure B.1,  $C_{sca}$  on Figure B.2,  $C_{bac}$  on Figure B.3,  $\omega_0$  on

## Appendix B. Radiative properties of monodisperse and polydisperse monomers

Figure B.5, the lidar ratio on Figure B.6 and  $\delta_p$  on Figure B.7. Within all these figures, the subfigure (a) systematically corresponds to aggregates composed of monodisperse monomers, while subfigure (b) corresponds to aggregates composed of polydisperse monomers.

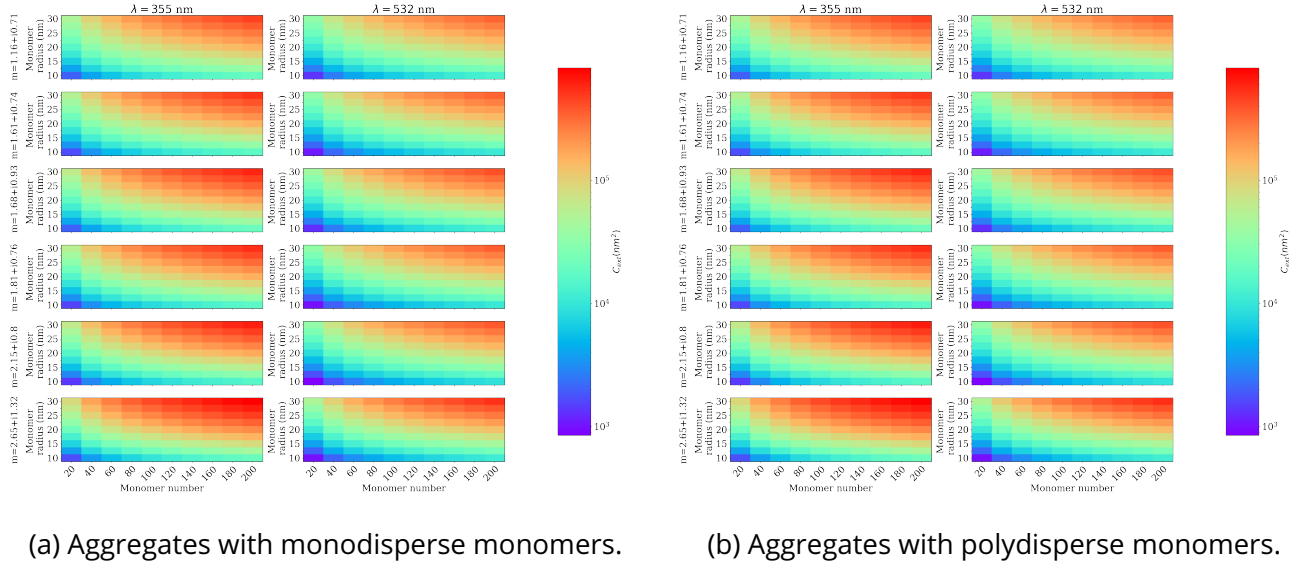


Figure B.1: Extinction cross-section.

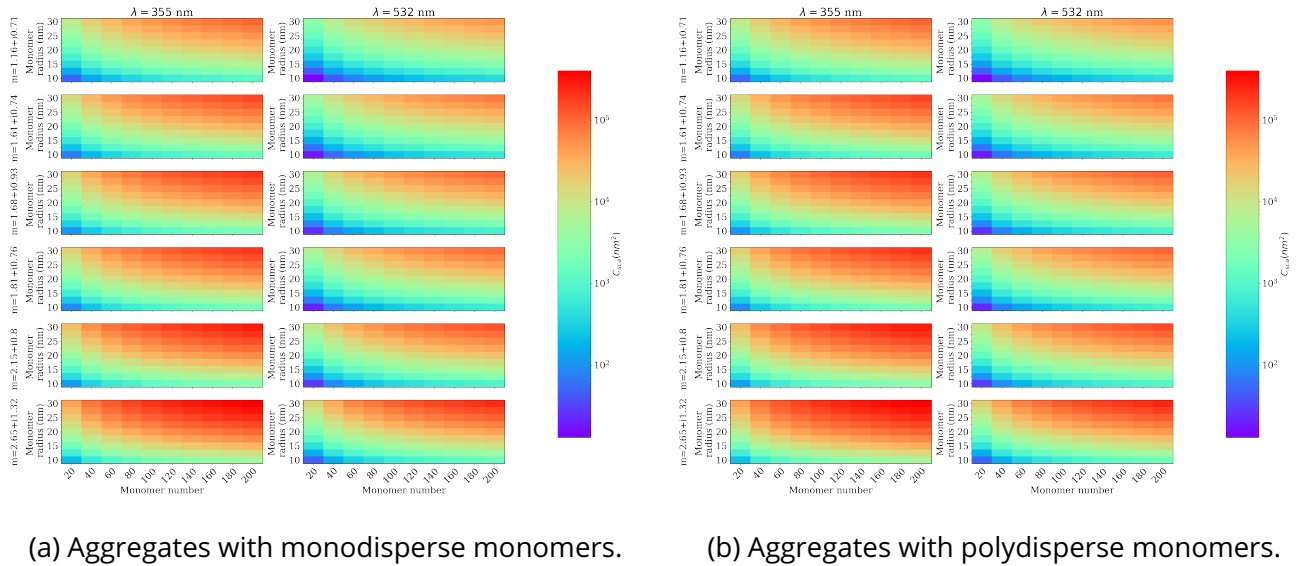


Figure B.2: Scattering cross-section.

## Appendix B. Radiative properties of monodisperse and polydisperse monomers

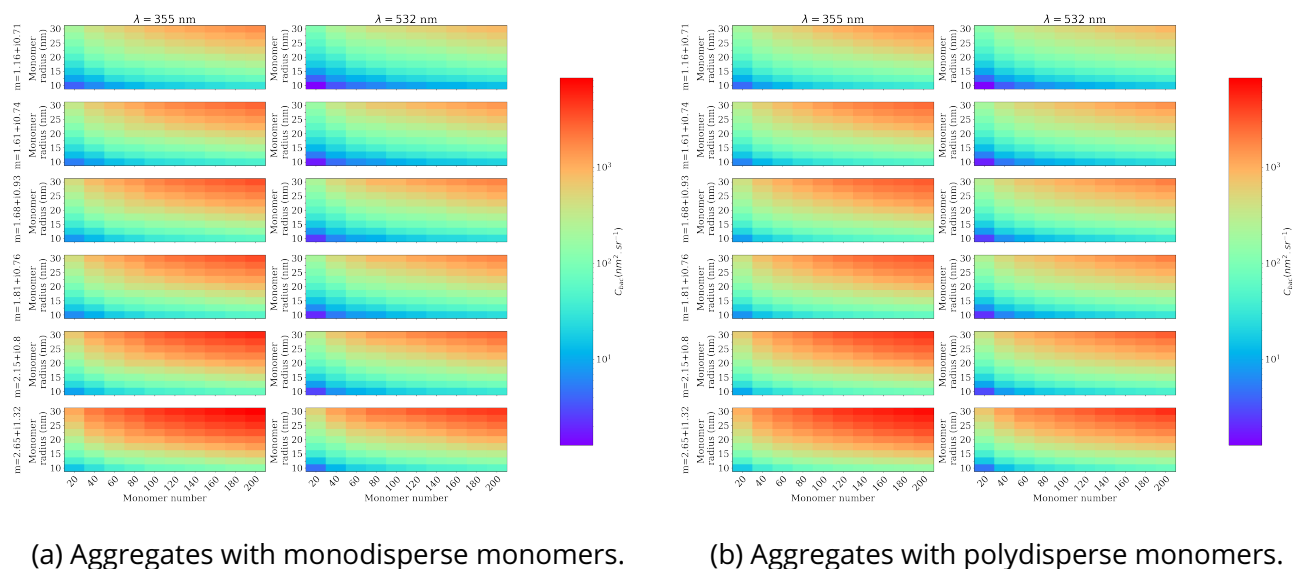
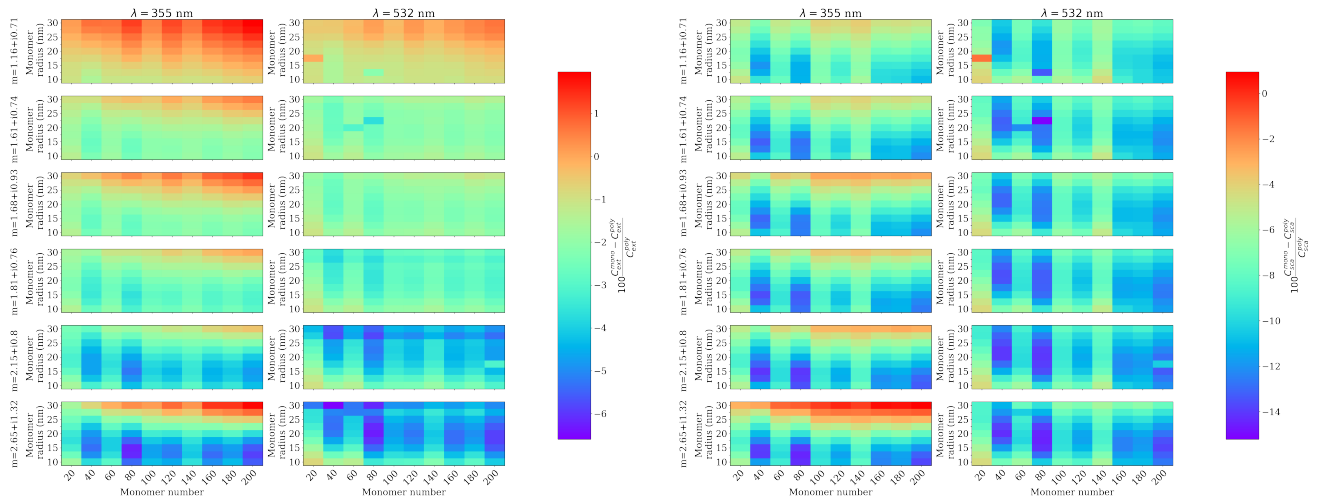


Figure B.3: Backscattering cross-section.

Figures B.1, B.2 and B.3 present respectively the extinction cross-sections, scattering cross-sections and backscattering cross-sections of the considered aggregates ensembles. Comparing the subfigures (a) and (b) of these figures, slight differences are apparent. However these are hard to observe due to the color scale and the large range it covers. Hence, in order to highlight these differences, Figure B.4 presents the relative differences between the cross-sections of aggregates composed of monodisperse monomers and those of aggregates composed of polydisperse monomers.

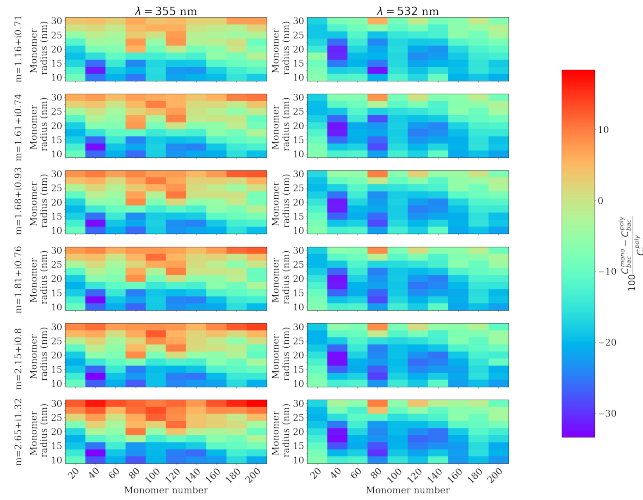
Considering the results presented in Figure B.4(a), it appears that the monodisperse ensembles extinction cross-sections are either under-evaluated or slightly over-evaluated when compared to the polydisperse ensembles. Indeed, they are found within 6% of each other. This difference is more pronounced when considering the scattering cross-section and the backscattering cross-section. The relative differences of the scattering cross-section presented on Figure B.4(b) are found negative in most cases, which indicates that the scattering cross-section of monodisperse ensemble are smaller than those of polydisperse ensembles. Moreover, up to a  $\approx 15\%$  difference can be observed between these two cases. Finally, large relative differences of the backscattering cross-section can also be observed in Figure B.4(c). The backscattering cross-section of the monodisperse ensembles can be found either higher or lower than those of the

## Appendix B. Radiative properties of monodisperse and polydisperse monomers



(a) Extinction cross-section.

(b) Scattering cross-section.

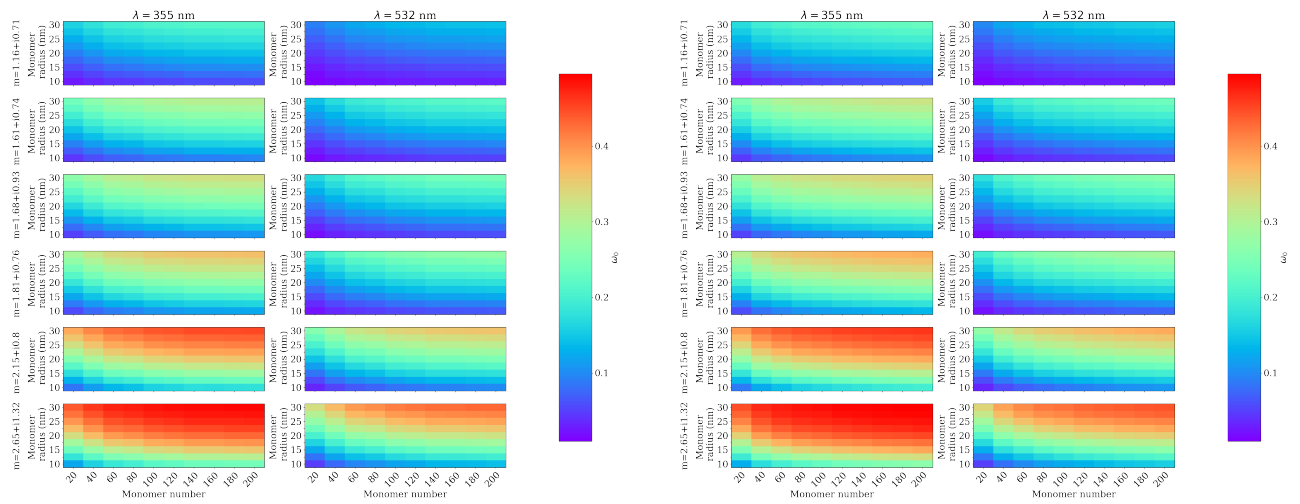


(c) Backscattering cross-section.

Figure B.4: Relative differences between the cross-sections of aggregates composed of monodisperse monomers and those of aggregates composed of polydisperse monomers.

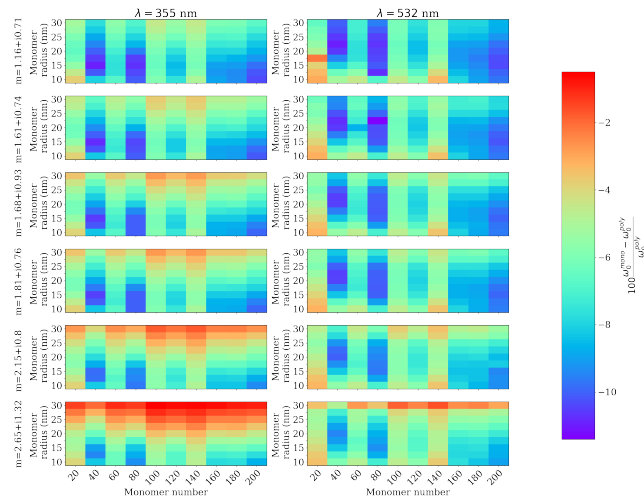
polydisperse ensembles depending on the micro-physical parameter, wavelength and optical index. The backscattering cross-section also present a larger range of variation than the extinction and scattering cross-sections. Indeed the relative difference is found within  $[-35, 15]\%$  for the backscattering cross-section. Another feature made apparent by the computation of the relative differences is the larger discrepancies found for ensembles with a number of monomers  $N_m = 40$  and  $N_m = 80$ . This is most probably due to an issue during the generation of the aggregates morphology. However, the specific culprit is hardly identifiable without an in depth morphological study, which is out of the scope of this appendix.

## Appendix B. Radiative properties of monodisperse and polydisperse monomers



(a) Aggregates with monodisperse monomers.

(b) Aggregates with polydisperse monomers.



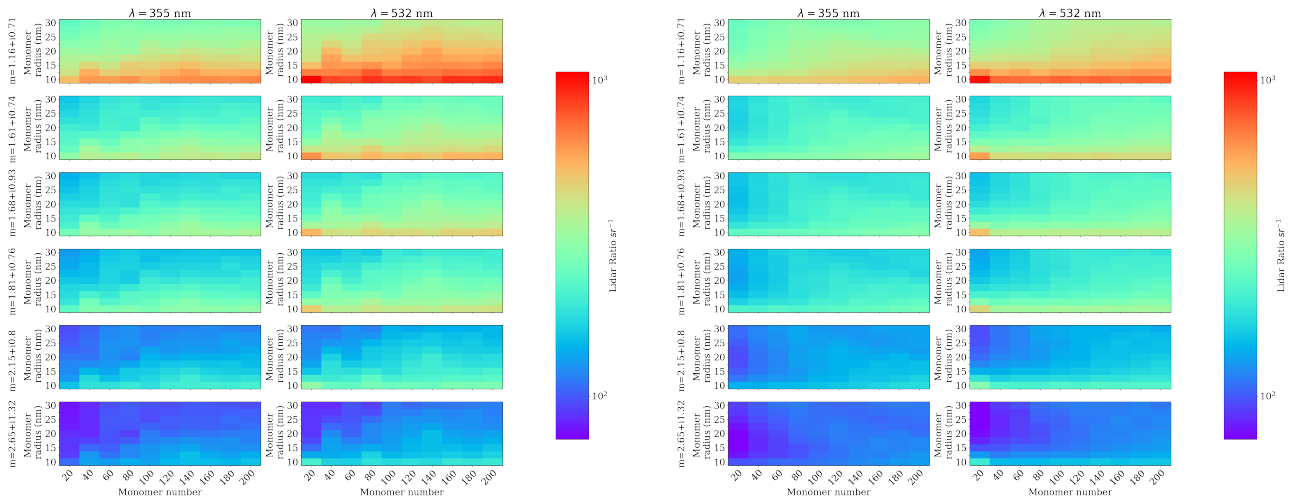
(c) Relative difference.

Figure B.5: Single-scattering albedo.

The single-scattering albedo presented on Figure B.5 also show minor differences between the monodisperse ensembles and the polydisperse ensembles. Subfigure B.5(c) show the relative difference between these two case. This last subfigure indicates that the single-scattering albedos of the monodisperse ensembles are lower than those of polydisperse ensembles. This feature can be interpreted by the differences in the extinction and scattering cross-sections computed in the monodisperse case and polydisperse case.

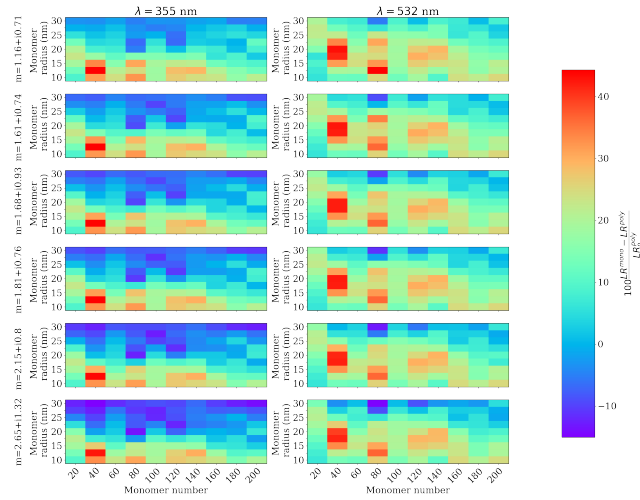
Similarly, the lidar ratio presented on Figure B.6(a) and (b) present similar values, although the lidar ratio of the monodisperse ensembles presents more localized variation for specific en-

## Appendix B. Radiative properties of monodisperse and polydisperse monomers



(a) Aggregates with monodisperse monomers.

(b) Aggregates with polydisperse monomers.



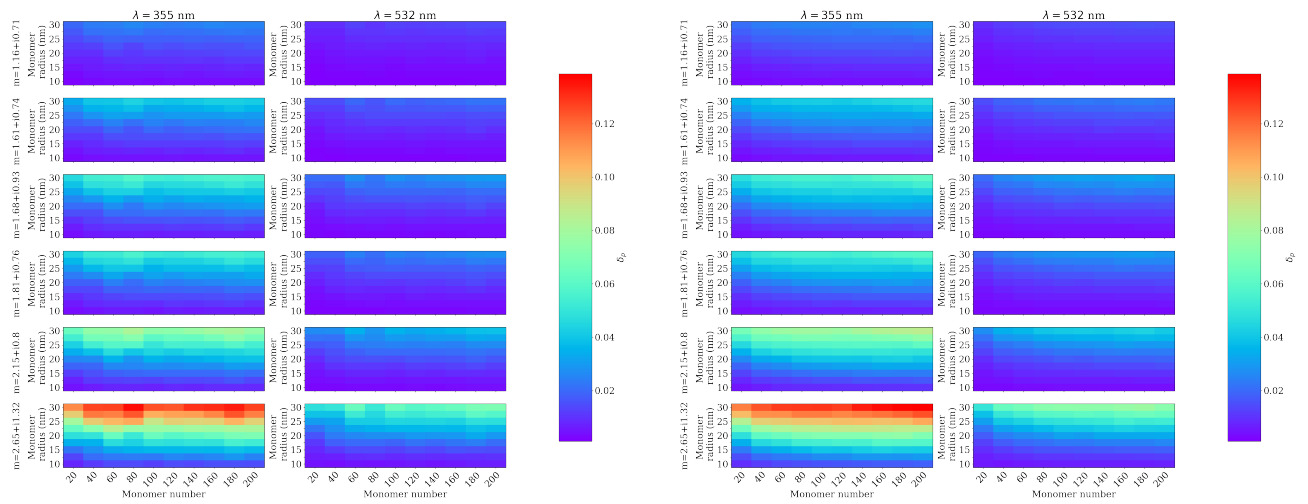
(c) Relative difference.

Figure B.6: Lidar ratio.

sembles. This supports the interpretation that the generation of the aggregates with monodisperse monomers morphology might be more unstable. The relative difference of the lidar ratio is found to have either positive or negative values depending on the micro-physical parameters, wavelength and refractive index. Once again, these differences can be interpreted by the relative evolution of the extinction cross-section and of the backscattering cross-section.

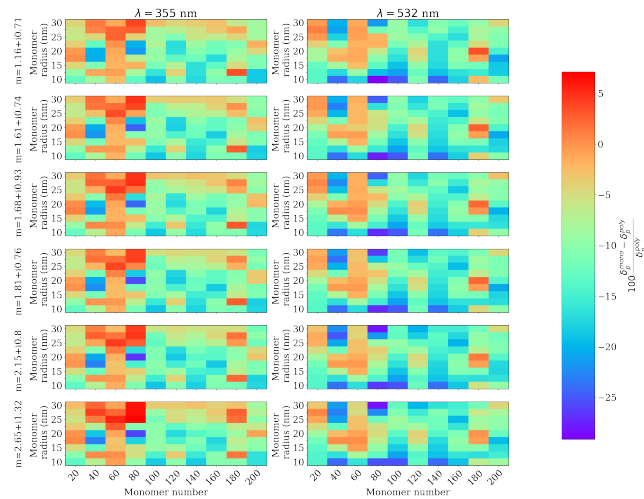
Finally, Figure B.7 presents the depolarization of aggregates composed of monodisperse monomers (Subfigure B.7(a)), polydisperse monomers (Subfigure B.7(b)) and the relative difference between these results (Subfigure B.7(c)). As stated in Subsection II.2.3, the LDR of the monodisperse evo-

## Appendix B. Radiative properties of monodisperse and polydisperse monomers



(a) Aggregates with monodisperse monomers.

(b) Aggregates with polydisperse monomers.



(c) Relative difference.

Figure B.7: Linear Depolarization Ratio.

lution with monomer number and radius presents more variability than the polydisperse results.

Overall, the results presented in this appendix shows monomer polydispersity does influence the radiative properties of soot fractal aggregate, with an increase of all the considered radiative properties except for the lidar ratio which decreases. Moreover, the angle-integrated radiative properties, *i.e.* the extinction and scattering cross-section, of monodisperse and polydisperse aggregates are in a better agreement than the angle-dependent properties such as the backscattering cross-section and the LDR. This suggests that process of scattering in the backward direction is especially sensitive to the fine morphological structure of the scatterer.



## Appendix C

# Backscattering experiment set-up and formalism

Equation I.2.26 presented in Section I.2.3 expresses the LDR in the backscattering direction as a function of the scattering matrix elements  $F_{11}(\pi)$  and  $F_{22}(\pi)$ . By rearranging the terms, this equation can also be formulated as :

$$\delta_p(\lambda) = \frac{1 - F_{22}(\pi, \lambda)/F_{11}(\pi, \lambda)}{1 + F_{22}(\pi, \lambda)/F_{11}(\pi, \lambda)} \quad (\text{C.1})$$

This reformulation expresses that the LDR can be evaluated without the knowledge of the specific values of the scattering matrix elements, as only the ratio between the second and first diagonal elements is needed. The evaluation of the ratio  $F_{22}(\pi, \lambda)/F_{11}(\pi, \lambda)$  is achieved by the mean of the experimental set-up presented in Figure C.1.

As this experimental set-up has been extensively described in the article from Miffre et al. [153], only a short description is provided here. The evaluation of the ratio  $F_{22}(\pi, \lambda)/F_{11}(\pi, \lambda)$  relies of the simultaneous emission of laser pulses at two wavelengths (*i.e.*  $\lambda = 355$  nm (UV) and  $\lambda = 532$  nm (VIS)) and the detection of the backscattered radiation by the particles in the overlapping volume of these two pulses. The optical components of interest for the evaluation of this ratio are two Polarization Beam-splitter Cube (PBC) and two Quarter-Wave Plate (QWP), one of each for each wavelength-specific optical pathway. The Stokes vector of the backscattered

radiation at the detector can then be expressed as :

$$\mathbf{I}^{sca} = \mathbf{PBC} \mathbf{QWP} \mathbf{F}(\pi) \mathbf{QWP} \mathbf{PBC} \mathbf{I}^{inc} \quad (\text{C.2})$$

where **PBC** and **QWP** are the Mueller matrices of the PBC and QWP respectively. In this equation and hereafter, the wavelength dependence of the scattering matrix elements and of the related quantities is implied. Considering a linearly polarized incident light (*i.e.*  $\mathbf{I}^{inc} = [1 \ 1 \ 0 \ 0]^T$ ), the first element of the scattered Stokes vector can be expressed as [153] :

$$I(\Psi) = I_0 [a - b \cos(4\Psi)] \quad (\text{C.3})$$

where the intensity  $I_0$  depends on the laser source and on the distance from the soot particles to the detector and  $\Psi$  is the angle between the QWP fast-axis and the scattering plane. The coefficients  $a$  and  $b$  are defined such as :

$$2a = F_{11}(\pi) + F_{22}(\pi) \quad (\text{C.4a})$$

$$2b = 3F_{22}(\pi) - F_{11}(\pi) \quad (\text{C.4b})$$

The ratio  $F_{22}(\pi, \lambda)/F_{11}(\pi, \lambda)$  can then be expressed as :

$$\left[ \frac{F_{22}(\pi)}{F_{11}(\pi)} \right]_{lab} = \frac{a + b}{3a - b} \quad (\text{C.5})$$

where the subscript *lab* indicates that this parameter is evaluated in laboratory. The following step of this methodology is then to proceed at the evaluation of the coefficients  $a$  and  $b$ . The evaluation of these coefficients is achieved by modulating the angle  $\Psi$  and proceeding to the measurement of the scattered intensity  $I(\Psi)$  at these different angles. The use of a regression method applied to Equation C.3 then yield the coefficients  $a$  and  $b$ , followed by the ratio  $[F_{22}(\pi)/F_{11}(\pi)]_{lab}$  according to Equation C.5 and finally the LDR  $\delta_{lab}$  using Equation C.1.

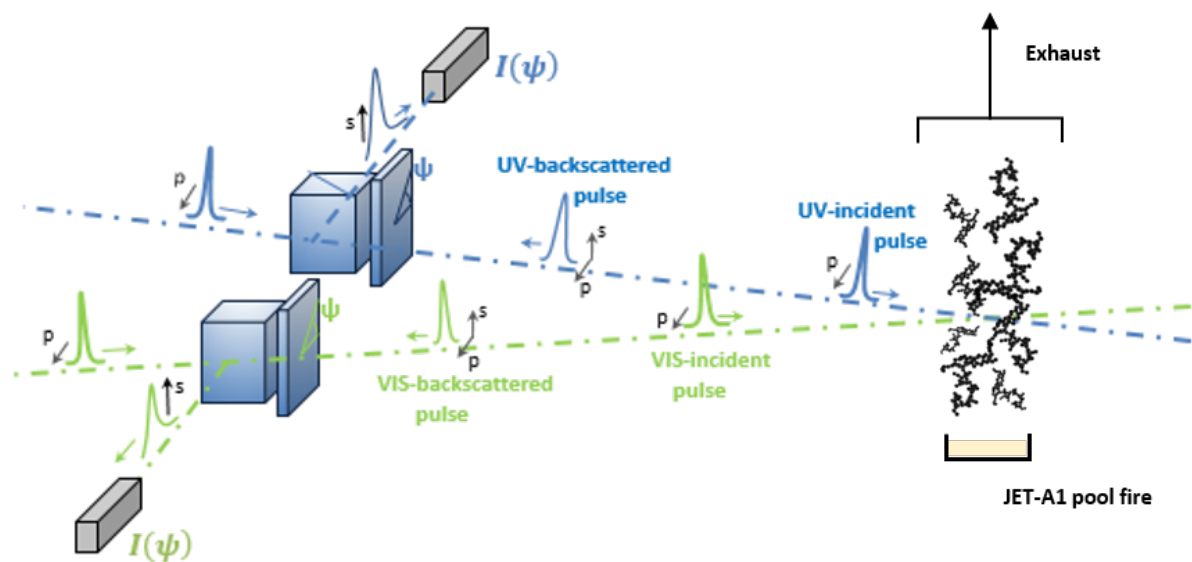


Figure C.1: Principle of the laboratory backscattering experimental set-up to evaluate the particles depolarization ratio LDR in laboratory ambient air, identical to the one presented in [153], but here applied to the particles released from a JET A-1 pool fire. A distance of 5 meters separates the pool fire from the detectors.



## Synthèse

Les particules de suie sont des aérosols émis lors de la combustion de matière organique. Plusieurs problématiques leur sont associées. Premièrement, la présence de ces particules dégrade la qualité de l'air, de par leurs propriétés cancérigènes. De plus, ces particules provoquent un forçage radiatif positif, c'est-à-dire un réchauffement de l'atmosphère. Afin d'évaluer l'impact des particules de suie sur le climat et sur la qualité de l'air, leurs émissions doivent ainsi être surveillées. Les instruments lidar peuvent permettre d'apporter les mesures nécessaires. Néanmoins, l'analyse de signaux lidar requiert la connaissance des propriétés radiatives des particules et cette analyse peut être sujette à des erreurs liées à la diffusion multiple. De plus, ces propriétés radiatives dépendent des caractéristiques microphysiques des particules, telles que leurs formes ou leurs tailles. L'objectif de cette thèse est de simuler des signaux lidar résolu en polarisation, acquis sur des particules de suie et prenant en compte la contribution de la diffusion multiple. Cela nécessite la modélisation de la morphologie et des propriétés radiatives des particules de suie, ainsi que le développement d'une méthode permettant de simuler les signaux lidar. L'analyse des signaux lidar ainsi modélisé permet alors d'identifier l'impact de la diffusion multiple sur les signaux lidar acquis sur des particules de suie.

La première étape est donc de modéliser les propriétés radiatives des particules de suie, ce qui nécessite également la définition du modèle morphologique. Dans cette thèse, les particules de suie sont modélisées comme des agrégats fractals composés de particules primaires sphériques. Ces particules primaires sont appelées monomères. Par la suite, la méthode de Superposition de T-Matrice et la théorie de Rayleigh-Debye-Gans pour les agrégats fractals sont utilisées afin de modéliser les propriétés radiatives de ces particules. L'impact des paramètres morphologiques

sur ces propriétés radiatives est étudié. Il a été observé que la variation du rayon des monomères a pour conséquence une forte variation de toutes les propriétés radiatives considérées. En revanche, une variation la dimension fractale ne provoque que de faibles variations. Les propriétés radiatives d'un second modèle morphologique correspondant à un superagrégat ont également été étudiées. Enfin, une évaluation expérimentale du ratio de dépolarisation des particules de suie dans l'air ambiant est également présentée. Cela permet d'identifier quels paramètres morphologiques et quels indices optiques permettent de reproduire les résultats expérimentaux. De plus, les limites des méthodes numériques utilisées peuvent également être identifiées.

Un modèle numérique de simulation de signaux lidar résolu en polarisation est développé en utilisant la méthode Monte-Carlo. Plusieurs techniques de réduction de variance ont été implémentées afin d'améliorer les performances de cette méthode. Ainsi les techniques d'"absorbtion weighting", de "peel-off scattering" et de "scattering splitting" permettent d'améliorer les performances du code. Plusieurs procédures de validation ont été réalisées et ont permis de vérifier la validité du code.

Enfin, des simulations numériques ont été entreprises afin d'évaluer l'impact de la diffusion multiple sur des signaux lidar résolus en polarisation acquis sur des particules de suie. Ce modèle numérique est également utilisé afin d'analyser un signal expérimental. Ceci permet d'évaluer la contribution de la diffusion multiple dans ce signal. Il apparaît que la diffusion multiple est très dépendante de plusieurs paramètres tels que l'indice optique ou le champ de vue du récepteur de l'instrument lidar. La diffusion multiple semble avoir un impact significatif à condition que le milieu diffusant présente une forte épaisseur optique. Ces résultats permettent ainsi de déterminer que l'approximation de diffusion simple, couramment utilisée lors de l'inversion lidar, est justifiée en l'absence de fortes épaisseurs optiques. Afin de compléter cette thèse, d'autres études sont nécessaires. En particulier, des études de sensibilité pourraient permettre de préciser la dépendance de la diffusion multiple par rapport aux paramètres optiques, instrumentaux et morphologiques. De plus, les résultats présentés dans cette thèse ne concernent que les particules de suie modélisées avec un modèle fractal. Ainsi, d'autres études sont nécessaires afin de prendre en compte d'autre paramètres morphologique tel que le "necking" ou le "coating", et

afin de prendre en compte d'autres types de particules pouvant être présentes dans les produits de combustion.



# Bibliography

- [1] T.F. Stocker, D. Qin, G.-K. Plattner, L.V. Alexander, S.K. Allen, N.L. Bindoff, F.-M. Bréon, J.A. Church, U. Cubasch, S. Emori, P. Forster, P. Friedlingstein, N. Gillett, J.M. Gregory, D.L. Hartmann, E. Jansen, B. Kirtman, R. Knutti, K. Krishna Kumar, P. Lemke, J. Marotzke, V. Masson-Delmotte, G.A. Meehl, I.I. Mokhov, S. Piao, V. Ramaswamy, D. Randall, M. Rhein, M. Rojas, C. Sabine, D. Shindell, L.D. Talley, D.G. Vaughan, and S.-P. Xie. *Technical Summary*, book section TS, page 33–115. Cambridge University Press, Cambridge, United Kingdom and New York, NY, USA, 2013. ISBN ISBN 978-1-107-66182-0. doi: 10.1017/CBO9781107415324.005. URL [www.climatechange2013.org](http://www.climatechange2013.org).
- [2] Lucas Paulien, Romain Ceolato, Frédéric Fossard, Patrick Rairoux, and Alain Miffre. (uv, vis) laboratory evaluation of the lidar depolarization ratio of freshly emitted soot aggregates from pool fire in ambient air at exact backscattering angle. *Journal of Quantitative Spectroscopy and Radiative Transfer*, 260:107451, 2021.
- [3] Dale R Tree and Kenth I Svensson. Soot processes in compression ignition engines. *Progress in energy and combustion science*, 33(3):272–309, 2007.
- [4] M Wentzel, H Gorzawski, K-H Naumann, H Saathoff, and S Weinbruch. Transmission electron microscopical and aerosol dynamical characterization of soot aerosols. *Journal of aerosol science*, 34(10):1347–1370, 2003.
- [5] R Jullien. Aggregation phenomena and fractal aggregates. *Contemporary Physics*, 28(5): 477–493, 1987.

- [6] J Yon, A Bescond, and F Liu. On the radiative properties of soot aggregates part 1: Necking and overlapping. *Journal of Quantitative Spectroscopy and Radiative Transfer*, 162:197–206, 2015.
- [7] Hsueh-chia Chang and TT Charalampopoulos. Determination of the wavelength dependence of refractive indices of flame soot. *Proceedings of the Royal Society of London. Series A: Mathematical and Physical Sciences*, 430(1880):577–591, 1990.
- [8] A Bescond, J Yon, F-X Ouf, C Rozé, A Coppalle, P Parent, Daniel Ferry, and C Laffon. Soot optical properties determined by analyzing extinction spectra in the visible near-uv: Toward an optical speciation according to constituents and structure. *Journal of Aerosol Science*, 101: 118–132, 2016.
- [9] M Schnaiter, H Horvath, O Möhler, K-H Naumann, H Saathoff, and OW Schöck. Uv-vis-nir spectral optical properties of soot and soot-containing aerosols. *Journal of Aerosol Science*, 34(10):1421–1444, 2003.
- [10] Odelle L Hadley and Thomas W Kirchstetter. Black-carbon reduction of snow albedo. *Nature Climate Change*, 2(6):437–440, 2012.
- [11] Ari Laaksonen, Jussi Malila, and Athanasios Nenes. Heterogeneous nucleation of water vapor on different types of black carbon particles. *Atmospheric Chemistry and Physics*, 20 (21):13579–13589, 2020.
- [12] Leonid Nichman, Martin Wolf, Paul Davidovits, Timothy B Onasch, Yue Zhang, Doug R Worsnop, Janarjan Bhandari, Claudio Mazzoleni, and Daniel J Cziczo. Laboratory study of the heterogeneous ice nucleation on black-carbon-containing aerosol. *Atmospheric Chemistry and Physics*, 19(19):12175–12194, 2019.
- [13] Eleanor J Highwood and Robert P Kinnersley. When smoke gets in our eyes: The multiple impacts of atmospheric black carbon on climate, air quality and health. *Environment International*, 32(4):560–566, 2006.

- [14] Rituraj Nirajan and Ashwani Kumar Thakur. The toxicological mechanisms of environmental soot (black carbon) and carbon black: focus on oxidative stress and inflammatory pathways. *Frontiers in immunology*, 8:763, 2017.
- [15] Tami C Bond, David G Streets, Kristen F Yarber, Sibyl M Nelson, Jung-Hun Woo, and Zbigniew Klimont. A technology-based global inventory of black and organic carbon emissions from combustion. *Journal of Geophysical Research: Atmospheres*, 109(D14), 2004.
- [16] PR Buseck, K Adachi, A Gelencsér, É Tompa, and M Pósfai. Are black carbon and soot the same? *Atmospheric Chemistry and Physics Discussions*, 12(9):24821–24846, 2012.
- [17] Stephen R Forrest and Thomas A Witten Jr. Long-range correlations in smoke-particle aggregates. *Journal of Physics A: Mathematical and General*, 12(5):L109, 1979.
- [18] RJ Samson, George W Mulholland, and JW Gentry. Structural analysis of soot agglomerates. *Langmuir*, 3(2):272–281, 1987.
- [19] AV Filippov, Mauricio Zurita, and Daniel E Rosner. Fractal-like aggregates: relation between morphology and physical properties. *Journal of colloid and interface science*, 229(1):261–273, 2000.
- [20] Raymond M Measures. Laser remote sensing: Fundamentals and applications(book). *New York, Wiley-Interscience, 1984, 521 p*, 1984.
- [21] Detlef Müller, Frank Wagner, Ulla Wandinger, Albert Ansmann, Manfred Wendisch, Dietrich Althausen, and Wolfgang von Hoyningen-Huene. Microphysical particle parameters from extinction and backscatter lidar data by inversion with regularization: experiment. *Applied Optics*, 39(12):1879–1892, 2000.
- [22] Melody Avery, David Winker, Andrew Heymsfield, Mark Vaughan, Stuart Young, Yongxiang Hu, and Charles Trepte. Cloud ice water content retrieved from the caliop space-based lidar. *Geophysical Research Letters*, 39(5), 2012.

- [23] James D Klett. Stable analytical inversion solution for processing lidar returns. *Applied optics*, 20(2):211–220, 1981.
- [24] Luc R Bissonnette. Lidar and multiple scattering. In *Lidar*, pages 43–103. Springer, 2005.
- [25] Albert Ansmann, Holger Baars, Matthias Tesche, Detlef Müller, Dietrich Althausen, Ronny Engelmann, Theotonio Pauliquevis, and Paulo Artaxo. Dust and smoke transport from africa to south america: Lidar profiling over cape verde and the amazon rainforest. *Geophysical Research Letters*, 36(11), 2009.
- [26] Albert Ansmann, Kevin Ohneiser, Rodanthi-Elisavet Mamouri, Daniel A Knopf, Igor Veselovskii, Holger Baars, Ronny Engelmann, Andreas Foth, Cristofer Jimenez, Patric Seifert, et al. Tropospheric and stratospheric wildfire smoke profiling with lidar: mass, surface area, ccn, and inp retrieval. *Atmospheric Chemistry and Physics*, 21(12):9779–9807, 2021.
- [27] Michael Fromm, Jerome Alfred, Karl Hoppel, John Hornstein, Richard Bevilacqua, Eric Shettle, René Servranckx, Zhanqing Li, and Brian Stocks. Observations of boreal forest fire smoke in the stratosphere by poam iii, sage ii, and lidar in 1998. *Geophysical Research Letters*, 27(9):1407–1410, 2000.
- [28] Mihály Pósfai, Renáta Simonics, Jia Li, Peter V Hobbs, and Peter R Buseck. Individual aerosol particles from biomass burning in southern africa: 1. compositions and size distributions of carbonaceous particles. *Journal of Geophysical Research: Atmospheres*, 108(D13), 2003.
- [29] Swarup China, Claudio Mazzoleni, Kyle Gorkowski, Allison C Aiken, and Manvendra K Dubey. Morphology and mixing state of individual freshly emitted wildfire carbonaceous particles. *Nature communications*, 4(1):1–7, 2013.
- [30] Ümit Özgür Köylü and Gerard M Faeth. Structure of overfire soot in buoyant turbulent diffusion flames at long residence times. *Combustion and Flame*, 89(2):140–156, 1992.
- [31] Peter H Joo, Ben Gigone, Elizabeth A Griffin, Moah Christensen, and Ömer L Gülder. Soot

- primary particle size dependence on combustion pressure in laminar ethylene diffusion flames. *Fuel*, 220:464–470, 2018.
- [32] Michael Frenklach, David W Clary, William C Gardiner Jr, and Stephen E Stein. Detailed kinetic modeling of soot formation in shock-tube pyrolysis of acetylene. In *Symposium (International) on Combustion*, volume 20, pages 887–901. Elsevier, 1985.
- [33] Michael Frenklach and Hai Wang. Detailed modeling of soot particle nucleation and growth. In *Symposium (International) on Combustion*, volume 23, pages 1559–1566. Elsevier, 1991.
- [34] Michael Frenklach. Reaction mechanism of soot formation in flames. *Physical chemistry chemical Physics*, 4(11):2028–2037, 2002.
- [35] Michael Frenklach. On surface growth mechanism of soot particles. In *Symposium (International) on Combustion*, volume 26, pages 2285–2293. Elsevier, 1996.
- [36] H Kellerer, R Koch, and S Wittig. Measurements of the growth and coagulation of soot particles in a high-pressure shock tube. *Combustion and Flame*, 120(1-2):188–199, 2000.
- [37] Hope A Michelsen, Meredith B Colket, Per-Erik Bengtsson, Andrea D'anna, Pascale Desgroux, Brian S Haynes, J Houston Miller, Graham J Nathan, Heinz Pitsch, and Hai Wang. A review of terminology used to describe soot formation and evolution under combustion and pyrolytic conditions. *ACS nano*, 14(10):12470–12490, 2020.
- [38] Randy L Vander Wal and Aaron J Tomasek. Soot nanostructure: dependence upon synthesis conditions. *Combustion and Flame*, 136(1-2):129–140, 2004.
- [39] Irvin Glassman. Soot formation in combustion processes. In *Symposium (international) on combustion*, volume 22, pages 295–311. Elsevier, 1989.
- [40] Benoit Mandelbrot. How long is the coast of britain? statistical self-similarity and fractional dimension. *science*, 156(3775):636–638, 1967.
- [41] Benoit B Mandelbrot and Benoit B Mandelbrot. *The fractal geometry of nature*, volume 1. WH freeman New York, 1982.

- [42] T Vicsek. Fractal models for diffusion controlled aggregation. *Journal of Physics A: Mathematical and General*, 16(17):L647, 1983.
- [43] Jian Cai, Ninglong Lu, and Christopher M Sorensen. Analysis of fractal cluster morphology parameters: structural coefficient and density autocorrelation function cutoff. *Journal of Colloid and Interface Science*, 171(2):470–473, 1995.
- [44] Leonard M Sander. Diffusion-limited aggregation: a kinetic critical phenomenon? *Contemporary Physics*, 41(4):203–218, 2000.
- [45] GC Bushell, YD Yan, D Woodfield, JUDY Raper, and ROSE Amal. On techniques for the measurement of the mass fractal dimension of aggregates. *Advances in Colloid and Interface Science*, 95(1):1–50, 2002.
- [46] Christopher M Sorensen and Gregory C Roberts. The prefactor of fractal aggregates. *Journal of colloid and interface science*, 186(2):447–452, 1997.
- [47] WR Heinson, CM Sorensen, and A Chakrabarti. A three parameter description of the structure of diffusion limited cluster fractal aggregates. *Journal of colloid and interface science*, 375(1):65–69, 2012.
- [48] Jia Liu, Qixing Zhang, Jinjun Wang, and Yongming Zhang. Light scattering matrix for soot aerosol: Comparisons between experimental measurements and numerical simulations. *Journal of Quantitative Spectroscopy and Radiative Transfer*, 246:106946, 2020.
- [49] Lucas Paulien, Romain Ceolato, Laurent Soucasse, Franck Enguehard, and Anouar Soufiani. Lidar-relevant radiative properties of soot fractal aggregate ensembles. *Journal of Quantitative Spectroscopy and Radiative Transfer*, 241:106706, 2020.
- [50] Magín Lapuerta, Francisco J Martos, and José M Herreros. Effect of engine operating conditions on the size of primary particles composing diesel soot agglomerates. *Journal of aerosol science*, 38(4):455–466, 2007.

- [51] J Yon, R Lemaire, E Therssen, P Desgroux, A Coppalle, and KF Ren. Examination of wavelength dependent soot optical properties of diesel and diesel/rapeseed methyl ester mixture by extinction spectra analysis and lii measurements. *Applied Physics B*, 104(2):253–271, 2011.
- [52] M Matti Maricq, Stephen J Harris, and Joseph J Szente. Soot size distributions in rich premixed ethylene flames. *Combustion and Flame*, 132(3):328–342, 2003.
- [53] A Bescond, J Yon, FX Ouf, Daniel Ferry, D Delhaye, D Gaffié, A Coppalle, and C Rozé. Automated determination of aggregate primary particle size distribution by tem image analysis: application to soot. *Aerosol Science and Technology*, 48(8):831–841, 2014.
- [54] Max L Eggersdorfer and Sotiris E Pratsinis. The structure of agglomerates consisting of polydisperse particles. *Aerosol Science and Technology*, 46(3):347–353, 2012.
- [55] KB Lee, MW Thring, and JM Beer. On the rate of combustion of soot in a laminar soot flame. *Combustion and Flame*, 6:137–145, 1962.
- [56] G Prado, J Jagoda, K Neoh, and J Lahaye. A study of soot formation in premixed propane/oxygen flames by in-situ optical techniques and sampling probes. In *Symposium (International) on Combustion*, volume 18, pages 1127–1136. Elsevier, 1981.
- [57] HX Zhang, CM Sorensen, ER Ramer, BJ Olivier, and JF Merklin. In situ optical structure factor measurements of an aggregating soot aerosol. *Langmuir*, 4(4):867–871, 1988.
- [58] CM Megaridis and RA Dobbins. Soot aerosol dynamics in a laminar ethylene diffusion flame. In *Symposium (International) on Combustion*, volume 22, pages 353–362. Elsevier, 1989.
- [59] Ümit Özgür Köylü, Gerard M Faeth, Tiago L Farias, and Maria da Gracia Carvalho. Fractal and projected structure properties of soot aggregates. *Combustion and Flame*, 100(4):621–633, 1995.
- [60] SS Krishnan, K-C Lin, and GM Faeth. Optical properties in the visible of overfire soot in large buoyant turbulent diffusion flames. *J. Heat transfer*, 122(3):517–524, 2000.

- [61] Jinyu Zhu, Mun Young Choi, George W Mulholland, Samuel L Manzello, Louis A Gritzko, and Jill Suo-Anttila. Measurement of visible and near-ir optical properties of soot produced from laminar flames. *Proceedings of the Combustion Institute*, 29(2):2367–2374, 2002.
- [62] Bing Hu, Bo Yang, and Umit O Koçlu. Soot measurements at the axis of an ethylene/air non-premixed turbulent jet flame. *Combustion and flame*, 134(1-2):93–106, 2003.
- [63] Timothy C Williams, Christopher R Shaddix, Kirk A Jensen, and Jill M Suo-Anttila. Measurement of the dimensionless extinction coefficient of soot within laminar diffusion flames. *International Journal of Heat and Mass Transfer*, 50(7-8):1616–1630, 2007.
- [64] Kirk A Jensen, Jill M Suo-Anttila, and Linda G Blevins. Measurement of soot morphology, chemistry, and optical properties in the visible and near-infrared spectrum in the flame zone and overfire region of large jp-8 pool fires. *Combustion science and technology*, 179(12):2453–2487, 2007.
- [65] Huaqiang Chu, Weiwei Han, Wenjian Cao, Changfa Tao, Mohsin Raza, and Longfei Chen. Experimental investigation of soot morphology and primary particle size along axial and radial direction of an ethylene diffusion flame via electron microscopy. *Journal of the Energy Institute*, 92(5):1294–1302, 2019.
- [66] Thomas A Witten and Leonard M Sander. Diffusion-limited aggregation. *Physical review B*, 27(9):5686, 1983.
- [67] Leonard M Sander, ZM Cheng, and Roy Richter. Diffusion-limited aggregation in three dimensions. *Physical Review B*, 28(11):6394, 1983.
- [68] Paul Meakin. Diffusion-controlled cluster formation in two, three, and four dimensions. *Physical Review A*, 27(1):604, 1983.
- [69] P Ramanlal and LM Sander. Theory of ballistic aggregation. *Physical review letters*, 54(16):1828, 1985.

- [70] Shoudan Liang and Leo P Kadanoff. Scaling in a ballistic aggregation model. *Physical Review A*, 31(4):2628, 1985.
- [71] Max Kolb, Robert Botet, and Rmi Jullien. Scaling of kinetically growing clusters. *Physical Review Letters*, 51(13):1123, 1983.
- [72] Paul Meakin. Diffusion-limited aggregation in three dimensions: results from a new cluster-cluster aggregation model. *Journal of colloid and interface science*, 102(2):491–504, 1984.
- [73] REMI Jullien and M Kolb. Hierarchical model for chemically limited cluster-cluster aggregation. *Journal of Physics A: Mathematical and General*, 17(12):L639, 1984.
- [74] Fereydoon Family, Paul Meakin, and Tamás Vicsek. Cluster size distribution in chemically controlled cluster–cluster aggregation. *The Journal of chemical physics*, 83(8):4144–4150, 1985.
- [75] Paul Meakin and Fereydoon Family. Structure and dynamics of reaction-limited aggregation. *Physical Review A*, 36(11):5498, 1987.
- [76] Remi Jullien and Paul Meakin. Simple models for the restructuring of three-dimensional ballistic aggregates. *Journal of Colloid and Interface science*, 127(1):265–272, 1989.
- [77] CM Sorensen. The mobility of fractal aggregates: a review. *Aerosol Science and Technology*, 45(7):765–779, 2011.
- [78] Romain Thouy and Remi Jullien. A cluster-cluster aggregation model with tunable fractal dimension. *Journal of Physics A: Mathematical and General*, 27(9):2953, 1994.
- [79] Daniel W Mackowski. Electrostatics analysis of radiative absorption by sphere clusters in the rayleigh limit: application to soot particles. *Applied optics*, 34(18):3535–3545, 1995.
- [80] José Morán, A Fuentes, F Liu, and J Yon. Fracval: An improved tunable algorithm of cluster-cluster aggregation for generation of fractal structures formed by polydisperse primary particles. *Computer Physics Communications*, 239:225–237, 2019.

- [81] S Prasanna, Ph Rivière, and A Soufiani. Effect of fractal parameters on absorption properties of soot in the infrared region. *Journal of Quantitative Spectroscopy and Radiative Transfer*, 148:141–155, 2014.
- [82] Hua Yu, Weijun Li, Yangmei Zhang, Peter Tunved, Manuel Dall’Osto, Xiaojing Shen, Junying Sun, Xiaoye Zhang, Jianchao Zhang, and Zongbo Shi. Organic coating on sulfate and soot particles during late summer in the svalbard archipelago. *Atmospheric Chemistry and Physics*, 19(15):10433–10446, 2019.
- [83] K Adachi and PR Buseck. Internally mixed soot, sulfates, and organic matter in aerosol particles from mexico city. *Atmospheric Chemistry and Physics*, 8(21):6469–6481, 2008.
- [84] William R Heinson, Pai Liu, and Rajan K Chakrabarty. Fractal scaling of coated soot aggregates. *Aerosol Science and Technology*, 51(1):12–19, 2017.
- [85] WH Dalzell and AF Sarofim. Optical constants of soot and their application to heat-flux calculations. 1969.
- [86] Kermit C Smyth and Christopher R Shaddix. The elusive history of  $m = 1.57 - 0.56i$  for the refractive index of soot. *Combustion and flame*, 107(3):314–320, 1996.
- [87] Tami C Bond and Robert W Bergstrom. Light absorption by carbonaceous particles: An investigative review. *Aerosol science and technology*, 40(1):27–67, 2006.
- [88] Michael I Mishchenko, Larry D Travis, and Andrew A Lacis. *Multiple scattering of light by particles: radiative transfer and coherent backscattering*. Cambridge University Press, 2006.
- [89] Craig F Bohren and Donald R Huffman. *Absorption and scattering of light by small particles*. John Wiley & Sons, 2008.
- [90] Matthew James Berg. *A microphysical model of scattering, absorption, and extinction in electromagnetic theory*. Kansas State University, 2008.
- [91] Michael I Mishchenko. *Electromagnetic scattering by particles and particle groups: an introduction*. Cambridge University Press, 2014.

- [92] Romain Ceolato and Matthew J Berg. Aerosol light extinction and backscattering: A review with a lidar perspective. *Journal of Quantitative Spectroscopy and Radiative Transfer*, page 107492, 2020.
- [93] Matthew J Berg, Christopher M Sorensen, and Amitabha Chakrabarti. Extinction and the optical theorem. part i. single particles. *JOSA A*, 25(7):1504–1513, 2008.
- [94] Matthew J Berg, Christopher M Sorensen, and Amitabha Chakrabarti. Extinction and the optical theorem. part ii. multiple particles. *JOSA A*, 25(7):1514–1520, 2008.
- [95] Gustav Mie. Beiträge zur optik trüber medien, speziell kolloidaler metallösungen. *Annalen der physik*, 330(3):377–445, 1908.
- [96] Thomas Wriedt. Mie theory: a review. *The Mie Theory*, pages 53–71, 2012.
- [97] Daniel W Mackowski. Calculation of total cross sections of multiple-sphere clusters. *JOSA A*, 11(11):2851–2861, 1994.
- [98] Romain Ceolato, Florian Gaudfrin, Olivier Pujol, Nicolas Riviere, Matthew J Berg, and Christopher M Sorensen. Lidar cross-sections of soot fractal aggregates: Assessment of equivalent-sphere models. *Journal of Quantitative Spectroscopy and Radiative Transfer*, 212: 39–44, 2018.
- [99] Tiago L Farias, Ümit Özgür Köylü, and M da G Carvalho. Range of validity of the rayleigh-debye-gans theory for optics of fractal aggregates. *Applied optics*, 35(33):6560–6567, 1996.
- [100] CM Sorensen. Light scattering by fractal aggregates: a review. *Aerosol Science & Technology*, 35(2):648–687, 2001.
- [101] Jérôme Yon, Claude Rozé, Thierry Girasole, Alexis Coppalle, and Loïc Méès. Extension of rdg-fa for scattering prediction of aggregates of soot taking into account interactions of large monomers. *Particle & Particle Systems Characterization*, 25(1):54–67, 2008.
- [102] Yan Zhao and Lin Ma. Applicable range of the rayleigh-debye-gans theory for calculating the scattering matrix of soot aggregates. *Applied optics*, 48(3):591–597, 2009.

- [103] Jérôme Yon, Fengshan Liu, Alexandre Bescond, Chloé Caumont-Prim, Claude Rozé, François-Xavier Ouf, and Alexis Coppalle. Effects of multiple scattering on radiative properties of soot fractal aggregates. *Journal of Quantitative Spectroscopy and Radiative Transfer*, 133:374–381, 2014.
- [104] Edward M Purcell and Carlton R Pennypacker. Scattering and absorption of light by non-spherical dielectric grains. *The Astrophysical Journal*, 186:705–714, 1973.
- [105] Bruce T Draine and Piotr J Flatau. Discrete-dipole approximation for scattering calculations. *Josa a*, 11(4):1491–1499, 1994.
- [106] RTH Collis and PB Russell. Lidar measurement of particles and gases by elastic backscattering and differential absorption. In *Laser monitoring of the atmosphere*, pages 71–151. Springer, 1976.
- [107] Paul McManamon. Review of ladar: a historic, yet emerging, sensor technology with rich phenomenology. *Optical Engineering*, 51(6):060901, 2012.
- [108] Heng Wang, Bin Wang, Bingbing Liu, Xiaoli Meng, and Guanghong Yang. Pedestrian recognition and tracking using 3d lidar for autonomous vehicle. *Robotics and Autonomous Systems*, 88:71–78, 2017.
- [109] Xinxin Du, Marcelo H Ang, and Daniela Rus. Car detection for autonomous vehicle: Lidar and vision fusion approach through deep learning framework. In *2017 IEEE/RSJ International Conference on Intelligent Robots and Systems (IROS)*, pages 749–754. IEEE, 2017.
- [110] Ralph A Haugerud, David J Harding, Samuel Y Johnson, Jerry L Harless, Craig S Weaver, and Brian L Sherrod. High-resolution lidar topography of the puget lowland, washington. *GSA Today*, 13(6):4–10, 2003.
- [111] Clément Mallet and Frédéric Bretar. Full-waveform topographic lidar: State-of-the-art. *ISPRS Journal of photogrammetry and remote sensing*, 64(1):1–16, 2009.

- [112] Claus Weitkamp. *Lidar: range-resolved optical remote sensing of the atmosphere*, volume 102. Springer Science & Business, 2006.
- [113] WN Chen, CC Tsao, and JB Nee. Rayleigh lidar temperature measurements in the upper troposphere and lower stratosphere. *Journal of Atmospheric and Solar-Terrestrial Physics*, 66(1):39–49, 2004.
- [114] Edward V Browell. Differential absorption lidar sensing of ozone. *Proceedings of the IEEE*, 77(3):419–432, 1989.
- [115] David N Whiteman, SH Melfi, and RA Ferrare. Raman lidar system for the measurement of water vapor and aerosols in the earth's atmosphere. *Applied optics*, 31(16):3068–3082, 1992.
- [116] G Vaughan, DP Wareing, SJ Pepler, L Thomas, and V Mitev. Atmospheric temperature measurements made by rotational raman scattering. *Applied optics*, 32(15):2758–2764, 1993.
- [117] Ulla Wandinger. Raman lidar. In *Lidar*, pages 241–271. Springer, 2005.
- [118] Petter Weibring, Thomas Johansson, Hans Edner, Sune Svanberg, Barbro Sundner, Valentina Raimondi, Giovanna Cecchi, and Luca Pantani. Fluorescence lidar imaging of historical monuments. *Applied Optics*, 40(33):6111–6120, 2001.
- [119] Marie-Lise Chanin, Anne Garnier, Alain Hauchecorne, and Jacques Porteneuve. A doppler lidar for measuring winds in the middle atmosphere. *Geophysical research letters*, 16(11):1273–1276, 1989.
- [120] William H Hunt, David M Winker, Mark A Vaughan, Kathleen A Powell, Patricia L Lucker, and Carl Weimer. Calipso lidar description and performance assessment. *Journal of Atmospheric and Oceanic Technology*, 26(7):1214–1228, 2009.
- [121] Grégory David, Alain Miffre, Benjamin Thomas, and Patrick Rairoux. Sensitive and accurate dual-wavelength uv-vis polarization detector for optical remote sensing of tropospheric aerosols. *Applied Physics B*, 108(1):197–216, 2012.

- [122] Ronny Engelmann, Thomas Kanitz, Holger Baars, Birgit Heese, Dietrich Althausen, Annett Skupin, Ulla Wandinger, Mika Komppula, Iwona S Stachlewska, Vassilis Amiridis, et al. The automated multiwavelength raman polarization and water-vapor lidar polly xt: the next generation. *Atmospheric Measurement Techniques*, 9(4):1767–1784, 2016.
- [123] Hajime Okamoto, Kaori Sato, Tomoaki Nishizawa, Nobuo Sugimoto, Toshiyuki Makino, Yoshitaka Jin, Atsushi Shimizu, Toshiaki Takano, and Masahiro Fujikawa. Development of a multiple-field-of-view multiple-scattering polarization lidar: comparison with cloud radar. *Optics express*, 24(26):30053–30067, 2016.
- [124] Romain Ceolato, Andres E Bedoya-Velásquez, and Vincent Mouysset. Short-range elastic backscatter micro-lidar for quantitative aerosol profiling with high range and temporal resolution. *Remote Sensing*, 12(20):3286, 2020.
- [125] YB Acharya, Som Sharma, and H Chandra. Signal induced noise in pmt detection of lidar signals. *Measurement*, 35(3):269–276, 2004.
- [126] Torkild Eriksen, Ulf-Peter Hoppe, Eivind V Thrane, and Tom A Blix. Rocketborne rayleigh lidar for in situ measurements of neutral atmospheric density. *Applied optics*, 38(12):2605–2613, 1999.
- [127] T Halldorsson and J Langerholc. Geometrical form factors for the lidar function. *Applied Optics*, 17(2):240–244, 1978.
- [128] Gary G Gimmestad. Reexamination of depolarization in lidar measurements. *Applied optics*, 47(21):3795–3802, 2008.
- [129] SR Pal and AI Carswell. Polarization properties of lidar backscattering from clouds. *Applied optics*, 12(7):1530–1535, 1973.
- [130] Kenneth Sassen and Richard L Petrilla. Lidar depolarization from multiple scattering in marine stratus clouds. *Applied optics*, 25(9):1450–1459, 1986.

- [131] Rj Allen and CMR Platt. Lidar for multiple backscattering and depolarization observations. *Applied optics*, 16(12):3193–3199, 1977.
- [132] Hajime Okamoto, Kaori Sato, Toshiyuki Makino, Tomoaki Nishizawa, Nobuo Sugimoto, Yoshitaka Jin, and Atsushi Shimizu. Depolarization ratio of clouds measured by multiple-field of view multiple scattering polarization lidar. In *EPJ Web of Conferences*, volume 119, page 11007. EDP Sciences, 2016.
- [133] CMR Platt. Remote sounding of high clouds. iii: Monte carlo calculations of multiple-scattered lidar returns. *Journal of Atmospheric Sciences*, 38(1):156–167, 1981.
- [134] Daniel T Gillespie. Stochastic-analytic approach to the calculation of multiply scattered lidar returns. *JOSA A*, 2(8):1307–1324, 1985.
- [135] Andrei V Starkov, M Noormohammadian, and Ulrich G Oppel. A stochastic model and a variance-reduction monte-carlo method for the calculation of light transport. *Applied Physics B*, 60(4):335–340, 1995.
- [136] Qiming Cai and Kuo-Nan Liou. Theory of time-dependent multiple backscattering from clouds. *Journal of Atmospheric Sciences*, 38(7):1452–1466, 1981.
- [137] Maria Mylonaki, Elina Giannakaki, Alexandros Papayannis, Christina-Anna Papanikolaou, Mika Komppula, Doina Nicolae, Nikolaos Papagiannopoulos, Aldo Amodeo, Holger Baars, and Ourania Soupiona. Aerosol type classification analysis using earlinet multiwavelength and depolarization lidar observations. *Atmospheric Chemistry and Physics*, 21(3):2211–2227, 2021.
- [138] DW Mackowski and MI Mishchenko. A multiple sphere t-matrix fortran code for use on parallel computer clusters. *Journal of Quantitative Spectroscopy and Radiative Transfer*, 112(13):2182–2192, 2011.
- [139] Fengshan Liu and Gregory J Smallwood. Radiative properties of numerically generated

- fractal soot aggregates: the importance of configuration averaging. *Journal of heat transfer*, 132(2):023308, 2010.
- [140] Daniel W Mackowski. A simplified model to predict the effects of aggregation on the absorption properties of soot particles. *Journal of Quantitative Spectroscopy and Radiative Transfer*, 100(1-3):237–249, 2006.
- [141] Florian Gaudfrin. *Lidar supercontinuum pour la caractérisation spectrale des milieux diffusants à haute résolution spatiale: Étude numérique et développement instrumental*. PhD thesis, Toulouse, ISAE, 2020.
- [142] N Lu and CM Sorensen. Depolarized light scattering from fractal soot aggregates. *Physical Review E*, 50(4):3109, 1994.
- [143] Rajan K Chakrabarty, Nicholas D Beres, Hans Moosmüller, Swarup China, Claudio Mazzoleni, Manvendra K Dubey, Li Liu, and Michael I Mishchenko. Soot superaggregates from flaming wildfires and their direct radiative forcing. *Scientific reports*, 4:5508, 2014.
- [144] Rajan K. Chakrabarty, Hans Moosmüller, Mark A. Garro, and Christopher B. Stipe. Observation of superaggregates from a reversed gravity low-sooting flame. *Aerosol Sci. Technol.*, 46, 2012.
- [145] Sean P. Kearney and Flint Pierce. Evidence of soot superaggregates in a turbulent pool fire. *Combust. Flame*, 159:3191–3198, 2012.
- [146] Romain Ceolato, Lucas Paulien, Justin B Maughan, Christopher M Sorensen, and Matthew J Berg. Radiative properties of soot fractal superaggregates including backscattering and depolarization. *Journal of Quantitative Spectroscopy and Radiative Transfer*, 247:106940, 2020.
- [147] F. G. Pierce. *Aggregation in Colloids and Aerosols*. Ph.D dissertation, Kansas State University, 2007.
- [148] Bifen Wu, Somesh P Roy, and Xinyu Zhao. Detailed modeling of a small-scale turbulent pool fire. *Combustion and Flame*, 214:224–237, 2020.

- [149] Thomas von Langenthal, Matthias Martin Sentko, Sebastian Schulz, Björn Stelzner, Dimosthenis Trimis, and Nikolaos Zarzalis. Experimental characterization of flame structure and soot volume fraction of premixed kerosene jet a-1 and surrogate flames. *Applied Sciences*, 11(11):4796, 2021.
- [150] Hadi Bordbar, Simo Hostikka, Pascal Boulet, and Gilles Parent. Numerically resolved line by line radiation spectrum of large kerosene pool fires. *Journal of Quantitative Spectroscopy and Radiative Transfer*, 254:107229, 2020.
- [151] Christopher M Sorensen, Wongyo Kim, Dan Fry, Dan Shi, and Amitabha Chakrabarti. Observation of soot superaggregates with a fractal dimension of 2.6 in laminar acetylene/air diffusion flames. *Langmuir*, 19(18):7560–7563, 2003.
- [152] Alexandre Bescond, Jérôme Yon, Thierry Girasole, Corentin Jouen, Claude Rozé, and Alexis Coppalle. Numerical investigation of the possibility to determine the primary particle size of fractal aggregates by measuring light depolarization. *Journal of Quantitative Spectroscopy and Radiative Transfer*, 126:130–139, 2013.
- [153] Alain Miffre, Tahar Mehri, Mirvatte Francis, and Patrick Rairoux. Uv–vis depolarization from arizona test dust particles at exact backscattering angle. *Journal of Quantitative Spectroscopy and Radiative Transfer*, 169:79–90, 2016.
- [154] Gunnar Heskestad. Fire plumes, flame height, and air entrainment. In *SFPE handbook of fire protection engineering*, pages 396–428. Springer, 2016.
- [155] PH Thomas. The size of flames from natural fires. In *Symposium (International) on Combustion*, volume 9, pages 844–859. Citeseer, 1963.
- [156] Dongmei Huang, Chenning Guo, and Long Shi. Experimental investigation on the morphology of soot aggregates from the burning of typical solid and liquid fuels. *Journal of Nanoparticle Research*, 19(3):96, 2017.

- [157] Chao Liu, Yan Yin, Fangchao Hu, Hongchun Jin, and Christopher M Sorensen. The effects of monomer size distribution on the radiative properties of black carbon aggregates. *Aerosol Science and Technology*, 49(10):928–940, 2015.
- [158] J Yon, Fengshan Liu, J Morán, and Andres Fuentes. Impact of the primary particle polydispersity on the radiative properties of soot aggregates. *Proceedings of the Combustion Institute*, 37(1):1151–1159, 2019.
- [159] Yu Wu, Tianhai Cheng, Lijuan Zheng, and Hao Chen. Effect of morphology on the optical properties of soot aggregated with spheroidal monomers. *Journal of Quantitative Spectroscopy and Radiative Transfer*, 168:158–169, 2016.
- [160] Michael I Mishchenko, Li Liu, and Daniel W Mackowski. T-matrix modeling of linear depolarization by morphologically complex soot and soot-containing aerosols. *Journal of Quantitative Spectroscopy and Radiative Transfer*, 123:135–144, 2013.
- [161] Nimeti Doner and Fengshan Liu. Impact of morphology on the radiative properties of fractal soot aggregates. *Journal of Quantitative Spectroscopy and Radiative Transfer*, 187:10–19, 2017.
- [162] Anthony J Illingworth, HW Barker, A Beljaars, Marie Ceccaldi, H Chepfer, Nicolas Clerbaux, J Cole, Julien Delanoë, C Domenech, David P Donovan, et al. The earthcare satellite: The next step forward in global measurements of clouds, aerosols, precipitation, and radiation. *Bulletin of the American Meteorological Society*, 96(8):1311–1332, 2015.
- [163] Martin Kerscher, Wilhelm Krichbaumer, Masoud Noormohammadian, and Ulrich G Ooppel. Polarized multiply scattered lidar signals. *Optical Review*, 2(4):304–307, 1995.
- [164] M Kerscher, M Noormohammadian, and UG Ooppel. Methoden zur bestimmung mikrophysikalischer parameter mit einem mehrkanal-polarisations-lidar. 1995.
- [165] Jessica C Ramella-Roman, Scott A Prah, and Steve L Jacques. Three monte carlo programs

- of polarized light transport into scattering media: part i. *Optics Express*, 13(12):4420–4438, 2005.
- [166] Ft Yusef-Zadeh, M Morris, and RL White. Bipolar reflection nebulae-monte carlo simulations. *The Astrophysical Journal*, 278:186–194, 1984.
- [167] Christian Peest, Peter Camps, Marko Stalevski, Maarten Baes, and Ralf Siebenmorgen. Polarization in monte carlo radiative transfer and dust scattering polarization signatures of spiral galaxies. *Astronomy & Astrophysics*, 601:A92, 2017.
- [168] A Krieger and S Wolf. The scattering order problem in monte carlo radiative transfer. *Astronomy & Astrophysics*, 645:A143, 2021.
- [169] Carole K Hayakawa, Jerome Spanier, and Vasan Venugopalan. Comparative analysis of discrete and continuous absorption weighting estimators used in monte carlo simulations of radiative transport in turbid media. *JOSA A*, 31(2):301–311, 2014.
- [170] Alireza Haghghat. *Monte Carlo methods for particle transport*. Crc Press Boca Raton, FL, 2015.
- [171] Qun Liu, Xiaoyu Cui, Weibiao Chen, Chong Liu, Jian Bai, Yupeng Zhang, Yudi Zhou, Zhipeng Liu, Peituo Xu, Haochi Che, et al. A semianalytic monte carlo radiative transfer model for polarized oceanic lidar: experiment-based comparisons and multiple scattering effects analyses. *Journal of Quantitative Spectroscopy and Radiative Transfer*, 237:106638, 2019.
- [172] Jianing Zhang. On sampling of scattering phase functions. *Astronomy and Computing*, 29:100329, 2019.
- [173] Qiang Lu and Qingming Luo. Phase function of monte carlo simulation of light transport in turbid media. In *Third International Conference on Photonics and Imaging in Biology and Medicine*, volume 5254, pages 122–130. International Society for Optics and Photonics, 2003.

- [174] Hironobu Iwabuchi. Efficient monte carlo methods for radiative transfer modeling. *Journal of the atmospheric sciences*, 63(9):2324–2339, 2006.
- [175] C Cornet, L C-Labonnote, and Frédéric Szczap. Three-dimensional polarized monte carlo atmospheric radiative transfer model (3dmcpol): 3d effects on polarized visible reflectances of a cirrus cloud. *Journal of Quantitative Spectroscopy and Radiative Transfer*, 111(1):174–186, 2010.
- [176] Yongxiang Hu, Zhaoyan Liu, David Winker, Mark Vaughan, Vincent Noel, Luc Bissonnette, Gilles Roy, and Matthew McGill. Simple relation between lidar multiple scattering and depolarization for water clouds. *Optics letters*, 31(12):1809–1811, 2006.
- [177] Natasha L Miles, Johannes Verlinde, and Eugene E Clothiaux. Cloud droplet size distributions in low-level stratiform clouds. *Journal of the atmospheric sciences*, 57(2):295–311, 2000.
- [178] Benjamin J Sumlin, William R Heinson, and Rajan K Chakrabarty. Retrieving the aerosol complex refractive index using pymiescatt: A mie computational package with visualization capabilities. *Journal of Quantitative Spectroscopy and Radiative Transfer*, 205:127–134, 2018.
- [179] Yong-X Hu, David Winker, Ping Yang, Bryan Baum, Lamont Poole, and Lelia Vann. Identification of cloud phase from picasso-cena lidar depolarization: A multiple scattering sensitivity study. *Journal of quantitative spectroscopy and radiative transfer*, 70(4-6):569–579, 2001.
- [180] Maarten Baes, Karl D Gordon, Tuomas Lunttila, Simone Bianchi, Peter Camps, Mika Juvela, and Rolf Kuiper. Composite biasing in monte carlo radiative transfer. *Astronomy & Astrophysics*, 590:A55, 2016.
- [181] Michael Kahnert and Ronald Scheirer. Multiple scattering by aerosols as seen from calipso—a monte-carlo modelling study. *Optics express*, 27(23):33683–33699, 2019.
- [182] Romain Ceolato, Andres Bedoya-Velasquez, Frederic Fossard, Vincent Mouysset, Lucas Paulien, Sidonie Lefebvre, Claudio Mazzoleni, Christopher Sorensen, Matthew Berg, and

Jerome Yon. Black carbon aerosol number and mass concentration measurements by picosecond short-range elastic backscatter lidar. 2021.

[183] Georgios A Kelesidis, Christian A Bruun, and Sotiris E Pratsinis. The impact of organic carbon on soot light absorption. *Carbon*, 172:742–749, 2021.

[184] Richard A Dobbins and Constantine M Megaridis. Absorption and scattering of light by polydisperse aggregates. *Applied optics*, 30(33):4747–4754, 1991.

[185] Li Liu and Michael I Mishchenko. Scattering and radiative properties of morphologically complex carbonaceous aerosols: A systematic modeling study. *Remote Sensing*, 10(10):1634, 2018.

[186] Michael Kahnert. Optical properties of black carbon aerosols encapsulated in a shell of sulfate: comparison of the closed cell model with a coated aggregate model. *Optics express*, 25(20):24579–24593, 2017.

**Titre:** Modélisation de signaux lidar résolus en polarisation pour la caractérisation d'agrégats fractals de suie avec prise en compte de la diffusion multiple

**Mots clés:** Lidar, Suie, Modélisation, Polarisation, Diffusion Multiple

**Résumé:** Afin d'évaluer l'impact des particules de suie sur le climat et sur la qualité de l'air, leurs émissions doivent être surveillées. Les instruments lidar peuvent permettre d'apporter les mesures nécessaires. Néanmoins, l'analyse de signaux lidar requiert la connaissance des propriétés radiatives des particules et cette analyse peut être sujette à des erreurs liées à la diffusion multiple. De plus, ces propriétés radiatives dépendent des caractéristiques microphysiques des particules, telles que leurs formes ou leurs tailles. L'objectif de cette thèse est de simuler des signaux lidar résolu en polarisation, acquis sur des particules de suie et prenant en compte la contribution de la diffusion multiple. Cela nécessite la modélisation de la morphologie et des propriétés radiatives des particules de suies, ainsi que le développement d'une méthode permettant de simuler les signaux lidar. Ainsi, plusieurs modèles morphologiques sont utilisés afin de simuler des particules de suie. La méthode de Superposition

de T-Matrice et la théorie de Rayleigh-Debye-Gans pour les agrégats fractals sont ensuite utilisées afin de modéliser les propriétés radiatives de ces particules. L'impact des paramètres morphologiques sur ces propriétés radiatives est étudié. Une évaluation expérimentale du ratio de dépolarisation des particules de suie dans l'air ambiant est également présentée. Cela permet d'identifier quels paramètres morphologiques et indices optiques permettent de reproduire les résultats expérimentaux. De plus, les limites des méthodes numériques utilisées peuvent également être identifiées. Un modèle numérique de simulation de signaux lidar résolu en polarisation est développé en utilisant la méthode Monte-Carlo. Des simulations numériques sont entreprises afin d'évaluer l'impact de la diffusion multiple sur des signaux lidar résolus en polarisation acquis sur des particules de suie. Ce modèle numérique est également utilisé afin d'analyser un signal expérimental. Ceci permet d'évaluer la contribution de la diffusion multiple dans ce signal.

**Title:** Modeling of polarization-resolved lidar signals for the characterization of soot fractal aggregates accounting for multiple scattering

**Keywords:** Lidar, Soot, Modeling, Polarization, Multiple Scattering

**Abstract:** To better ascertain the effect of soot particles on climate change and air quality, the monitoring of the emission of these particles is needed. Lidar instruments can provide such measurements. Nevertheless, the analysis of lidar signals requires the knowledge of the particles radiative properties and can be subject to error due to multiple-scattering effects. Moreover, the radiative properties of such particles depend on their micro-physical characteristics, such as shape and size. The objective of this thesis is to simulate polarization-resolved lidar signals acquired on soot particles accounting for multiple-scattering. This requires the modelling of the morphology and of the radiative properties of these particles and the development of a lidar signal simulation code. Several morphological models are used to simulate soot particles. The Superposition T-Matrix method and the Rayleigh-Debye-Gans

for Fractal Aggregates theory are then used to compute their radiative properties. The impacts of the morphological parameters on the radiative properties are studied. A laboratory evaluation of the linear depolarization ratio of soot particles in ambient air is also presented and the range of morphological parameters and optical indices reproducing the experimental results is identified. The limits of the numerical model are also highlighted. A numerical model is developed for the simulation of polarization-resolved lidar signals using the Monte-Carlo method. Simulations are undertaken to investigate if lidar measurements performed over scattering media composed of freshly emitted soot particles are influenced by multiple-scattering, and to quantify this impact. The lidar signal simulation model is also used to reanalyse experimental lidar signals. This allows the evaluation of the contribution of multiple-scattering in the retrieved signal.